

A Cumulative Dissertation approved by the Department of Materials Science
in fulfillment of the requirements for the degree of Doktor-Rerum Naturalium (Dr. rer. nat.)

Formability, synthesis and properties of perovskite-type oxynitrides

M. Sc. Wenjie Li

From Shaanxi, Xi'an, China

Matrikel-Nr. 1818136



TECHNISCHE
UNIVERSITÄT
DARMSTADT

Referee: Prof. Dr. Ralf Riedel

Co-referee: Prof. Dr. Zhijian Shen

Fachbereich Material- und Geowissenschaften
Technische Universität Darmstadt

Date of submission: 17.08.2015

Date of oral examination: 24.11.2015

Darmstadt 2015

D 17

Declaration

M. Sc. Wenjie Li
Nieder-Ramstädter-str. 11
64283 Darmstadt

Declaration

This work described in this thesis was carried out at the Department of Materials Science, Technische Universität Darmstadt during the period October 2011 to June 2015. This thesis represents the author's original work, except where otherwise stated, and no part of it has been submitted for a degree at any other university. Prior to the submission of this thesis, some work has been published as described in the relevant chapters herein.

Eidesstattliche Erklärung

Hiermit erkläre ich an Eides statt, dass ich die vorliegende Dissertation selbstständig und nur mit den angegebenen Hilfsmitteln angefertigt habe. Von mir wurde weder an der Technischen Universität Darmstadt noch einer anderen Hochschule ein Promotionsversuch unternommen.

Darmstadt, den 10.08.2015

Wenjie Li

Acknowledgements

Acknowledgements

I would like to acknowledge all the people who supported me during my PhD period:

- My deep thanks and respect to Prof. Dr. Ralf Riedel, who gave me the opportunity to work in his group. Many thanks for his supervision, constant support and encouragement during my study.
- My heartfelt gratitude to Prof. Dr. Aleksander Gurlo and PD Dr. Emanuel Ionescu, who led me into the oxynitride field. Warm thanks for their outstanding scientific supervision, productive discussions and encouragement during my entire PhD period, which improved my work and working discipline.
- Thanks to Prof. Alexandra Navrotsky, Dr. Amir Hossein Tavakoli, Dr. Philip Jones from UC Davis for calorimetric experimental support and discussion.
- I would like to acknowledge the beam scientists Dr. Denis Cheptiakov, Dr. Vladimir Pomjakushin, Dr. Stefan Zander and Dr. Emmanuelle Suard from PSI (SINQ), HZB (E9) and ILL (D2B) for their technical support with neutron experiments.
- Thanks to Dipl.-Ing. Claudia Fasel for elemental analysis instruction, TG/MS measurements and lots of technical help in daily lab work.
- I'd like to acknowledge M. Sc. Duan Li from the Stockholm University for the close collaboration with SPS, SEM and TEM experiments and measurements.
- Thanks to Dipl.-Ing. Jean-Christophe Jaud for the XRD measurement introduction.
- Thanks to Dr. Erwin Hildebrandt for the help with SQUID instruction.
- Warm thanks to Dr. Bekheet Maged for teaching me Fullprof refinement and nice discussions.
- Thanks to M. Sc. Cristina Schitco and M. Sc. Qingbo Wen for the help of BET measurements.
- Thanks to Dipl.-Ing. Lukas Schlicker for the instruction of photocatalytic instrument.
- Thanks to M. Sc. Jia Yuan for the help of SEM measurements.
- Thanks to M. Sc. Van Lam Nguyen from the University of Trento for the help of electrical conductivity measurements.
- Thanks to all the FUNEA partners for the memorable moment we spend together and the people involved in the FUNEA for their great effort on the organization of practical courses.
- Thanks to M. Sc. Jia Yuan, M. Sc. Cong Zhou, M. Sc. Qingbo Wen and M. Sc. Xifan Wang for helping with lab works and Böbling Karen, Arnold Nadine, Tania Fielder-Valderrama, Shobha Herur and Su-Chen Chang for the help with documentation.
- Warm thanks to my officemates M. Sc. Sarabjeet Kaur, M. Sc. Cristina Schitco and M. Sc. Cong Zhou who are companying me, helping me, comforting me and supporting me in the last four years.
- Thanks to all the DF members for the great time we spend together during my PhD.
- Thanks to all the friends I met here in Darmstadt and all over the world for sharing great time with you guys on football, beer, party, journey and everything.
- I would like to greatly acknowledge the FUNEA-Functional Nitrides for Energy Applications project funded by the European Union Seventh Framework Programme (FP7/2007-2013) for the financial support.
- Lastly my thanks go to my beloved parents and family for their loving considerations and great confidence in me all through these years. A special thanks to my wife, Na Liu, for all her support in the past and her love for life.

Dedicated to my wife and parents

“Learn today. Lead tomorrow.”

“Where there is a will there is a way”

“有志者，事竟成”

The presented cumulative dissertation summarizes the essential scientific findings, which were reported to the scientific community in the following peer-reviewed journals. The reports itself [1] – [5] are enclosed in the Chapter *Cumulative Publications* of this thesis.

- [1] W. J. Li, E. Ionescu, R. Riedel and A. Gurlo, “Can we predict the formability of perovskite oxynitrides from tolerance and octahedral factors?”, *Journal of Materials Chemistry A*, **2013**, 1, (39), 12239-12245
- [2] W. J. Li, D. Li, X. Gao, A. Gurlo, S. Zander, P. Jones, A. Navrotsky, Z. J. Shen, R. Riedel and E. Ionescu, “A study on the thermal conversion of scheelite-type ABO_4 into perovskite-type $AB(O,N)_3$ ”, *Dalton Transactions*, **2015**, 44, 8238-8246
- [3] W. J. Li, D. Li, A. Gurlo, Z. J. Shen, R. Riedel and E. Ionescu, “Synthesis and rapid sintering of dense $SrA(O,N)_3$ ($A=Mo, W$) oxynitride ceramics”, *Journal of the European Ceramic Society*, 35 (**2015**), 3273-3281
- [4] D. Li, W. J. Li, C. Fasel, J. Shen and R. Riedel, “Sinterability of the oxynitride $LaTiO_2N$ with perovskite-type structure”, *Journal of Alloys and Compounds*, 586 (**2014**), 567-573
- [5] W. J. Li, A. Gurlo, R. Riedel and E. Ionescu, “Perovskite-type solid-solution $SrMo_{1-x}W_x(O,N)_3$ oxynitrides: synthesis, structure and magnetic properties”, *Zeitschrift für Anorganische und Allgemeine Chemie*, **2015**, 641, (8-9), 1533-1539

Table of contents

Declaration	I
Acknowledgements	II
Table of contents	V
List of abbreviations	VII
1. Introduction.....	1
1.1 Perovskite materials	1
1.1.1. Merit of oxides, nitrides and oxynitrides	1
1.1.2. Formability of perovskite oxides and corresponding oxynitrides.....	1
1.1.3. Synthesis of oxynitrides	2
1.2 Oxide precursors	8
1.2.1. Perovskite	9
1.2.2. Scheelite.....	10
1.2.3. Pyrochlore	11
1.3 Anionic ordering	13
1.4 Applications of oxynitrides	15
1.4.1. Band theory	15
1.4.2. Optical properties.....	16
1.4.3. Photocatalytic properties	19
1.4.4. Conductivity.....	24
1.4.5. Magnetic properties.....	26
1.5 Scope of the present work	28
2. Critical assessment of the present thesis	30
2.1 The formability of perovskite-type oxynitrides.....	30
2.1.1. Results and discussion.....	30
2.1.2. Statement of personal contribution.....	34
2.2 A study on the thermal conversion of scheelite-type ABO_4 into perovskite-type $AB(O,N)_3$	36
2.2.1. Results and discussion.....	36
2.2.2. Statement of personal contribution.....	45
2.3 Densification of perovskite-type oxynitride ceramics.....	47
2.3.1. Results and discussion.....	47
2.3.2. Statement of personal contribution.....	57
2.4 Solid-solution perovskite-type $SrMo_{1-x}W_x(O,N)_3$ oxynitrides	59
2.4.1. Results and discussion.....	59
2.4.2. Statement of personal contribution.....	63
3. A preliminary study on the synthesis and photocatalytic properties of $BaTa(O,N)_3$.....	64

3.1	Introduction.....	64
3.2	Experimental method.....	64
3.2.1	<i>Synthesis</i>	64
3.2.2	<i>Sample characterization</i>	65
3.2.3	<i>Photocatalytic test</i>	65
3.3	Results and discussion.....	66
3.3.1	<i>Thermal ammonolysis</i>	66
3.3.2	<i>Microstructure of as-synthesized oxynitrides</i>	74
3.3.3	<i>UV-Vis spectroscopy and band gaps</i>	76
3.3.4	<i>Photocatalytic properties</i>	78
3.4	Conclusions.....	82
4.	Summary and Outlook.....	84
4.1	Summary.....	84
4.2	Outlook.....	86
5.	References.....	88
	Cumulative publications.....	93
	List of publications	
	Curriculum Vitae	

List of abbreviations

AK	Arbeitskreis / Working group
ΔG_f^0	Standard Gibbs free energy of formation at 298.15 K (25 °C)
ΔG	Gibbs free energy of formation
ΔH_f^0	Standard enthalpy of formation at 298.15 K (25 °C)
ΔH	Enthalpy of formation
S^0	Standard entropy of formation at 298.15 K (25 °C)
CB	Conduction band
VB	Valence band
CN	Coordination number
E_g	Band gap
TD	Theoretical density
MB	Methylene blue
MO	Methyl orange
RhB	Rhodamine B
σ	Electrical conductivity
ρ	Electrical resistivity
χ	Magnetic susceptibility
w%	Weight percent
$t_{\text{tolerance}}$	Tolerance factor
$t_{\text{octahedral}}$	Octahedral factor
LC	Large amount of commercial powder
SC	Small amount of commercial powder

AS	As-synthesized powder
NH _{xxx}	Ammonolysis at xxx °C
SMW	SrMo _(1-x) W _x O ₄
SSR	Solid state reaction
PCM	Polymeric complex method
PCM_900_Na	Ammonolysis of the oxide precursor synthesized via PCM with NaCl
SSR_900_NaK	Ammonolysis of the oxide precursor synthesized via SSR with NaCl/KCl
SrMoO ₄ _NH700_24H	Ammonolysis of the SrMoO ₄ at 700 °C for 24 hours
k _{obs}	Limiting rate constant of the photocatalytic reaction
PSC	Powder-Solution-Composite
XRD	X-ray diffraction
ND	Neutron diffraction
FTIR	Fourier transformed infrared spectroscopy
EDS	Energy dispersive X-ray spectroscopy
SEM	Scanning electron microscopy
HRTEM	High-resolution transmission electron microscopy
TEM	Transmission electron microscopy
TG/MS	Thermogravimetry coupled with mass spectroscopy
TGA	Thermogravimetric analysis
DTA	Differential thermal analysis
SPS	Spark plasma sintering
SQUID	Superconducting quantum interference device
BET	Brunauer-Emmett-Teller theory

1. Introduction

1.1 Perovskite materials

1.1.1. Merit of oxides, nitrides and oxynitrides

Perovskite materials can be represented by the composition ABX_3 , with A being a relatively large cation of usually low charge, such as rare earth, alkaline earth or alkali metal, the smaller B cations being typically transition metals, and X is an anion such as O^{2-} , N^{3-} , SO_4^{2-} or F. Oxygen and nitrogen have lots of similarities, *e.g.*, their ionic radii ^[1, 2], electronegativity, polarizabilities and coordination in solid state as summarized in Table 1.1 ^[1, 3, 4]. Thus, it is quite easy to substitute each other leading to similar crystallographic structures, such as oxynitrides, oxyfluorides *etc.* Despite the mentioned similarities, they also have distinct crystallochemical and electronic properties. Hence, oxygen and nitrogen substitutions can strongly affect the properties of materials due to the different charges and the corresponding difference of ionicity of the metal-anion bond.

Table 1.1 Crystallochemical and electronic properties of O and N

Parameters	O	N
Charge (z)	-2	-3
Ionic radii (Å) (for CN=IV)	1.40	1.50
Coordination number (CN)	II - VIII	II - VIII
Electronegativity	3.4	3.0
Atomic polarizability (Å ³)	0.80	1.10
Electron affinity (A - A ^{Z-} , kJ/mol)	601	1736
Bond energy A-A (kJ/mol)	498	941

Nitrides are thermodynamically less stable than oxides and the triple bond in molecular nitrogen is extremely strong. Meanwhile, the preparation of pure nitrides is rather difficult as well. Nevertheless, oxynitrides can combine the advantages of both oxides and nitrides and have greater stability in air and moisture if compared to that of metal nitrides. In addition, they allow for the formation of perovskite compounds with compositions which are not achievable in perovskite oxides resulting in promising physical and chemical properties. Due to the development of synthetic methodology within the last decades, perovskite-type oxynitrides have been investigated intensively concerning their novel and intriguing physical and chemical properties.

1.1.2. Formability of perovskite oxides and corresponding oxynitrides

The vast majority of functional ceramics used nowadays are based on mixed metal oxides. Among them, perovskite-type oxides remain prominent ^[5]. Numerous perovskite-type oxides have been intensively addressed in various application fields ^[5-7]. Consequently, regularities governing the formation of perovskite-type oxide compounds used to further guide the exploration of new oxide materials were studied considered by using different approaches ^[8-12], which promote the development of synthesis work ^[13-19]. Compared to oxide,

the formability of perovskite oxynitrides is actually to be uncovered. Only few studies have been reported for anion bonding ^[20, 21], distribution ^[22], or functionality prediction of perovskite oxynitrides ^[23, 24]. However, a simple tool that allows for the first assessment of the formability of perovskite oxynitrides and helps in selecting suitable compositions for the synthesis as it has been done for perovskite oxides has been missing so far.

1.1.3. Synthesis of oxynitrides

The conventional route for oxynitride synthesis is the thermal ammonolysis of oxides, which in general can apply a nitrogen source either from N₂ or NH₃. However, the high stability of the N₂ molecule (the enthalpy of dissociation is 945 kJ/mol, approximately twice as large as that of the O₂ molecule) normally requests an extremely high activation energy. It was proven experimentally that the H₂/N₂-mixtures do not enhance effective nitridation as well. ^[25] Actually, ammonia NH₃ is widely used as nitriding source at ambient atmosphere in the temperature range of T= 600 ~ 1100 °C.

The dissociation of ammonia at the sample surface, suggested as forming active nitriding species (N, NH, NH₂) and molecular H₂, is the major reason why ammonia NH₃ is so effective. ^[26, 27] The overall dissociation behavior of ammonia at temperature below 500 °C can be summarized as Equation 1-1; whereas, the competition from Equation 1-1 to 1-4 always exists (Figure 1.1). However, molecule N₂ is not effective for nitridation, and by analogy with the nitridation of metals, a more important consideration at high temperature is the generation of active nitrogen species ^[27], as shown following from Equation 1-2 to Equation 1-4. These active nitrogen species react with the powder sample on the surface.



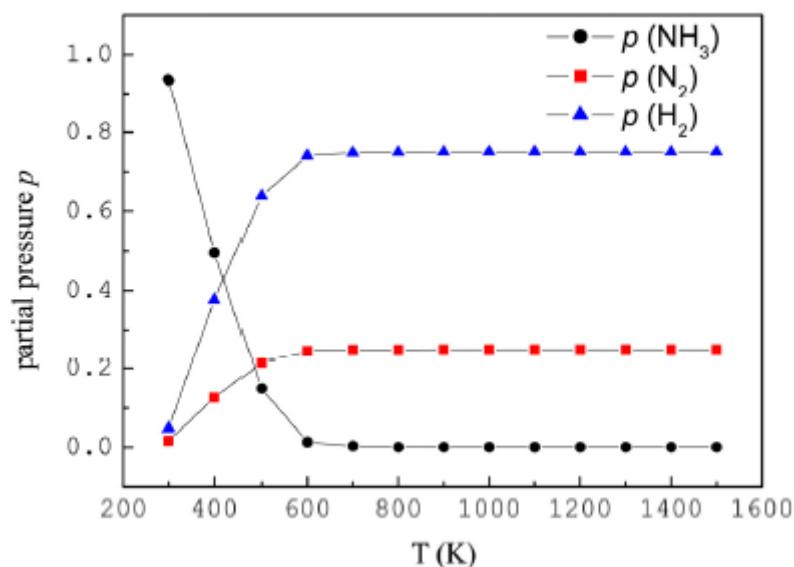


Figure 1.1 Temperature dependence of equilibrium partial pressure of gaseous NH_3 , H_2 and N_2 [28]

Meanwhile, the exchange between oxide anions and absorbed nitrogen occurs and hydrogen reacts with oxygen to form water which is removed by means of flowing gas system, thus preventing possible back-side reactions. The formation of thermodynamic stable molecules such as H_2O ($\Delta G_f^0(1000) = 192.603 \text{ kJ/mol}$) and CO_2 ($\Delta G_f^0(1000) = -395.865 \text{ kJ/mol}$) as well as the overall entropy increase is the major driving force of the ammonolysis procedure. Thus, it is important to increase ammonia flow with temperature, which speeds up water removal and the renewal of active nitrating species over the sample. Certainly, besides the gas flow rate, there are numerous intrinsic and extrinsic parameters such as temperature distribution, reaction time, sample placement, furnace configuration as well as the homogeneity and nature of the precursor, which can influence the ammonolysis reaction process as following:

- a) Both the reaction rate and degree of ammonia dissociation increases along the furnace tube till reaching a maximum near the start of the hot zone and decreases sharply after the hot zone [27]. In order to minimize a premature dissociation of ammonia, it is important to limit the exposure of NH_3 to elevated temperatures prior to the reaction zone, as shown in Figure 1.2 (a) [29]. Thus, the sample should be placed as close as possible from the inlet to guarantee the reaction zone located in the homogeneous temperature zone.
- b) The upper limitation of the ammonolysis temperature is controlled by enhanced NH_3 decomposition and structure instability of the oxynitrides [29, 30]. While, the lower limit on temperature is defined by the reaction kinetics. [31]
- c) As mentioned above, the increasing of the flow rate is beneficial for the thermal ammonolysis. However, there are limitations as well. Inadequate high flow rate may result in the formation of

binary nitride impurity, *i.e.*, Ta_3N_5 in the $BaTaO_2N$ system^[29], which implies that solid-state transport is insufficient to stabilize mixed anion $Ta(O,N)_6$ octahedra, while nitridation to binary components occur at the surface.

- d) Sample placement, which is related to temperature distribution, flow rate, gas composition *etc.*, contribute to the formation of oxynitride as well. Brophy *et. al.*^[29] reported that cell volume decreased with the distance of sample away from gas inlet (Figure 1.2 b). Thus, it is difficult to synthesize large amount of homogeneous oxynitride in one experiment via conventional furnace.
- e) Rotary furnace has been developed in recent years^[32, 33]. It can enhance the sample surface exposure to the NH_3 stream and commonly improve the powder homogeneity. As it has been reported^[29], ~ 30 g $BaTaO_2N_{0.98(3)}$, with nearly ideal stoichiometry, was synthesized via rotary furnace at 1000 °C for 20 h.
- f) The most important feature to determine the thermal ammonolysis behavior is the homogeneity and nature of precursors. Both amorphous and crystalline oxides are considered as suitable precursors.

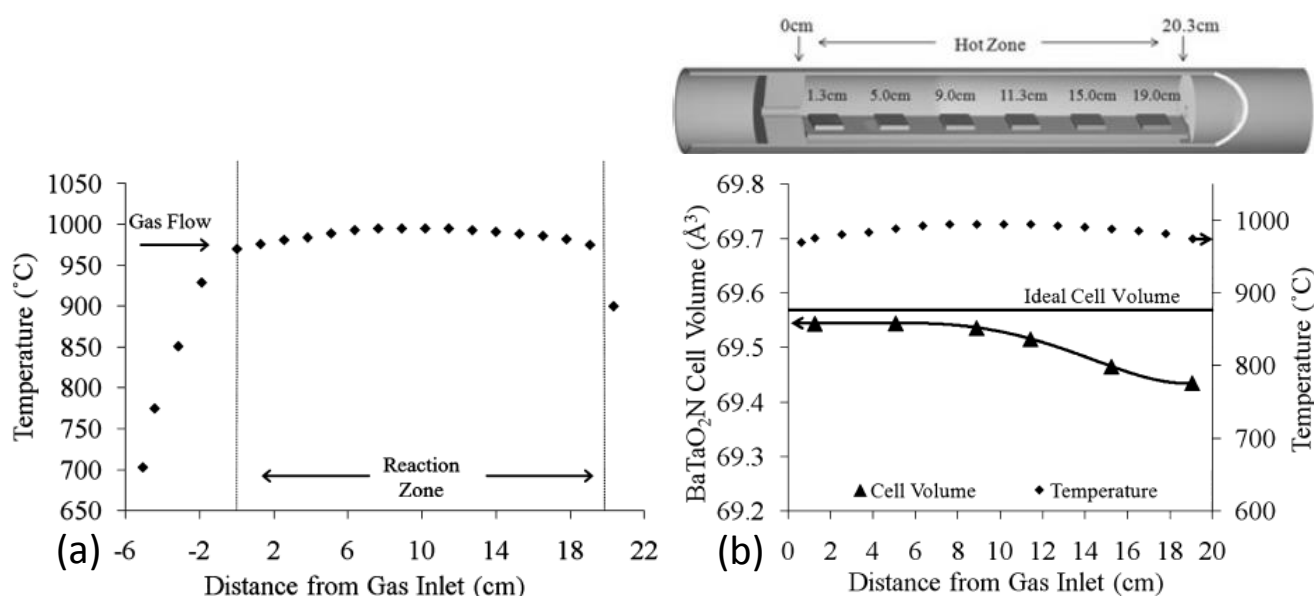


Figure 1.2 The determinant parameters upon thermal ammonolysis (a) temperature profile of furnace at a setpoint of 1000 °C; (b) $BaTaO_2N$ cell volume as a function of distance from gas inlet (1000 °C, 20 h, 2.5 cm^3/min , NH_3 flow). Ideal cell volume obtained^[34]^[29]

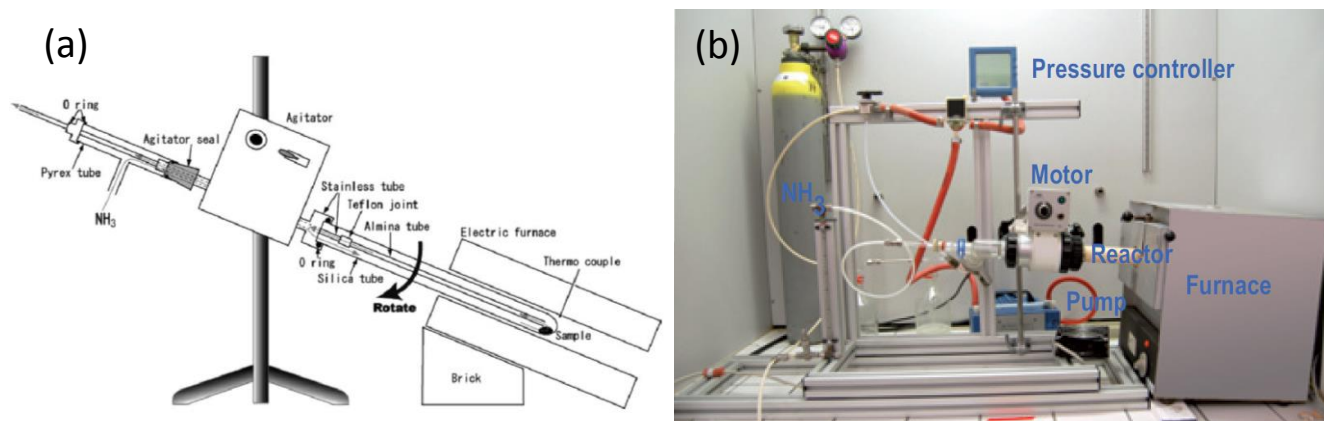


Figure 1.3 Schematic of the handmade rotary furnace: (a) Katsumata *et al.* [33]; (b) R. Aguiar *et al.* [32]

In order to overcome the disadvantages of conventional thermal ammonolysis, a few novel synthesis approaches have been investigated in the past. For examples, a technique based on the introduction of oxophilic molecules, such as CCl_4 , into the reaction mixture was reported by Kachina in 2012 [35]. The treatment of titanium dioxide powders by $\text{NH}_3 - \text{CCl}_4$ mixtures shows a great advantage on equilibrium conditions (Figure 1.4) and leads to highly dispersed N-doped TiO_2 , which showed a stronger red shift in optical absorption and enhanced photocatalytic activity under visible light, as demonstrated for two following reactions (Equation 1-5 and Equation 1-6) of formic acid oxidation and photocatalytic production of hydrogen from methanol. Another benefit for this route is that the nitridation temperature can be significantly decreased by introducing CCl_4 due to a favorable change of the reaction thermodynamics. Not only a higher specific surface area of materials can be obtained as a result of avoiding sintering, but also a higher amount of nitrogen is introduced.

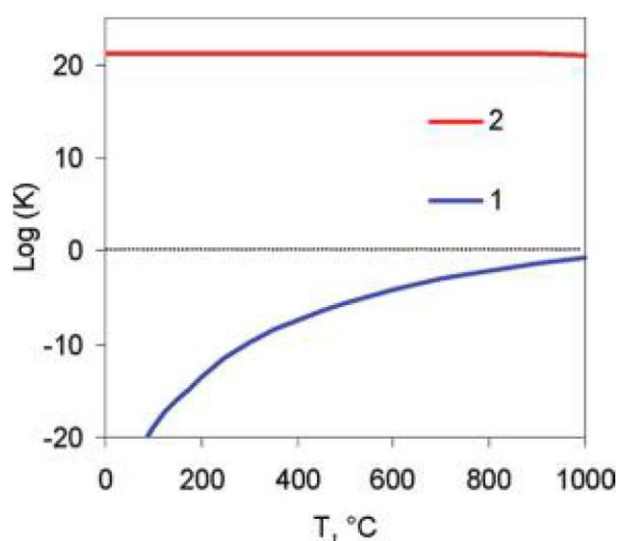
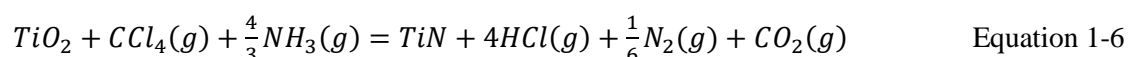
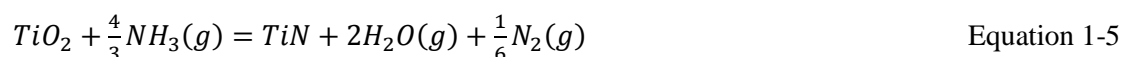


Figure 1.4 Equilibrium constants of TiO_2 nitridation to TiN vs temperature, according to reactions 1-5 (blue line 1) and 1-6 (red line 2)

[35]

Other reactive nitrogen source, *i.e.* urea, offers a feasible route for oxynitride synthesis as well. Ternary $ATaO_2N$ ($A=Ca, Sr, Ba$), $ANbO_2N$ ($A=Sr, Ba$), $LaTiO_2N$ and $SrMoO_{3-x}N_x$ oxynitride nanoparticles have been prepared by mixing metal oxides with excess urea and subsequently heating in N_2 atmosphere [36]. Decomposition of urea offers active ammonia upon 250 °C, *i.e.*:



Flux additives are known to expedite thermal ionic diffusion in the solid state by providing a molten medium, thereby lowering the activation barriers to the synthesis and sintering of ceramics. Using halide mineralizers (*e.g.* NaCl/KCl) as a flux can decrease the ammonolysis temperature and reaction time significantly [37-39]. With these halide additives, $SrNbO_2N$, $BaNbO_2N$ and $CaTaO_2N$ were obtained by ammonolysis at 950 °C for 36, 72 and 18 hours respectively compared to the halide-free approach which required 54, 90 and 36 hours respectively [39]. Moreover, flux-assisted ammonolysis can lead to a higher degree of crystallinity and a lower N/O ratio, resulting in a decrease in the concentration of optical defects in the oxynitride products and chromaticity of oxynitride is enhanced significantly (Figure 1.5) [38].

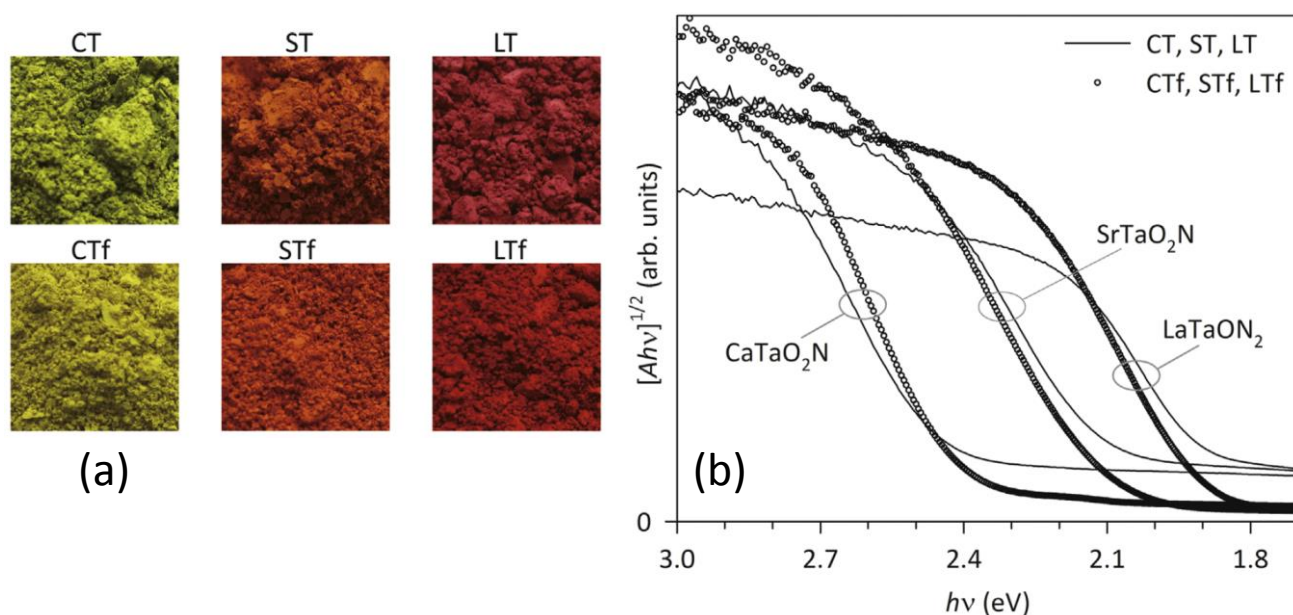
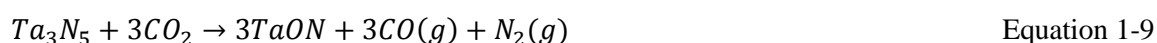


Figure 1.5 (a) Photographic images and (b) UV-Vis absorbance spectra of $CaTaO_2N$ (CT, CTf), $SrTaO_2N$ (ST, STf) and $LaTaON_2$ (LT, LTf) [38] (f indicates flux)

Direct high-pressure solid-state reaction without the use of gaseous ammonia or nitrogen atmospheres provides another convenient route for oxynitride synthesis because the pressure suppresses decomposition and stabilizes structures with high coordination numbers such as perovskite and spinel, *i.e.*, ternary spinel Ga_3O_3N by direct reaction of Ga_2O_3 and GaN at 5 GPa pressure and 1500 ~ 1700 °C [40] or La_2VO_3N by La_2O_3 and VN at

5 GPa and 1200 °C^[41]. New oxynitrides of $RZrO_2N$ ($R=Pr, Nd$ and Sm) have been synthesized via direct solid-state reaction of R_2O_3 with Zr_2ON_2 at 1200 ~ 1500 °C under 2 ~ 3 GPa pressure^[42]. On the other hand, direct high-temperature solid-state reactions with nitrogen atmosphere is essential to prevent reduction of early transition metal. Clark *et. al.* reported that $ATaO_2N$ ($A=Ca, Ba, Sr$) was synthesized through AO and $TaON$ at 1 atm of pure N_2 gas for few hours between 1200 ~ 1500 °C^[43] and they mentioned the method of inductive heating they applied ensures that the nitrogen atmosphere above the sample is maintained free of oxygen and water. Tassel *et. al.* illustrated that $MnTaO_2N$ adopts the $LiNbO_3$ -type structure is synthesized at 6 GPa and 1400 °C^[44]. According to Sun's work^[45], $SrTaO_2N$ was achieved via heating of $Ta_3N_5/SrCO_3$ mixture at 700 ~ 1100 °C in flowing N_2 of 100 ml/min as shown in the following reactions:



So far, the formation of perovskite-type oxynitrides of the general formula $AB(O,N)_3$ (or $(A^1, A^2)B(O,N)_3, A(B^1, B^2)(O,N)_3$) has been summarized in following Table 1.2.

Table 1.2 State of the art of perovskite-type oxynitrides, their structures and synthesis methods

Compounds	Space group	Synthesis route	Ref.
$SrWO_2N$	$Pm\bar{3}m$	$SrWO_4, NH_3, 900\text{ }^\circ\text{C}, 72\text{ h}$	[46]
$SrMoO_{2.5}N_{0.5}$	$Pm\bar{3}m$	$SrMoO_4, NH_3, 800\text{ }^\circ\text{C}, 48\text{ h}$	[46]
$BaTaO_2N$	$Pm\bar{3}m$	$BaCO_3 + Ta_2O_5, NH_3, 1000\text{ }^\circ\text{C}, 60\text{ h}$ with intermediate grindings	[47, 48]
		$BaO + TaON, N_2, 1500\text{ }^\circ\text{C}, 3\text{ h}$	[43]
$BaNbO_2N$	$Pm\bar{3}m$	$BaCO_3 + Nb_2O_5, NH_3, 950\text{ }^\circ\text{C}, 60\text{ h}$ with intermediate grindings	[47, 48]
$EuNbO_2N$	$Pm\bar{3}m$	$EuNbO_4, NH_3, 840\text{ }^\circ\text{C}, 12\text{ h} \times 3\text{ times}$	[49]
$EuTaO_2N$	$Pm\bar{3}m$	$Eu_2O_3 + TaCl_5$ (citrate route), $NH_3, 1000\text{ }^\circ\text{C}, 15\text{ h}$	[50]
$EuWO_{1.58}N_{1.42}$	$Pm\bar{3}m$	$Eu_2W_2O_9, 900\text{ }^\circ\text{C}, 24\text{ h} \times 2\text{ times}$	[51]
$Ca_xSr_{1-x}WO_2N$ ($x=0.25, 0.5$)	$Pm\bar{3}m$	$Ca_xSr_{1-x}WO_4$ (solid state), $900\text{ }^\circ\text{C}, 5\text{ h}$	[52]
$Ba_{1-x}Sr_xTaO_2N$	$Pm\bar{3}m$	$BaTaO_2N + SrTaO_2N, NH_3, 850\text{ }^\circ\text{C}$	[53]
$SrMo_{1-x}W_x(O,N)_3$	$Pm\bar{3}m$	$SrMo_{1-x}W_xO_4$ (solvothermal), $NH_3, 700 \sim 900\text{ }^\circ\text{C}, 6\text{ h}$	[54]
$BaA_{0.2}Ta_{0.8}O_{2.8}N_{0.2}$ ($A=Li, Na$)	$Pm\bar{3}m$	$BaCO_3 + Ta_2O_5$ to $Ba_5Ta_4O_{15}$, then $Ba_5Ta_4O_{15} + A_2CO_3, NH_3$, firstly $750\text{ }^\circ\text{C}$ 12 h, then $900\text{ }^\circ\text{C}$ 12 h \times 3 times, and finally $950\text{ }^\circ\text{C}$ 12 h \times 3 times	[55]
$Sr_{1-x}La_xTiO_{3-x}N_x$	$Pm\bar{3}m \sim \bar{1}I$	$Sr_{1-x}La_xTiO_y, NH_3, 950 \sim 1000\text{ }^\circ\text{C}, 15\text{ h}$	[56]
$Ba_{1-x}La_xTiO_{3-x}N_x$	$Pm\bar{3}m \sim \bar{1}I$	$Ba_{1-x}La_xTiO_y, NH_3, 950 \sim 1000\text{ }^\circ\text{C}, 15\text{ h}$	[56]
$SrTi_{1-x}Nb_x(O,N)_3$	$Pm\bar{3}m \sim I4/mcm$	$SrTi_{1-x}Nb_xO_{3+0.5x}$ (Pechini route) + flux, $850\text{ }^\circ\text{C}, 24\text{ h}$	[57]
$AZr_xTa_{1-x}O_{2+x}N_{1-x}$ ($A=Ba^{2+}, Sr^{2+}, Ca^{2+}$)	$Pm\bar{3}m \sim Pcmn$	$A-Ta-Zr$ sol gel, $NH_3, 1000\text{ }^\circ\text{C}, 12 \sim 96\text{ h}$	[58]
	$Pnma$	$LaNbO_4$ + flux, NH_3 (rotating reactor), $1050\text{ }^\circ\text{C}, 31\text{ h}$	[59]

		CaCO ₃ + Ta ₂ O ₅ , NH ₃ , 1000 °C	[60]
CaTaO ₂ N	<i>Pnma</i>	CaCO ₃ + TaCl ₅ (citrate route), NH ₃ , 1000 °C, 15 h	[50]
		CaO + TaON, N ₂ , 1400 °C, 1 h	[43]
NdTiO ₂ N	<i>Pnma</i>	Nd ₂ Ti ₂ O ₇ (solid state), 950 °C, 20 + 6 + 6 h with intermediate grindings	[61]
LaZrO ₂ N	<i>Pnma</i>	La ₂ Zr ₂ O ₇ (citrate route), 950 °C, 24 h (20 cycles) with intermediate grindings	[61]
CaNbO ₂ N	<i>Pnma</i>	Ca(NO ₃) ₂ •4H ₂ O + NbCl ₅ (citrate route) + flux, NH ₃ , 750 °C, 55 h	[39]
		CaCO ₃ + Nb ₂ O ₅ + flux, NH ₃ , 750 °C, 80 h	
NdNbON ₂	<i>Pnma</i>	NdNbO ₄ (solid state), NH ₃ , 900 °C, 16 h	[62]
PrNbON ₂	<i>Pnma</i>	PrNbO ₄ (solid state), NH ₃ , 900 °C, 16 h	[62]
A _{0.5} La _{0.5} TaO _{1.5} N _{1.5} (A=Ba ²⁺ , Sr ²⁺ , Ca ²⁺)	<i>Pnma</i>	La ₂ O ₃ + ACO ₃ + Ta ₂ O ₅ , NH ₃ , 1000 °C, 20 + 20 h	[63]
Ca _{1-x} Eu _x Ta(O,N) ₃	<i>Pnma</i> (<i>x</i> <0.4) <i>Pm</i> $\bar{3}$ <i>m</i> (<i>x</i> ≥0.4)	CaCO ₃ + Eu ₂ O ₃ + TaCl ₅ (citrate route), NH ₃ , 1000 °C, 15 h	[50]
Ca _{1-x} La _x TaO _{2-x} N _{1+x}	<i>Pnma</i> ~ <i>C2/m</i>	CaCO ₃ + La ₂ O ₃ + Ta ₂ O ₅ + flux, NH ₃ , 850 °C, 20 ~ 60 h	[64]
PrZrO ₂ N	<i>Pmna</i>	Pr ₂ O ₃ + Zr ₂ ON ₂ , 900 ~ 1300 °C and 1 ~ 10 GPa	[42]
NdZrO ₂ N	<i>Pmna</i>	Nd ₂ O ₃ + Zr ₂ ON ₂ , 900 ~ 1300 °C and 1 ~ 10 GPa	[42]
SmZrO ₂ N	<i>Pmna</i>	Sm ₂ O ₃ + Zr ₂ ON ₂ , 1200 ~ 1500 °C and 1 ~ 10 GPa	[42]
CaMoO _{1.7} N _{1.3}	<i>Pbnm</i>	CaMoO ₃ (reduced from CaMoO ₄), NH ₃ , 600 ~ 900 °C, 20 h	[65]
NdVO ₂ N	<i>Pbnm</i>	NdVO ₄ , NH ₃ , 700 °C, 80 h with intermediate grindings	[66]
SrNbO ₂ N	<i>I4/mcm</i>	SrCO ₃ + Nb ₂ O ₅ , NH ₃ , 950 ~ 1000 °C, 20 h × 4 times	[37]
		SrCO ₃ + TaCl ₅ (citrate route), NH ₃ , 1000 °C, 12 h	[67]
SrTaO ₂ N	<i>I4/mcm</i>	SrO + TaON, N ₂ , 1500 °C, 3 h	[43]
		SrCO ₃ + Ta ₂ O ₅ , NH ₃ , 1000 °C	[60]
SrA _{0.2} Ta _{0.8} O _{2.8} N _{0.2} (A=Li, Na)	<i>I4/mcm</i>	SrCO ₃ + Ta ₂ O ₅ to Sr ₅ Ta ₄ O ₁₅ , then Sr ₅ Ta ₄ O ₁₅ + A ₂ CO ₃ , NH ₃ , 900 °C, 12 h × 3 times	[55]
LaWO _{0.6} N _{2.4}	<i>I$\bar{4}$</i>	La ₂ W ₂ O ₉ , NH ₃ , 700 ~ 900 °C	[68]
LaTiO ₂ N	<i>Imma</i>	La ₂ Ti ₂ O ₇ (solid state), 950 °C, 20 + 6 + 6 h with intermediate grindings	[61]
MnTaO ₂ N	<i>R3c</i>	MnO + TaON, N ₂ , 1400 °C, 1 h, 6 GPa	[44]
LaTaON ₂	<i>C2/m</i>	LaTaO ₄ , NH ₃ , 1000 °C, 10 h × 3 with intermediate grindings	[69]
LaVO _{2.1} N _{0.9}	-	LaVO ₄ , NH ₃ , 650 ~ 850 °C	[70]
NdWO _{0.8} N _{2.2}	-	Nd ₂ W ₂ O ₉ , NH ₃ , 700 ~ 900 °C	[71]
BaSc _{1/3} Ta _{2/3} O _{8/3} N _{1/3}	<i>P2₁/n</i>	BaCO ₃ + Sc ₂ O ₃ + Ta ₂ O ₅ , NH ₃ , 1000 °C, 15 h	[72]
LaMg _{1/3} Ta _{2/3} O ₂ N	<i>P2₁/n</i>	La ₂ O ₃ + MgO + Ta ₂ O ₅ , NH ₃ , 870 °C, 15 h	[72]
LaMg _{1/2} Ta _{1/2} O _{5/2} N _{1/2}			

1.2 Oxide precursors

The nature of the starting materials (oxide precursors) used for the oxynitride synthesis is rather critical [73]. In general, solid state reaction via mixed binary oxides is the most convenient method but the highest limitation regarding to their relative low homogeneity and reactivity. Therefore, it is not easy to achieve phase pure materials even under high temperature and long treatment time, which is not beneficial to the nitridation process as we discussed above. Compared to conventional solid state reactions, wet-chemical-based methods

involving liquid phases are more efficient due to their small and homogeneous particle size, large specific surface area *etc.* For instance, ABO_2N ($A=Ca, Sr$; $B=Nb, Ta$) oxynitrides prepared from amorphous xerogel oxide precursors can be synthesized at lower temperature and shorter reaction time as compared with crystalline counterparts prepared by solid state reaction^[39] as well as TaO_xN_y photocatalysts from Sol-Gel-Derived method^[74], $SrTaO_2N$ from citrate route^[67] and so on.

Besides the formation of oxide precursor, including morphology and microstructure, the crystal structure of starting materials plays a key role for the synthesis of perovskite-type oxynitrides. There are three major crystal structures as the best candidates of oxide precursors that have been proven in last decades: perovskite, scheelite and pyrochlore.

1.2.1. Perovskite

Ideal perovskites have the general formula ABX_3 , where the A-site cations are typically larger than the B-site cations and similar in size to the X-site anions^[75]. The atomic arrangement in this structure was first observed for the mineral perovskite, $CaTiO_3$. Figure 1.6 shows that the A cations are surrounded by 12 anions in cubo-octahedral coordination (12-fold) and the B cations are surrounded by 6 anions in octahedral coordination (6-fold). Perovskites have the ideal structure adopt the cubic $Pm\bar{3}m$ space group. $SrTiO_3$ is commonly regarded as the archetypal cubic perovskite as its structure approaches closely that of the ideal ABX_3 .

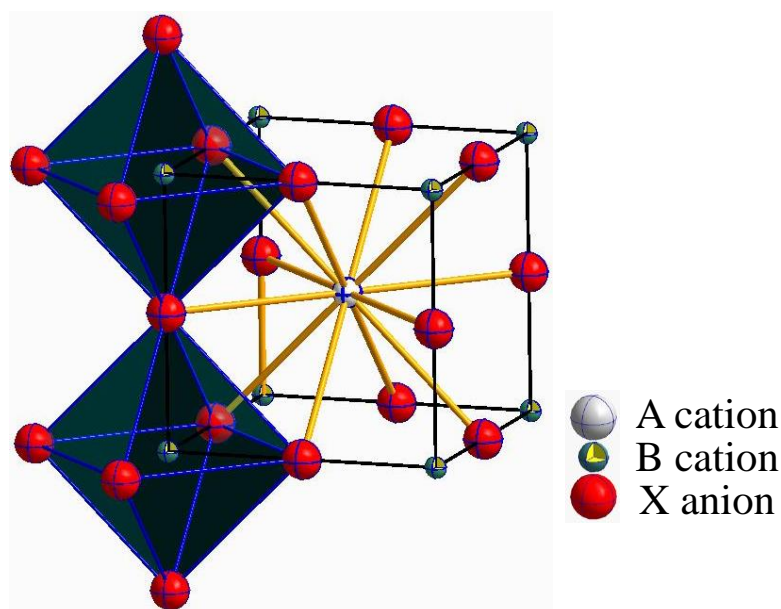


Figure 1.6 The ideal ABX_3 perovskite structure

However, most perovskite structures (oxides and oxynitrides) are distorted and do not have the ideal cubic symmetry (see from Table 1.2 and Table 1.3). The degree of distortion as well as the tilting of the BX_6 octahedral unit can be used as parameters to evaluate the stability and formability of the perovskite phase^[76-78].

Jahn-Teller distortions might be observed resulted from electronic degeneracies in the perovskite structure as well.

Table 1.3 Different symmetries of perovskite-type oxynitrides synthesized so far

Structure	Space group	Parameters
Cubic	$Pm\bar{3}m$	$a=b=c, \alpha=\beta=\gamma=90^\circ$
Tetragonal	$I4/mcm, \bar{I}4, Imma$	$a=b\neq c, \alpha=\beta=\gamma=90^\circ$
Orthorhombic	$Pnma, Pmna$	$a\neq b\neq c, \alpha=\beta=\gamma=90^\circ$
Monoclinic	$C2/m, P2_1/n$	$a\neq b\neq c, \alpha=\gamma=90^\circ, \beta\neq 120^\circ$
Triclinic	$\bar{I}1$	$a\neq b\neq c, \alpha\neq\beta\neq\gamma\neq 90^\circ$

Cations substitution in perovskite oxides can lead to the multifunctionality^[79], as shown in Figure 1.7. Similarly, perovskite-type oxynitrides also show high flexibility and a wide range of chemical and physical properties due to the structure distortion as well as the defects and combinations of different cations and anions with a variety of oxidation states. However, perovskite oxides are not popular as oxide precursors of the corresponding oxynitrides. Only limited compounds show the possibilities along perovskite oxide - perovskite oxynitride route, e.g., $\text{CaMoO}_{1.7}\text{N}_{1.3}$ ^[65] was synthesized by perovskite-type CaMoO_3 , $\text{SrMoO}_{2.76}\text{N}_{0.24}$ can be obtained from SrMoO_3 ^[80], as well as $\text{LaFeO}_{3-x}\text{N}_x$ ^[81], which is quite doubt due to the extremely low nitrogen content ($\text{LaFeO}_{2.9535}\text{N}_{0.0537}$).

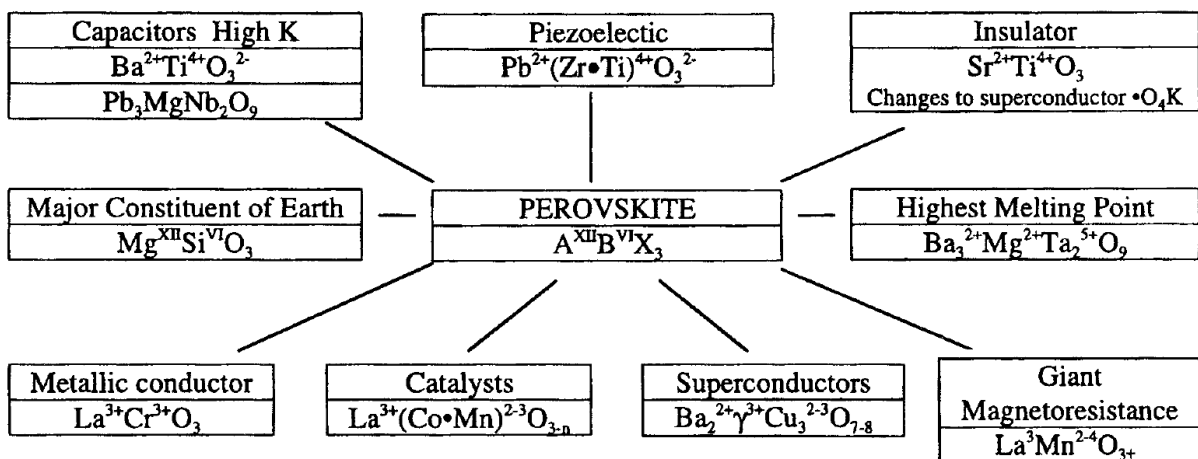


Figure 1.7 Multifunctional properties of perovskite oxide materials with cations substitution^[79]

1.2.2. Scheelite

Apart from being the major one of tungsten and famous for its fluorescence, scheelite (ABX_4) is of interest because of its interesting coordination. Scheelite consists of A-site eight-fold coordinated by BX_4 tetrahedra^[82]. A-site cation coordination polyhedron can be described approximately as a square antiprism (Figure 1.8). The scheelite structure is generally expressed in $I4_1/a$ symmetry as ABX_4 , where A and B are two different cations, alkali-/alkaline-earth or rare-earth metals/transition metals, respectively. Scheelite mainly contains three combinations of charges on the A, B and X sites, which are either (2+, 6+, 2-), (3+, 5+, 2-) or (1+, 3+, 1-). In case of (2+, 6+, 2-), A^{2+} is an alkaline-earth (Ca^{2+} , Sr^{2+} or Ba^{2+}), while B^{6+} is a transition metal (Mo^{6+} , W^{6+}), such as $CaWO_4$, $SrMoO_4$ ^[83-87]. In this thesis, ABO_4 ($A=Ca^{2+}$, Sr^{2+} , Ba^{2+} ; $B=Mo^{6+}$, W^{6+}) has been used to obtain perovskite $AB(O,N)_3$ oxynitride. In the (3+, 5+, 2-) combination, A^{3+} can be a rare-earth (La^{3+} , Pr^{3+} , Nd^{3+} , Sm^{3+} or Eu^{3+}), while B^{5+} can be a transition metal (V^{5+} , Nb^{5+} or Ta^{5+}), such as in $LaNbO_4$ ^[88], $La(Nd)VO_4$ ^[89, 90], $Pr(Nd/Sm)NbO_4$ ^[91, 92]. These scheelite oxides are commonly used as oxide precursors for perovskite-type oxynitrides^[52, 62, 66, 70] as well. In terms of (1+, 3+, 1-), A^+ can be an alkali metal (Li^+ , Na^+ , K^+ or Cs^+), while B^{3+} can be a rare-earth (Er^{3+} , Tm^{3+} , Ho^{3+} or Dy^{3+}), X^- can be a halogen (F), such as $LiDyF_4$, $LiHoF_4$ ^[93, 94]. These scheelite materials are of interest for their electronic^[95], luminescent^[96, 97] (with rare-earth doping), optical^[98] and magnetic^[99, 100] properties, but not for counterpart perovskite oxynitrides.

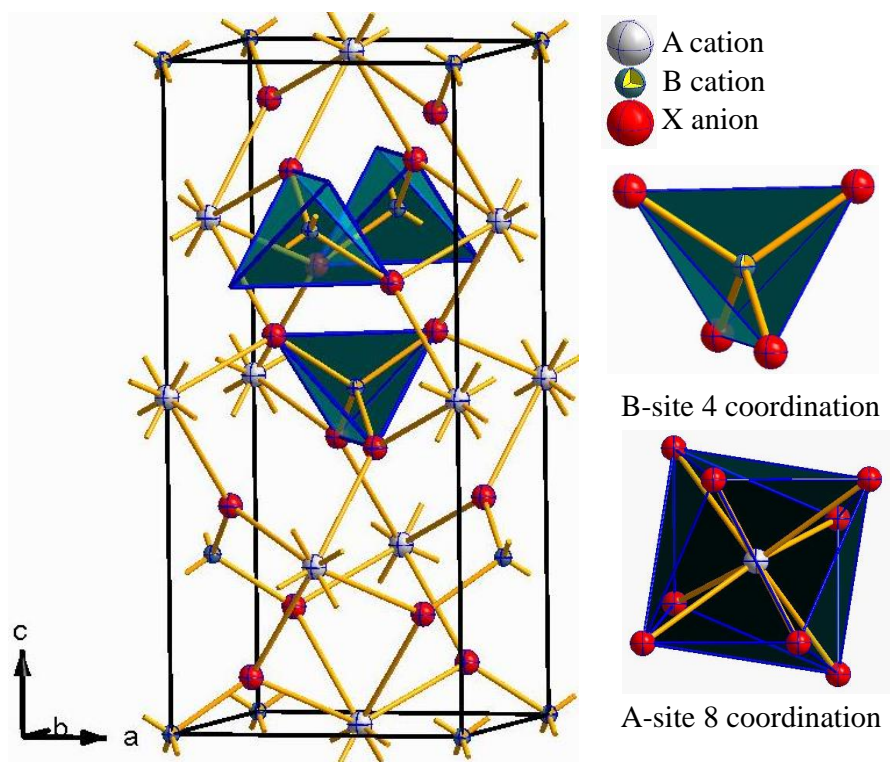


Figure 1.8 The ideal ABX_4 scheelite structure

1.2.3. Pyrochlore

The fluorite structure, *e.g.* CaF₂, with AX₂ formula crystallizes in the space group $Fm\bar{3}m$, where the A cations have 8-fold coordination in fcc arrangement and X anions have 4-fold coordination (Figure 1.9) ^[101, 102].

The pyrochlore structure is related to the fluorite crystal structure expressed in $Fd\bar{3}m$ symmetry. It is derived by A/B cations ordering and by introducing an anion vacancy into the fluorite structure (Figure 1.10). The general crystal structure of pyrochlore describes materials with A₂B₂X₆ and A₂B₂X₇ formula, where the A and B are rare-earth or transition metals and X anions are more common as oxygen; *e.g.*, Y₂Ti₂O₇. The pyrochlore structure is a super structure derivative of the simple fluorite structure (AO₂ = A₄O₈, where the A and B cations are ordered along the <110> direction. The additional anion vacancy resides in the tetrahedral interstice between adjacent B-site cations. These systems are particularly susceptible to geometrical frustration and interesting magnetic effects ^[103, 104].

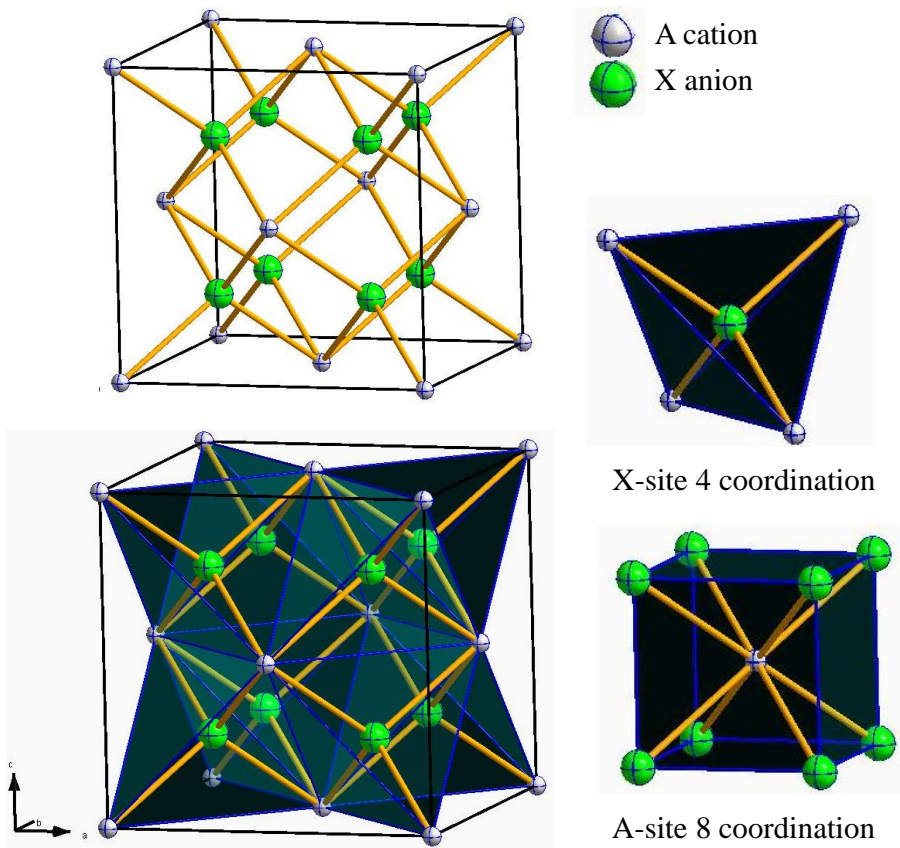
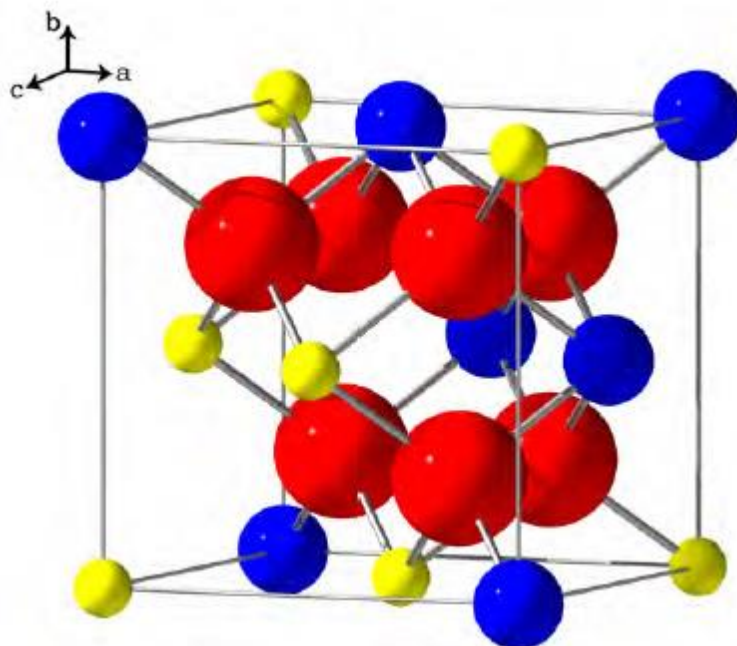


Figure 1.9 Fluorite structure

Figure 1.10 1/8 pyrochlore unit cell structure ^[105]

The pyrochlore structure shows various physical properties due to their high compositional diversity, structural flexibility as well as high anion vacancy concentrations, varying from spin ice systems ($\text{Dy}_2\text{Ti}_2\text{O}_7$) ^[106], spin glass systems ($\text{Y}_2\text{Mo}_2\text{O}_7$) ^[107], electronic insulators ($\text{La}_2\text{Zr}_2\text{O}_7$) ^[108], ionic conductors ($\text{Gd}_2\text{Zr}_2\text{O}_7$) ^[109], metallic conductivity, ($\text{Bi}_2\text{Ru}_2\text{O}_{7-y}$) ^[110], dielectric/piezo-/ferro-electric behavior ($\text{Cd}_2\text{Nb}_2\text{O}_7$, $\text{Cd}_2\text{Nb}_2\text{O}_6\text{S}$, $\text{Ln}_2\text{Ti}_2\text{O}_7$) ^[102], superconducting materials ($\text{Cd}_2\text{Re}_2\text{O}_7$) ^[111], to colossal magnetoresistances in $\text{Tl}_{2-x}\text{Sc}_x\text{Mn}_2\text{O}_7$ ($0 \leq x \leq 0.5$) ^[112].

The pyrochlore-type oxide precursors can be found in Table 1.2 to achieve counterpart perovskite-type oxynitrides via thermal ammonolysis, *e.g.*, $\text{Nd}_2\text{Ti}_2\text{O}_7$, $\text{La}_2\text{Zr}_2\text{O}_7$ and $\text{La}_2\text{Ti}_2\text{O}_7$ ^[61]. However, none of these structural evolution studies (perovskite oxide – perovskite oxynitride, scheelite oxide – perovskite oxynitride or pyrochlore oxide – perovskite oxynitride) has been detailed studied so far.

1.3 Anionic ordering

In general, the properties of perovskites are sensitive to small structure distortions that may result from tilting or deformations of the MX_6 octahedra ^[113]. Thus, anionic ordering (oxide/nitride) of oxynitrides is expected to be crucial with respect to their properties. A completely ordered O/N arrangement was reported for the baddeleyite-type and K_2NiF_4 -type oxynitrides, *e.g.*, TaON ^[114], $\text{Sr}_2\text{NbO}_{3.3}\text{N}_{0.7}$, $\text{Sr}_2\text{TaO}_3\text{N}$, $\text{Ba}_2\text{TaO}_3\text{N}$ ^[43, 115] and $\text{Nd}_2\text{AlO}_3\text{N}$ ^[116].

Theoretically, there are two preferred anionic configuration in case of ordering: *cis*- and *trans*-configuration. In terms of perovskite-type oxynitrides, it can be described as in Figure 1.11. The various properties of perovskite-type oxynitrides may be sensitive to oxide/nitride ordering. For instance, O/N ordering is expected to be important in directing the B-cation displacements in dielectric materials ^[113]. Yang *et al.*

studied anionic ordering in SrMO_2N ($M=\text{Nb}, \text{Ta}$) phases using variable-temperature neutron diffraction and electron diffraction^[113] and revealed that local anion order may be described as the formation of disordered zigzag M-N chains (Figure 1.12) in two dimensions at low temperatures. Oró-Solé *et. al.* demonstrated that the structure of NdVO_2N contains layers of spontaneously segregated *cis*-nitride chains^[66]. Zhang *et. al.* illustrated the short-range O/N ordering involving a *cis*-configuration in TaO_4N_2 octahedra together with large anionic displacement within the *ab* plane on their axial position in terms of local tilting of the octahedral, which is likely to play a key role in the unusual dielectric behavior of SrTaO_2N ^[67]. A partially ordered O/N distribution in SrNbO_2N was discussed by Ebbinghaus^[117] via comparing powder neutron diffraction patterns measured at room temperature (293 K) and low temperature (1.5 K). However, the principles of either partial or complete anion-ordering in perovskite-type oxynitrides are still a matter of debate.

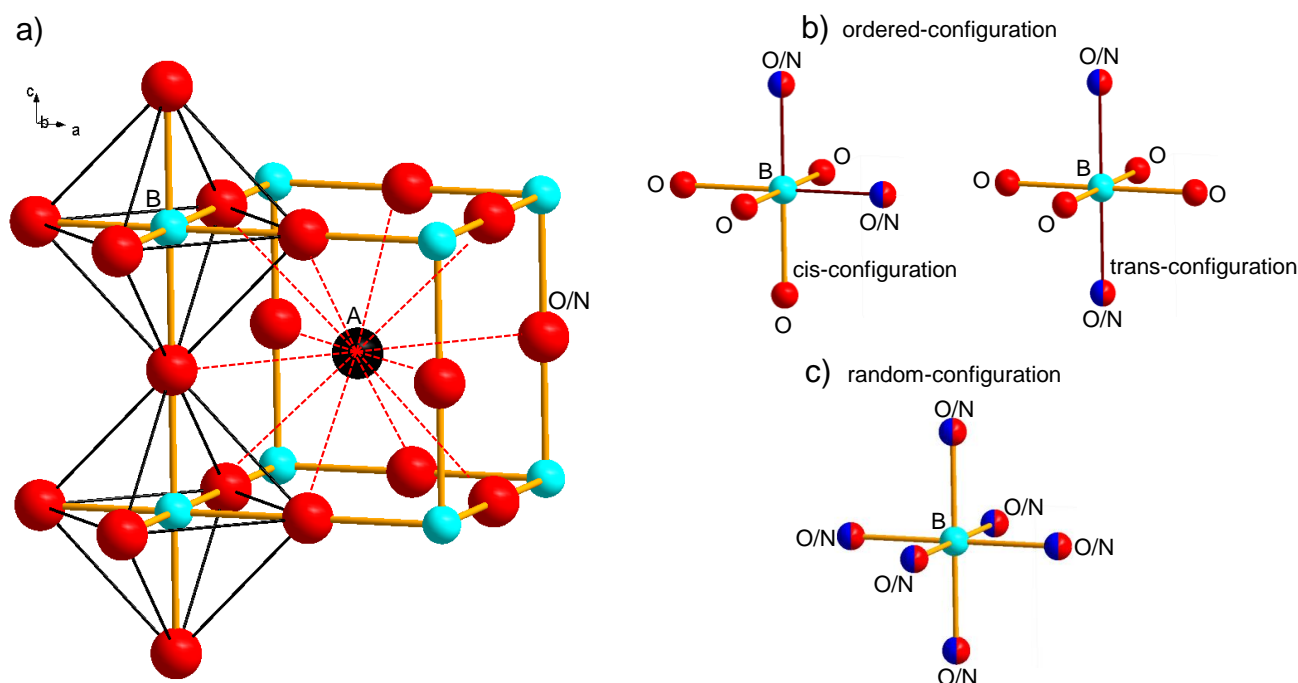


Figure 1.11. (a) An undistorted ABX_3 (X=O, N) perovskite structure: a 3D network of corner-shared BX_6 octahedra incorporate the 12-fold coordinated A-cations. (b, c) Nitrogen atoms can be either randomly distributed or *cis*-/*trans*-ordered forming cross-linked -N-B-N-chains^[118].

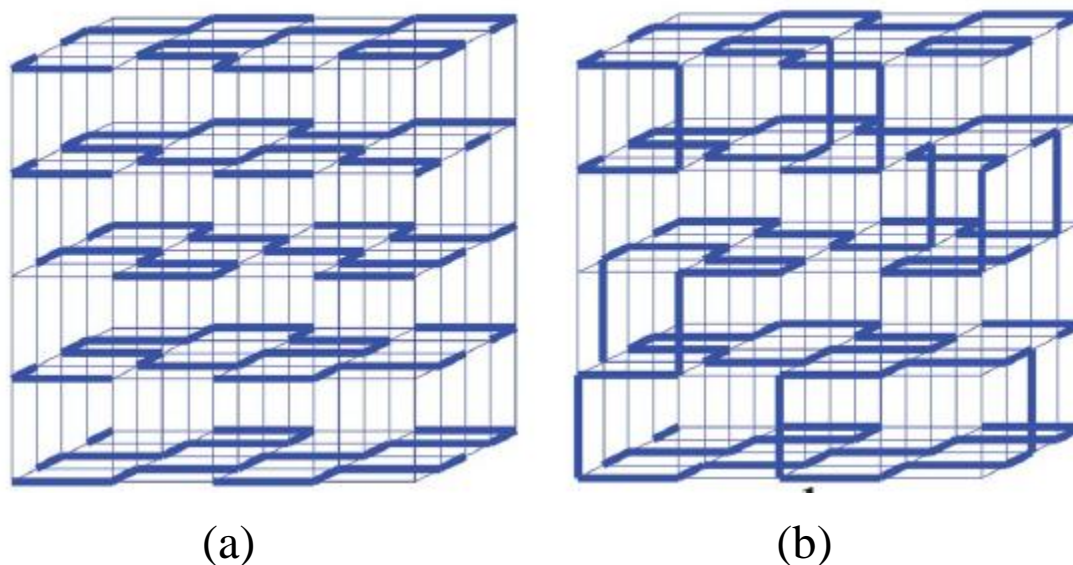


Figure 1.12 $\text{cis}-(\text{MN})_n$ chain formation arising from local anion order in SrMO_2N ($M=\text{Nb, Ta}$) perovskites. Heavy lines correspond to M-N-M units. Disorder of chains within planes (a) is observed in the pseudo-cubic phase of SrNbO_2N and at higher temperatures a partial occupation of the out-of-plane anion site corresponds to the chains jumping between successive planes (b). ^[113, 119]

Nevertheless, it is still difficult to investigate anionic ordering experimentally in terms of perovskite-type oxynitrides. Theoretical works have been developed recently to predict the anionic ordering. For example, Fuertes ^[22] shown that Pauling's second rule gives a good and a priori estimate of anions distributions in mixed oxyanion systems (*e.g.*, oxynitrides and oxyhalides) with diverse compositions and structure types. Anion distribution in terms of total-energy calculations was studied ^[20] via both first-principles electronic-structure calculations and molecular-dynamics simulations for alkaline-earth-based tantalum and niobium oxynitrides; a clear preference for arrangement which lead to short Ta-N and longer Ta-O bonds was concluded. First-principles calculation was used to study relaxor-type ferroelectric behavior without chemical inhomogeneity in BaTaO_2N and SrTaO_2N ^[120]. A general Pauling ice-rules formula was used to correlate the order of displacements in ferroelectric perovskites by calculating the extensive molar entropies for $\text{SrMoO}_{2.5}\text{N}_{0.5}$ and BaTaO_2N ^[121, 122].

In general, both experimental and theoretical approaches are still far from understanding the anionic ordering of perovskite oxynitrides at the moment, especially the experimental work. Although neutron scattering provides a good scattering contrast between oxygen and nitrogen, the combinations of diffraction, spectroscopy, pair distribution function and modeling methods are highly required in order to understand and design the anionic-ordering within crystalline oxynitrides ^[122].

1.4 Applications of oxynitrides

1.4.1. Band theory

Solid materials can be generally divided into three types: insulator, semiconductor and conductor, which can be explained by the band theory. Band gaps (E_g) are essentially an energy range in a solid where no electron states can exist. It generally refers to the energy difference between the top of valence band (VB) and the bottom of conduction band (CB) in insulators and semiconductors. The Fermi level is the total chemical potential for electrons and is usually denoted by μ or E_F [123]. The Fermi level of a body is a thermodynamic quantity, and its significance is the thermodynamic work required to add one electron to the body (not counting the work required to remove the electron from wherever it came from).

As shown in Figure 1.13 a, the electrons in the VB are separated by a large forbidden gap from the CB in insulators. Most solid oxides are insulators, especially the oxide precursors used for oxynitrides preparation, *e.g.*, ABO_4 ($A=Ca, Sr, Ba$; $B=Mo, W$), $La_2Ti_2O_7/La_2Zr_2O_7$, TiO_2 and Ta_2O_5 . While the doping of insulators can dramatically change their optical properties, it is still not enough to overcome the large band gap to make them good conductors of electricity. A semiconductor has an empty CB and a small band gap compared to an insulator. With some additional energy, such as thermal excitation or photo excitation, the electrons can be promoted from the filled VB to empty CB leading to current passing through a semiconductor. The doping of semiconductors has a much more dramatic effect on their electrical conductivity. By contrast, the band of metal is partially filled. The overlap of VB and CB results in at least a fraction of electrons on VB can move through the materials, or in other words, good electrical conductivity.

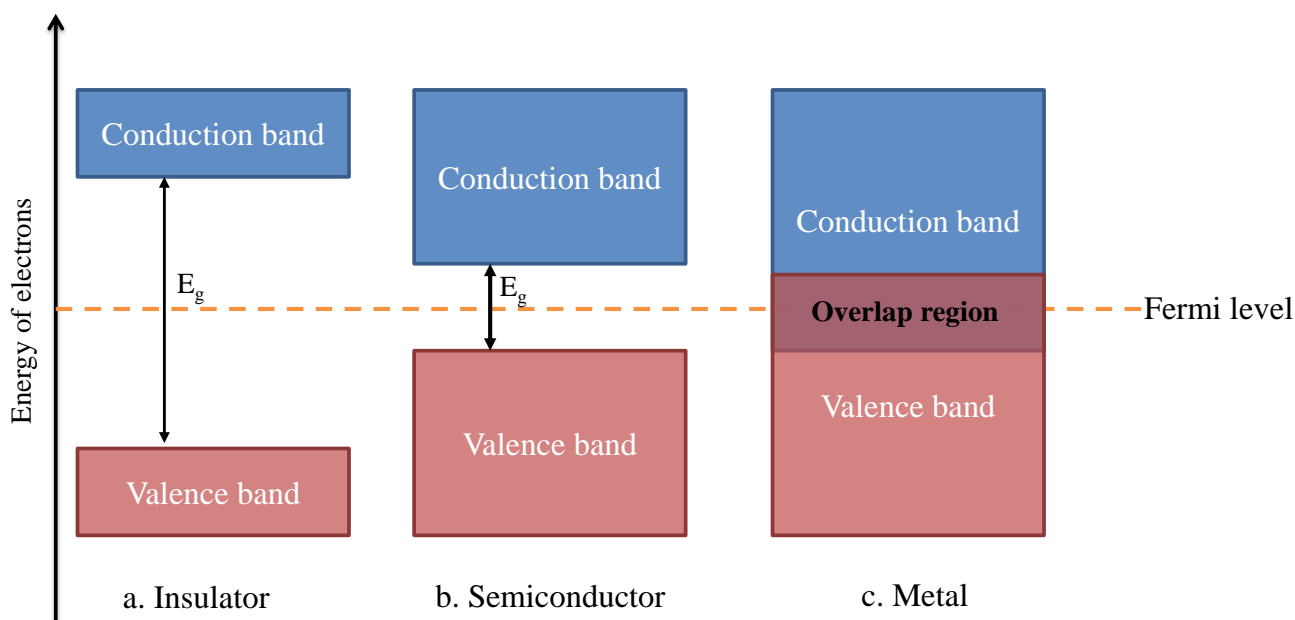


Figure 1.13 Schematic energy bands of solid materials [124]

1.4.2. Optical properties

Optical properties of materials are constantly related to their band structure. The electronic structure of simple perovskite-type oxides near the Fermi level is formed mainly by mixing of frontier d -orbitals of the B-site metal and $2p$ -orbitals of oxygen. The top of the valence band is constituted by oxygen non-bonding $2p$ -orbitals, whereas the bottom of conduction band is represented by the anti-bonding $2p$ - nd orbitals. The nitrogen-substitution can significantly modify the electronic structure of the parent oxide primarily at the valence band. Due to the lower electronegativity of nitrogen, the higher energy level of the nitrogen $2p$ -orbitals (or we can express it as donor level between valence and conduction bands) can decrease the band gap, resulting in semiconducting compounds, for example $\text{SrTiO}_3/\text{SrTiO}_2\text{N}$ (Figure 1.14). Particularly the oxynitrides have clearly distinguished visual colors from the oxides of isoelectronic d^0 configuration. Depending on the cation composition and nitrogen content, the oxynitrides display various colors ranging from white to yellow, red and dark brown, which has an implication to the non-toxic pigment applications, as shown in Figure 1.15. A comprehensive list of optical band gaps of perovskite-type oxynitrides has been summarized in Table 1.4.

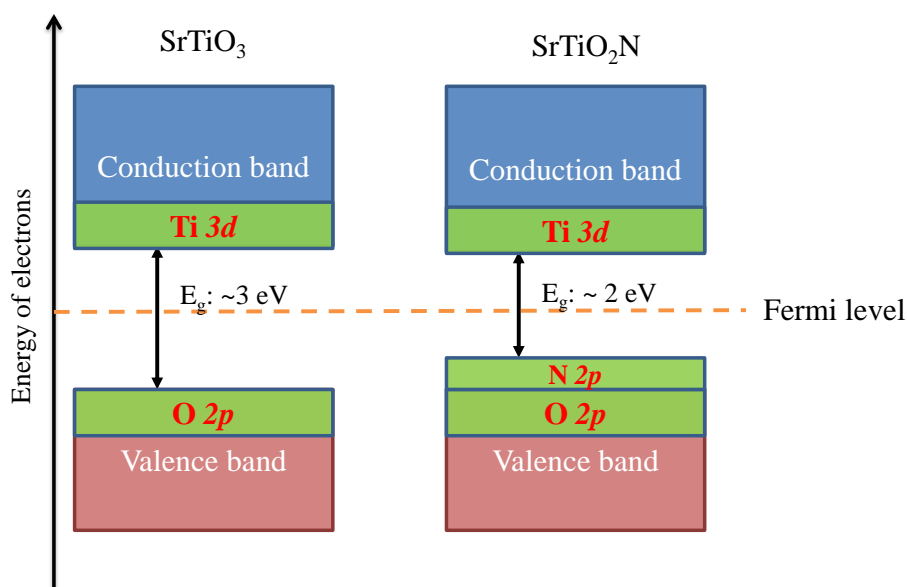


Figure 1.14 Schematic energy bands of perovskite-type SrTiO_3 oxide and SrTiO_2N oxynitride

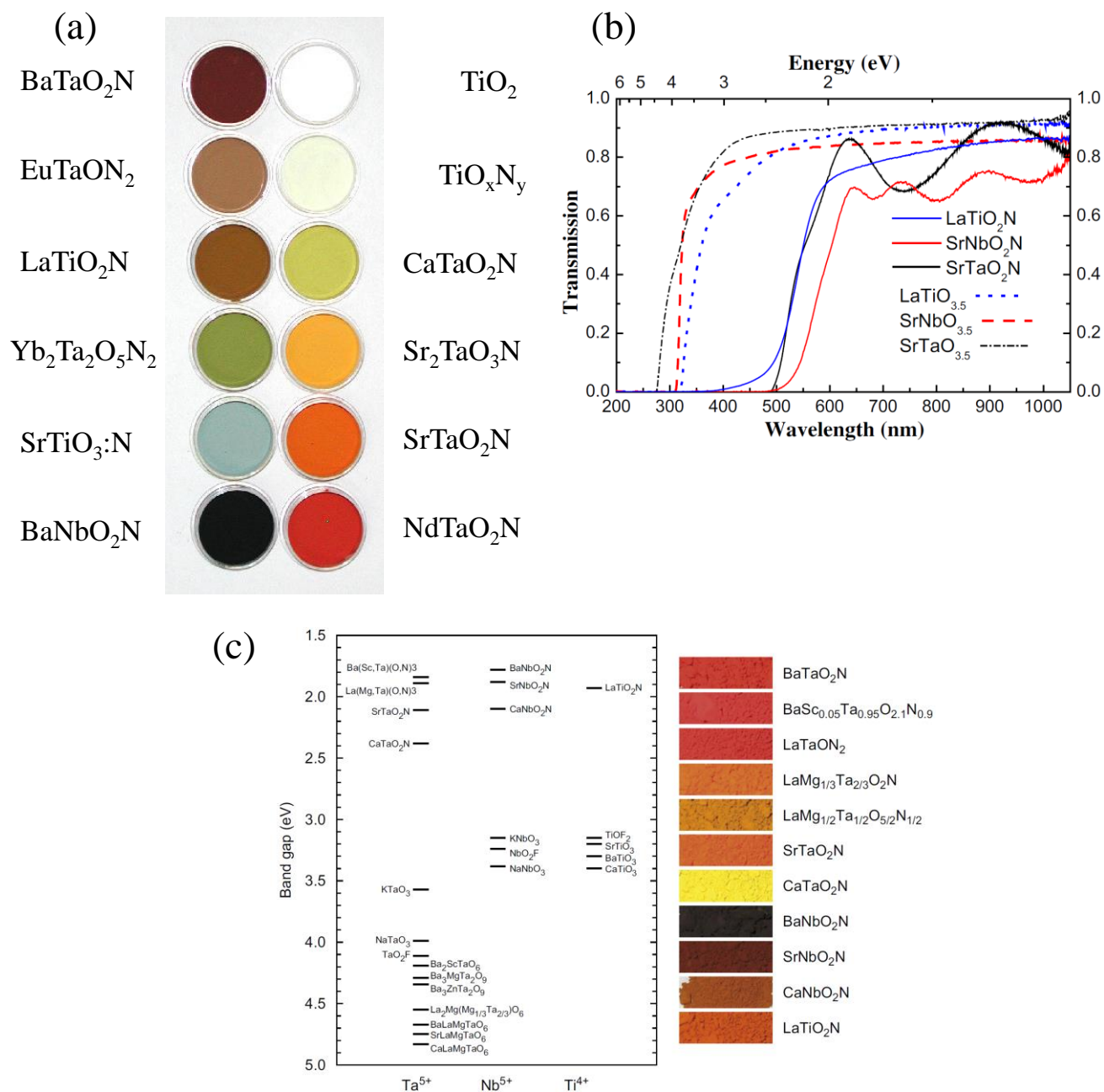


Figure 1.15 (a) Powder samples of oxynitrides and TiO_2 [32] (b) Absorption curves of selected oxides and corresponding oxynitrides [125, 126] (c) Band gaps of various perovskites having Ta^{5+} , Nb^{5+} , or Ti^{4+} as the octahedral atom [72]

Table 1.4 Optical band gaps and colors of ternary perovskite-type oxynitrides so far

Compounds	Band gap, eV	Color	Ref.
SrWO_2N	/	Black	[46]
$\text{SrMoO}_{2.5}\text{N}_{0.5}$	/	Black	[46]
BaTaO_2N	1.8	Red - Brown	[43, 47, 48]
BaNbO_2N	1.8	Black - brown	[47, 48]
EuNbO_2N	/	Black	[49]
EuTaO_2N	/	Dark - yellow green	[50]
$\text{EuWO}_{1.58}\text{N}_{1.42}$	/	Black	[51]

$\text{Ca}_x\text{Sr}_{1-x}\text{WO}_2\text{N}$ ($x=0.25, 0.5$)	/	Black	[52]
$\text{Ba}_{1-x}\text{Sr}_x\text{TaO}_2\text{N}$	/	Brown	[53]
$\text{SrMo}_{1-x}\text{W}_x(\text{O},\text{N})_3$	/	Black	[54]
$\text{BaA}_{0.2}\text{Ta}_{0.8}\text{O}_{2.8}\text{N}_{0.2}$ ($A=\text{Li}, \text{Na}$)	2.01 ~ 2.12	Brown - red brown	[55]
$\text{Sr}_{1-x}\text{La}_x\text{TiO}_{3-x}\text{N}_x$	2.49 ~ 2.02	Red - orange – ocher – green – apple green	[56]
$\text{Ba}_{1-x}\text{La}_x\text{TiO}_{3-x}\text{N}_x$	/	Brown – pale brown – khaki – dark green	[56]
$\text{SrTi}_{1-x}\text{Nb}_x(\text{O},\text{N})_3$	3.24 ~ 1.82	Blue – green – red - brown	[57]
$\text{AZr}_x\text{Ta}_{1-x}\text{O}_{2+x}\text{N}_{1-x}$ ($A=\text{Ba}^{2+}, \text{Sr}^{2+}, \text{Ca}^{2+}$)	/	Yellow – green – dark brown - grey	[58]
LaNbON_2	1.7	/	[59]
CaTaO_2N	2.4 ~ 2.75	Yellow	[43, 50, 60]
NdTiO_2N	/	Brown	[61]
LaZrO_2N	/	White	[61]
CaNbO_2N	2.1	Ochre	[39]
NdNbON_2	/	/	[62]
PrNbON_2	/	/	[62]
$\text{A}_{0.5}\text{La}_{0.5}\text{TaO}_{1.5}\text{N}_{1.5}$ ($A=\text{Ba}^{2+}, \text{Sr}^{2+}, \text{Ca}^{2+}$)	/	/	[63]
$\text{Ca}_{1-x}\text{Eu}_x\text{Ta}(\text{O},\text{N})_3$	/	/	[50]
$\text{Ca}_{1-x}\text{La}_x\text{TaO}_{2-x}\text{N}_{1+x}$	2.75 ~ 2.0	Yellow – deep red	[64]
PrZrO_2N	/	/	[42]
NdZrO_2N	/	/	[42]
SmZrO_2N	/	/	[42]
$\text{CaMoO}_{1.7}\text{N}_{1.3}$	/	Black	[65]
NdVO_2N	/	Black	[66]
SrNbO_2N	1.9	Dull - brown	[37]
SrTaO_2N	2.1	Orange - red	[43, 60, 67]
$\text{SrA}_{0.2}\text{Ta}_{0.8}\text{O}_{2.8}\text{N}_{0.2}$ ($A=\text{Li}, \text{Na}$)	2.24 ~ 2.42	Yellow - orange	[55]
$\text{LaWO}_{0.6}\text{N}_{2.4}$	/	Black	[68]
LaTiO_2N	2.0 ~ 2.1	Brown	[61]
MnTaO_2N	/	/	[44]
LaTaON_2	2.0 ~ 2.1	Red	[69]
$\text{LaVO}_{2.1}\text{N}_{0.9}$	/	Black	[70]
$\text{NdWO}_{0.8}\text{N}_{2.2}$	/	Black	[71]
$\text{BaSc}_{1/3}\text{Ta}_{2/3}\text{O}_{8/3}\text{N}_{1/3}$	1.8	Red	[72]
$\text{LaMg}_{1/3}\text{Ta}_{2/3}\text{O}_2\text{N}$	1.9	Orange	[72]
$\text{LaMg}_{1/2}\text{Ta}_{1/2}\text{O}_{5/2}\text{N}_{1/2}$		Ocher	

1.4.3. Photocatalytic properties

1.4.3.1. Photocatalytic water splitting

Photocatalytic water splitting is an artificial photosynthesis process with photocatalysis in a photoelectrochemical cell used for the dissociation of water into its constituent parts, hydrogen (H_2) and oxygen (O_2) with the ideal stoichiometric ratio of 2:1, using either artificial or natural light, as shown in Figure 1.16 and Equation 1-11.

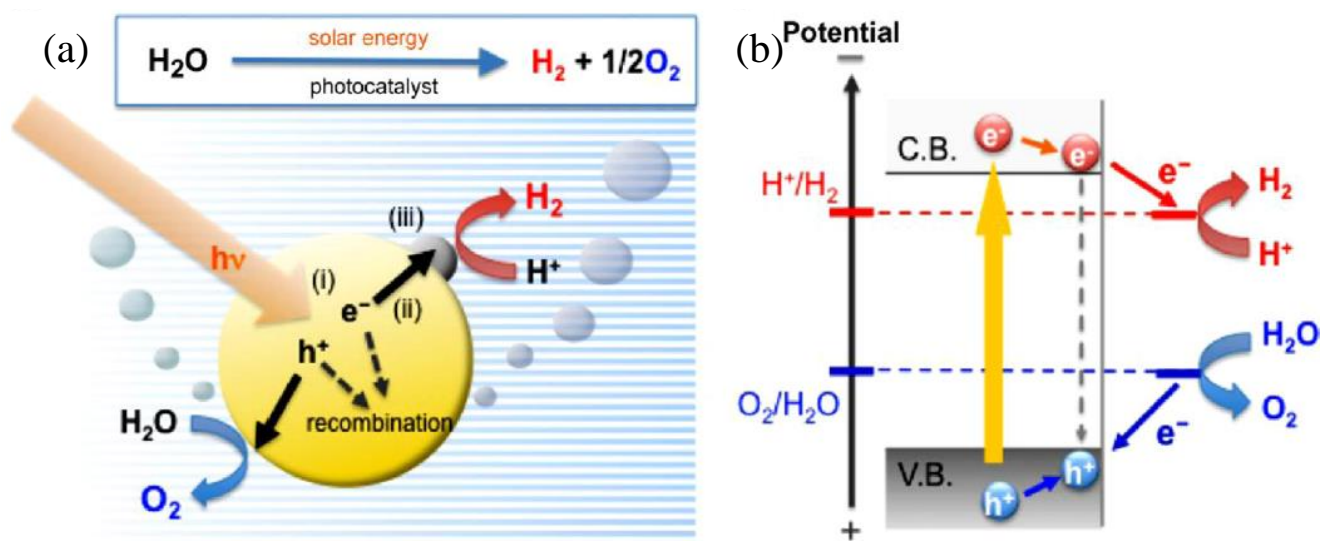
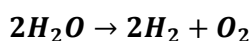


Figure 1.16 Schematic illustration of water splitting over semiconductor photocatalysts ^[127].

The process of water splitting is a highly endothermic process ($\Delta H > 0$), which occurs naturally when photon energy is absorbed and converted into the chemical energy through a complex biological pathway. The prime measure of the photocatalyst effectiveness is the quantum efficiency (QE), which is

$$\text{QE (\%)} = (\text{Photochemical reaction rate}) / (\text{Photon absorption rate}) \times 100\%$$



Equation 1-11

First water oxidation has been performed over *n*-type TiO_2 (rutile) irradiated with UV-light ($\lambda < 415 \text{ nm}$) with around 10 % quantum efficiency ^[128]. The QE was further promoted up to ~ 29 % by using photochemical diodes, that is impregnation of a noble metal (*e.g.*, Pt, Au and Pd) on the surface of *n*-type TiO_2 for more effective electron-hole separation in 1977 ^[129]. Nowadays more than hundreds of materials are known either to catalyze water oxidation (produce O_2) or reduction (produce H_2) ^[130]. Perovskite-related oxides thus received much attention due to their most effective performance resulted from the suitable valence and conduction band positions as well as good photochemical stability. In general, efficient photocatalytic materials contain either transition-metal cations with a d^0 electronic configuration (*e.g.*, Ta^{5+} , Ti^{4+} , Zr^{4+} , Nb^{5+} , Mo^{6+} and W^{6+}) or typical metal cations with d^{10} electronic configuration (*e.g.*, In^{3+} , Sn^{4+} , Ga^{3+} , Ge^{5+} and Sb^{5+}) as principal cation components ^[131]. The highest quantum efficiencies have been reported for NiO-modified La/KTaO₃ (QE = 56 %) using water under UV light ^[132]. Both titanate ATiO_3 ($A = \text{Sr}^{2+}$, Co^{2+} , Zn^{2+} and Ni^{2+}) ^[133-136] and tantalate ATaO_3 ($A = \text{Li}^+$, Na^+ and K^+) ^[137, 138] have attracted significant attention and shown remarkable photocatalytic properties. However, the major serious disadvantage of perovskite-type oxides catalysts is their relatively large band gaps activated only by UV-radiation source. Thus, they are rather ineffective to convert solar energy because the sunlight which reaches the earth surface contains just around 5 % of UV-radiation ^[28].

There are some optional visible-light-responsive oxide photocatalysts, such as WO_3 ^[127, 139-141] or BiVO_4 ^[142-145]. Whereas, these oxides cannot produce H_2 from water due to their conduction bands being too low for water reduction (Figure 1.17 b). Although some non-oxide, such as sulfides^[146-152] and nitrides^[153, 154], semiconductors can possess appropriate band levels for water splitting under visible light (Figure 1.17 c), they are just generally unstable and readily become deactivated through photocorrosion or self-oxidation, rather than evolving O_2 .

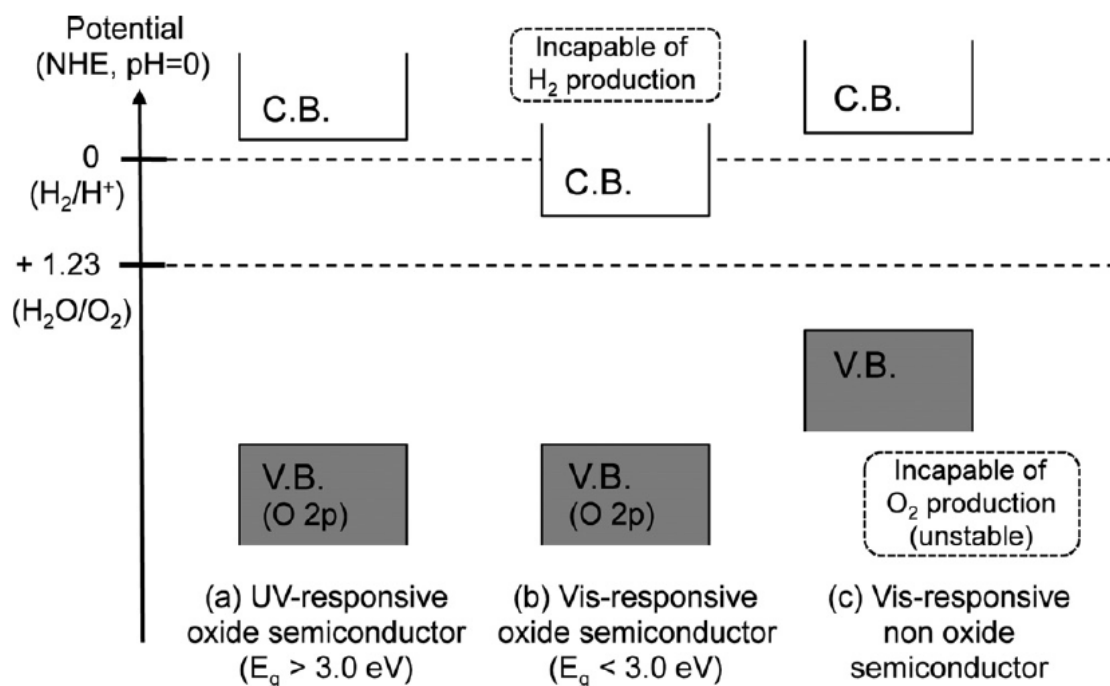


Figure 1.17 Band energy levels of various semiconductors^[127]

Perovskite-type oxynitrides are good candidates which combine the advantages of oxides and non-oxides, *i.e.*, suitable band gaps to harvest visible light, suitable energy level to produce H_2 (theoretically and experimentally, Figure 1.18) and good stability^[155] compared to sulfides or nitrides. Recently, perovskite-type oxynitrides have attracted considerable attention as perspective photocatalysts utilizing solar energy and operating under visible-light^[119, 125, 131]. Higashi et al. reported that the Pt-loaded CaTaO_2N and BaTaO_2N are active for H_2 evolution in the presence of methanol / I^- as an electron donor^[155, 156]. Maeda et al. demonstrated nearly stoichiometric H_2 and O_2 evolution was achieved using a $\text{SrNbO}_2\text{N}/\text{FTO}$ electrode modified with colloidal IrO_2 as a water oxidation promoter^[157]. B. Siritanaratkul et. al. illustrated that Pt- CaNbO_2N was active for H_2 and O_2 evolution from methanol and aqueous AgNO_3 , respectively^[158]. Zhang et. al. reported a CoO_x -modified LaTiO_2N was able to achieve high water oxidation performance^[159]. Ueda et al. presented a Co-cocatalyst modified photoanode of particulate BaTaO_2N for H_2 and O_2 production^[160].

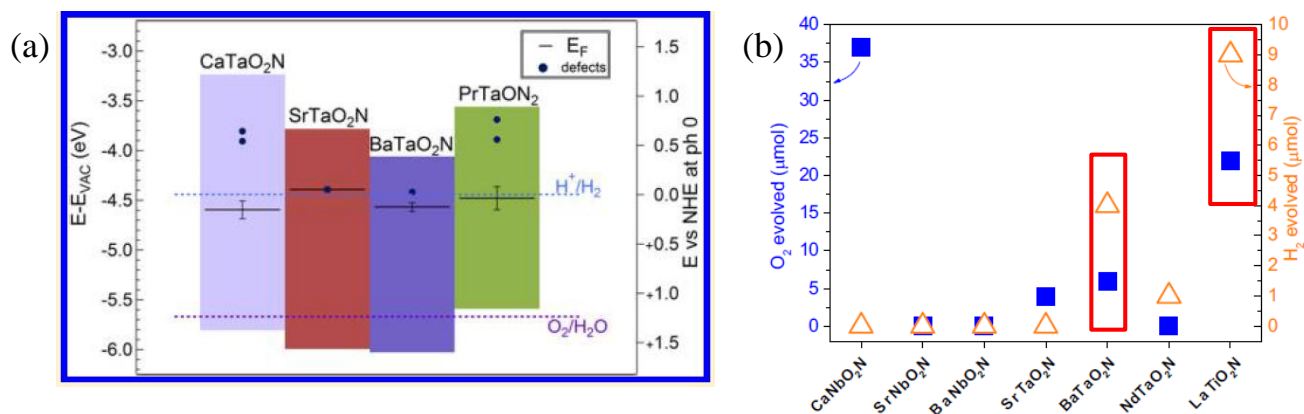


Figure 1.18 (a) Energy-level diagrams of tantalum oxynitrides showing E_{CB} and E_{VB} as well as band gap (colored) and defect levels obtained from XPS and DRCLS, E_F obtained from KPFM, and H_2O redox potentials $^{[161]}$; (b) O_2 and H_2 evolution for selected perovskite-type oxynitride resulting from 5 hours of reaction $^{[32]}$

1.4.3.2. Photocatalysis in solution

During printing and dyeing process, nearly 15 % of dyes are lost and released in the effluent water of textile industry, which contain reactive dyes, toxic chlorolignin and dark coloration $^{[162, 163]}$. Photocatalysis can be used in water purification to remove biological matters (*e.g.* bacteria, viruses, germs and fungi), organic compounds like pesticides or solvents (alcohols, aldehydes, phenols, etc.) or hazardous metals deriving from industry (*e.g.* reduction from Cr^{6+} to Cr^{3+}) in contaminated wastewater $^{[125]}$.

Photo-degradation is the alteration of a molecule by photons, which can break up the molecules into smaller and extremely reactive pieces. Similar with water splitting, the degradation of organic molecules is initiated by the absorption of a photon. The energy of an absorbed photon is transferred to electrons in the molecule and briefly changes their configuration, *e.g.* promotes the molecule from a ground state to an excited state. Moreover, excited state molecules are not kinetically stable in the presence of O_2 or H_2O and easily spontaneously decompose. Proposed degradation paths are shown in Figure 1.19 $^{[164]}$ and Figure 1.20 $^{[162]}$.

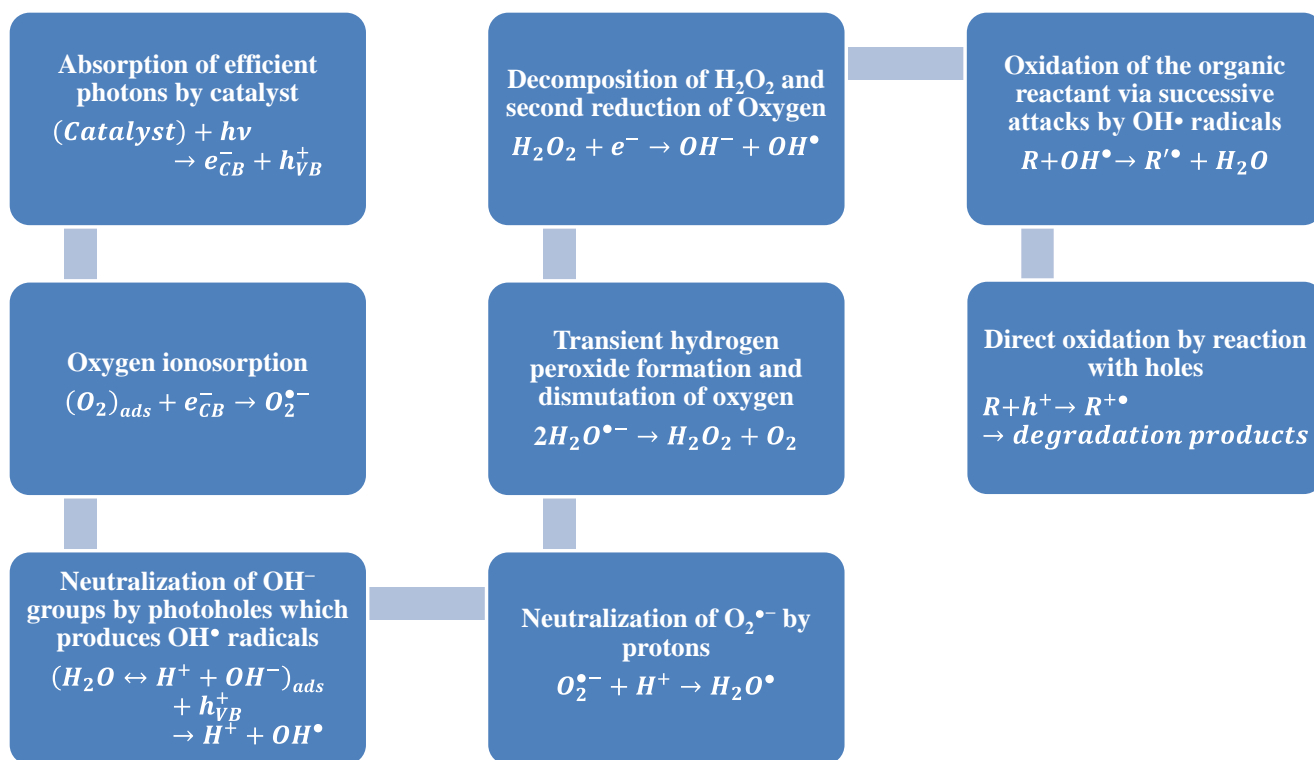


Figure 1.19 Proposed photodegradation reaction path by Houas et. al. [164]

TiO_2 is a promising photocatalyst for numerous photodegradation applications [165, 166]. However, similar with the water splitting case, it can only absorb UV-light. Therefore, efficient visible-light photocatalysis arises plenty of attentions again. Breault *et. al.* reported alloyed $TiO_2:N$, $TiO_2:Nb$ and $TiO_2:(Nb, N)$ show a significantly lower energy absorption edge of 2.0 eV and great performance to photodegrade methylene blue (MB) dye catalytically [167]. F-doped TiO_2 achieves the highest photocatalytic degradation rate of 91% by Yu *et. al.* [168]. Charanpahari *et. al.* illustrated a photocatalytic activity of a visible-light active N-doped GeO_2 , which can degrade Rhodamine B and Acid violet 7 efficiently [169].

Only few perovskite-type oxynitrides for photodegradation application have been reported so far. Liu *et. al.* demonstrated that $NaTaO_{3-x}N_x$ shows efficient visible-light photocatalytic activity for degradation of MB [163] and Methyl orange (MO) [162], and it exhibits outstanding stability during the degradation process, suggesting a promising utilization of such photocatalysts. Ebbinghaus *et. al.* discussed that N-doped $BaTiO_3$ as a promising candidate for visible light induced oxidation of organic compounds and it might be applicable for the photocatalytic processing of sewages, *e.g.* from hospitals [125].

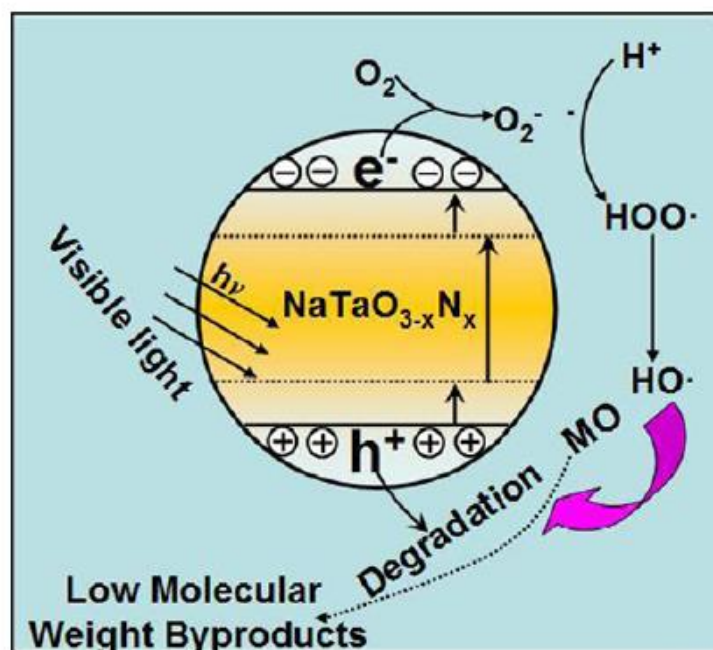


Figure 1.20 Proposed mechanism for the visible-light photocatalytic reaction of dyes on $\text{NaTaO}_{3-x}\text{N}_x$ catalyst ^[162]

1.4.4. Conductivity

Electrical conductivity is a measure of how well a material accommodates the movement of an electric charge. Conductivity σ is related to the concentration of electrons, charge and mobility of charge carriers according to

$$\sigma = n|e|\mu_e \quad \text{Equation 1-12}$$

where, n is the concentration of electrons, e is the electric charge, and μ_e is the carrier mobility. In general, higher conductivity has the higher concentration of charge carriers with high mobility. The inverse of the conductivity is resistivity (ρ), defined as

$$\rho = 1/\sigma \quad \text{Equation 1-13}$$

The conductivity is one of the properties of materials that varies most widely, from $10^{-7} \sim 10^{-8}$ ($\Omega \cdot \text{m}$) typical of metals to 10^{20} ($\Omega \cdot \text{m}$) for good electrical insulators. Semiconductors have conductivities in the range of 10^{-6} to 10^4 ($\Omega \cdot \text{m}$). The conductivities of these materials have different temperature dependences (Figure 1.21). The superconductor has a similar behavior with metal above a certain critical temperature (T_c), while below T_c the materials counter a superconducting state in which the resistivity decreases to zero.

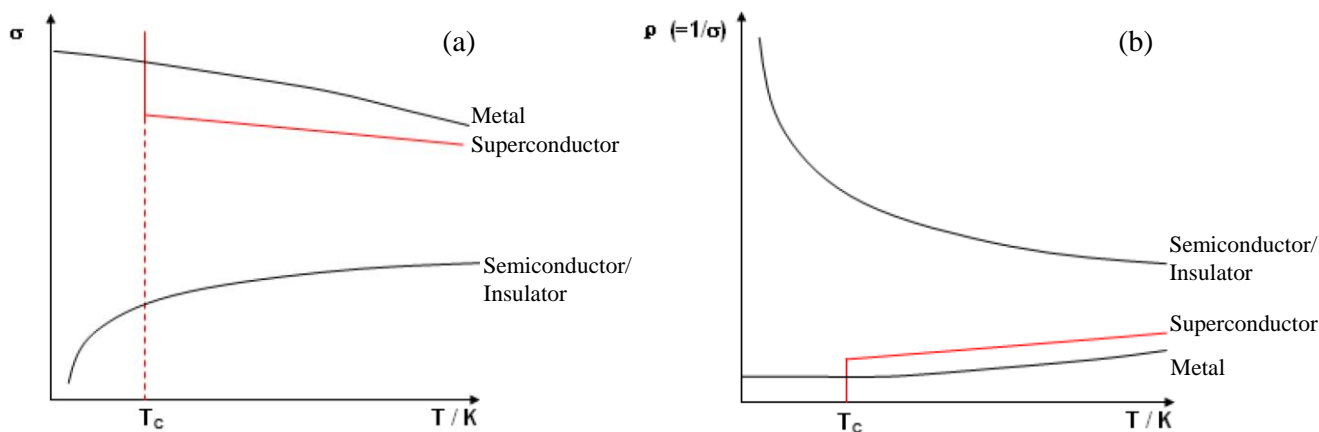


Figure 1.21 Temperature dependence of (a) conductivity and (b) resistivity ^[101]

Antoine *et al.* ^[70] presented that perovskite $\text{LaVO}_{3-x}\text{N}_x$ ($0 < x < 0.9$) oxynitrides exhibit a characteristic p-type semiconducting behavior. Fawcett *et al.* ^[46] reported temperature independent electrical dc resistivity of SrWO_2N and $\text{SrMoO}_{2.5}\text{N}_{0.5}$ of $1 \text{ } \Omega \cdot \text{cm}$ and $0.2 \text{ } \Omega \cdot \text{cm}$ respectively, in the temperature range 60 – 300 K. Logvinovich *et al.* demonstrated that a low thermal conductivity and semiconductinglike electrical resistivity was observed for SrMoO_2N ^[170]. However, since the electrical resistivity or conductivity measurements were usually performed on bars of pressed and sintered powders, the obtained values are to be corrected concerning the remaining porosity and possible phase decomposition. An approach that can measure electrical conductivity in powder form would be more reliable.

Recently, Ingram *et al.* ^[171] proposed for the first time a method, called “Powder-Solution-Composite” (PSC) technique, in which the impedance spectroscopy was used to measure both the conductivity of slurry, formed by mixing the studied ceramic powders and the electrolyte, and the conductivity of the electrolyte alone. Then the electrical conductivity of the investigated ceramic powders was obtained by plotting the conductivity of the composite versus the electrolyte. The PSC method lowers the error in measuring electrical conductivity of the ceramic powders compared to the previously reported powder methods since grain-boundary effect is negligible. This method has been used to measure electrical conductivity of different ceramic powders such as $\text{Ag}_2\text{V}_4\text{O}_{11}$, $\text{Ag}_4\text{V}_2\text{O}_6\text{F}_2$, CeAgOS , BiCuOS , SiOCN and ZnO nanowires ^[172-176]. The results obtained by this method were comparable with the bulk conductivity of the same materials measured by conventional methods.

In the present work, the electrical conductivity was measured applying this PSC method. Impedance spectroscopy was applied on slurries with different electrolytes conductivity prepared by mixing as-synthesized oxynitride powders and an electrolyte. The frequency tested was in the range of $10 - 10^{-6}$ Hz, the applied voltage was 5 mV recording five experimental data points for each decade. As electrolyte, an aqueous solution of Na_2SO_4 was chosen to provide a nonaggressive electrolyte (especially for the stainless steel electrodes). First Na_2SO_4 solutions with the ceramic powders was kept constant (0.75) for all measurements. The slurries were placed into a polyethylene tube (4.76 mm of internal diameter and 20 mm long), as shown in Figure 1.22, and then carefully pressed by two stainless steel ending plugs whose ending surface was polished to mirror finish. Inner spacing between two electrodes was about 2 mm and represented the electro-chemical cell with two

electrodes geometry where the composite slurry was placed^[176]. The electrical impedance spectroscopy of the slurries was measured by connecting the two stainless steel electrodes to the potentiostat (AutoLab Electrochemical Potentiostat PGSTAT 302N, Utrecht, the Netherlands).

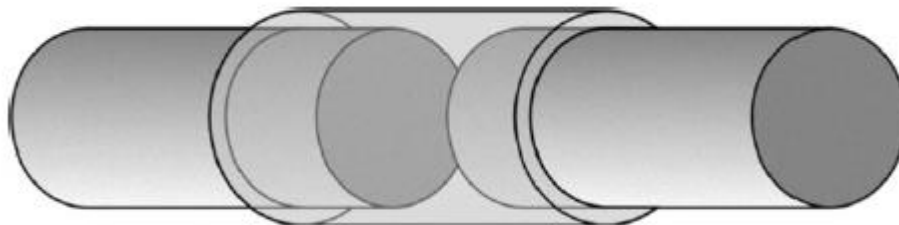


Figure 1.22 Apparatus for the electrical conductivity measurements

1.4.5. Magnetic properties

Every material exhibits kind of magnetic behavior, which arises from the behavior of electrons. The magnetic moment originates from both spin momentum (S) and orbital angular momentum (L) of the unpaired electrons. The S is intrinsic to the electrons; while L is strongly influenced by the local environment. The magnetic moment of an atom is defined as:

$$\mu = -g\mu_B J \quad \text{Equation 1-14}$$

where the ground state value is $J = |L - S|$ when the shell is less than half full and $J = L + S$ when the shell is more than half full, μ_B is the Bohr magnetron. And g is the gyromagnetic ratio, defined by the Landé equation:

$$g = \frac{3J(J+1) + S(S+1) - L(L+1)}{2J(J+1)} \quad \text{Equation 1-15}$$

Paramagnetic materials always have unpaired electrons; whereas, all electrons of diamagnetic materials are paired. The magnetic moments of paramagnetic materials are disordered which will be partly aligned parallel to the field when the external magnetic field was applied. The magnetization of a material (M) is defined as:

$$\chi = M/H \quad \text{Equation 1-16}$$

where, χ is the magnetic susceptibility, H is external magnetic field.

The χ values are quite different for various materials as observed by their temperature and field dependencies. Generally, diamagnetic materials have a small and slightly negative χ , resulted from the realignment of electron orbitals due to the perturbation by the applied field. For most paramagnetic materials

(no interaction between adjacent spins), the relationship between χ and temperature is defined by Curie Law [177].

$$\chi = C/T \tag{Equation 1-17}$$

where C is the Curie constant.

For ferromagnetic and antiferromagnetic materials, there are interactions between adjacent spins. The high temperature paramagnetic region of ferromagnetic and antiferromagnetic materials is described by the Curie-Weiss Law [178].

$$\chi = \frac{c}{T-\theta} \tag{Equation 1-18}$$

where θ is the Weiss constant. The θ values depend on the dominant interaction between paramagnetic species, as shown in Figure 1.23.

Unlike ferromagnetic materials, paramagnetic materials do not retain any magnetization in the absence of an externally applied magnetic field, because thermal motion causes the spins to become randomly oriented without it. Thus, the total magnetization will drop to zero when the applied field is removed. Even in the presence of the field there is only a small induced magnetization because only a small fraction of the spins will be oriented by the field. This fraction is proportional to the field strength and this explains the linear dependency.

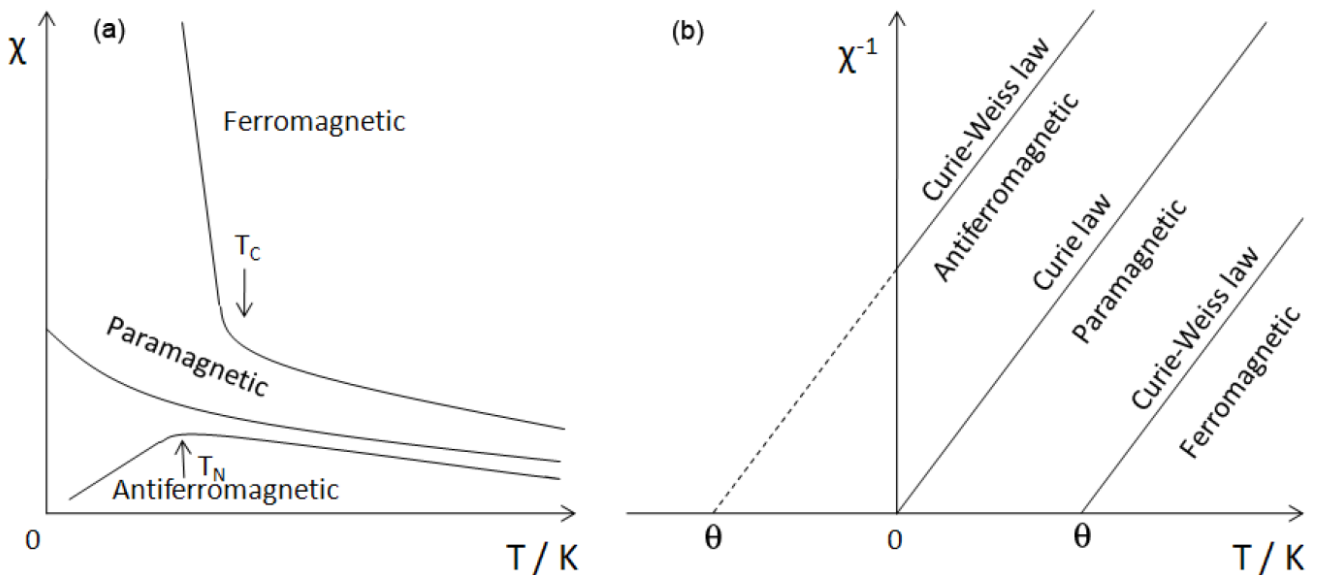


Figure 1.23 Temperature dependent behaviors of (a) susceptibility and (b) inverse susceptibility for different types of magnetic materials [178].

Antoine et. al. ^[70] presented that a sharp characteristic of the presence of an antiferromagnetic ordering was observed at low temperature for perovskite $\text{LaVO}_{3-x}\text{N}_x$ ($0 < x < 0.9$) oxynitrides, and the effect of the magnetic ordering became weaker and weaker with the increasing of nitrogen content. A Pauli-paramagnetic behavior was introduced in the temperature range 100 – 300 K for SrMoO_2N by Fawcett et. al. ^[46]. Oro-Sole et. al. ^[66] illustrated that Curie-Weiss and temperature-independent paramagnetic contributions are presented in NdVO_2N oxynitride. Tassel et. al. ^[44] reported a helical spin order at 25 K for MnTaO_2N , which offers an advanced opportunity for developing magnetic polar materials.

1.5 Scope of the present work

The whole thesis is divided into three parts. The first part of the present work (section 2.1 and publication [1]) is dedicated to the prediction of the formability of perovskite-type oxynitrides. A model that utilizes the tolerance and octahedral factors was developed for assessing the formability of the perovskite structure in oxynitrides and for predicting new perovskite-type oxynitrides that has not been synthesized so far.

The second part of the present work (section 2.2 – 2.4 and publications [2] – [5]) describes Mo and W-containing perovskite-type oxynitrides, including their synthesis, structure evolution, densification, solid-solution materials, as well as magnetic and electrical properties investigation. Following aspects have been addressed:

- Synthesis of scheelite-type oxide precursors and study the microstructure of precursors prepared via different synthesis approach (hydrothermal and solvothermal method).
- a) Compare the nitridation behavior between solvothermal synthesized and commercial oxide precursors; b) Try to understand the structure evolution from scheelite ABO_4 to perovskite $\text{AB}(\text{O,N})_4$ induced by nitrogen incorporation. The as-synthesized oxynitrides were characterized by XRD, neutron diffraction, elemental analysis, FTIR and Raman, SEM-EDS and TG/MS, as well as HRTEM in order to analyze their chemical and phase compositions, crystal structure, microstructure and thermal stability.
- Focus on rapid sintering behavior of dense $\text{SrA}(\text{O,N})$ ($A=\text{Mo, W}$) oxynitride ceramics by SPS (Spark plasma sintering). Selected oxynitrides with pure phase were sintered by SPS in order to achieve fully dense monolith materials with minimum decomposition. The compacted monoliths were characterized by elemental analysis, electron microscopy (SEM, TEM) coupled with energy dispersive X-ray spectroscopy (EDS), as well as XRD combined with Rietveld refinement in order to analyze the chemical and phase compositions, microstructure and relative density of as-sintered monoliths.
- Synthesis of the solid-solution perovskite-type $\text{SrMo}_{1-x}\text{W}_x(\text{O,N})_3$ ($x=0.05 - 0.95$) oxynitrides. The as-synthesized oxynitrides were characterized by XRD and neutron diffraction with Rietveld refinement, elemental analysis, SEM and TEM in order to clarify their chemical and phase compositions as well as microstructure. The superconducting quantum interference device (SQUID) and Powder-

Solution-Composites (PSC) methods were employed to investigate the magnetic and electrical properties of as-synthesized solid-solution oxynitrides.

In the third part of the present work (section 3), the preparation of Ba-Ta oxide precursors via solid state reaction (SSR) and polymeric complex method (PCM), followed by flux/mineralizer-assisted thermal ammonolysis, is introduced. The influence of the ammonolysis temperature, flux on the chemical and phase composition was discussed by XRD combined with Rietveld refinement, elemental analysis, SEM and UV-Vis spectroscopy. Selected BaTaO₂N were tested as photodegradation catalysts under visible-light.

2. Critical assessment of the present thesis

2.1 The formability of perovskite-type oxynitrides

The content of this Chapter is published in:

[1] W. J. Li, E. Ionescu, R. Riedel and A. Gurlo, “Can we predict the formability of perovskite oxynitrides from tolerance and octahedral factors?”, *Journal of Materials Chemistry A*, **2013**, 1, (39), 12239-12245

In the present work, we calculate and apply the octahedral and tolerance factors for predicting the formability of perovskite structures in metal oxynitrides. Our approach consists of three steps. First, we derive expressions for calculating the octahedral and tolerance factors in oxynitrides taking into account the difference in ionic radii and in interatomic distances for nitrogen and oxygen coordinated cations. In the second step we consider already synthesized, perovskite oxynitrides in the form of binary $ABO_{3-x}N_x$ and cation-substituted $A'_{1-y}A''_yB'_{1-z}B''_zO_{3-x}N_x$ oxynitrides and identify the region of stability of the perovskite structure in the structure field maps. And finally, we apply the stability field, identified in the previous step, for predicting the formability of new, not yet synthesized, perovskite oxynitrides. And the discussion of the main results that can guide the future synthesis of oxynitride perovskites not realized so far is presented.

2.1.1. Results and discussion

Goldschmidt's tolerance factor has been widely accepted as a criterion for the formation of the oxide perovskite structure, as well as octahedral factor. Both of them are given as following:

$$t_{tolerance} = \frac{(r_A + r_O)}{\sqrt{2}(r_B + r_O)} \quad \text{Equation 2-1}$$

$$t_{octahedral} = \frac{r_B}{r_O} \quad \text{Equation 2-2}$$

where r_A , r_B , r_O are the ionic radii of A, B and O, respectively. Geometrically, for an ideal perovskite, the $t_{tolerance}$ value should be equal to 1.0. However, Goldschmidt found that, as an experimental fact, $t_{tolerance}$ values of most cubic perovskite oxides are in the range of 0.8 ~ 0.9, and distorted perovskites occur in somehow wider range of $t_{tolerance}$. However, the formability of perovskite-type oxynitrides is still completely blank up to now.

The expressions for tolerance and octahedral factors for perovskite oxides cannot be used for the estimation of perovskite structure in anion-substituted compounds due to an alteration of the experimental cation-anion distances in oxynitrides, as well as a difference and non-systematic variation in ionic radii for nitrogen and oxygen coordinated cations.

Therefore, we derive new expressions for calculating tolerance and octahedral factors in perovskite oxynitrides from (i) the experimental cation-anion distances, (ii) ionic radii and (iii) bond-valence parameters in consideration of disordered structures ^[43, 60]. And we inspect all three approaches for (i) confirming the clustering of perovskite oxynitrides and for (ii) verifying the stability fields of perovskite oxynitrides in structure maps.

The main result is that in all (four) cases we observe clustering of perovskite structures from which the structure field of perovskite structure is delineated (Figure 2.1). This is an important finding showing that all approaches identify the same trends in the perovskite structure stability allowing in this way the search for new, unknown, perovskite oxynitrides that have not been synthesized yet. In addition to that, we observe a trend in clustering of compounds with similar crystal symmetry (Figure 2.2). However, for the prediction, we applied the ionic radii approach considering the Shannon-Prewitt ionic radii^{1,221} in oxides due to some limitations of the other two approaches (see publication [1]).

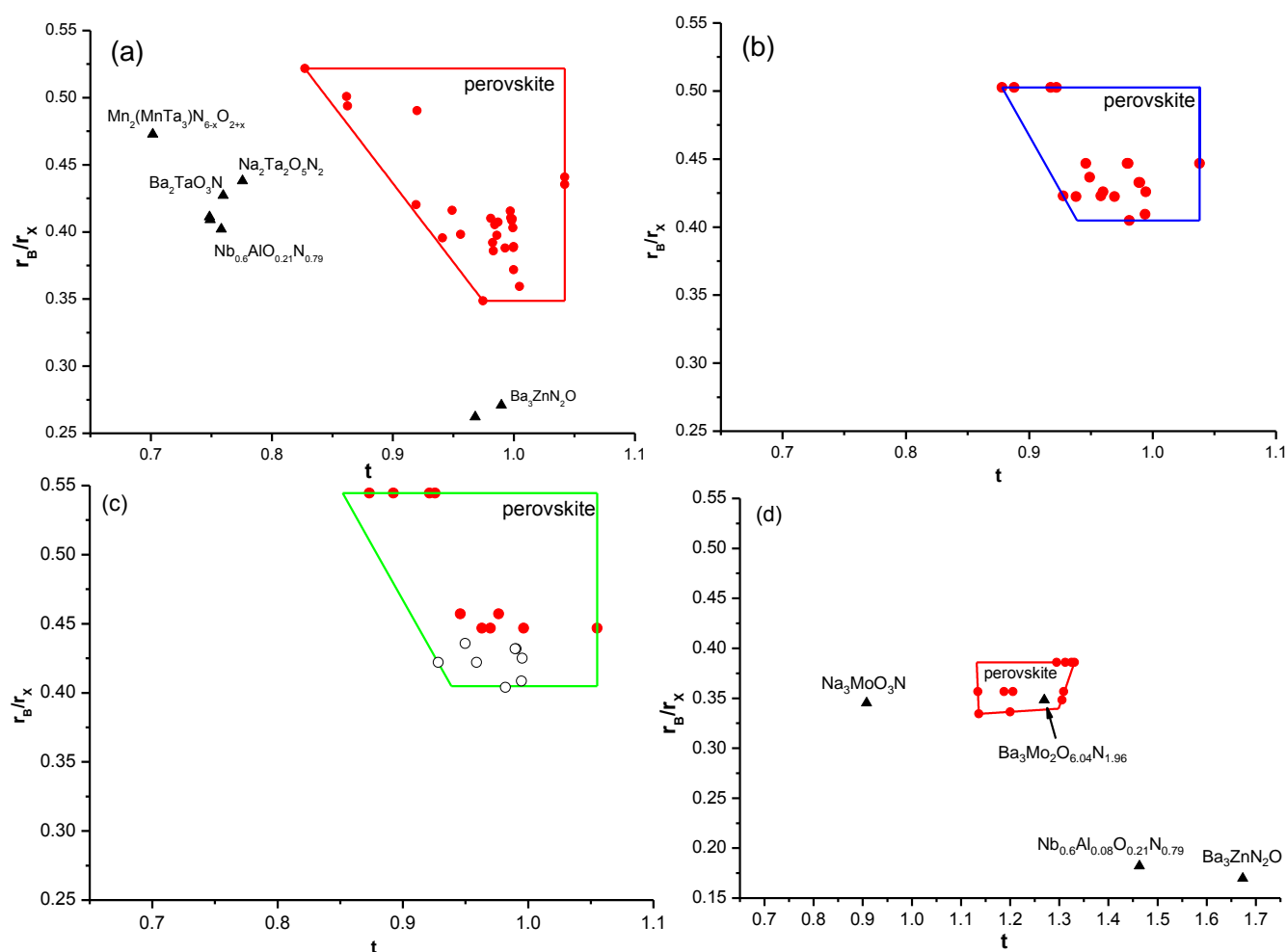


Figure 2.1 Structure field maps for oxynitrides showing the octahedral versus tolerance parameter calculated from (a) the average cation-anion distances, (b) ionic radii and (d) the bond-valence parameters. Shannon-Prewitt ^[1, 179] cationic radii in oxides are applied in (b); Baur cationic radii in nitrides ^[2] are applied in (c); the bond-valence parameters ^[180] are applied in (d). In (c) the black squares refer to the perovskites for which Baur's radii are not available; in the calculation we applied Shannon-Prewitt ^[1, 179] cationic radii in oxides.

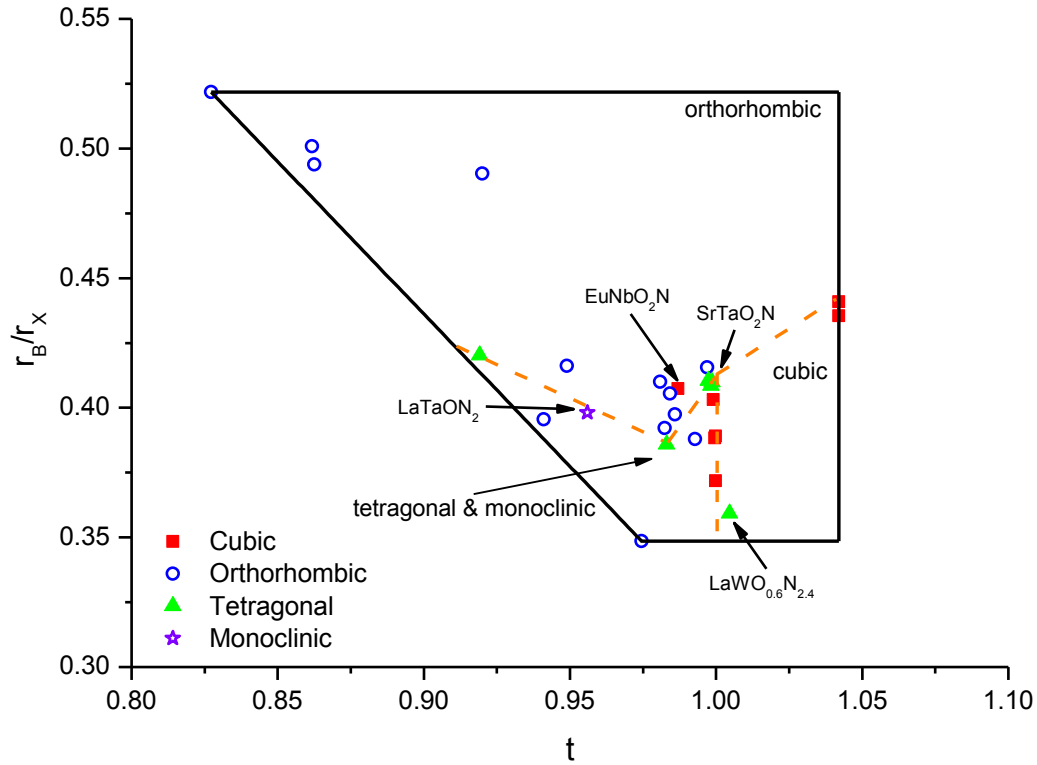


Figure 2.2 Location of perovskite-type oxynitrides with different crystal symmetry in the structure field map from Figure 2.1

Table 2.1 The tolerance and octahedral factors calculated for perovskite oxynitrides in the ionic radii approximation

Perovskite	Tolerance factor	Octahedral factor
ABO_3	$\frac{r_A + r_O}{\sqrt{2}(r_B + r_O)}$	r_B/r_O
ABO_2N	$\frac{[(r_A + r_o)^8 (r_A + r_N)^4]^{1/12}}{\sqrt{2}[(r_B + r_o)^4 (r_B + r_N)^2]^{1/6}}$	$r_B / (r_O^4 \cdot r_N^2)^{1/6}$
$ABON_2$	$\frac{[(r_A + r_o)^4 (r_A + r_N)^8]^{1/12}}{\sqrt{2}[(r_B + r_o)^2 (r_B + r_N)^4]^{1/6}}$	$r_B / (r_O^2 \cdot r_N^4)^{1/6}$
ABN_3	$\frac{r_A + r_N}{\sqrt{2}(r_B + r_N)}$	r_B/r_N

As stressed above, we follow the approach based on ionic radii in oxide (see expressions in Table 2.1). The combination of A and B cations in $AB(O,N)_3$ perovskites applied for the calculation are displayed in Table 2.2. We identified several oxynitrides that may exist in the perovskite structure and are not synthesized so far, which are marked as “P” summarized in Table 2.3.

Table 2.2 Combination of A and B cations in AB(O,N)₃ perovskites applied for the calculation of the tolerance and octahedral factors listed and displayed in the Figure 2.3

AB(O,N) ₃ perovskites	A-site	B-site
A ⁺ B ⁶⁺ O ₂ N	Li ⁺ , Na ⁺ , K ⁺	Mo ⁶⁺ , W ⁶⁺
A ²⁺ B ⁵⁺ O ₂ N	Mg ²⁺ , Ca ²⁺ , Sr ²⁺ , Ba ²⁺ , Zn ²⁺ , Cd ²⁺ , Eu ²⁺	V ⁵⁺ , Nb ⁵⁺ , Ta ⁵⁺ , Mo ⁵⁺ , W ⁵⁺
A ²⁺ B ⁶⁺ ON ₂	Mg ²⁺ , Ca ²⁺ , Sr ²⁺ , Ba ²⁺ , Zn ²⁺ , Cd ²⁺ , Eu ²⁺	Mo ⁶⁺ , W ⁶⁺
A ³⁺ B ⁴⁺ O ₂ N	Sc ³⁺ , Y ³⁺ , Ga ³⁺ , In ³⁺ , La ³⁺ , Pr ³⁺ , Nd ³⁺ , Sm ³⁺	Si ⁴⁺ , Ge ⁴⁺ , Sn ⁴⁺ , Ti ⁴⁺ , Zr ⁴⁺ , Hf ⁴⁺ , Mn ⁴⁺ , Fe ⁴⁺ , Co ⁴⁺ , V ⁴⁺ , Nb ⁴⁺ , Ta ⁴⁺ , Mo ⁴⁺ , W ⁴⁺
A ³⁺ B ⁵⁺ ON ₂	Sc ³⁺ , Y ³⁺ , Ga ³⁺ , In ³⁺ , La ³⁺ , Pr ³⁺ , Nd ³⁺ , Sm ³⁺	V ⁵⁺ , Nb ⁵⁺ , Ta ⁵⁺ , Mo ⁵⁺ , W ⁵⁺

Table 2.3 The formability of perovskite oxynitrides for ABO₂N (A¹⁺-B⁶⁺, A²⁺-B⁵⁺ and A³⁺-B⁴⁺) and ABON₂ (A²⁺-B⁶⁺ and A³⁺-B⁵⁺) compositions.

Site	A-site																			
	Li ⁺	Na ⁺	K ⁺	Mg ²⁺	Ca ²⁺	Sr ²⁺	Ba ²⁺	Zn ²⁺	Cd ²⁺	Eu ²⁺	Sc ³⁺	Y ³⁺	Ga ³⁺	In ³⁺	La ³⁺	Pr ³⁺	Nd ³⁺	Sm ³⁺		
B-site	Si ⁴⁺										N	N	N	N	N	N	N	N	N	
	Ge ⁴⁺										N	N	N	N	N	N	N	N	N	
	Sn ⁴⁺										N	P	N	N	P	P	P	P	N	
	Ti ⁴⁺										N	P	N	N	S/P	P	S/P	S/P	N	
	Zr ⁴⁺										N	P	N	N	S/P	S/P	S/P	S/P	S/P	
	Hf ⁴⁺										N	P	N	N	P	P	P	P	N	
	Mn ⁴⁺										N	N	N	N	N	N	N	N	N	
	Fe ⁴⁺										N	P	N	N	P	P	P	P	P	
	Co ⁴⁺										N	N	N	N	N	N	N	N	N	
	V ⁴⁺										N	P	N	N	S ^a /P	P	S/P	S/P	P	
	Nb ⁴⁺										N	P	N	N	P	P	P	P	N	
	Ta ⁴⁺										N	P	N	N	P	P	P	P	N	
	Mo ⁴⁺										N	P	N	N	P	P	P	P	N	
	W ⁴⁺										N	P	N	N	P	P	P	P	N	
	V ⁵⁺				N	N	N	N	N	N	N	N	N	N	N	N	N	N	N	N
	Nb ⁵⁺				N	S/P	S/P	S/P	N	P	S/P	N	N	N	N	S/P	S/P	N	N	
	Ta ⁵⁺				N	S/P	S/P	S/P	N	P	S/P	N	N	N	N	S/P	P	N	N	
	Mo ⁵⁺				N	S ^a /P	S ^a /P	N	N	P	P	N	N	N	N	P	P	P	N	
W ⁵⁺				N	P	S/P	N	N	P	S ^a /P	N	N	N	N	S ^a P	P	S ^a /P	N		
Mo ⁶⁺	P	P	N	N	N	N	N	N	N	N										
W ⁶⁺	P	P	N	N	P	P	N	N	P	P										

S - perovskite oxynitrides synthesized so far, P- perovskite oxynitrides predicted in our model, N – perovskite structure is not stable; ^a non-stoichiometric perovskites CaMoO_{1.7}N_{1.3}, SrMo_{2.5}N_{0.5}, EuWO_{1.58}N_{1.42}, LaWO_{0.6}N_{2.4}, LaVO_{2.1}N_{0.9} and NdWO_{0.8}N_{2.2}

Several theoretical studies suggest promising functionalities in new, not yet synthesized perovskite oxynitride compounds. Among the potentially piezoelectric oxynitrides, YSiO₂N and YGeO₂N^[24] are not stable

in the perovskite-type structure; YZrO_2N and YSnO_2N [24] are in turn formable, whereas for possible candidate of photocatalytic oxynitrides MgTaO_2N is not formable; YTiO_2N , CdTaO_2N and CdNbO_2N [23] appear as being feasible. Interestingly, Zn^{2+} , Cd^{2+} , Y^{3+} , Hf^{4+} , Fe^{4+} and Sn^{4+} , as well as Pr^{3+} , Nd^{3+} , Sm^{3+} , which have never been synthesized yet, should form a number of oxynitrides with perovskite structure (Figure 2.3). Therefore, our model is valuable for designing and guiding the synthesis of novel perovskites structures in oxynitrides.

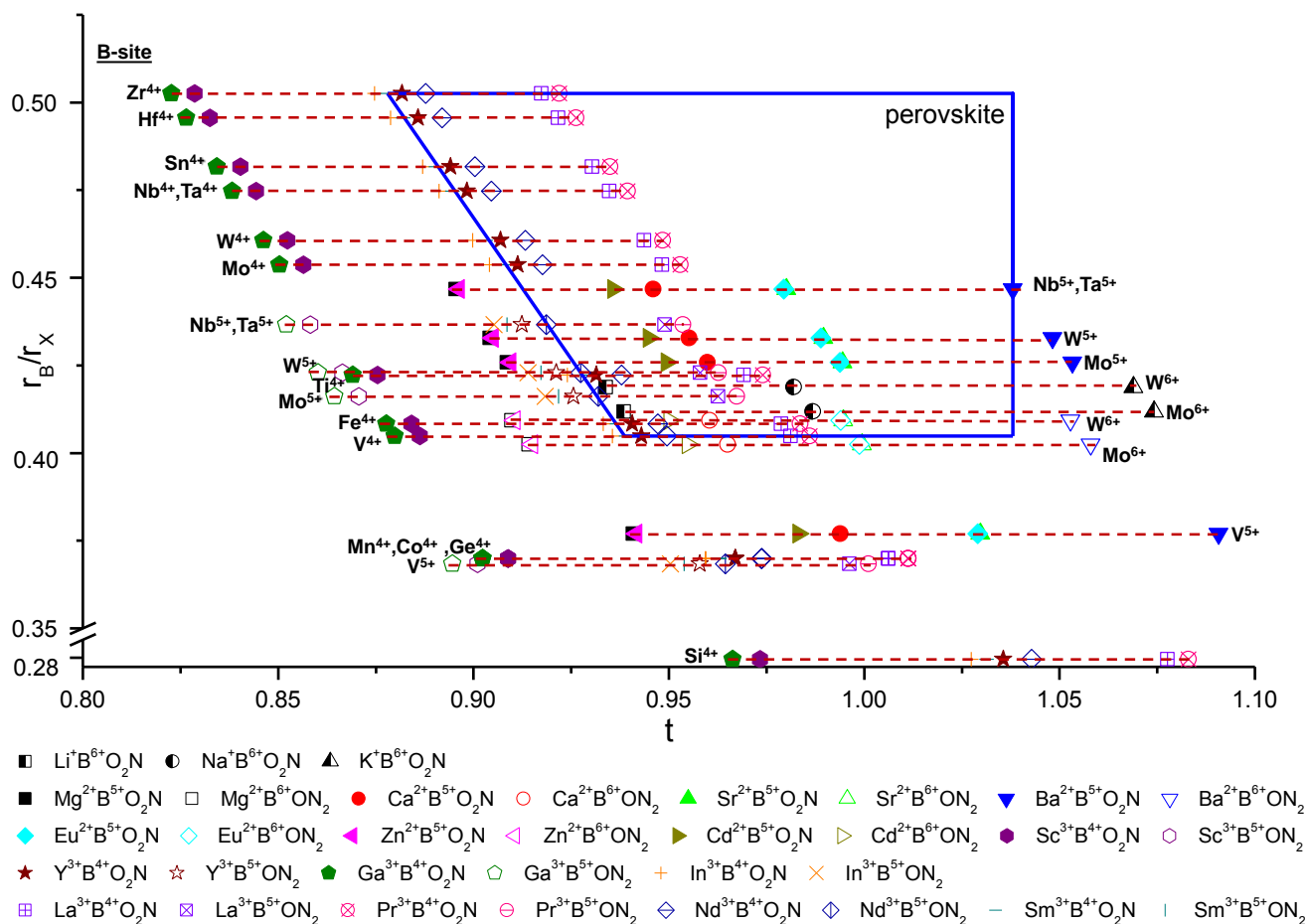


Figure 2.3 Structure field map for perovskite oxynitrides showing the octahedral versus tolerance parameter calculated according to Table 2.1 by applying the Shannon-Prewitt radii [1, 179].

2.1.2. Statement of personal contribution

[1] W. J. Li, E. Ionescu, R. Riedel and A. Gurlo, "Can we predict the formability of perovskite oxynitrides from tolerance and octahedral factors?", *Journal of Materials Chemistry A*, **2013**, 1, (39), 12239-12245

The idea behind this work was developed by myself. All the work was carried out by myself, including model establishment and data processing. The manuscript was written by myself and revised and approved of by Prof. Dr. Aleksander Gurlo, Dr. Emanuel Ionescu and Prof. Dr. Ralf Riedel.

2.2 A study on the thermal conversion of scheelite-type ABO_4 into perovskite-type $AB(O,N)_3$

The partial content of this Chapter is published in:

[2] W. J. Li, D. Li, X. Gao, A. Gurlo, S. Zander, P. Jones, A. Navrotsky, Z. J. Shen, R. Riedel and E. Ionescu, "A study on the thermal conversion of scheelite-type ABO_4 into perovskite-type $AB(O,N)_3$ ", Dalton Transactions, 2015, 44, 8238-8246

Some unpublished results have been discussed in Chapter 2.2.1.1 and 2.2.1.2.

In Chapter 2.2, the preparation of scheelite-type ABO_4 ($A=Ca, Sr, Ba$; $B=Mo, W$) oxide precursor via solvothermal and hydrothermal approaches, followed by thermal ammonolysis (only for solvothermal one), is presented. The influence of different approaches on microstructure of oxide precursors, as well as thermal ammonolysis behavior of solvothermal synthesized powders compared to that of commercial powders, is presented. From the perspective of solvothermal synthesized materials, a study on the thermal conversion of scheelite-type ABO_4 into perovskite-type $AB(O,N)_3$ under ammonia atmosphere is addressed by means of XRD, neutron diffraction, elemental analysis, FTIR, TG, TEM and calorimetric measurement.

2.2.1. Results and discussion

Scheelite-type oxide precursors (i.e., $SrMoO_4$, $SrWO_4$, $BaMoO_4$, $BaWO_4$, $CaMoO_4$ and $CaWO_4$) were synthesized via solvo-/hydro- thermal method by mixing $Sr(NO_3)_2$, $Ba(NO_3)_2$ or $Ca(NO_3)_2 \cdot 4H_2O$ in an equimolar ratio with $Na_2MoO_4 \cdot 4H_2O$ or $Na_2WO_4 \cdot 4H_2O$ in ethylenediamine/ H_2O under vigorous stirring, then subsequently reacted in an autoclave with Teflon lining at 200 °C for 24 h. The post-treated solvothermally synthesized powders were dried by centrifugation and heating at 60 °C and thermally ammonolyzed at temperature between 400 and 900 °C for 4 – 24 h.

2.2.1.1. The synthesis of scheelite-type oxide precursors

Solvo- and hydrothermal methods show numerous advantages for nano-materials synthesis: 1) most materials can be made soluble in proper solvent by heating and pressuring the system close to its critical point; 2) significant improvement in the chemical activity of the reactant, the possibility to replace the solid-state method, and materials which may not be obtained via solid-state reaction may be prepared through hydrothermal/solvothermal synthesis; 3) novel compounds of metastable state and other specific condensed state may be synthesized as well; 4) easy and precise control of the size, shape distribution, crystallinity of the final product through adjusting the parameters such as reaction temperature, reaction time, solvent type, surfactant type, precursor type etc.; 5) substances which have low melting-points, high in vapor pressures and low thermal stability may be obtained by using these techniques.

Therefore, they are beneficial to synthesize the nanomaterial with fine particle size and homogeneity, which is supposed to be beneficial for a successful thermal ammonolysis process due to the enhancement of solid diffusion process. XRD patterns (Figure 2.4) reveal that the single pure scheelite-type phase with sharp reflections was achieved for all the oxides. The Rietveld refinement results (Figure 2.5) show perfect fit between observed and calculated results. The calculated average particle size according to Equation 2-3 is given in Table 2.4 and Table 2.5.

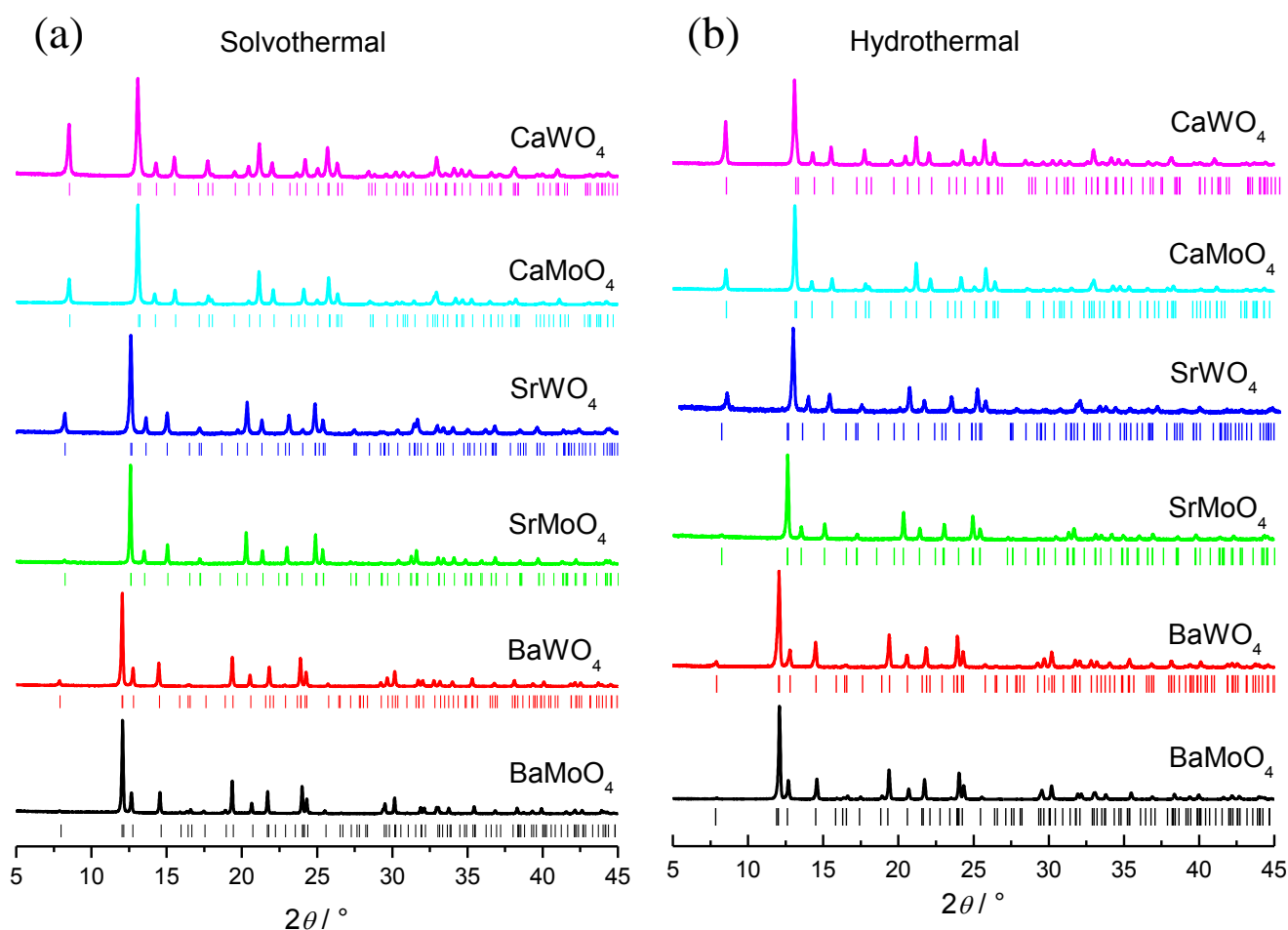


Figure 2.4 XRD patterns of the scheelite-type ABO_4 oxide precursors synthesized by solvothermal (a) and hydrothermal (b) method

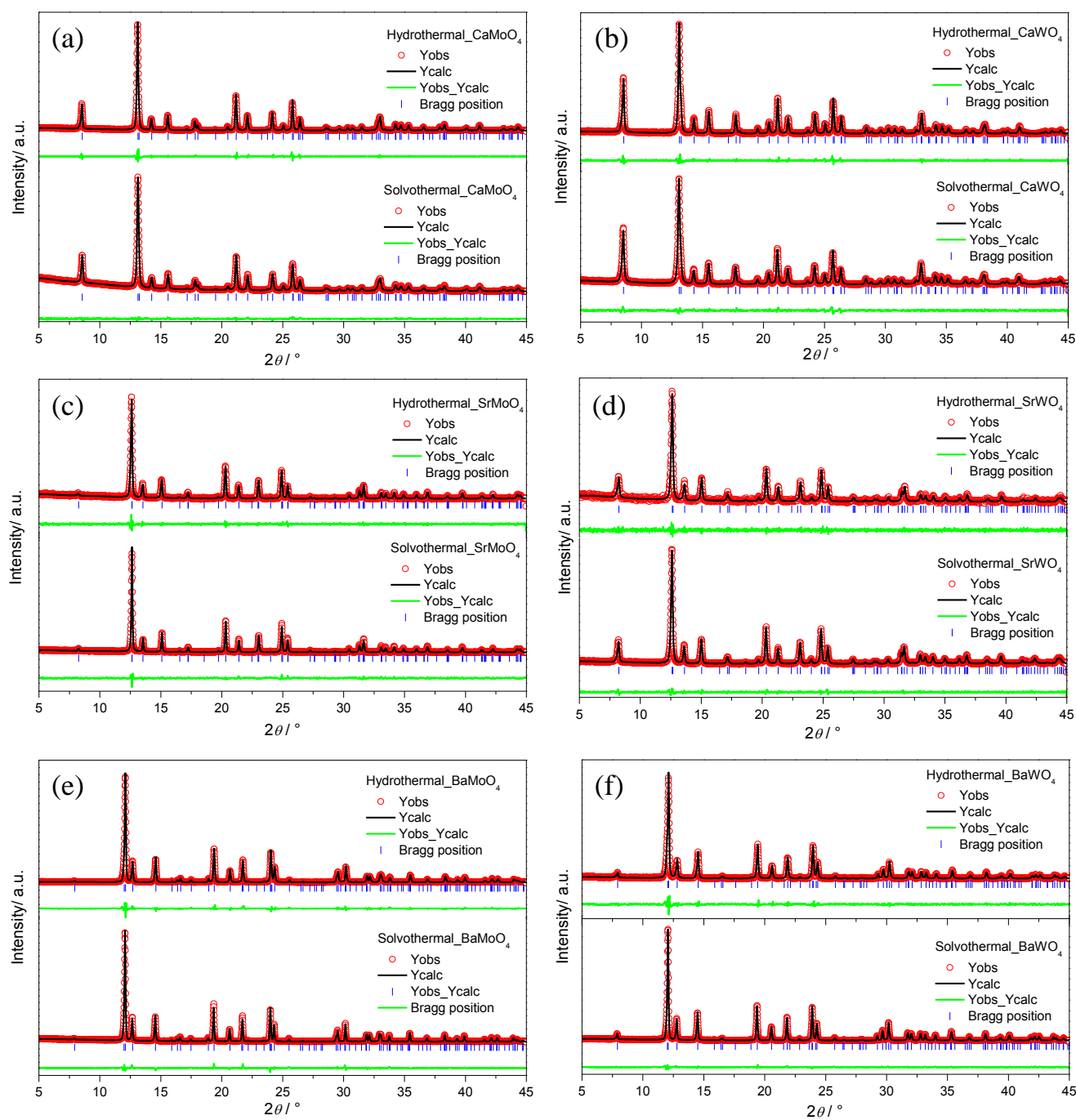


Figure 2.5 Rietveld patterns of the X-ray powder diffraction data of samples obtained by hydrothermal and solvothermal synthesis at 200 °C for 24 h for (a) CaMoO_4 ; (b) CaWO_4 ; (c) SrMoO_4 ; (d) SrWO_4 ; (e) BaMoO_4 ; (f) BaWO_4 . Blue tick marks are Bragg peak positions of tetragonal I $41/a$ scheelite-type ABO_4 (bottom). Green line at the bottom denotes the difference intensities between the observed and calculated profiles.

Table 2.4 Crystal structure data of ABO₄ oxides (I 41/a) obtained by hydrothermal synthesis at 200 °C for 24 h

Parameters		BaMoO ₄	BaWO ₄	SrMoO ₄	SrWO ₄	CaMoO ₄	CaWO ₄
a,b [Å]		5.58721(9)	5.61124(16)	5.40372(14)	5.42006(26)	5.23042(10)	5.24980(11)
c [Å]		12.83433(23)	12.71478(40)	12.04318(36)	11.95590(66)	11.44167(23)	11.38858(26)
Ba (4b)	x, y, z	0, 0.25, 0.625	0, 0.25, 0.625	0, 0.25, 0.625	0, 0.25, 0.625	0, 0.25, 0.625	0, 0.25, 0.625
Mo/W (4a)	x, y, z	0, 0.25, 0.125	0, 0.25, 0.125	0, 0.25, 0.125	0, 0.25, 0.125	0, 0.25, 0.125	0, 0.25, 0.125
O1 (16f)	x	0.23838(107)	0.23768(236)	0.23966(159)	0.23520(306)	0.15116(71)	0.15687(154)
	y	0.12864(101)	0.12665(222)	0.11041(130)	0.10296(307)	0.00585(70)	0.00921(130)
	z	0.05256(47)	0.04791(97)	0.04317(57)	0.04313(127)	0.20907(30)	0.20953(60)
χ^2		1.84	1.2	1.05	0.97	1.67	1.28
chi2		3.61	1.53	1.22	1.06	2.95	1.82
Calculated particle size /nm		137.0	60.7	86.9	43.5	91.7	56.4

Table 2.5 Crystal structure data of ABO₄ oxides (I 41/a) obtained by solvothermal synthesis at 200 °C for 24 h

Parameters		BaMoO ₄	BaWO ₄	SrMoO ₄	SrWO ₄	CaMoO ₄	CaWO ₄
a,b [Å]		5.59582(8)	5.62316(6)	5.40535(19)	5.42622(13)	5.23546(12)	5.25711(12)
c [Å]		12.85160(21)	12.74085(15)	12.04630(45)	11.97166(32)	11.45122(28)	11.40163(28)
Ba (4b)	x, y, z	0, 0.25, 0.625	0, 0.25, 0.625	0, 0.25, 0.625	0, 0.25, 0.625	0, 0.25, 0.625	0, 0.25, 0.625
Mo/W (4a)	x, y, z	0, 0.25, 0.125	0, 0.25, 0.125	0, 0.25, 0.125	0, 0.25, 0.125	0, 0.25, 0.125	0, 0.25, 0.125
O1 (16f)	x	0.24065(113)	0.23224(112)	0.24339(133)	0.23661(159)	0.15304(82)	0.15910(149)
	y	0.13375(102)	0.12477(107)	0.11454(113)	0.10324(162)	0.00877(80)	0.01310(123)
	z	0.05578(48)	0.05116(47)	0.04111(50)	0.04286(68)	0.21001(32)	0.21117(58)
χ^2		1.76	1.48	1.27	1.09	1.22	1.18
chi2		3.27	2.40	2.00	1.31	1.62	1.51
Calculated particle size /nm		134.2	199.5	90.2	49	46.2	36.3

$$Particle\ size = \frac{25.87216}{Y}$$

Equation 2-3

where Y is a parameter to be determined via refinement. In this case, Thompson-Cox-Hastings pseudo-Voigt function^[181] (Npr=7) is applied. Parameters (U, V, W and X) were fixed according to intrinsic parameters of X-ray instrument, and only Y is refined.

The calculated average particle sizes do not show a distinct difference between the solvo- and hydrothermal results, besides BaWO₄ compounds. However, SEM images reveal that the as-synthesized powders by solvothermal method are more homogeneous than that by hydrothermal method. It is probably resulted from the inner atmosphere (i.e., solubility and pressure created by ethylenediamine) is more beneficial for our objective materials.

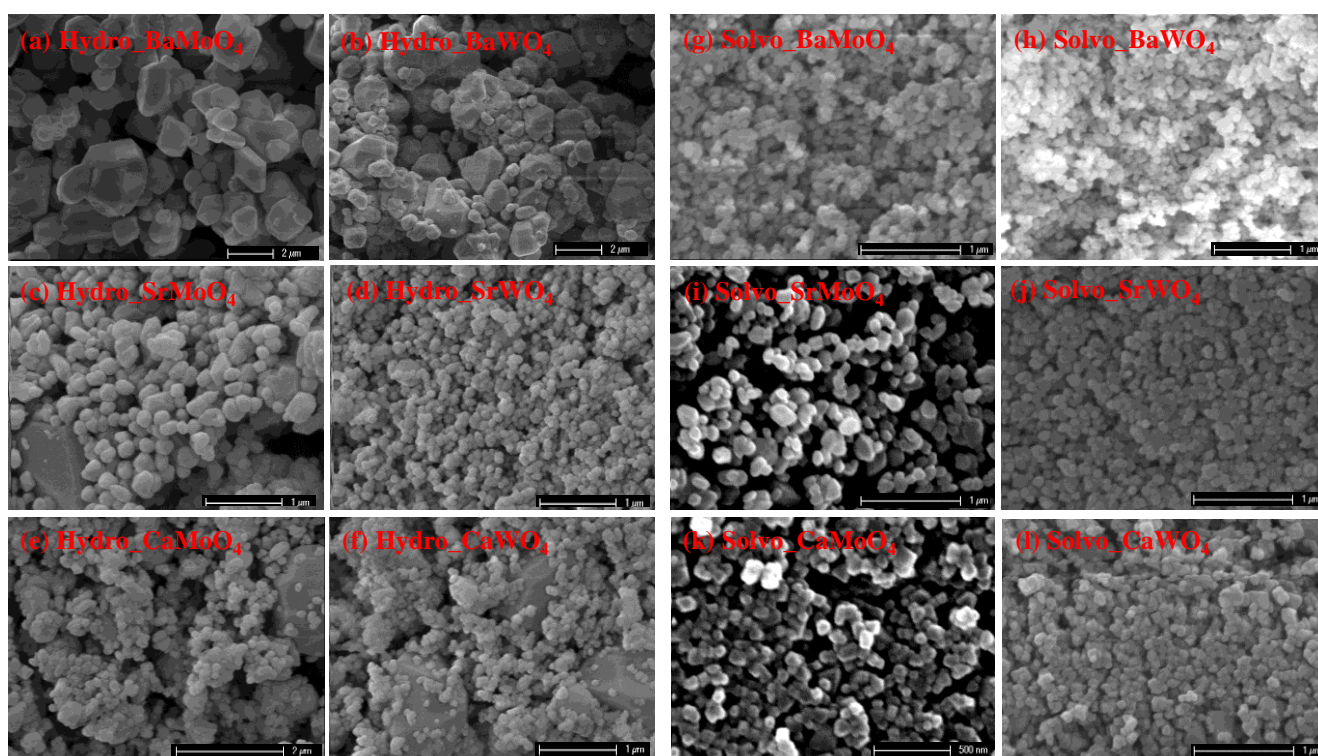


Figure 2.6 SEM images of as-synthesized oxide precursors by Hydrothermal (a) – (f) and Solvothermal (g) – (l) method

2.2.1.2. Comparison of commercial and as-synthesized powders

Since these scheelite-type ABO₄ oxide precursors are commercially available, we compared the ammonolysis behavior of selected commercial and as-synthesized powders. The SEM images (Figure 2.7) show the significantly different morphology. Commercial powders exhibit a much larger particle size and stronger agglomeration than as-synthesized powders, which imply the lower reactivity for commercial powders.

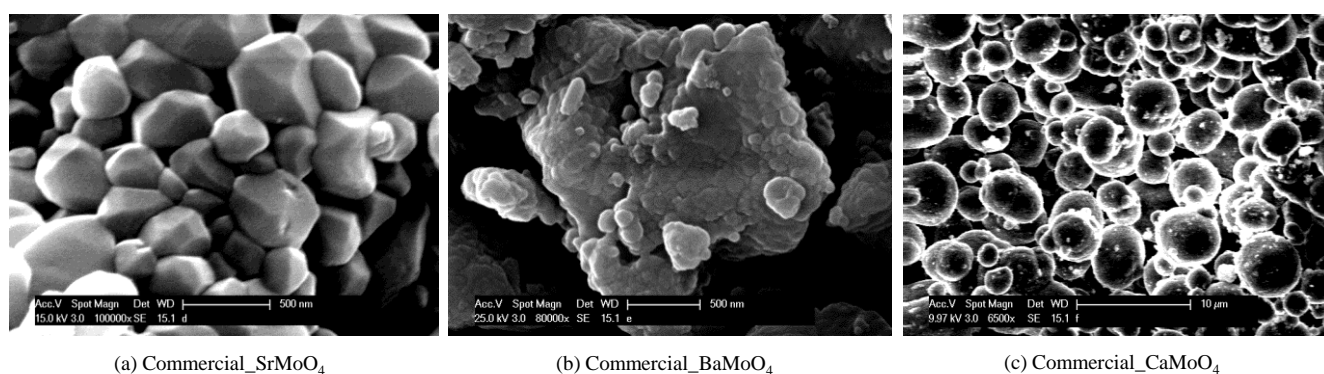


Figure 2.7 SEM images of commercial powders (a) SrMoO_4 , (b) BaMoO_4 and (c) CaMoO_4 .

XRD patterns (Figure 2.8) reveal that commercial powders show much weaker ammonolyzed capability compared to that of the as-synthesized powders under the same nitridation condition (*e.g.*, BaMoO_4 and SrMoO_4). The more amounts of powder are, the less of powder can be nitrided due to the limited diffusion rate. Compared to as-synthesized powders, commercial SrMoO_4 powder seems to be rather weaker to react with ammonia, thus ca. 32.55 (38) wt% of SrMoO_4 still remained after ammonolysis at $700\text{ }^\circ\text{C}$ for 4 h (Figure 2.9). This is definitely related to the low solid diffusion rate due to the microstructure of powders. Considering all above results, we choose the powders synthesized via the solvothermal method to carry out further ammonolysis.

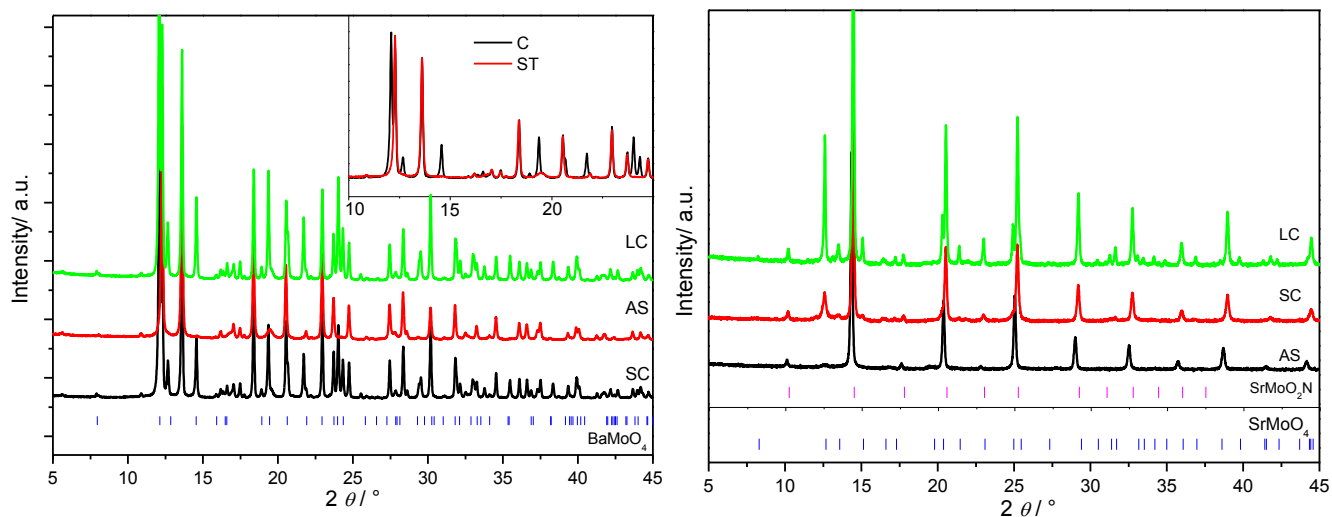


Figure 2.8 XRD patterns of as-synthesized and commercial (a) BaMoO_4 and (b) SrMoO_4 after ammonolysis under $700\text{ }^\circ\text{C}$ for 4 hours (LC: large amount of commercial powder; SC: small amount of commercial powder; AS: as-synthesized powder)

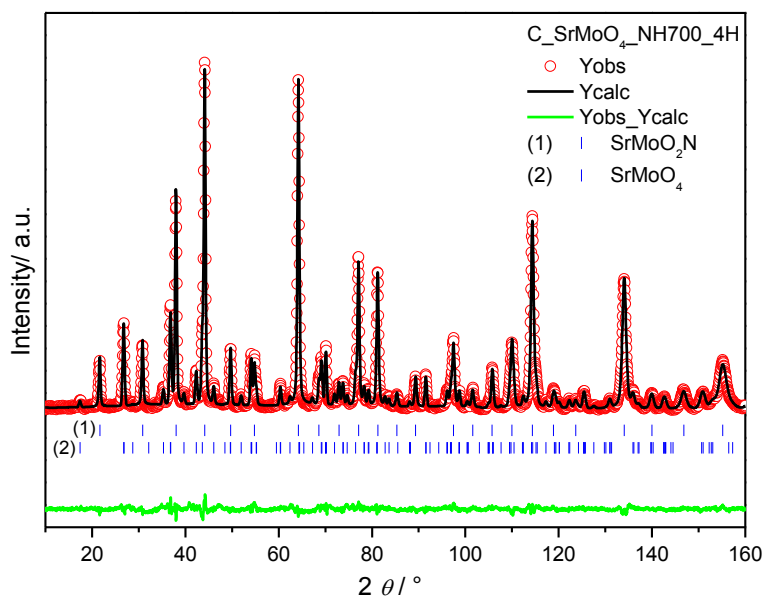


Figure 2.9 Rietveld patterns of the Neutron powder diffraction data of samples obtained from the ammonolysis of commercial SrMoO_4 at $700\text{ }^\circ\text{C}$ for 4 hours. Blue tick marks are Bragg peak positions of related phase (bottom). Green line at the bottom denotes the difference intensities between the observed and calculated profiles.

2.2.1.3. A study on the thermal conversion from scheelite ABO_4 into perovskite $\text{AB}(\text{O},\text{N})_3$

The reaction of BaBO_4 with ammonia up to $900\text{ }^\circ\text{C}$ leads to the formation of rhombohedral $\text{Ba}_3\text{B}_2(\text{O},\text{N})_8$ and the corresponding binary metal nitrides Mo_3N_2 and $\text{W}_{4.6}\text{N}_4$ (as for $\text{B} = \text{Mo}$ and W , respectively). The absence of the perovskite-type $\text{BaB}(\text{O},\text{N})_3$ is consistent with the experimental work of Liu et al.^[182] and our previously prediction^[183]. Similar behavior was observed for CaBO_4 , which converts upon ammonolysis into mixtures of oxides (CaO and Ca_3WO_6) and nitrides (Mo_3N_2 , Mo_2N , MoN and $\text{W}_{4.6}\text{N}_4$, for $\text{B} = \text{Mo}$ and W , respectively).

XRD measurements (Figure 2.10) confirm that SrMoO_4 and SrWO_4 convert into cubic perovskite SrMoO_2N and $\text{SrWO}_{1.5}\text{N}_{1.5}$ at $700\text{ }^\circ\text{C}$ and $900\text{ }^\circ\text{C}$ respectively. Interestingly, the Sr,W -based system can accommodate more nitrogen than its analogous Sr,Mo -based system. Nevertheless the O/N ratio still cannot be pushed down to 0.5.

An interesting phenomenon during the ammonolysis of SrMoO_4 at $600\text{ }^\circ\text{C}$ relates to the incorporation of 2.23 wt% nitrogen without the formation of any new crystalline phase; thus, the color of the sample changed from white to light-grayish and the FTIR spectrum showed a new absorption band at 978 cm^{-1} related to $(\text{MoO}_3\text{N})^{3-}$ units in tetrahedral coordination, as also observed in $\text{Ba}_3\text{Mo}_3(\text{O},\text{N})_8$ (Figure 2.11). This indicates that an intermediate scheelite-type oxynitride phase $\text{SrMoO}_{4-x}\text{N}_x$ ($x = 0.39$ in our experiment) forms at $600\text{ }^\circ\text{C}$, which, however, subsequently rearranges into the perovskite structure while taking up more nitrogen.

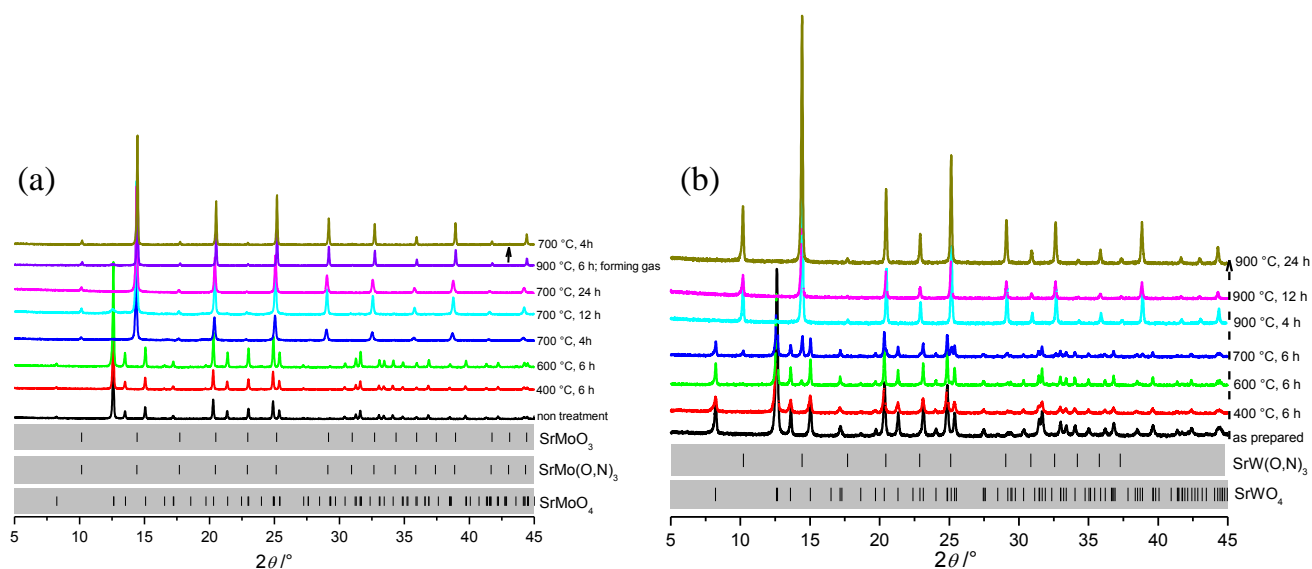


Figure 2.10 (a) XRD patterns of SrMoO_4 after heating at 400, 600 and 700 °C for different times under an ammonia flow and the reduced SrMoO_3 from SrMoO_4 by using forming gas (mixture of 5 vol% H_2 and 95 vol% N_2). Arrow indicates the diffraction pattern of the oxynitride obtained upon ammonolysis of SrMoO_4 ; (b) XRD patterns of SrWO_4 after heating at 400, 600, 700 and 900 °C for different times under an ammonia flow.

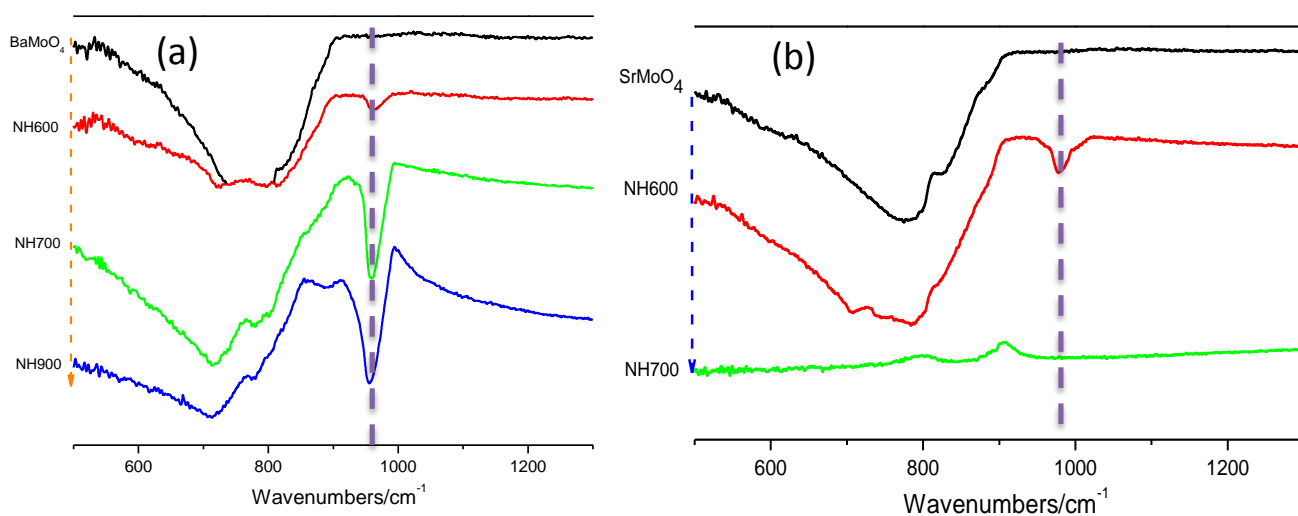


Figure 2.11 FTIR spectrum of the as-synthesized materials: (a) BaMoO_4 and the resulting oxynitrides from ammonolysis at 600, 700 and 900 °C for 6 h; (b) SrMoO_4 and the resulting oxynitrides from ammonolysis at 600 and 700 °C for 6 h

The nitrogen content of the phase-pure perovskite-type oxynitride (empirical formula $\text{SrMo}_{2.77(3)}\text{N}_{0.23(3)}$, see the Rietveld refinement data of the neutron diffraction pattern shown in Figure 2.12) obtained from the perovskite-type SrMoO_3 was significantly lower than that of the oxynitride obtained under the same conditions from SrMoO_4 ($\text{SrMo}_{2.19(2)}\text{N}_{0.81(2)}$). This obviously relates to the oxidation state of Mo in $\text{SrMo}^{6+}\text{O}_4$ and $\text{SrMo}^{4+}\text{O}_3$. The formation of hydrogen due to the dissociation of ammonia at high temperature is beneficial for the reduction of the B-site cation in scheelite-type oxides (i.e. from $\text{A}^{2+}\text{B}^{6+}\text{O}_4$ to $\text{A}^{2+}\text{B}^{5+}\text{O}_2\text{N}$). In case of using perovskite oxides as precursors for perovskite oxynitrides, the B-site cation has to be oxidized in

order to compensate for the increase of the negative charge resulting from nitrogen incorporation, which can actually drawback the reaction.

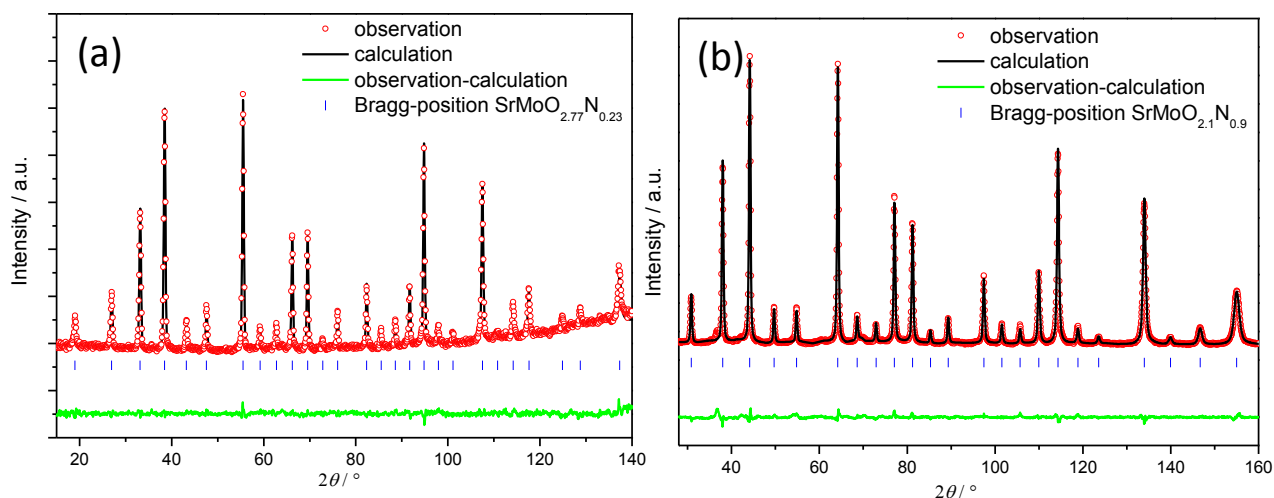


Figure 2.12 Rietveld patterns of the neutron powder diffraction data of the sample obtained upon ammonolysis of the (a) SrMoO_3 at 700 °C for 4 h (FIREPOD, E9); (b) SrMoO_4 at 700 °C for 4 h (HRPT, SINQ). Blue tick marks are Bragg peak positions of related phase as (a) $\text{SrMoO}_{2.77(3)}\text{N}_{0.23(3)}$; (b) $\text{SrMoO}_{2.19(2)}\text{N}_{0.81(2)}$. Green line at the bottom denotes the difference intensities between the observed and calculated profiles.

High temperature oxidative-solution calorimetry was used to determine the enthalpies of formation of the prepared oxynitride samples. This method is well developed^[184-187] and has been applied previously to study nitrides^[188-190] and oxynitrides^[191-193]. Using this technique, ~ 5 mg pellets, made by pressing the powders into a die with a diameter of 1 mm, were dropped from room temperature into molten sodium molybdate ($3\text{Na}_2\text{O}\cdot 4\text{MoO}_3$) solvent at 701 °C in a custom made Tian-Calvet twin microcalorimeter^[184, 186]. The oxynitride samples were oxidized prior to dissolution within the melt. N_2 gas generated by the oxidation reaction was evolved by continuous flushing the headspace above the solvent in the calorimeter using an oxygen flow at 60 mL/min. The reaction rate of the pellet with solvent was accelerated and oxidizing conditions maintained by bubbling oxygen through the solvent at 6 mL/min. For high temperature drop-solution calorimetry of the oxide samples, the same measurement conditions, as described above, were applied. 6-8 pellets of each composition were dropped to obtain appropriate statistics. The calorimeter was calibrated using the heat contents of platinum rods and alumina pellets, respectively, for the oxynitride and oxide samples.

The enthalpy of formation of SrMoO_4 (-260.2 ± 0.5 kJ/g-atom) is ~ 36 kJ/g-atom more exothermic than that of $\text{SrMoO}_{1.96}\text{N}_{1.04}$ (-223.8 ± 0.7 kJ/g-atom). Likewise, the enthalpy of formation of SrWO_4 (-273.4 ± 0.5 kJ/g-atom) is ~ 83 kJ/g-atom more exothermic than that of $\text{SrWO}_{1.5}\text{N}_{1.5}$ (-190.4 ± 0.7 kJ/g-atom). Thus, perovskite-type oxynitrides show less favorable enthalpies of formation than their corresponding scheelite-type oxides. Furthermore, the difference of the enthalpy of formation for Sr-W is larger than that of Sr-Mo. This

suggests that forming the Sr-W oxynitride is less favorable and requires higher temperature (as observed), probably for both thermodynamic and kinetic reasons. The Gibbs free energy (ΔG) of the ammonolysis reactions for SrMoO_4 and SrWO_4 was calculated, as shown in Figure 2.13. It indicates that the reaction is spontaneous at temperature exceeding 992 K (*i.e.*, 719 °C) for SrWO_4 , whereas for SrMoO_4 the reaction seems to be thermodynamically favorable at any of the temperatures used for its ammonolysis. It is worth pointing out that only a thermodynamic consideration might not be enough to describe the ammonolysis processes of the scheelite oxides. The kinetics (*e.g.*, activation energy) of the ammonolysis probably also play an important role and thus could explain why the conversion of SrMoO_4 into perovskite oxynitride needs temperature exceeding 600 °C and proceeds through an intermediate phase.

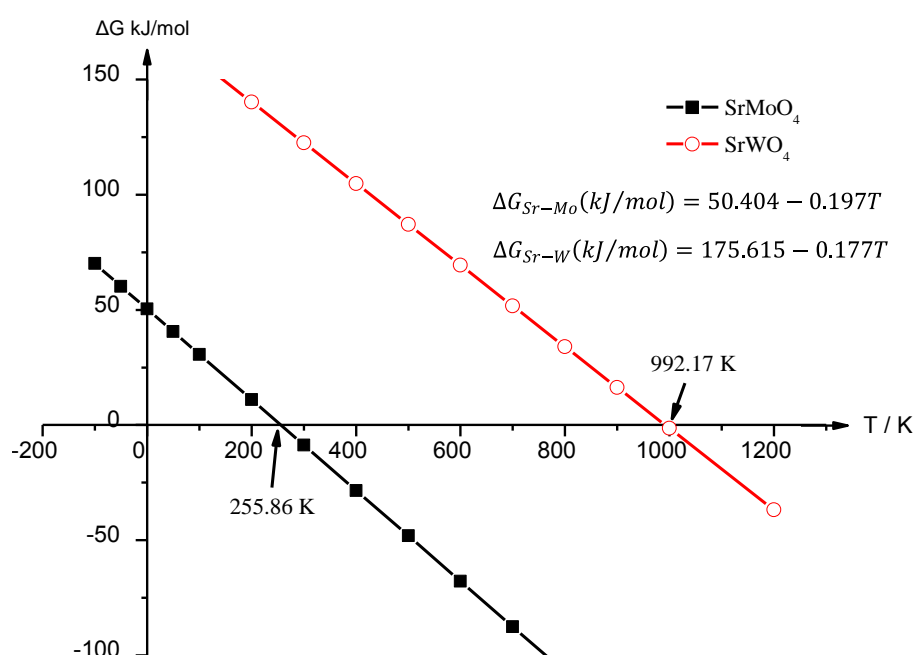


Figure 2.13 Gibbs free energy (ΔG) for the ammonolysis of SrMoO_4 and SrWO_4 as function of the temperature.

The values of the tolerance factors for oxides and oxynitrides calculated from the ionic radii based on our previous work^[183] indicate that the formation of the corresponding perovskite oxynitrides for SrMoO_3 , SrWO_3 , CaMoO_3 and CaWO_3 is favorable. However, large basic cations like Ca typically stabilize higher oxidation states of the transition metals (Mo, W in our case)^[194, 195] leads to the failure of conversion for Ca scheelite-type oxides.

2.2.2. Statement of personal contribution

[2] W. J. Li, D. Li, X. Gao, A. Gurlo, S. Zander, P. Jones, A. Navrotsky, Z. J. Shen, R. Riedel and E. Ionescu, "A study on the thermal conversion of scheelite-type ABO_4 into perovskite-type $AB(O,N)_3$ ", *Dalton Transactions*, **2015**, 44, 8238-8246

The idea behind this work was developed by myself. All experimental work related to material synthesis and preparation was carried out by myself. The neutron diffraction was accomplished by myself at the Swiss Spallation Neutron Source (SINQ), Paul Scherrer Institute, Villigen, Switzerland and Fine Resolution Powder Diffractometer (FIREPOD, E9) at the BERII of the Helmholtz-Zentrum Berlin (HZB), Germany, supported by Dr. Denis Sheptyakov and Dr. Stefan Zander respectively. All characterization work and data process were performed by myself, except TEM (M. Sc. Duan Li, AK Prof. Dr. Zhijian Shen, Stockholm University), TG (Dr. Samuel Bernard, AK Prof. Dr. Philip Miele, IEM, University Montpellier 2) and High temperature oxidative solution calorimetry (Dr. Philip Jones, AK Prof. Dr. Alexandra Navrotsky, University of California Davis). The manuscript was written by myself and revised and approved of by Duan Li, Prof. Dr. Aleksander Gurlo, Prof. Dr. Alexandra Navrotsky, Prof. Dr. Ralf Riedel and Dr. Emanuel Ionescu.

2.3 Densification of perovskite-type oxynitride ceramics

The partial content of this Chapter is published in:

[3] W. J. Li, D. Li, A. Gurlo, Z. J. Shen, R. Riedel and E. Ionescu, “Synthesis and rapid sintering of dense $\text{SrA}(\text{O},\text{N})_3$ (A=Mo, W) oxynitride ceramics”, *Journal of the European Ceramic Society*, **2015**, 35, 3273-3281

[4] D. Li, W. J. Li, C. Fasel, J. Shen and R. Riedel, “Sinterability of the oxynitride LaTiO_2N with perovskite-type structure”, *Journal of Alloys and Compounds*, **586** (2014), 567-573

Some unpublished results have been discussed in this chapter as well.

In Chapter 2.3, the preparation of scheelite-type SrMoO_4 and SrWO_4 via solvothermal approach, followed by thermal ammonolysis, is presented. Based on the thermal stability study, the sinterability of the oxynitrides, $\text{SrMo}(\text{O},\text{N})_3$, $\text{SrW}(\text{O},\text{N})_3$ and LaTiO_2N , was investigated by spark plasma sintering (SPS).

2.3.1. Results and discussion

The scheelite-type oxide precursors of SrMoO_4 and SrWO_4 were prepared by solvothermal method in the same way we did in Chapter 2.2. Four groups of phase pure oxynitride, labeled as $\text{SrMoO}_4\text{-NH700_12H}$, $\text{SrMoO}_4\text{-NH700_24H}$, $\text{SrWO}_4\text{-NH900_12H}$ and $\text{SrWO}_4\text{-NH900_24H}$ (Figure 2.14 and Table 2.6), respectively, were selected for further SPS consolidation study.

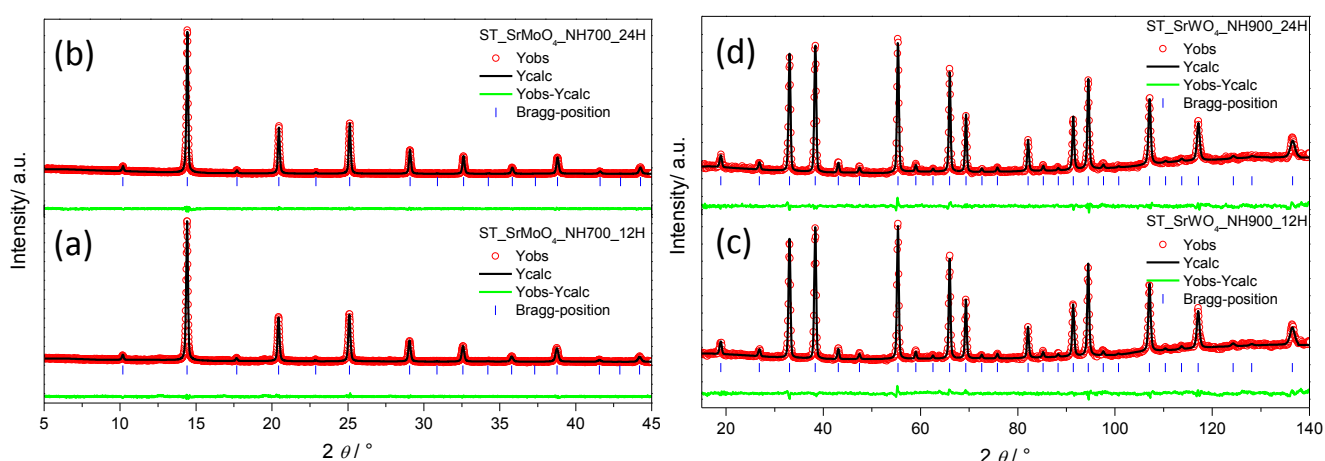


Figure 2.14 Rietveld refinement of X-ray diffraction and Neutron diffraction patterns of the sample obtained from the ammonolysis of SrMoO_4 at 700 °C for 12 (a) and 24 hours (b) as well as SrWO_4 at 900 °C for 12 (c) and 24 hours (d). Blue tick marks are Bragg peak positions of $\text{SrMo}(\text{O},\text{N})_3$ and $\text{SrW}(\text{O},\text{N})_3$, respectively. The green lines at the bottom denote the different intensities between the observed and calculated profiles.

Table 2.6 Crystal structure data for SrMo(O,N)₃ and SrW(O,N)₃ powder samples

Parameters	SrMoO ₄ _NH700_12H	SrMoO ₄ _NH700_24H	SrWO ₄ _NH900_12H	SrWO ₄ _NH900_24H	
Radiation	X-ray Mo K _α	X-ray Mo K _α	Neutron (HRPT, PSI)	Neutron (HRPT, PSI)	
λ, Å	0.7093	0.7093	1.494	1.494	
S.G.	<i>Pmm</i> , Nr. 221	<i>Pmm</i> , Nr. 221	<i>Pmm</i> , Nr. 221	<i>Pmm</i> , Nr. 221	
Z	1	1	1	1	
a,b, c, Å	3.99851(20)	3.99427(13)	3.98451(6)	3.98379(8)	
Sr	x, y, z	0.5, 0.5, 0.5	0.5, 0.5, 0.5	0.5, 0.5, 0.5	
	Biso, Å ²	0.926(67)	0.761(46)	0.577(44)	0.601(46)
	Occ.	1.0	1.0	1.0	1.0
Mo	x, y, z	0.0, 0.0, 0.0	0.0, 0.0, 0.0	0.0, 0.0, 0.0	
	Biso, Å ²	1.148(69)	0.965(47)	0.693(46)	0.853(49)
	Occ.	1.0	1.0	1.0	1.0
O/N	x, y, z	0.5, 0.0, 0.0	0.5, 0.0, 0.0	0.5, 0.0, 0.0	
	Biso, Å ²	1.498(120)	0.857(88)	0.725(21)	0.693(23)
	Occ.	1.96/1.04 ^a	1.82/1.18 ^a	1.449/1.551	1.364/1.636
χ ²	1.069	1.079	1.152	1.152	
R _p	2.06	1.93	2.11	2.26	
wR _p	2.64	2.43	2.65	2.85	
Chi2	1.38	1.42	1.39	1.61	

^a Fixed by elemental analysis results without refinement.

Spark plasma sintering (SPS) is known as field assisted sintering technique (FAST) or pulsed electric current sintering (PECS) ^[196]. The main characteristic of SPS is that the pulsed DC current directly passes through the graphite die, as well as the powder compact, in case of conductive samples under an applied pressure up to 100 MPa. The heat generation is internal, in contrast to the conventional hot pressing, where the heat is provided by external heating elements. Moreover, since the currents pass through the die and the sample at the same time, the entire sample is homogeneously heated, and also benefits from self-heating caused by spark discharges generated in the voids between particles and therefore allow full densification to take place rapidly ^[197]. Spark discharges in the voids momentarily cause local high temperatures resulting in vaporization and melting at the surface of particles, which facilitates neck formation around the contact area between them, leading to a highly sintered compact ^[198]. SPS has a very high heating and cooling rates, hence the sintering process generally is very fast (within a few minutes) compared to conventional sintering which may take hours or days. Thus, nano sized powders can be sintered without considerable grain growth. The atmosphere can be either vacuum or inert gas and can be tailored for different samples.

TGA/DTA curves (Figure 2.15 – Figure 2.18) show that SrMo(O,N)₃ is undergoing a gradually and steadily mass loss in argon and nitrogen, and thermodynamically unstable above ca. 300 °C in argon, ca. 400 °C in air and ca. 800 °C in nitrogen. On the contrary, SrW(O,N)₃ is thermodynamically stable up to ca. 1000 °C in

argon/nitrogen and ca. 500 °C in air. However, it undergoes a sharp mass loss from ca. 1000 °C to 1150 °C in argon and nitrogen. LaTiO_2N is thermodynamically unstable above ca. 400 °C in air and 800 °C in argon. Both TGA/DTA and XRD results reveal that it seems impossible to completely avoid decomposition during sintering; but it is possible to adjust the parameters during sintering to suppress these decompositions.

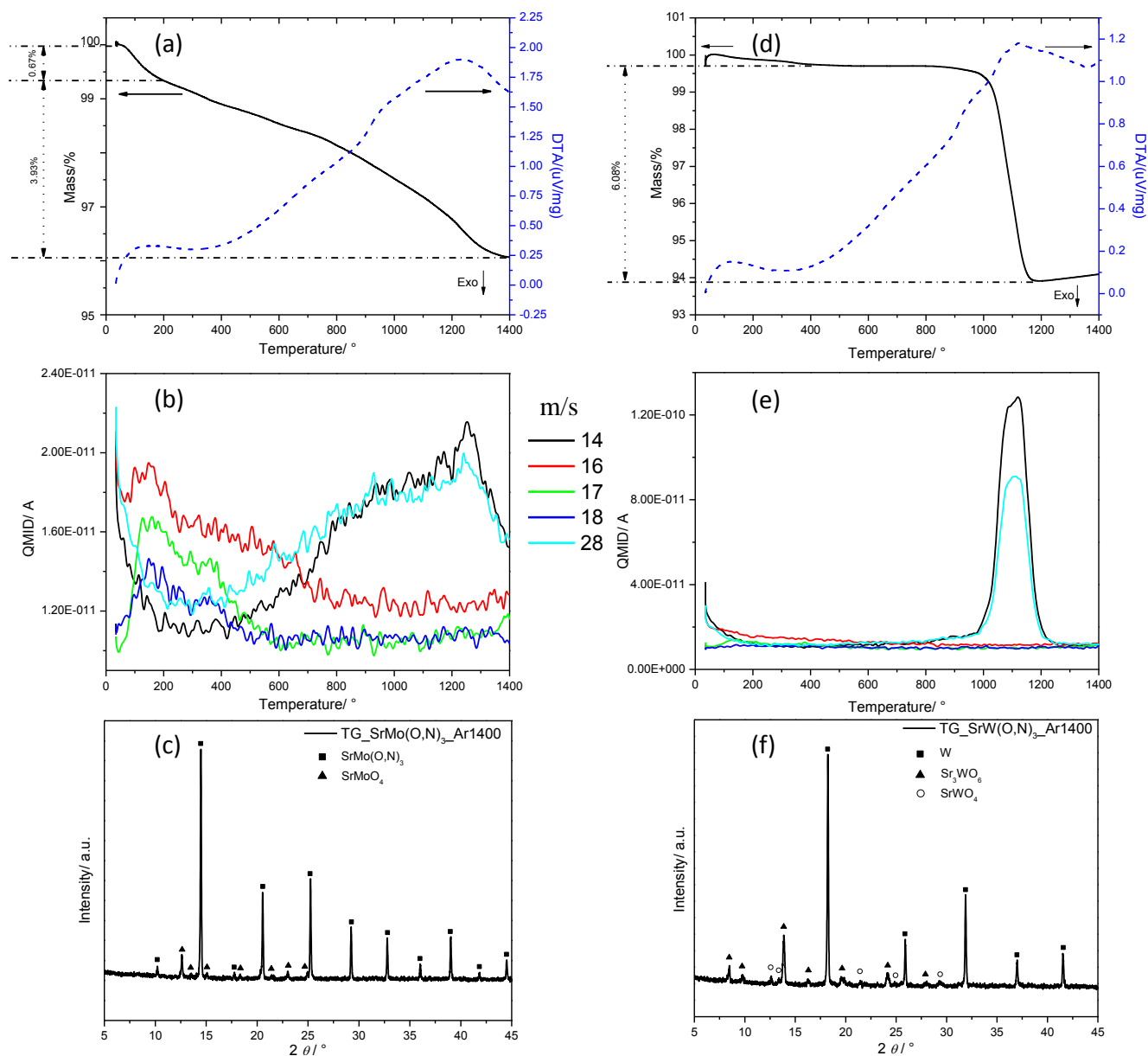


Figure 2.15 TGA/DTA curves and corresponding QMID ion current curves under argon for $\text{SrMoO}_4\text{-NH700}_{12\text{H}}$ (a and b) and $\text{SrWO}_4\text{-NH900}_{12\text{H}}$ (d and e), respectively. XRD patterns of the sample after TG measurement, SrMo(O,N)_3 (c) and SrW(O,N)_3 (f)

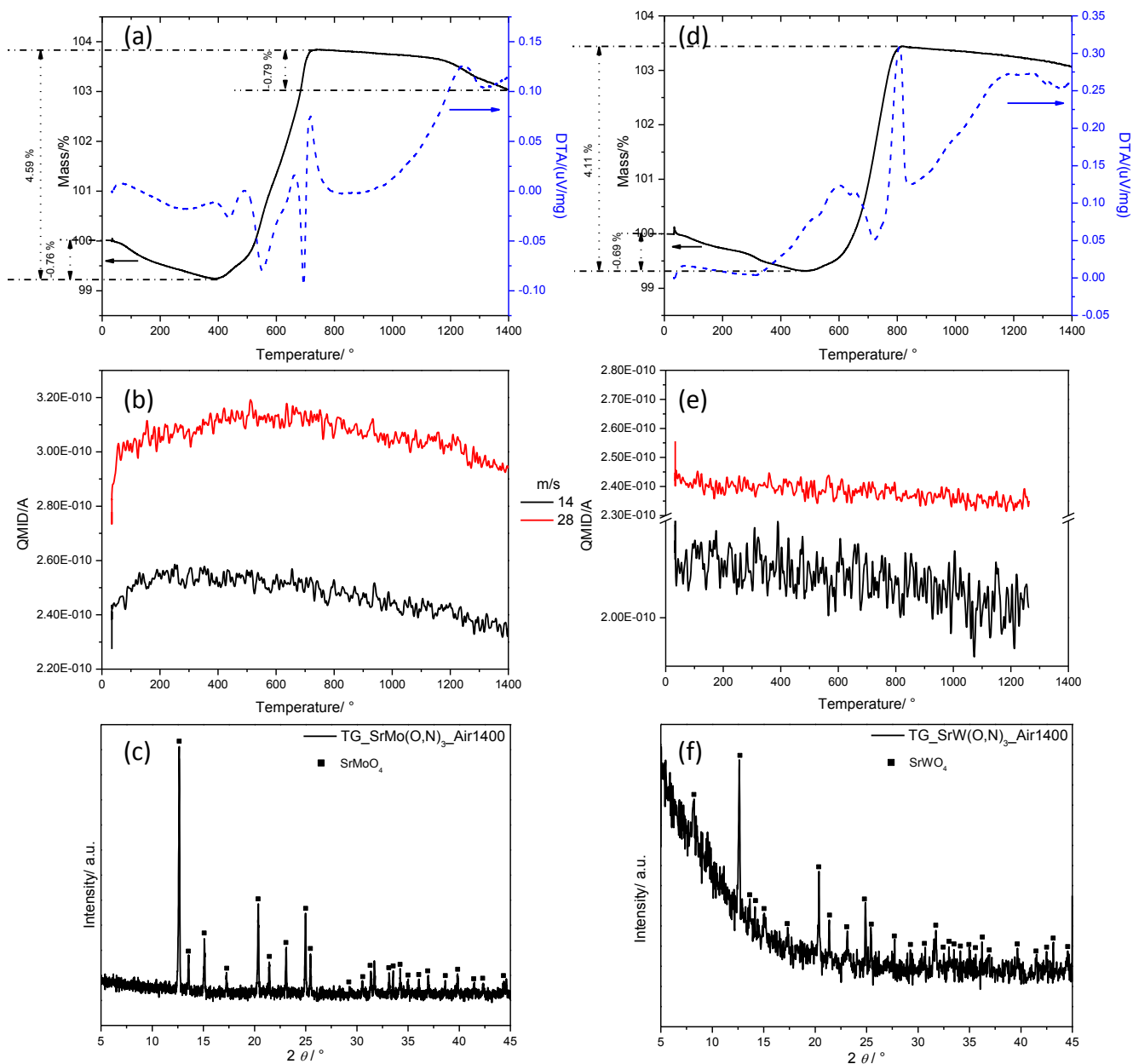


Figure 2.16 TGA/DTA curves and corresponding QMID ion current curves under Air for SrMoO₄_NH700_12H (a and b) and SrWO₄_NH900_12H (d and e), respectively. XRD patterns of the sample after TG measurement, SrMo(O,N)₃ (c) and SrW(O,N)₃ (f)

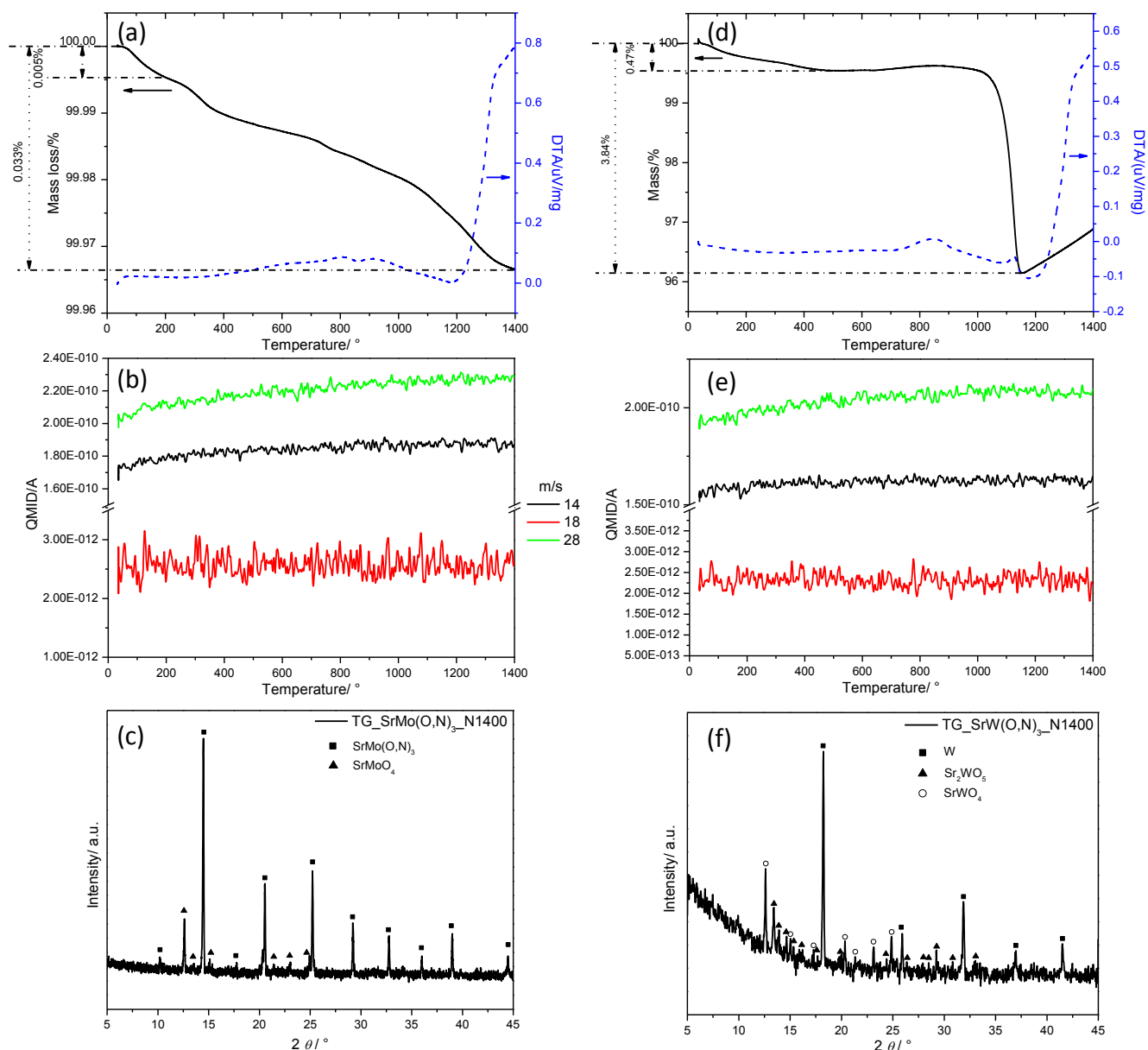
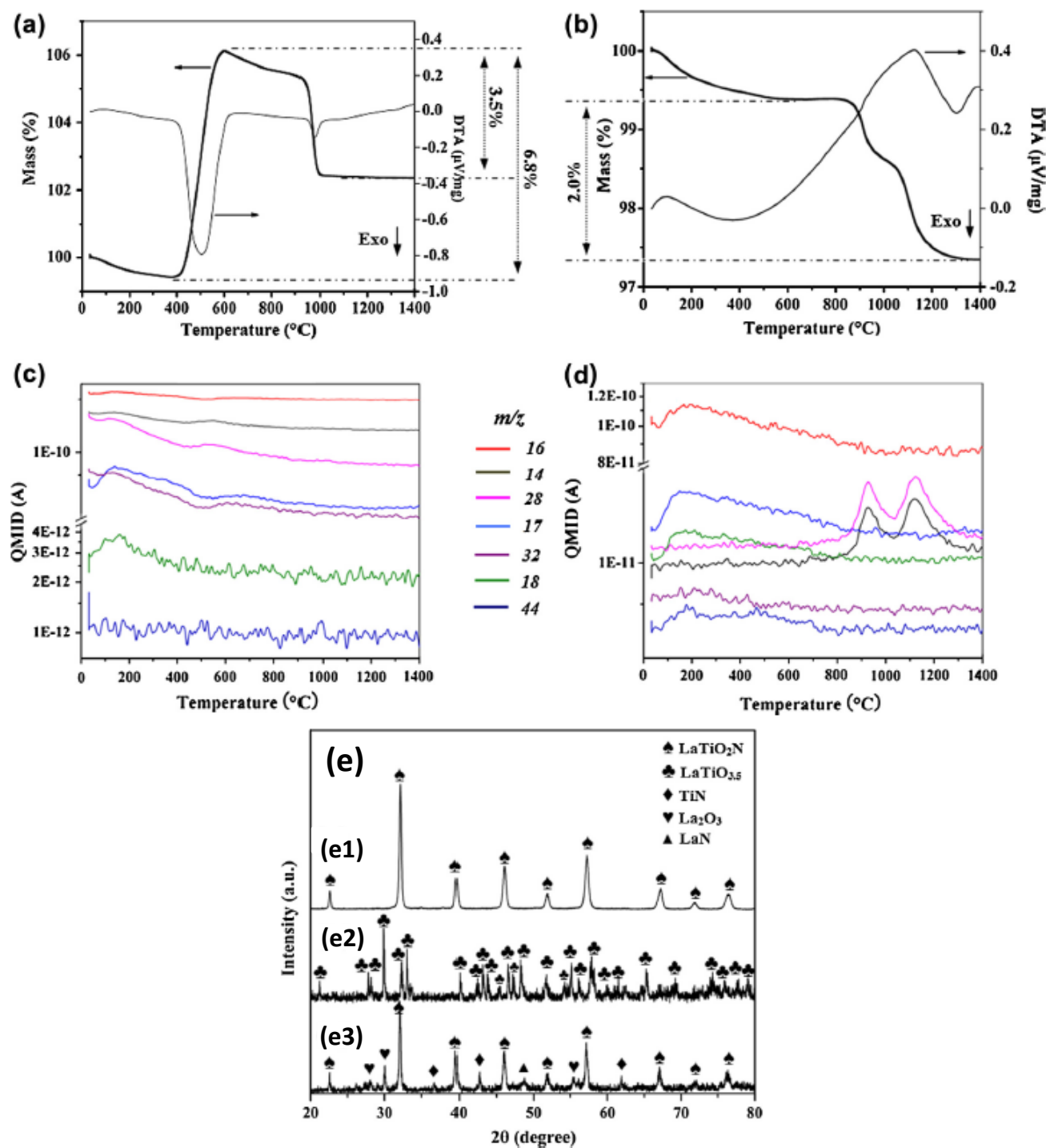


Figure 2.17 TGA/DTA curves and corresponding QMID ion current curves under Nitrogen for SrMoO₄_NH700_12H (a and b) and SrWO₄_NH900_12H (d and e), respectively. XRD patterns of the sample after TG measurement, SrMo(O,N)₃ (c) and SrW(O,N)₃ (f)

Figure 2.18 TGA/DTA curves and corresponding QMID ion current curves under air (a and c) and argon flow (b and d) for LaTiO₂N.XRD patterns of the sample after TG measurement for LaTiO₂N (e)

Different heating rate and sintering temperature (Table 2.7) for SrMo(O,N)₃ and SrW(O,N)₃ were tested while a uniaxial pressure of 100 GPa was applied at 600 °C until the end of the sintering cycle with 1 min dwelling in all cases. Meanwhile, different combinations of sintering parameters were discussed for LaTiO₂N (Table 2.9).

Table 2.7 Sintering parameters, density, and O/N content of the as-synthesized powders and as-sintered samples

Sample	Sintering parameters					Density			O/N content (wt%)	
	Atomsphere	Heating rate (°C/min)	Temperature (°C)	Dwell time (min)	Pressure (MPa)	Geometrical (g/cm ³)	Skeletal (g/cm ³)	Open Porosity (vol%)	As-synthesized	As-sintered
SrMoO₄_NH700_12H (SrMoO _{2.09} N _{0.91})	Vacuum	400	1200	1	100	5.67	5.73	1.0		14.820 (O)
									13.94 (O)	1.214 (N)
	Nitrogen	400	1200	1	100	5.52	5.65	2.3	6.318 (N)	14.38 (O)
										2.174 (N)
SrMoO₄_NH700_24H (SrMoO _{1.96} N _{1.04})	Vacuum	400	1200	1	100	6.03	6.03	0	12.75 (O)	16.110 (O)
									7.187 (N)	1.662 (N)
SrWO₄_NH900_12H (SrWO _{1.42} N _{1.58})	Vacuum	300	1250	1	100	6.81	7.36	7.6		11.060 (O)
									8.114 (O)	0.9193 (N)
	Nitrogen	300	1250	1	100	6.06	6.94	12.7	7.006 (N)	9.421 (O)
										1.237 (N)
SrWO₄_NH900_24H (SrWO _{1.39} N _{1.61})	Vacuum	300	1250	1	100	5.87	6.44	8.7	7.977 (O)	13.890 (O)
									7.148 (N)	0.8707 (N)

XRD patterns (Figure 2.19) and Rietveld refinement results (Figure 2.21 and Table 2.8) of $\text{SrMo}(\text{O,N})_3$ and $\text{SrW}(\text{O,N})_3$ reveal that $\text{SrMo}(\text{O,N})_3$ is significantly more resistant with respect to decomposition in vacuum than $\text{SrW}(\text{O,N})_3$ and thus monoliths of $\text{SrMo}(\text{O,N})_3$ with near fully dense are obtained, as confirmed by SEM results as well (Figure 2.20). Surprisingly, the nitrogen atmosphere which is expected to be more beneficial for oxynitride densification shows even worse ability to prevent the decomposition of oxynitride phases, and leads to much higher open porosity. In terms of vacuum atmosphere, several oxides (SrMoO_4 , Sr_3MoO_6 and $\text{Sr}_3\text{Mo}_2\text{O}_7$; and Sr_3WO_6 , SrWO_4 for $\text{SrW}(\text{O,N})_3$) and nitrides (Mo_2N ; WN), as well as metallic Mo and W were observed. Regarding to nitrogen atmosphere, $\text{SrMo}(\text{O,N})_3$ decomposed completely into oxides ($\text{Sr}_3\text{Mo}_2\text{O}_7$, Sr_3MoO_6 and SrMoO_4) and nitrides (Mo_2N); while $\text{SrW}(\text{O,N})_3$ decomposed into metallic W, W_3N_4 and $\text{Sr}_3\text{WO}_6/\text{SrWO}_4$.

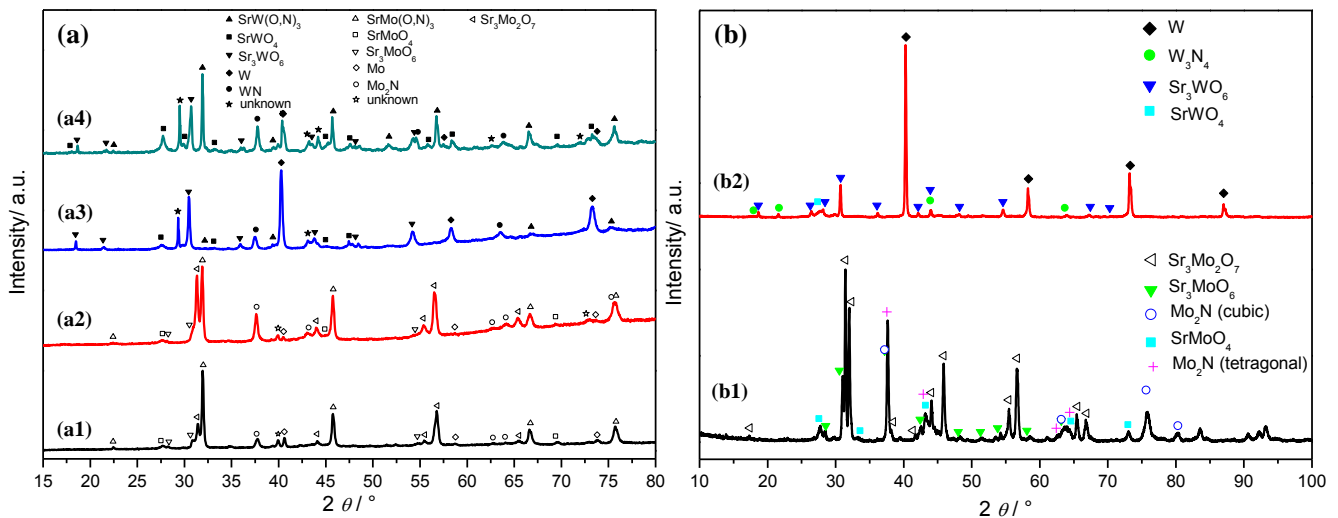


Figure 2.19 X-ray diffraction patterns for the as-sintered samples under vacuum atmosphere (a) $\text{SrMoO}_4\text{-NH700_12H}$ (a1), $\text{SrMoO}_4\text{-NH700_24H}$ (a2), $\text{SrWO}_4\text{-NH900_12H}$ (a3) and $\text{SrWO}_4\text{-NH900_24H}$ (a4); (b) under nitrogen atmosphere $\text{SrMoO}_4\text{-NH700_12H}$ (b1) and $\text{SrWO}_4\text{-NH900_12H}$ (b2)

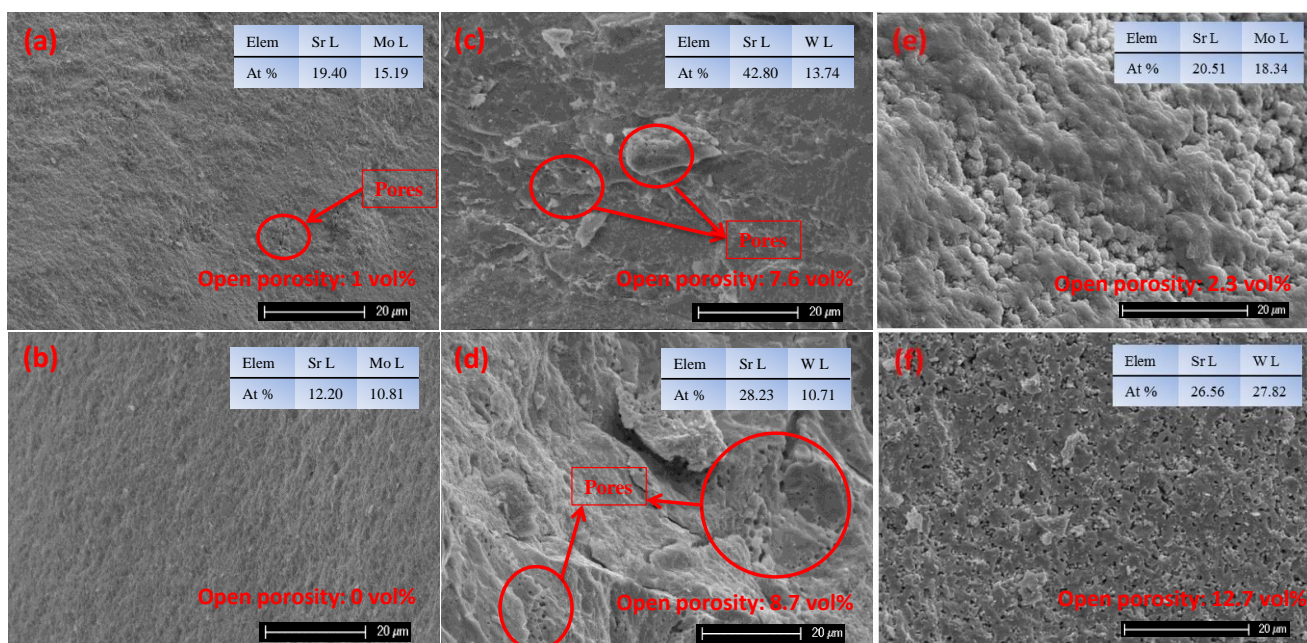


Figure 2.20 SEM images for the cross-section of the sintered monolith samples under vacuum SrMoO₄_NH700_12H (a); SrMoO₄_NH700_24H (b); SrWO₄_NH900_12H (c) and SrWO₄_NH900_24H (d) and under nitrogen SrMoO₄_NH700_12H I; SrWO₄_NH900_12H (f)

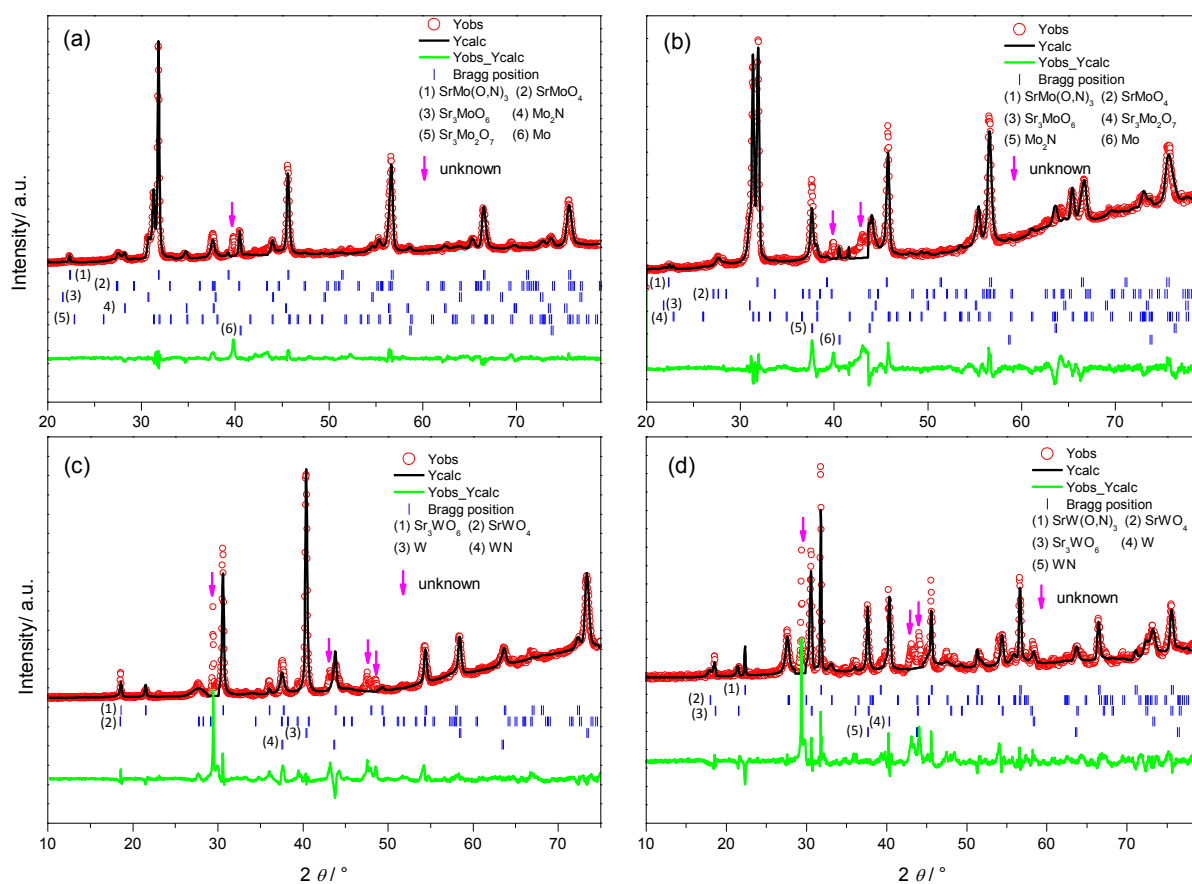
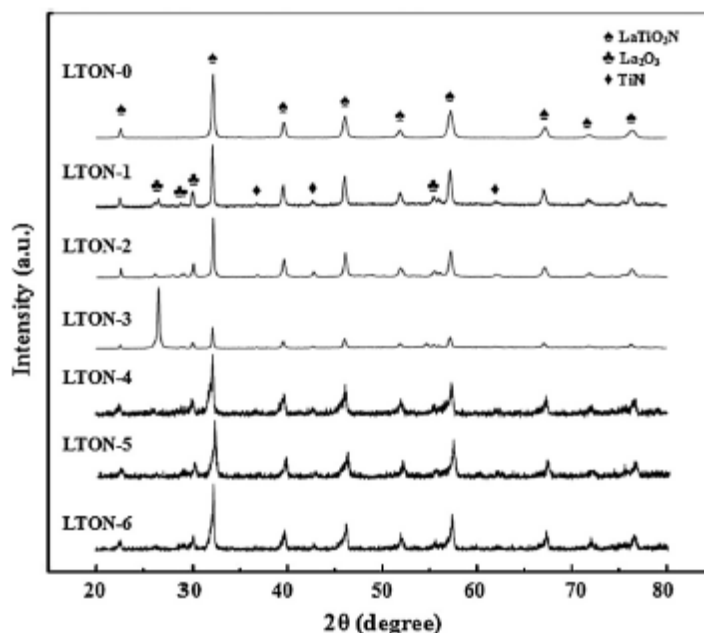


Figure 2.21 Rietveld refinement of X-ray diffraction patterns of the as-sintered bulk samples SrMoO₄_NH700_12H (a), SrMoO₄_NH700_24H (b), SrWO₄_NH900_12H (c) and SrWO₄_NH900_24H (d). Blue tick marks are Bragg peak positions of different phases, respectively. The green lines at the bottom denote the different intensities between the observed and calculated profiles

Table 2.8 Approximate phase compositions of the as-sintered bulk samples

SPS_Phase compositions / wt%	SrMo(O,N) ₃ (Pm-3m, No. 221)	SrMoO ₄ (I 41/a, No. 88)	Sr ₃ MoO ₆ (Fm-3m, No. 225)	Mo ₂ N (Fm-3m, No. 225)	Sr ₃ Mo ₂ O ₇ (I4/mmm, No. 139)	Mo (Im-3m, No. 229)
SrMoO ₄ _NH700_12H	36.21	5.02	9.25	10.43	32.96	6.13
SrMoO ₄ _NH700_24H	23.91	4.01	11.13	15.28	44.85	0.81
SPS_Phase compositions / wt%	Sr ₃ WO ₆ (Fm-3m, No. 225)	SrWO ₄ (I 41/a, No. 88)	SrW(O,N) ₃ (Pm-3m, No. 221)	W (Im-3m, No. 229)	WN (Fm-3m, No. 225)	/
SrWO ₄ _NH900_12H	40.13	11.89	0.00	32.12	15.86	/
SrWO ₄ _NH900_24H	26.68	18.27	13.57	8.85	32.64	/

For LaTiO₂N, the highest relative density of 94 vol% with a residual LaTiO₂N of 86 wt% was achieved in a sample prepared at 1350 °C for dwelling of 1 min under 125 Mpa when a heating rate of 250 °C/min was applied. SPS process demonstrates a desirable densification approach considering both purity and density because the conventional sintering can only achieve very low density ceramics (< 70 % TD) with high purity^[198, 199]. XRD results suggest that besides the characteristic peaks of crystalline LaTiO₂N, all the sintered compacts contained some impurities which can be ascribed to La₂O₃ and TiN, see Figure 2.22 and Table 2.9.

Figure 2.22 XRD patterns of LaTiO₂N powder (LTON-0) and the as-sintered LaTiO₂N ceramics named LTON-1 to LTON-6 in Table

2.9

Table 2.9 Sintering parameters, relative density, LaTiO₂N phase content and chemical composition of LaTiO₂N powders and as-sintered samples

Sample	Sintering parameters				Relative Density (% TD)	LaTiO ₂ N Phase content (wt%)	Chemical Composition (N/O, atomic ratio)
	Heating rate (°C/min)	Temperature (°C)	Dwell time (min)	Pressure (Mpa)			
LaTiO ₂ N ^a	-	-	-	-	-	100	0.50
LTON-0	-	-	-	-	-	100	0.46
LTON-0 ^b	-	-	-	-	-	0	0.0034
LTON-0 ^c	-	-	-	-	-	-	0.23
LTON-1	250	1350	1	125	94	86	0.31
LTON-2	250	1250	1	75	74	93	0.33
LTON-3	250	1400	2	100	93	57	-
LTON-4	100	1300	5	75	81	66	-
LTON-5	100	1300	5	100	88	67	-
LTON-6	300	1350	2	100	91	90	-

^a: Theoretical stoichiometry

^b: After TGA/DTA/MS measurement in air

^c: After TGA/DTA/MS measurement in argon

2.3.2. Statement of personal contribution

[3] W. J. Li, D. Li, A. Gurlo, Z. J. Shen, R. Riedel and E. Ionescu, "Synthesis and rapid sintering of dense SrA(O,N)₃ (A=Mo, W) oxynitride ceramics", *Journal of the European Ceramic Society*, **2015**, 35, 3273-3281

The idea behind this work was developed by myself. All experimental work related to material synthesis and preparation was carried out by myself. The neutron diffraction was accomplished by myself at Fine Resolution Powder Diffractometer (FIREPOD, E9) at the BERII of the Helmholtz-Zentrum Berlin (HZB), Germany, supported by Dr. Stefan Zander. The SPS processing was performed by M. Sc. Duan Li (AK Prof. Dr. Zhijian Shen, Stockholm University). All characterization work and data process were performed by myself, except TEM (M. Sc. Duan Li, AK Prof. Dr. Zhijian Shen, Stockholm University) and TGA/DTA (Dipl.-Ing.

Claudia Fasel, AK Prof. Dr. Ralf Riedel). The manuscript was written by myself and revised and approved of by Duan Li, Prof. Dr. Aleksander Gurlo, Prof. Dr. Zhijian Shen, Prof. Dr. Ralf Riedel and PD Dr. Emanuel Ionescu.

[4] D. Li, W. J. Li, C. Fasel, J. Shen and R. Riedel, “Sinterability of the oxynitride LaTiO_2N with perovskite-type structure”, *Journal of Alloys and Compounds*, 586 (2014), 567-573

The most of experimental work of this study was performed by M. Sc. Duan Li under FUNEA project (AK Prof. Dr. Zhijian Shen, Stockholm University). My particular contribution is related to elemental analysis, FTIR, TGA/DTA and UV-Vis spectrum analysis, as well as data interpretation and discussion of above results. The manuscript was written by M. Sc. Duan Li and revised and approved of by myself, Dipl.-Ing. Claudia Fasel, Prof. Dr. Zhijian Shen and Prof. Dr. Ralf Riedel.

2.4 Solid-solution perovskite-type $\text{SrMo}_{1-x}\text{W}_x(\text{O,N})_3$ oxynitrides

[5] W. J. Li, A. Gurlo, R. Riedel and E. Ionescu, "Perovskite-type solid-solution $\text{SrMo}_{1-x}\text{W}_x(\text{O,N})_3$ oxynitrides: synthesis, structure and magnetic properties", *Zeitschrift für Anorganische und Allgemeine Chemie*, **2015**, 641, (8-9), 1533-1539

In the present Chapter, the synthesis of novel solid-solution scheelite-type $\text{SrMo}_{1-x}\text{W}_x\text{O}_4$ oxide and perovskite-type $\text{SrMo}_{1-x}\text{W}_x(\text{O,N})_3$ oxynitrides via solvothermal approach, followed by thermal ammonolysis, is introduced. The chemical and phase composition with respect to ammonolysis temperature is carefully characterized by XRD and neutron diffraction. The magnetic properties of selected oxynitrides were addressed. In addition a preliminary assessment on their electrical conductivity for selected samples is presented.

2.4.1. Results and discussion

Scheelite-type $\text{SrMo}_{1-x}\text{W}_x\text{O}_4$ oxide precursors were synthesized via solvothermal approach by mixing $\text{Sr}(\text{NO}_3)_2$ in an equimolar ratio with $\text{Na}_2\text{MoO}_4 \cdot 4\text{H}_2\text{O}$ and $\text{Na}_2\text{WO}_4 \cdot 4\text{H}_2\text{O}$ in ethylenediamine under vigorous stirring, then subsequently reacted in an autoclave with Teflon lining and heated at 200 °C for 24 h. The post-treated powders by centrifugation and drying at 60 °C overnight were thermal ammonolyzed between 700 and 900 °C for 6 or 12 h named as NH700, NH800 and NH900. The ratio of Mo/W was adjusted according to $x = 0.05, 0.15, 0.25, 0.4, 0.5, 0.6, 0.75, 0.85$ and 0.95 (referred to as SMW1, 2, 3, 4, 5, 6, 7, 8, 9, respectively).

XRD patterns and lattice constants obtained via Rietveld refinement in Figure 2.23 reveal that phase-pure scheelite-type oxides in solid-solution were achieved for all compositions.

The corresponding perovskite-type oxynitrides are formable upon thermal treatment in ammonia atmosphere only in a limited compositional range, i.e. for $x \leq 0.25$ and $x \geq 0.6$; whereas for $0.25 < x < 0.6$ decomposition processes occur and furnish different oxides (e.g. Sr_3WO_6 and Sr_3WO_5) and nitrides ($\text{Mo}_x\text{N}_y/\text{W}_x\text{N}_y$), as confirmed by XRD patterns (Figure 2.24) and elemental analysis results. It appears that none of phase-pure solid-solution oxynitride was achieved (the purest one is SMW7_NH800_12H with ca. 92.7 wt% fraction of oxynitride phase). The formation of entropy and enthalpy of solid solutions strongly depends on composition, which may further attribute to the formation of different electronic state of Mo and W ions ^[200]. Furthermore, the electronegativity difference between molybdenum and tungsten (e.g. 2.2 and 1.7, respectively) ^[201] can probably lead to structural distortion due to Mo/W-O/N bond changing.

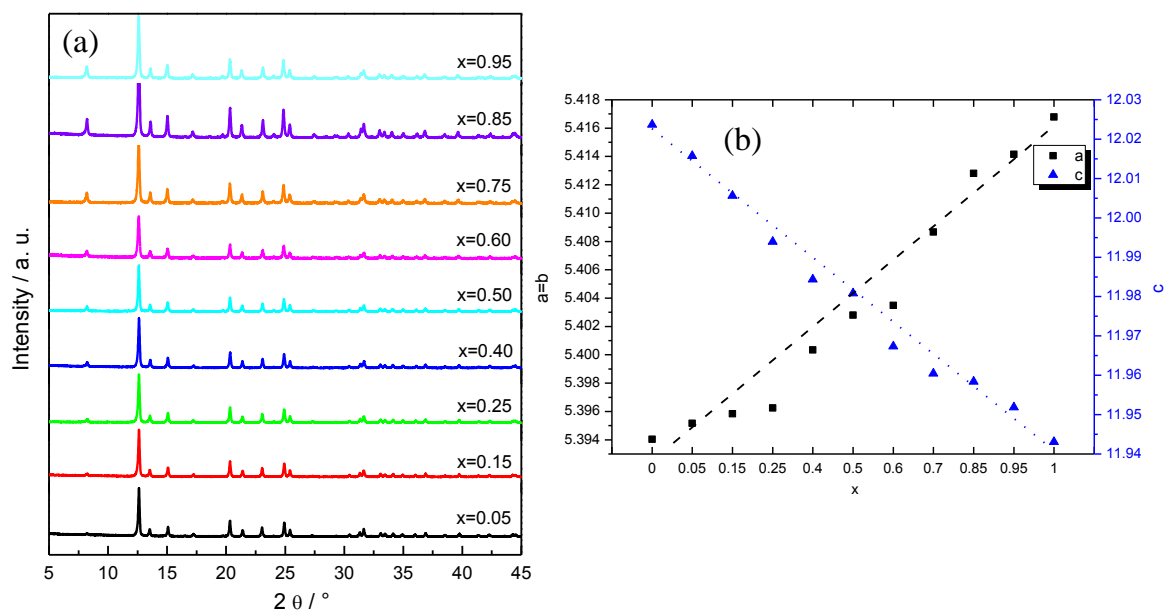


Figure 2.23 X-ray diffraction patterns of different compositions (a) and lattice constants obtained via Rietveld refinement (b) for the as-synthesized solid solution oxide precursors ($\text{SrMo}_{1-x}\text{W}_x\text{O}_4$) when $x = 0.0, 0.05, 0.15, 0.25, 0.4, 0.5, 0.6, 0.75, 0.85, 0.95$ and 1.0

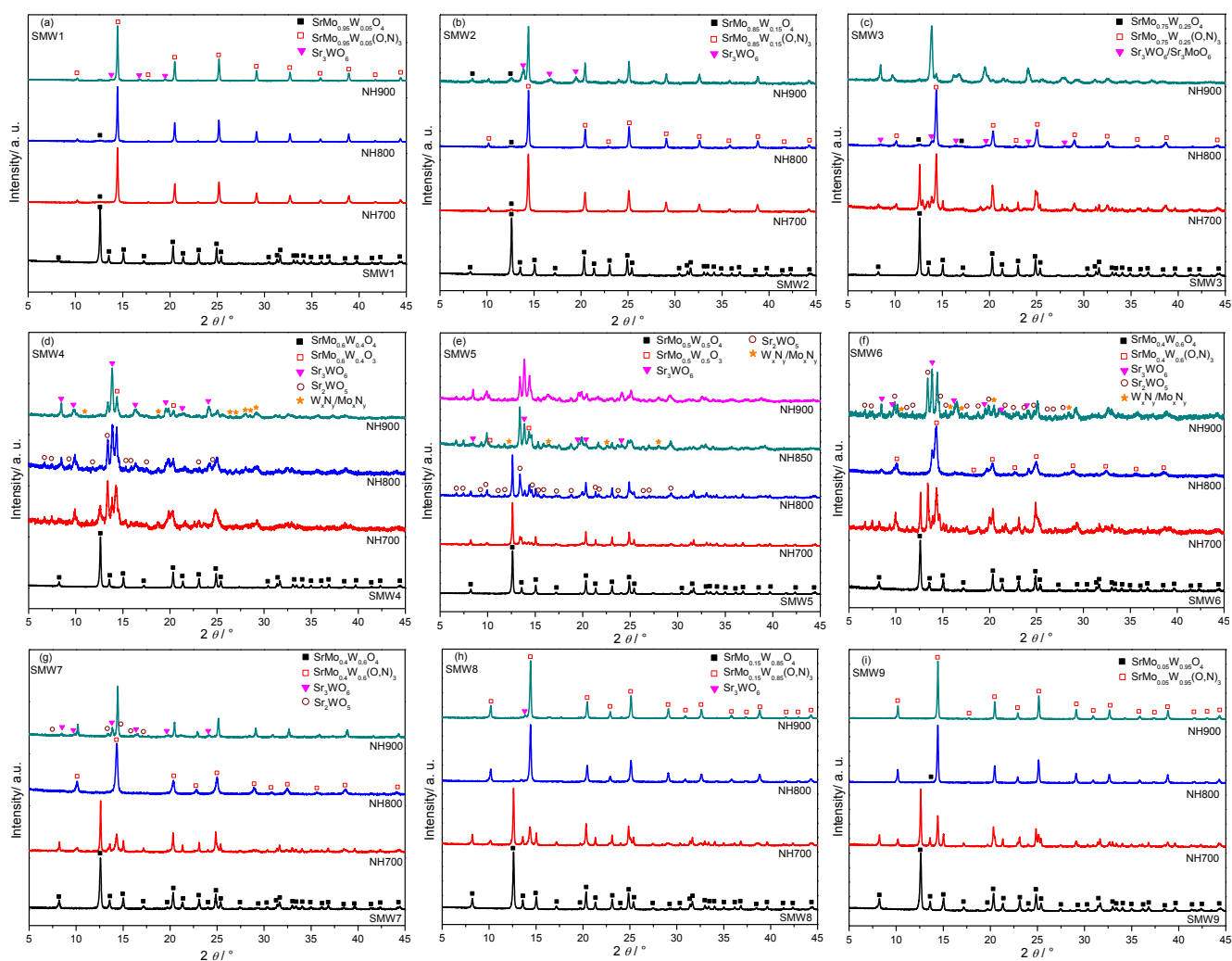


Figure 2.24 X-ray diffraction patterns of $\text{SrMo}_{1-x}\text{W}_x\text{O}_4$ and $\text{SrMo}_{1-x}\text{W}_x(\text{O},\text{N})_3$ with different compositions, *i.e.*, $x = 0.05, 0.15, 0.25, 0.4, 0.5, 0.6, 0.75, 0.85, 0.95$, before and after annealing under an ammonia flow between 700 and 900 $^\circ\text{C}$ for 6 hours

Selected oxynitrides exhibit a temperature-independent paramagnetic behavior between 70 K and 300 K. The magnetic susceptibility increases below 70 K, which relates to a Curie behavior superposed to the temperature-independent Pauli paramagnetism^{25,251,263}. Similarly with SrMoO₂N, an anomalous hyperbolic crest at ~ 45.5 K was observed as well, which might relate to molecular oxygen trapped within the perovskite oxynitride. Bulk oxygen melts at $T = 54$ K and the paramagnetic γ -phase transforms into the antiferromagnetic β -phase at $T = 44$ K. A carefully preparation work in glove box excludes the possibilities from external factors (i.e. sample holder or chamber, environment, *etc.*). We consider here an analogous mechanism for the generation of molecular oxygen within our perovskite solid-solution oxynitrides as we recently proposed and discussed for SrMoO₂N and SrWO_{1.5}N_{1.5}^[80]. Thus, a scheelite-type oxynitride phase might have formed intermediary and leads to the formation of molecular oxygen, which is trapped within the pores and shows the anomalous magnetic behavior mentioned above.

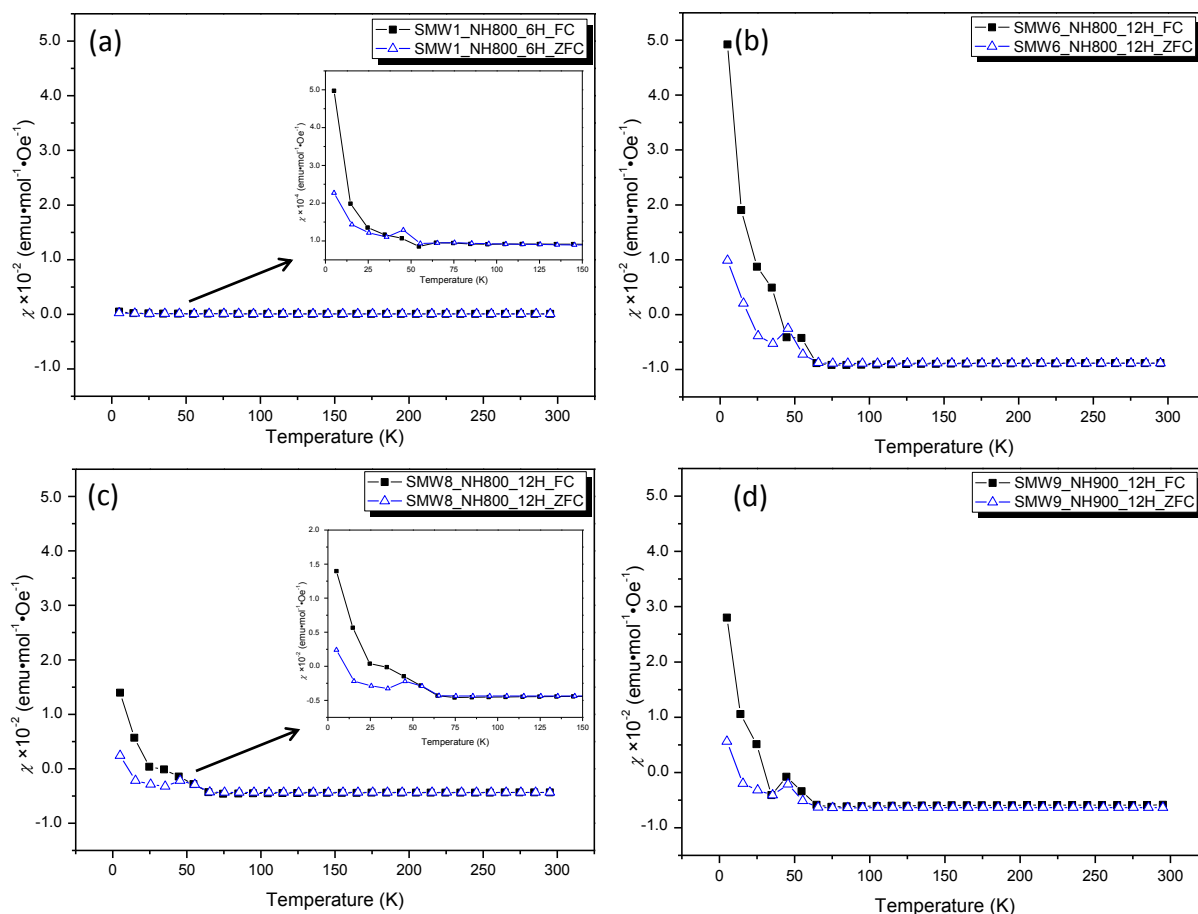


Figure 2.25 The temperature-dependent magnetic susceptibility of (a) SMW1 ($x = 0.05$) under ammonia flow at 800 °C for 6 h, the insert shows that in smaller scale ($\chi \sim 10^{-4}$), (b) SMW6 ($x = 0.6$) under ammonia flow at 800 °C for 12 h, (c) SMW8 ($x = 0.85$) under ammonia flow at 800 °C for 12 h, the insert shows that in smaller scale ($\chi \sim 2 \times 10^{-2}$), and (d) SMW9 ($x = 0.95$) under ammonia flow at 900 °C for 12 h measured with a SQUID magnetometer

Figure 2.26 summarizes the electrical conductivity of selected as-synthesized oxynitride powders measured by the PSC method (discussed in section 1.4.4). In general, it seems there is no clear tendency of conductivity changing with the changing of phase fraction of impurities. However, there are approximately two to three orders of magnitude smaller than $\text{SrMo}(\text{O},\text{N})_3$ and $\text{SrW}(\text{O},\text{N})_3$ that reported by Fawcett ^[46] due to the presence of oxide phases in most cases. SMW2 exhibits the lowest σ value resulted from highest amount of oxide phase (more than 50 wt%) and relative low nitrogen content in oxynitride ($\text{SrMo}_{0.85}\text{W}_{0.15}\text{O}_{2.15(6)}\text{N}_{0.85(6)}$). On the contrary, SMW6 shows the highest σ value even with less than 50 wt% oxynitride phase, which is probably attributed to the presence of large amount of Sr_3WO_6 and relative high nitrogen content ($\text{SrMo}_{0.4}\text{W}_{0.6}\text{O}_{1.35(5)}\text{N}_{1.65(5)}$). From SMW7 to SMW9, σ value is decreasing.

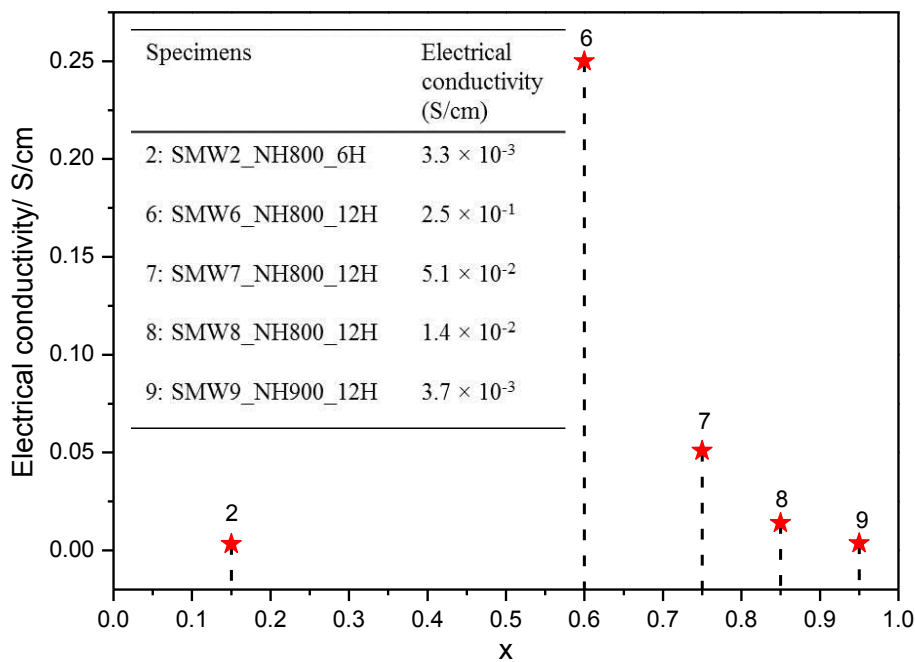


Figure 2.26 Electrical conductivity of selected as-synthesized oxynitride powders

This could be explained as comprehensive functions including following factors from high priority to low:

1) The fraction of oxynitride phase: the band gap decreases due to the nitrogen incorporation. The higher its amount of oxynitride phase, the stronger its semiconducting-like behavior among the investigated samples. Thus, SMW7 specimen shows the highest electrical conductivity among the $\text{SrMo}_{1-x}\text{W}_x(\text{O},\text{N})_4 + \text{SrMo}_{1-x}\text{W}_x\text{O}_4$ compositions.

2) The tungsten content: lower electrical resistivity of $\text{SrMoO}_{2.5}\text{N}_{0.5}$ ($\sim 0.2 \Omega\cdot\text{cm}$) compared to that of SrWO_2N ($\sim 1 \Omega\cdot\text{cm}$) was observed by Fawcett ^[46]. Similarly, the electrical conductivity of solid-solution oxynitride decreases with the increasing of tungsten content. On the other hand, grain-boundary effects resulted

from multi-phases can significantly influence the conductivity^[46]. This is probably an important reason why our results are two to three orders of magnitude smaller than that in literature.

3) The nitrogen content: generally, higher nitrogen content always leads to smaller band gap in oxynitrides, which indicates higher electrical conductivity. However, it has minor impact compared to the influence of phase composition as we observed. In our case, it can be easily overlapped by the impact of the oxide phase. That's why SMW8 does not exhibit higher σ value than SMW7 even though SMW8 has highest nitrogen content in all series of samples.

2.4.2. Statement of personal contribution

[5] W. J. Li, A. Gurlo, R. Riedel and E. Ionescu, "Perovskite-type solid-solution $\text{SrMo}_{1-x}\text{W}_x(\text{O,N})_3$ oxynitrides: synthesis, structure and magnetic properties", *Zeitschrift für Anorganische und Allgemeine Chemie*, **2015**, 641, (8-9), 1533-1539

The idea behind this work was developed by myself. The neutron diffraction data were collected by myself at the Swiss Spallation Neutron Source (SINQ), Paul Scherrer Institute, Villigen, Switzerland and High-resolution two-axis diffractometer (DIF, D2B) at the Institute Laue-Langevin (ILL, Grenoble) in France, supported by Dr. Vladimir Pomjakushin and Dr. Emmanuelle Suard respectively. All the synthesis, characterization and data processing were carried out by myself, except TEM (M. Sc. Duan Li, AK Prof. Dr. Zhijian Shen, Stockholm University). The manuscript was written by myself and revised and approved of by Prof. Dr. Aleksander Gurlo, Prof. Dr. Ralf Riedel and Dr. Emanuel Ionescu.

3. A preliminary study on the synthesis and photocatalytic properties of BaTa(O,N)₃

3.1 Introduction

Semiconductor photocatalysts have attracted extensive attention due to their high potential in water splitting^[127, 131, 202] and photodegradation^[167, 169, 203] applications. Nowadays, organic pollution has become a major source of environmental pollution in industrial waste water and thus the photocatalytic degradation process is an effective technique for cleaning these water bodies. TiO₂ is a promising photocatalyst that however requires UV activation due to its wide bandgap, similar for Bi₂O₃, ZnO, SnO₂^[204-206] and GeO₂^[169].

Recently, a great deal of interest has been devoted to visible-light driven photocatalysts, *e.g.* N-doped Ta₂O₅ and ZrO₂-TaON solid solution^[207], N-doped GeO₂^[169], (Ga_{1-x}Zn_x)(N_{1-x}O_x) solid solution^[208], (Zn_{1+x}Ge)(N₂O) solid solution^[209] and (Zn_xTiO_yN_z)^[210]. Perovskite-type oxynitrides even arises intensively attention due to their perfectly suitable band gap for visible-light around 1.8 – 2.5 eV^[119, 125, 131], *e.g.* Pt-ATaO₂N (A=Ca, Sr, Ba)^[155], IrO₂ co-catalyst SrNbO₂N^[157], Pt-ANbO₂N (A=Ca, Sr)^[158], Co-modified LaTiO₂N^[159], and Co and CoO_x modified BaTaO₂N and BaNbO₂N^[156, 160, 211]. However, these promising perovskite oxynitrides were addressed only for water splitting applications, rarely for photodegradation. N-doped NaTaO₃ compounds (NaTaO_{3-x}N_x) was synthesized via solid state reaction and hydrothermal process, which show effective photocatalytic activity for the degradation of Methyl Orange (MO) and Methylene Blue (MB), respectively^[162, 163]. However, low N content (max. NaTaO_{2.946}N_{0.054}, E_g= ~ 3.9 eV) enables only UV irradiation. Aguiar^[32] reported photodegradation activities of SrTaO₂N and LaTiO₂N for MB and acetone, respectively. Nevertheless, studies on typical perovskite-type oxynitrides for photodegradation activities by visible-light are still rare.

The choice of mineralizer additives for assisting ammonolysis can serve as useful variables for tuning the synthesis conditions, physical and chemical properties of the final oxynitrides^[38]. In particular, the additive of chloride salts, *i.e.* NaCl, KCl, NH₄Cl *etc.*, can lower the temperature and shorten the annealing time for ammonolysis reaction remarkably^[39, 64]. The mineralizer can facilitate the formation of the desired oxynitride by providing a molten medium, which significantly enhances ionic diffusion. It can also affect the crystal morphology of the oxynitrides by increasing the crystal growth rate.

In the present work, BaTaO₂N compounds were synthesized via Solid State Reaction (SSR) and Polymeric Complex Method (PCM) followed by thermal ammonolysis. The influence of different mineralizers (NaCl, KCl and NaCl/KCl) and the temperature on their phase compositions and microstructure were investigated. The photocatalytic activity of the BaTaO₂N catalysts was tested for the degradation of MB and Rhodamine B (RhB) aqueous solution under visible-light irradiation.

3.2 Experimental method

3.2.1 Synthesis

The oxide precursors were prepared in two different routes: Polymeric Complex Method and Solid State Reaction (referred to PCM and SSR, respectively).

In case of PCM, BaCO₃ and tantalum ethoxide (Ta(OC₂H₅)₅) were mixed in an equimolar ratio with ethylene glycol (C₂H₄(OH)₂) under vigorous stirring. Then citric acid (HOC(COOH)(CH₂COOH)₂), as a complexing agent was mixed with methanol (CH₃OH). The above solutions were mixed together and heated up to 127 °C for 3 – 4 hours until the mixture becomes viscous, then was cooled down to 97 °C. Subsequently, vacuum condensation was carried out to remove methanol and to obtain a polymer resin at 97 °C and then naturally cool down at room temperature. Afterwards, the pyrolysis of resin was performed at 400 °C for 1 h to remove the organics and subsequently calcined at 800 °C for 2 h in air to obtain the final oxide precursor.

For the SSR method, BaCO₃ and Ta₂O₅ were mixed together in a ratio of 2:1 with acetone by ball milling for 1 day. The resulting mixture was dried at 60 °C overnight leading to the powdered oxide precursor. The as-obtained SSR precursor was used directly for further ammonolysis without any calcination ^[39].

The resulting oxide precursors from both PCM and SSR routes were mixed in an equiweight ratio with mineralizer (NaCl/KCl), as summarized in Table 3.1. The PCM precursors were ammonolyzed at 700, 800, 900 and 1000 °C for 16 h, labeled as PCM_NHxxx (xxx: 700, 800, 900 and 1000). The SSR precursors were ammonolyzed at 700, 800, 900 and 1000 °C for 40 h, marked as SSR_NH NHxxx (xxx: 700, 800, 900 and 1000). The Schlenk system used for thermal ammonolysis is specifically limited to small batch sizes (about 0.3 – 0.5 g) to maximize exposure to flowing NH₃ and maximize product homogeneity. The as-synthesized oxynitrides were rinsed 5 times with de-ionized water and ethanol alternately. Centrifugation and drying at 60 °C overnight led to the final products.

Table 3.1 The ratio between oxide precursor and mineralizer used in this work

Mineralizer	NaCl	KCl	NaCl/KCl	No mineralizer
Mineralizer/oxide precursor (in weight)	1:1	1:1	0.5:0.5:1	\

3.2.2 Sample characterization

The crystalline phase composition of the as-synthesized samples was analyzed by using powder X-ray diffraction (XRD, STOE STADI P) with Mo K α radiation (wavelength 0.7093 Å). The selected samples were performed via Rietveld refinement. The oxygen and nitrogen contents of the synthesized samples were determined by the hot gas extraction method using a LECO TC436 analyzer. The microstructures of specimens were examined by scanning electron microscopy (SEM, JEOL JSM – 7000F). The optical spectra were recorded in the wavelength range of 200 ~ 800 nm by using UV-Vis spectrometer (Perkin Elmer UV/VIS/IR spectrometer 900 Lambda). The band gap of as-synthesized oxynitride was calculated according to Shapiro's method ^[212].

3.2.3 Photocatalytic test

Photocatalytic degradation experiments were carried out by exposing methylene blue (MB) and Rhodamine B (RhB) in water to visible-light irradiation. A halogen lamp (150 W) was used to irradiate a quartz reactor vessel. A water-cooling system was applied between the reaction vessel and the lamp to keep reaction temperature at ~ 25 °C. The initial concentration of MB aqueous solution was chosen as 2.5×10^{-5} mol/L and 10^{-6} mol/L. While the initial concentration of RhB aqueous solution was chosen as 10^{-5} mol/L. The amount of the tested photocatalysts was 0.4 g/L. The suspended solution was ultrasonic dispersed and stirred in the dark for 1 h to reach the adsorption-desorption equilibrium and then placed in front of visible lamp. After desired time intervals of irradiation, the suspension was taken and centrifuged to separate the catalyst from dye solution in order to avoid absorption and scattering. Then the supernatant solution was collected and analyzed by recording the characteristic absorption of MB at ~ 665 nm and RhB at ~ 553 nm using the UV-vis spectrometer to determine the dye concentration.

3.3 Results and discussion

3.3.1 Thermal ammonolysis

3.3.1.1. PCM samples

As shown in Figure 3.1, all samples treated at 700 °C already formed the BaTaO₂N oxynitride phase, accompanied with oxides (Ba₃Ta₅O₁₅ and BaTa₂O₆) and nitride (Ta₃N₅). However, the mineralizer-assisted ammonolysis enhanced the formation of oxynitride phase significantly, especially for the NaCl/KCl case, which showed a content of 90.7 wt% BaTaO₂N already (Figure 3.2 a and Table 3.3). At 800 °C, BaTaO₂N, Ba₃Ta₅O₁₅ and Ta₃N₅ mixture phases were observed with different fractions at different temperatures. At 900 °C, the oxide phase almost disappeared except for the 900_NaCl/KCl compound. The Ta₃N₅ phase was observed for 900_NaCl compound as major component. Up to 1000 °C, only Ta₃N₅ phase was detected besides the main BaTaO₂N phase. More than half amount of Ta₃N₅ (~ 50.35 wt%) was observed for 1000_NaCl sample. The purest oxynitride was obtained at 1000 °C without mineralizer (~ 97.7 wt% BaTaO₂N). With the increasing of temperature, the color of powders changed from light-yellow to red-brown. The color, nitrogen content, phase compositions and calculated band gap are summarized in Table 3.2.

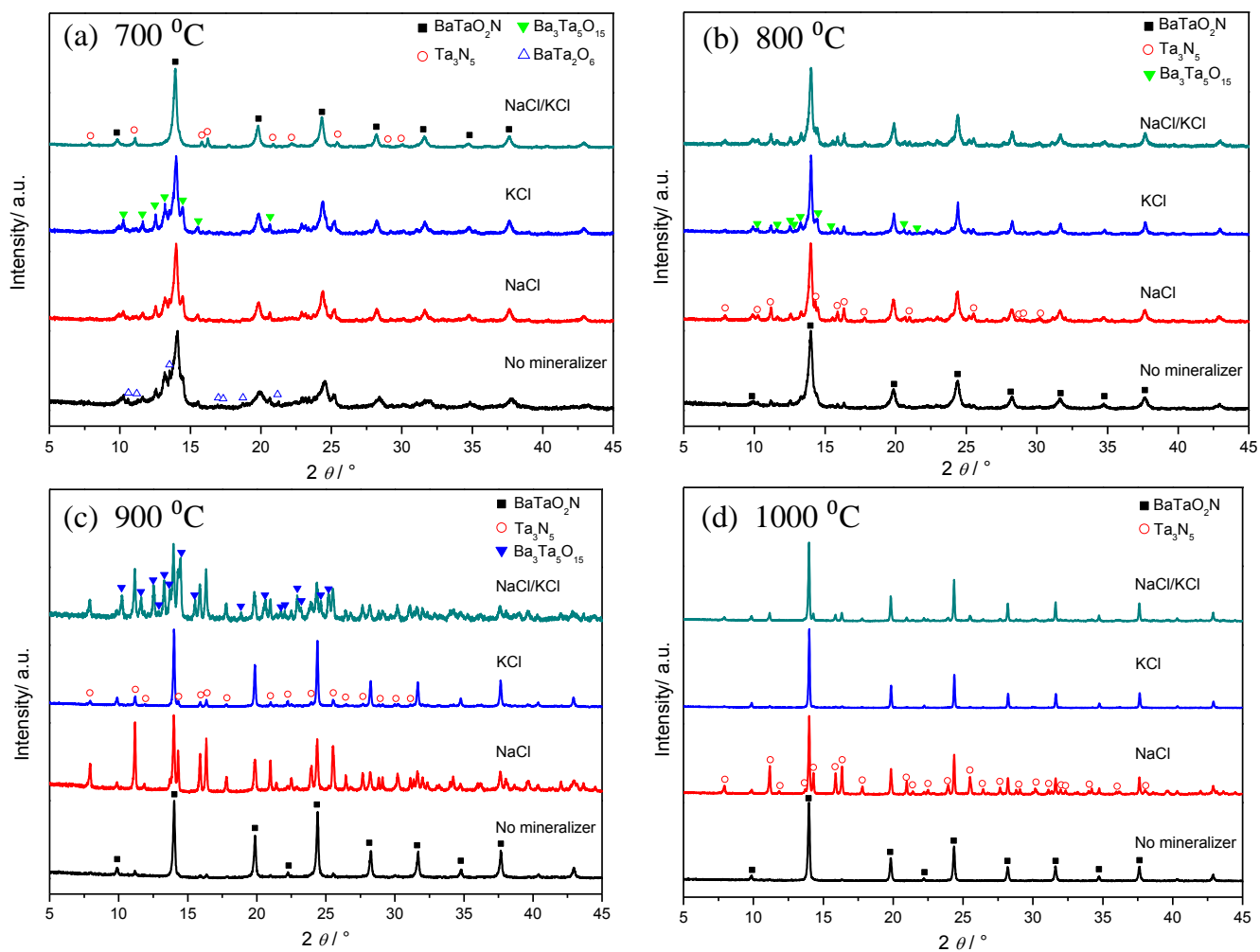
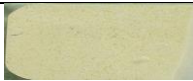














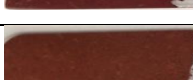


Figure 3.1 X-ray diffraction patterns of oxynitrides ammonolyzed from the PCM precursor with and without mineralizers (NaCl, KCl or NaCl/KCl) at (a) 700 °C, (b) 800 °C, (c) 900 °C and (d) 1000 °C

Table 3.2 Color, nitrogen content, phase compositions and band gap of as-synthesized oxynitrides from PCM oxide precursor

Samples (PCM)	Color	N (wt%)	Observed phases	Band gap (eV) ^a
700		/	BaTaO ₂ N + BaTa ₂ O ₆ + Ba ₃ Ta ₅ O ₁₅	2.99
700_NaCl		/	BaTaO ₂ N + Ba ₃ Ta ₅ O ₁₅	2.03 ~ 2.53
700_KCl		/	BaTaO ₂ N + Ba ₃ Ta ₅ O ₁₅	2.36 ~ 2.64
700_NaCl/KCl		1.59(1)	BaTaO ₂ N + Ta ₃ N ₅	2.05
800		4.88 (21)	BaTaO ₂ N + Ba ₃ Ta ₅ O ₁₅ + Ta ₃ N ₅	2.04 ~ 2.30
800_NaCl		5.37 (9)	BaTaO ₂ N + Ba ₃ Ta ₅ O ₁₅ + Ta ₃ N ₅	2.05 ~ 2.68
800_KCl		5.16 (34)	BaTaO ₂ N + Ba ₃ Ta ₅ O ₁₅ + Ta ₃ N ₅	2.01 ~ 2.18
800_NaCl/KCl		5.43 (17)	BaTaO ₂ N + Ba ₃ Ta ₅ O ₁₅ + Ta ₃ N ₅	2.05 ~ 2.40
900		5.91 (23)	BaTaO ₂ N + Ta ₃ N ₅	1.96
900_NaCl		8.51 (8)	BaTaO ₂ N + Ta ₃ N ₅	2.03
900_KCl		6.79 (13)	BaTaO ₂ N + Ta ₃ N ₅	1.95
900_NaCl/KCl		4.76 (42)	BaTaO ₂ N + Ba ₃ Ta ₅ O ₁₅ + Ta ₃ N ₅	2.05 ~ 2.48
1000		4.14 (15)	BaTaO ₂ N + Ta ₃ N ₅	1.89
1000_NaCl		7.02 (11)	BaTaO ₂ N + Ta ₃ N ₅	2.00
1000_KCl		4.35 (21)	BaTaO ₂ N + Ta ₃ N ₅	1.84
1000_NaCl/KCl		6.55 (15)	BaTaO ₂ N + Ta ₃ N ₅	1.90

^a: The band gap was considered in a small range for the samples containing the oxides impurities resulting in absorption shoulder, as shown in Figure 3.7 and Figure 3.8

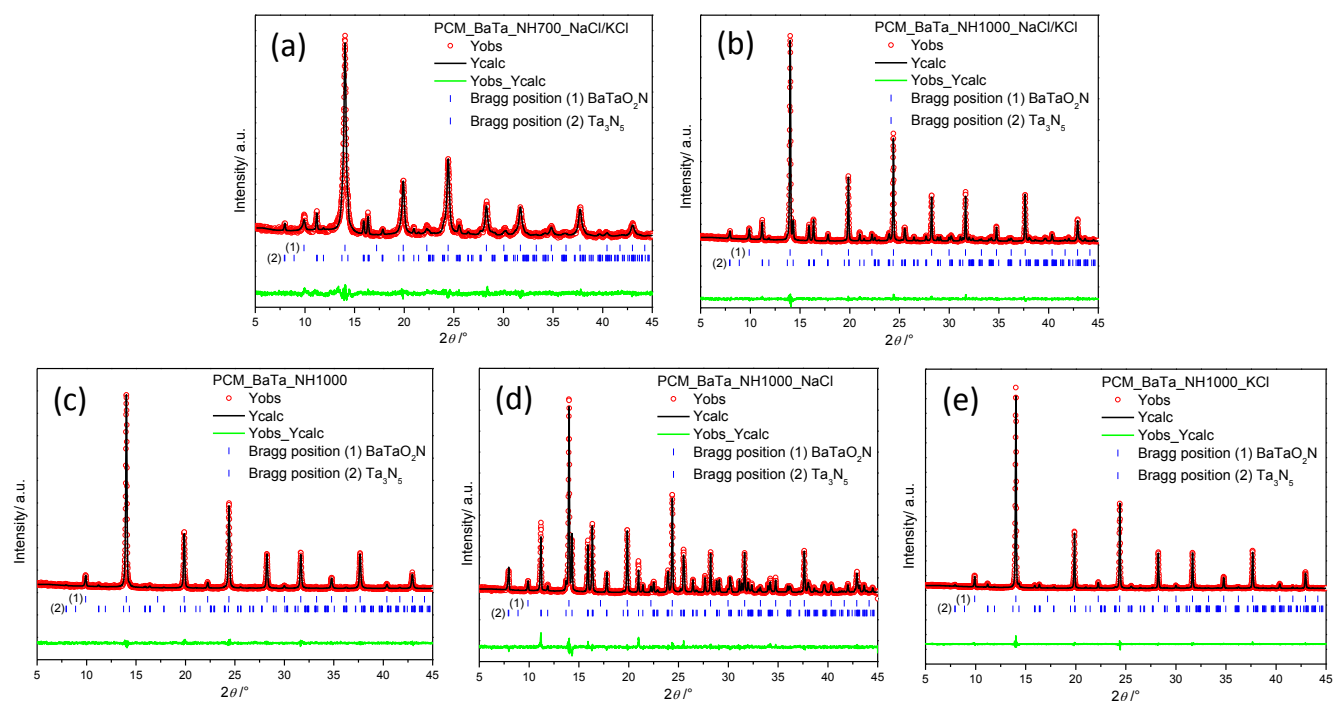


Figure 3.2 Rietveld refinement of the X-ray powder diffraction patterns of the selected samples obtained from the ammonolysis of PCM precursor (a) 700 °C with NaCl/KCl, (b) 1000 °C with NaCl/KCl, (c) 1000 °C, (d) 1000 °C with NaCl and (e) 1000 °C with KCl for 16 hours

Table 3.3 Phase compositions and lattice parameters of the selected samples obtained via the ammonolysis of PCM precursor from Rietveld refinement of the XRD patterns

Specimens / phase compositions	BaTaO ₂ N (<i>Pm-3m</i> , Nr. 221, Z=1)	Ta ₃ N ₅ (<i>CmCm</i> , Nr. 63, Z=4)
PCM_NH700_NaCl/KCl	90.71 (90) wt% a=4.1045 (6) Å	9.29 (33) wt% a=3.8966 (10) Å, b=10.2030 (30) Å, c=10.2685 (29) Å
PCM_NH1000_NaCl/KCl	77.37 (58) wt% a=4.1125 (2) Å	22.63 (34) wt% a=3.8917 (3) Å, b=10.2254 (8) Å, c=10.2751 (8) Å
PCM_NH1000	97.73 (70) wt% a=4.1106 (3) Å	2.27 (22) wt% a=3.8829 (30) Å, b=10.2274 (98) Å, c=10.2564 (89) Å
PCM_NH1000_NaCl	50.18 (45) wt% a=4.1138 (2) Å	49.82 (49) wt% a=3.8945 (2) Å, b=10.2283 (6) Å, c=10.2804 (6) Å
PCM_NH1000_KCl	95.07 (46) wt% a=4.1107 (1) Å	4.93 (18) wt% a=3.8906 (5) Å, b=10.2251 (15) Å, c=10.2716 (14) Å

3.3.1.2. SSR samples

As shown in Figure 3.3, the ammonolysis of SSR precursor at 700 °C for 40 h exhibits weaker nitridation behavior compared to that of PCM precursor at 700 °C. Only 700_NaCl and 700_NaCl/KCl samples formed BaTaO₂N oxynitride phase. And small amount of Ta₂O₅ retained besides other oxide phases (Ba₅Ta₄O₁₅ and BaTa₂O₆), as given in Table 3.4. Ammonolysis at 800 °C enhanced the nitridation process, *i.e.*

SSR_800_NaCl and SSR_800_KCl contained more than 77 wt% BaTaO₂N oxynitride phase (Table 3.5). XRD measurements confirm that the ammonolysis at 900 °C lead to the formation of only small amount of Ta₃N₅ (all less than 15 wt%) beside the major oxynitride phase. The standard N content calculated from their stoichiometric formula of BaTaO₂N and Ta₃N₅ is 3.84 wt% and 11.44 wt%, respectively. The experimental measured N contents of as-synthesized oxynitrides at 900 °C are always higher than 3.84 wt% due to the contribution of Ta₃N₅, which is consistent with the XRD results. Up to 1000 °C, SSR_1000 still shows reasonable amount of BaTaO₂N (~ 94 wt%); while SSR_1000_NaCl/KCl exhibited less than 65 wt% oxynitride phase. Moreover, SSR_1000_NaCl and SSR_1000_KCl almost converted to Ta₃N₅ completely. Slightly lower N content (10.8 and 11.3 wt%, respectively) for them indicated that tiny amount of Ba-containing compounds might be still there, which can rarely be observed due to the detective limitation of Laboratory X-ray instrument. On the other hand, the missing of Ba-containing compounds is also probably due to the formation of BaO, which is soluble in water to form Ba(OH)₂. The color of oxynitride powders changed as well, from slight-yellow to red-brown according to different phase compositions. The color, nitrogen content, phase compositions and calculated band gap were summarized in Table 3.4.

The appearance of the Ta₃N₅ phase in BaTaO₂N system was observed frequently according to other respects [37, 48, 155, 156, 213, 214]. The sub-absorptions or monotonically increasing absorptions at wavelength longer than ca. 650 nm were observed. This phenomenon is known to be attributed to the presence of anion vacancies or reduced metal cation species (e.g. Ta⁴⁺) [155], where the available electrons can readily be excited to empty conduction band via absorbing photon with low energies. The generation of anion vacancies or reduced tantalum species originates from the inhomogeneity in the occurrence of barium and tantalum species in the oxide precursors, which further can lead to phase separation between barium- and tantalum-rich phases during the thermal ammonolysis. Thus, the tantalum-rich phases can probably contribute to the formation of Ta₃N₅ impurity phase. On the other hand, over-ammonolysis due to the high ammonia flow rate could probably be associated with the appearance of Ta₃N₅ impurity phase as well. Mineralizer-assisted ammonolysis generally enhanced the formation of Ta₃N₅ impurity phase, as revealed by XRD, refinement, elemental analysis and UV-vis spectroscopy.

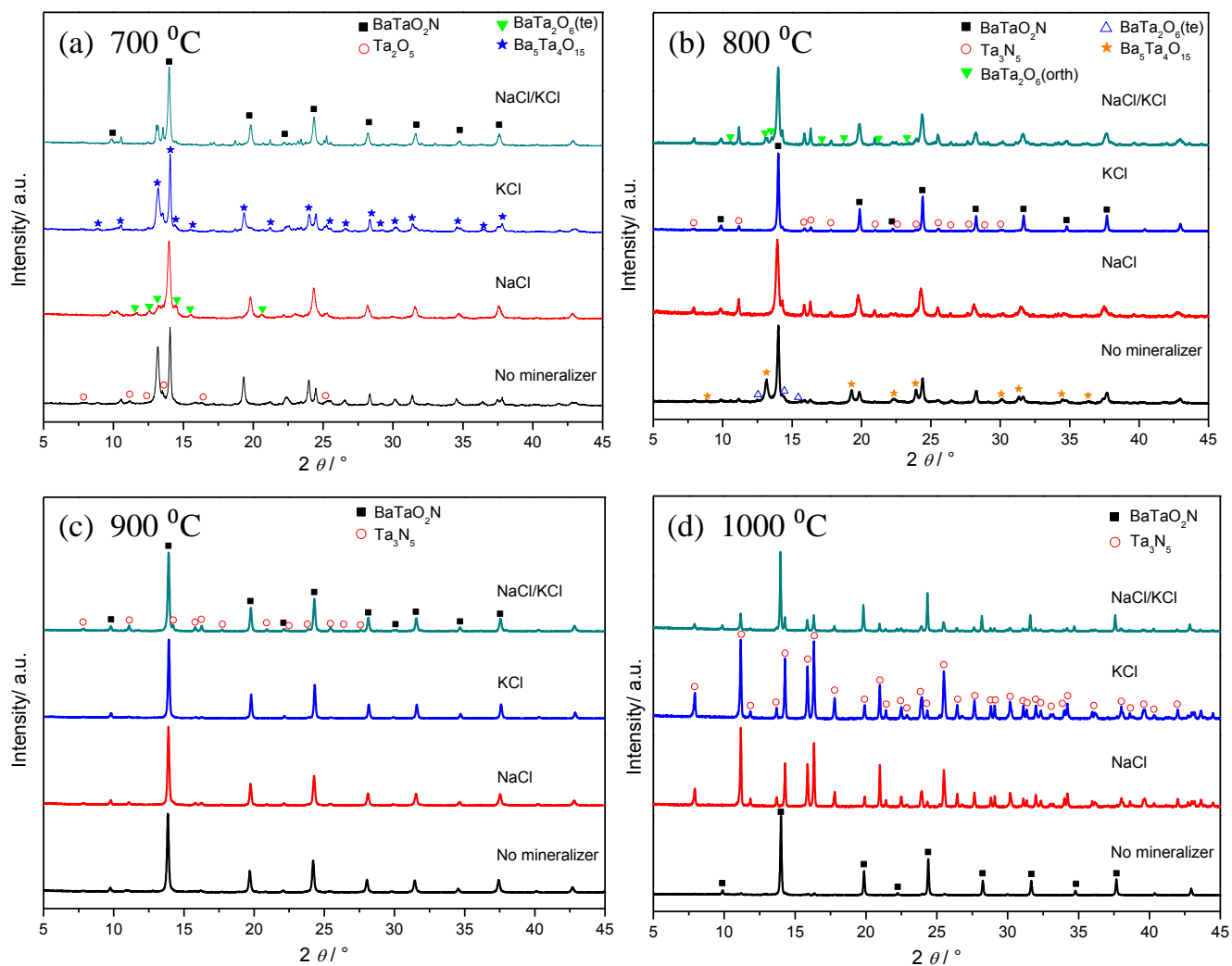



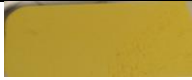














Figure 3.3 X-ray diffraction patterns of oxynitrides ammonolyzed from SSR precursor with and without mineralizers (NaCl, KCl or NaCl/KCl) at (a) 700 °C, (b) 800 °C, (c) 900 °C and (d) 1000 °C for 40 hours

Table 3.4 Color, nitrogen content, XRD analysis and band gap after nitridation of SSR oxide precursor

Samples (SSR)	Color	N (wt%)	Observed phases	Band gap (eV) ^a
700		/	Ba ₅ Ta ₄ O ₁₅ + Ta ₂ O ₅	2.05 ~ 2.93
700_NaCl		/	BaTaO ₂ N + BaTa ₂ O ₆ (tetragonal) + Ta ₂ O ₅	2.4 ~ 2.69
700_KCl		/	Ba ₅ Ta ₄ O ₁₅ + BaTaO ₂ N + BaTa ₂ O ₆ (tetragonal)	2.3 ~ 2.67
700_NaCl/KCl		/	BaTaO ₂ N + BaTa ₂ O ₆ (tetragonal)	2.37 ~ 2.57
800		5.68(43)	BaTaO ₂ N + Ta ₃ N ₅ + Ba ₅ Ta ₄ O ₁₅ + BaTa ₂ O ₆ (tetragonal)	2.06 ~ 2.37
800_NaCl		4.98(19)	BaTaO ₂ N + Ta ₃ N ₅	2.08
800_KCl		6.91(21)	BaTaO ₂ N + Ta ₃ N ₅	2.06
800_NaCl/KCl		6.65(51)	BaTaO ₂ N + Ta ₃ N ₅ + BaTa ₂ O ₆ (orthorhombic)	2.0 ~ 2.12
900		5.84(18)	BaTaO ₂ N + Ta ₃ N ₅	1.88
900_NaCl		6.83(12)	BaTaO ₂ N + Ta ₃ N ₅	1.89
900_KCl		5.97(22)	BaTaO ₂ N + Ta ₃ N ₅	1.88
900_NaCl/KCl		6.46(14)	BaTaO ₂ N + Ta ₃ N ₅	1.93
1000		4.56(28)	BaTaO ₂ N + Ta ₃ N ₅	1.87
1000_NaCl		10.82(8)	Ta ₃ N ₅	2.05
1000_KCl		11.29(17)	Ta ₃ N ₅	2.03
1000_NaCl/KCl		6.63(16)	BaTaO ₂ N + Ta ₃ N ₅	1.92

^a: The band gap was considered in a small range for the samples containing the oxides impurities resulting in absorption shoulder, as shown in Figure 3.7 and Figure 3.8

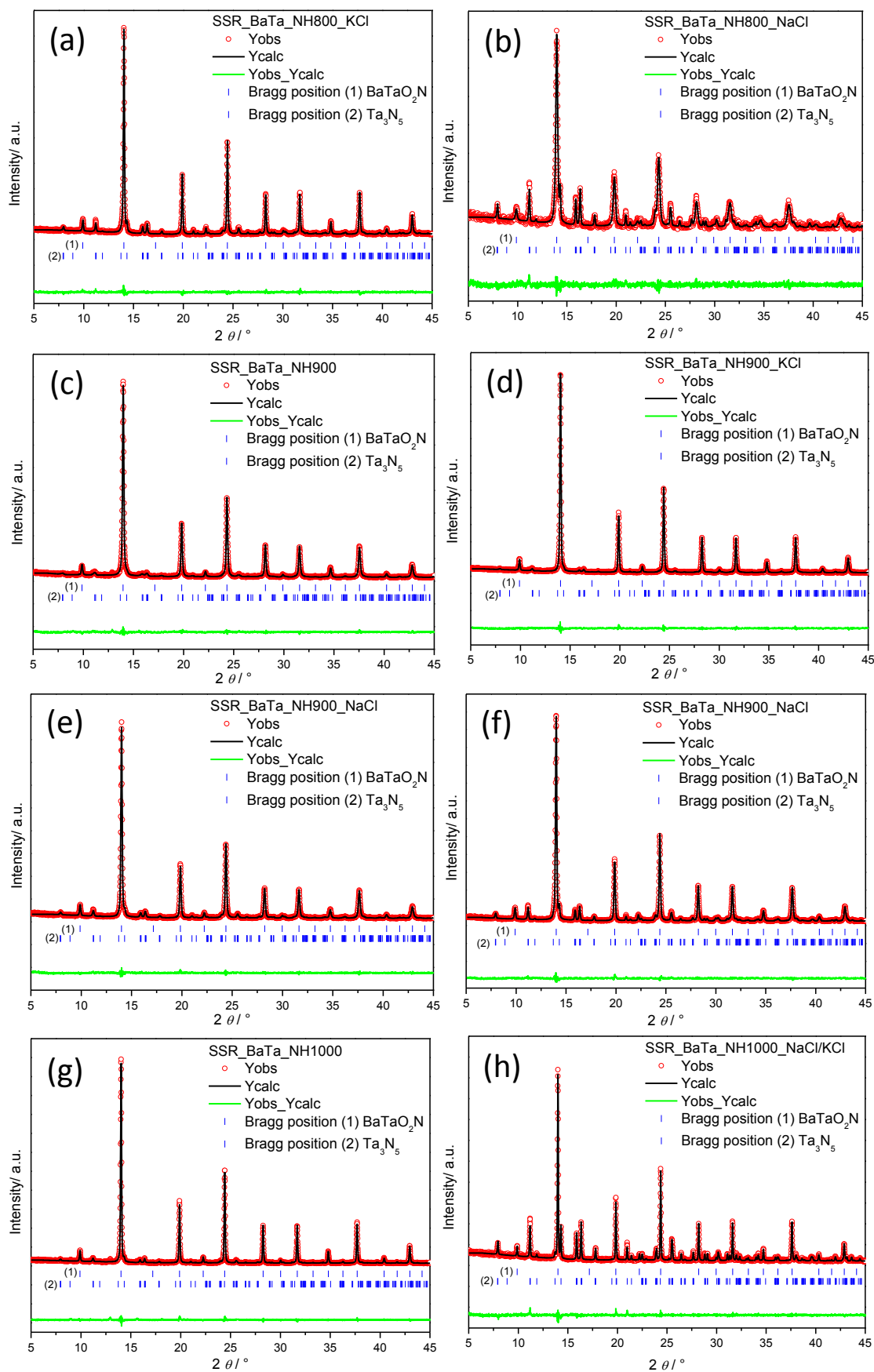


Figure 3.4 Rietveld refinement of the X-ray powder diffraction patterns of the selected samples obtained from the ammonolysis of SSR precursor (a) 800 °C with KCl, (b) 800 °C with NaCl, (c) 900 °C, (d) 900 °C with KCl, (e) 900 °C with NaCl, (f) 900 °C with NaCl/KCl, (g) 1000 °C, (h) 1000 °C with NaCl/KCl for 40 hours

Table 3.5 Phase compositions and lattice parameters of the selected samples obtained via the ammonolysis of SSR precursor from Rietveld refinement of the XRD patterns

Specimens / phase compositions	BaTaO ₂ N (<i>Pm-3m</i> , Nr. 221, Z=1)	Ta ₃ N ₅ (<i>CmCm</i> , Nr. 63, Z=4)
SSR_NH800_KCl	87.35 (53) wt% a=4.1045 (2) Å	12.65 (28) wt% a=3.8882 (5) Å, b=10.2041 (14) Å, c=10.2655 (14) Å
SSR_NH800_NaCl	77.10 (85) wt% a=4.1229 (6) Å	22.90 (54) wt% a=3.8955 (8) Å, b=10.2197 (20) Å, c=10.2786 (22) Å
SSR_NH900	92.80 (57) wt% a=4.1229 (3) Å	7.20 (33) wt% a=3.9075 (20) Å, b=10.2242 (65) Å, c=10.2665 (61) Å
SSR_NH900_KCl	95.39 (45) wt% a=4.1068 (2) Å	4.61 (21) wt% a=3.8903 (14) Å, b=10.2087 (43) Å, c=10.2577 (40) Å
SSR_NH900_NaCl	90.00 (50) wt% a=4.1137 (3) Å	10.00 (24) wt% a=3.8899 (8) Å, b=10.2237 (24) Å, c=10.2756 (23) Å
SSR_NH900_NaCl/KCl	85.45 (41) wt% a=4.1110 (2) Å	14.55 (19) wt% a=3.8895 (4) Å, b=10.2194 (11) Å, c=10.2702 (10) Å
SSR_NH1000	94.13 (52) wt% a=4.1075 (2) Å	5.87 (22) wt% a=3.8868 (7) Å, b=10.2051 (20) Å, c=10.2572 (19) Å
SSR_NH1000_NaCl/KCl	63.21 (52) wt% a=4.1166 (2) Å	36.79 (45) wt% a=3.8950 (3) Å, b=10.2372 (6) Å, c=10.2858 (6) Å

3.3.2 Microstructure of as-synthesized oxynitrides

As shown in Figure 3.5, the microstructure of oxynitrides displayed discernible cube edges and faces with dimensions of 0.5 ~ 1 μm, indicating the crystal habit of the primitive perovskite block and high crystallinity. Rod-like microstructure represented the Ta₃N₅ with orthorhombic structure. The particle size increased with the increasing of temperature only slightly. Moreover, the agglomeration of oxynitride without mineralizer is stronger than that of mineralizer-assisted samples.

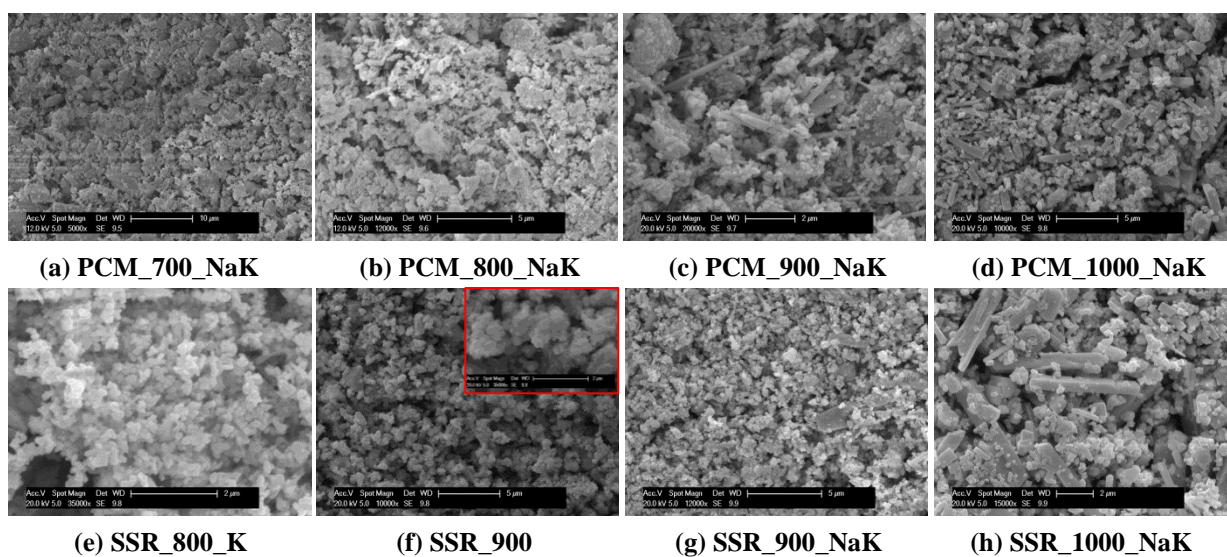


Figure 3.5 SEM images for the selected powder samples of oxynitride synthesized from PCM (a - d) and SSR (e - h) precursor

As shown in Figure 3.6, the specific surface area decreases with the increasing of temperature due to the growing of grain size. Considering the different oxide precursors, it demonstrates a mineralizer-dependent effect for SSR samples. For instance, the mineralizer-assisted oxynitrides show higher specific surface area than that of none-assisted oxynitrides, as well as the SSR oxide precursor (*i.e.* 8.06, 6.66, 13.85, 9.67 and 10.22 m²/g for SSR oxide precursor, SSR_900, SSR_900_Na, SSR_900_K and SSR_900_NaK, respectively). This is probably because that the formation of melting liquid phase at the boundary^[38] weakens the agglomeration during ammonolysis, as confirmed by SEM images as well. While PCM samples reveal only a temperature-dependent effect with respect to specific surface area due to a high surface area of their oxide precursor (*i.e.* 21.49 m²/g). On the other hand, porosity could be empirically presented by C values (related to the affinity of the solid with the adsorbate, and so to the heat of adsorption, *i.e.* mesoporous structure is expecting when C is larger than 100)^[215]. For our oxynitrides, none of them is close to it probably because that high temperature ammonolysis leads to compact particles, except SSR_1000, which is still unclear.

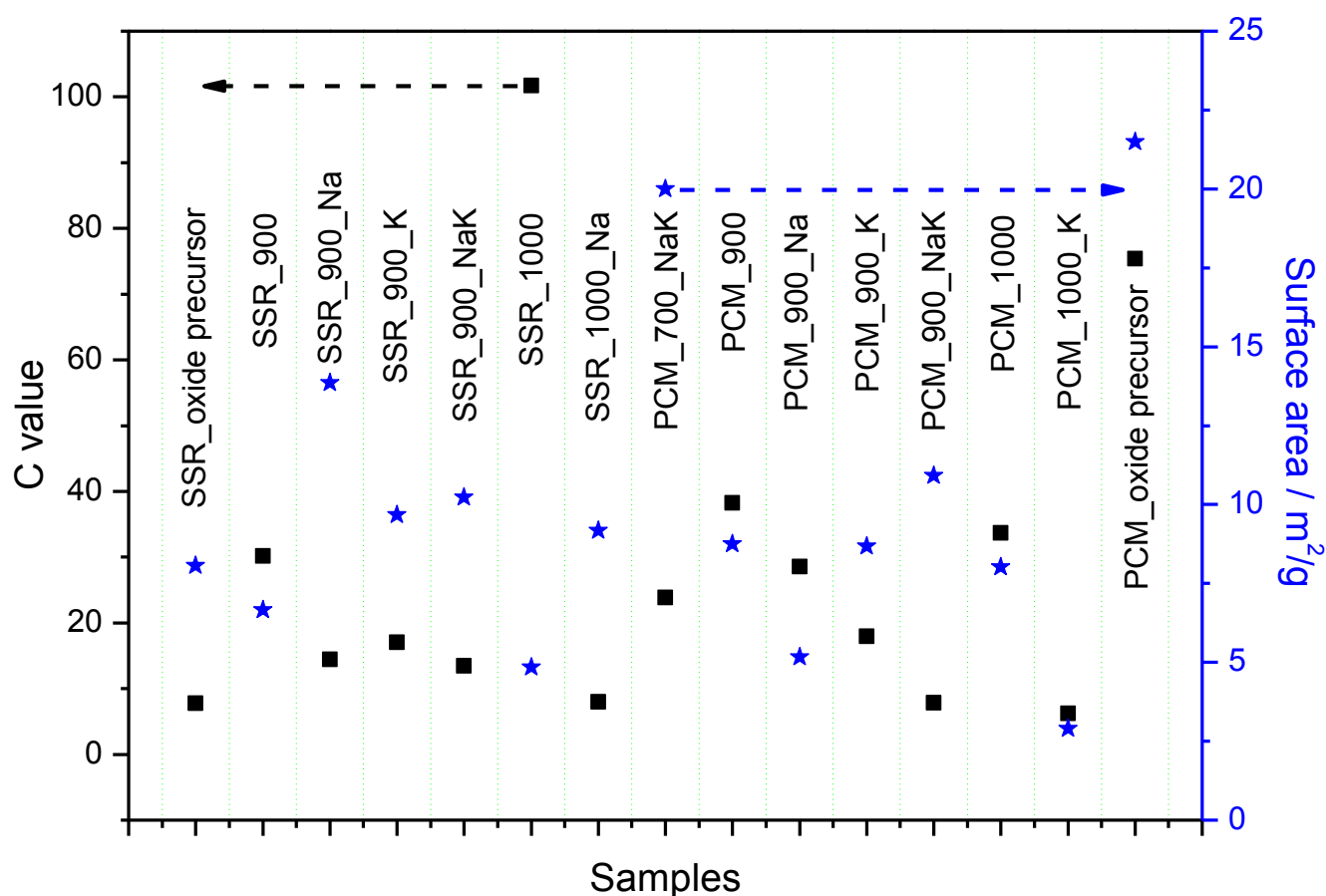


Figure 3.6 Specific surface area and porous structure of selected as-synthesized oxynitrides

3.3.3 UV-Vis spectroscopy and band gaps

Figure 3.7 (PCM samples) and Figure 3.8 (SSR samples) give the spectra of the oxynitrides in comparison to the corresponding oxides. And calculated band gaps according to Shapiro's method ^[212] are summarized in Table 3.2 and Table 3.4. In terms of PCM samples, the absorption edge of oxide precursor is in the UV region at ca. 315 nm. For the ammonolyzed oxynitrides, the onset of absorption is dramatically shifted to longer wavelength (roughly 500 ~ 650 nm). The shoulders for some of these oxynitrides are most likely due to trace impurities of oxides and nitride. In general, higher ammonolysis temperature leads to larger absorption shift (smaller band gap). It seems that the mineralizer only benefits the nitridation process at low temperature, i.e. 700 °C. Upon 800 °C, it either favors decreasing the band gap of as-synthesized oxynitride only slightly, or shows negative impact (*i.e.* over-ammonolysis leads to higher fraction of Ta₃N₅, which has higher band gap, ca. 2.05 eV).

Similar for SSR samples, the onset of absorption shifts to visible-light range as well. The calculated band gap varies from ca. 1.87 to 3.0 eV depending on the chemical/phase compositions. Compared to the effect of mineralizers on PCM samples, the mineralizer works more efficiently on the SSR samples due to their initially lower reactivity. It gives the slightest impact on band gap of the oxynitride ammonolyzed at 900 °C, which implies that this is the optimum reaction temperature for the SSR samples. The formation of nearly pure Ta₃N₅ phase for SSR_1000_Na and SSR_1000_K leads to a very sharp absorption edge at ca. 610 nm. In most cases, the sub-absorption shoulder appears between 600 and 800 nm indicating the formation of reduced cation ions (*i.e.* Ta⁴⁺) as defect which could probably lower their photocatalytic performance by offering electron-hole combination center ^[161]. However, it is still not clear how mineralizers influence on the formation of these defects. Detailed microscopy, *i. e.* TEM, is required to investigate it.

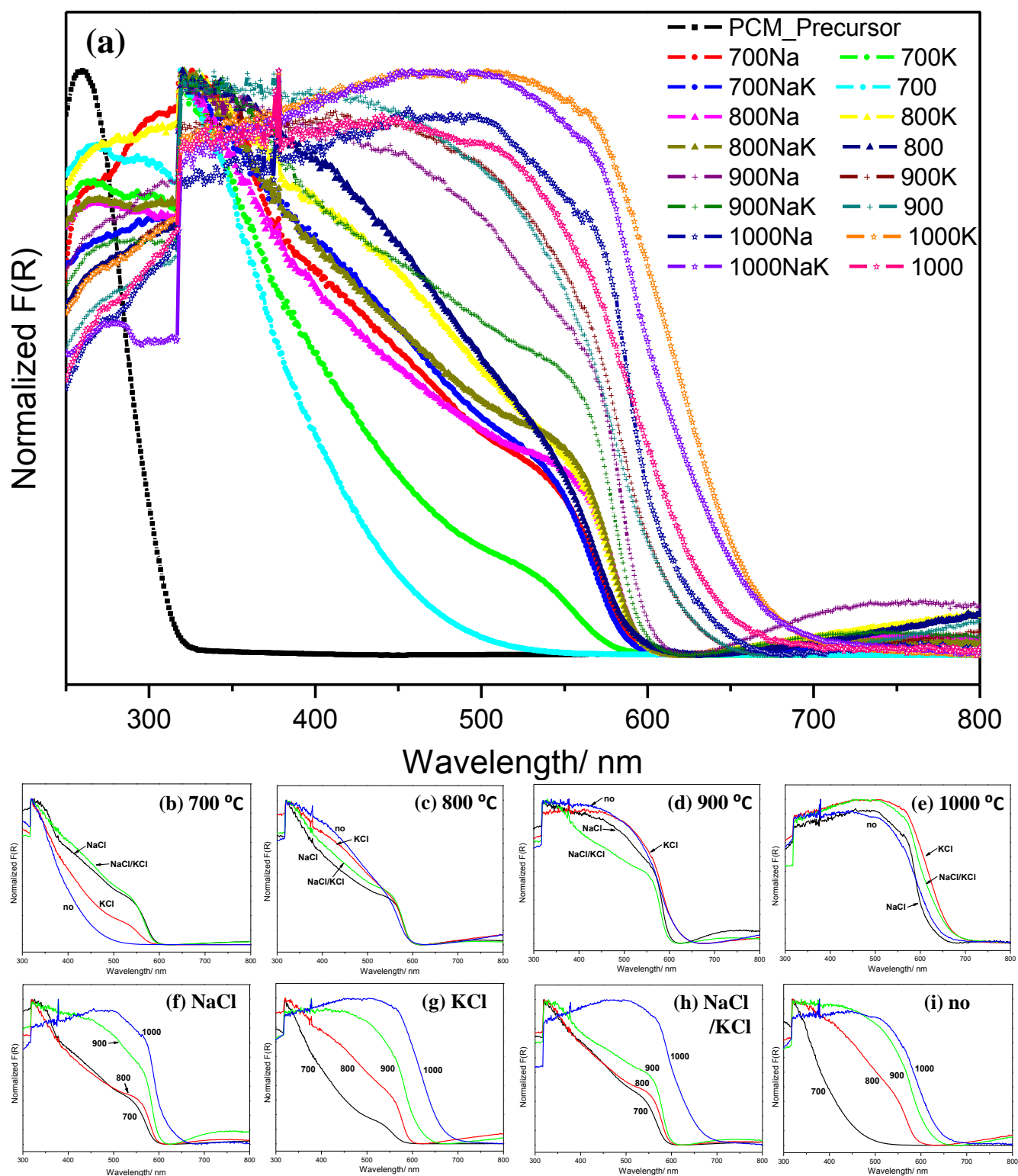


Figure 3.7 UV-vis diffuse reflectance spectra of oxynitrides ammonolyzed from PCM precursor (a) all the samples at 700, 800, 900 and 1000 °C with NaCl, KCl, NaCl/KCl or without mineralizer, (b) different mineralizers at 700 °C, (c) different mineralizers at 800 °C, (d) different mineralizers at 900 °C, (e) different mineralizers at 1000 °C, (f) different temperatures with NaCl, (g) different temperatures with KCl, (h) different temperatures with NaCl/KCl, and (i) different temperatures without mineralizers

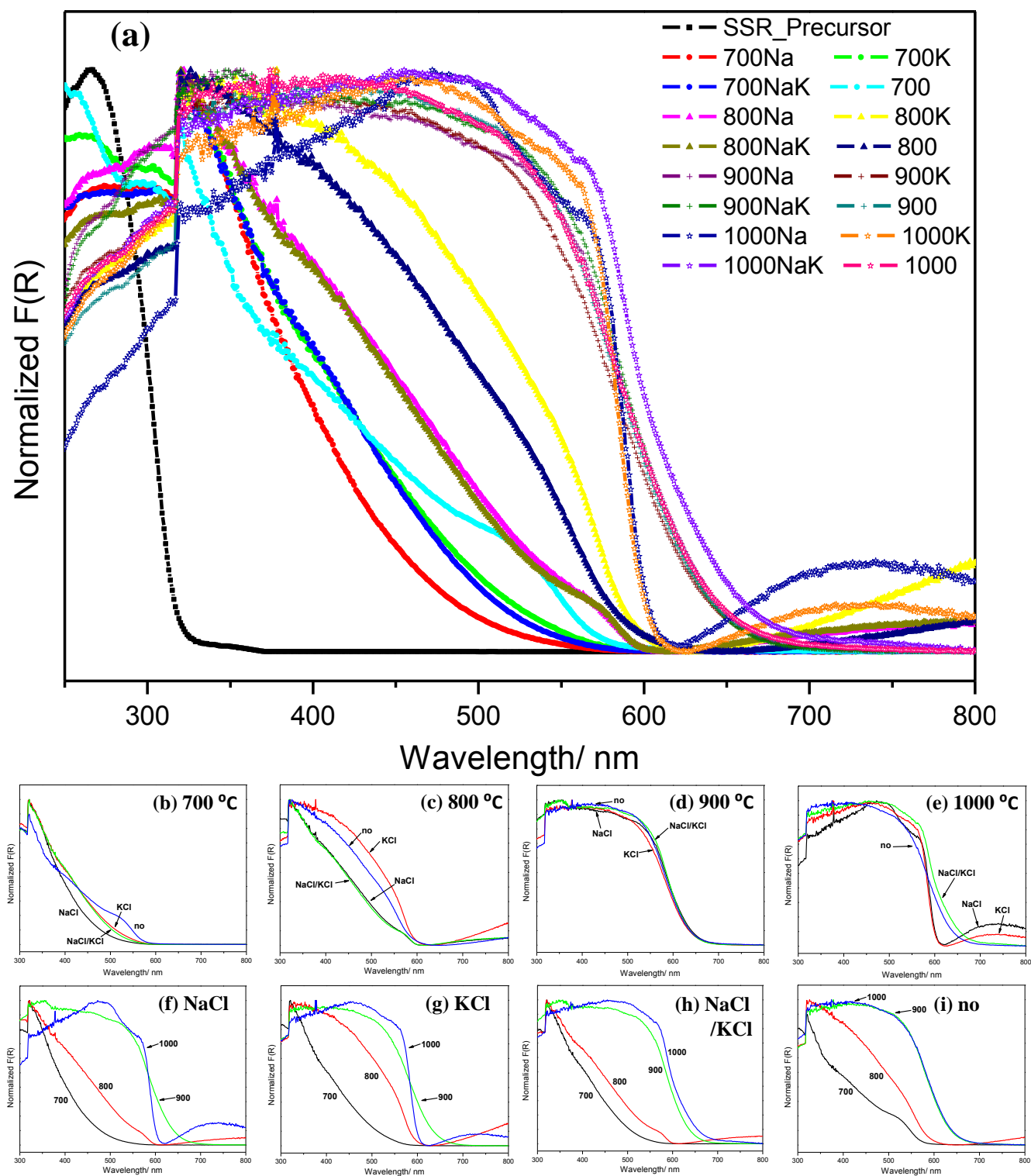


Figure 3.8 UV-vis diffuse reflectance spectra of oxynitrides ammonolyzed from SSR precursor (a) all the samples at 700, 800, 900 and 1000 °C with NaCl, KCl, NaCl/KCl or without mineralizer, (b) different mineralizers at 700 °C, (c) different mineralizers at 800 °C, (d) different mineralizers at 900 °C, (e) different mineralizers at 1000 °C, (f) different temperatures with NaCl, (g) different temperatures with KCl, (h) different temperatures with NaCl/KCl, and (i) different temperatures without mineralizers

3.3.4 Photocatalytic properties

The photodegradation of RhB by the as-synthesized BaTaO₂N was investigated, as shown in Figure 3.9. However, only less than 7.5% of RhB is degraded for SSR_800K compound after 10 h of irradiation under visible light. It indicates that BaTaO₂N is not active for the degradation of RhB dye with visible light.

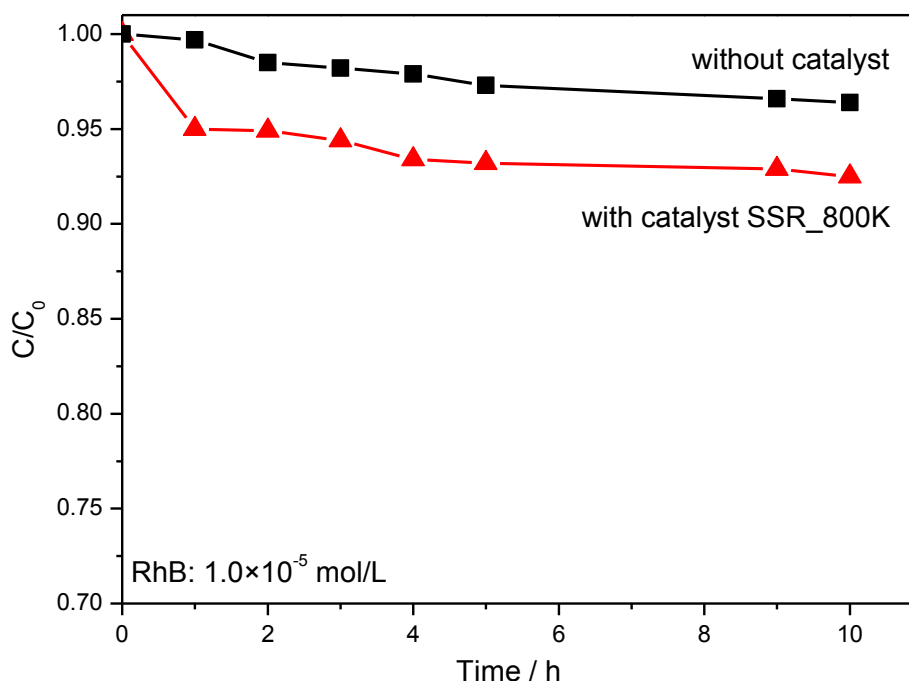


Figure 3.9 Degradation profile of RhB (1.0×10^{-5} mol/L) under visible light irradiation: without catalyst (black), with catalyst SSR_800K (red)

The photodegradation of MB was investigated as well. After 6 h of irradiation under visible light without catalyst, no significant changes in MB concentration were observed. The experiments were performed by varying the MB concentration at 2.5×10^{-5} and 1.0×10^{-6} mol/L while using same amount of photocatalysts (0.4 g/L). Figure 3.10 shows that after 10 h of irradiation under visible light SSR_1000 degrades ca. 27.5% of MB (2.5×10^{-5} mol/L), compared to just ca. 16% for PCM_900 catalyst. Similarly, PCM_900 just degrades ca. 15% of MB (1×10^{-6} mol/L) after 6 h of irradiation under visible light, compared to ca. 22% for SSR_1000 catalyst. The two key aspects to consider for enhancing catalytic activity are (1) increasing the surface area for faster dye absorption in the dark and (2) tuning the composition to lower the band gap and delocalize charge carriers^[167]. Since the surface area of SSR_1000 (ca. $5 \text{ m}^2/\text{g}$) and PCM_900 (ca. $8.5 \text{ m}^2/\text{g}$) compounds is quite low and no significant difference, the band gap takes the major responsibility for the different photocatalytic activity. The catalyst with lower band gap (1.87 eV for SSR_1000, 1.96 eV for PCM_900) shows a stronger photocatalytic activity.

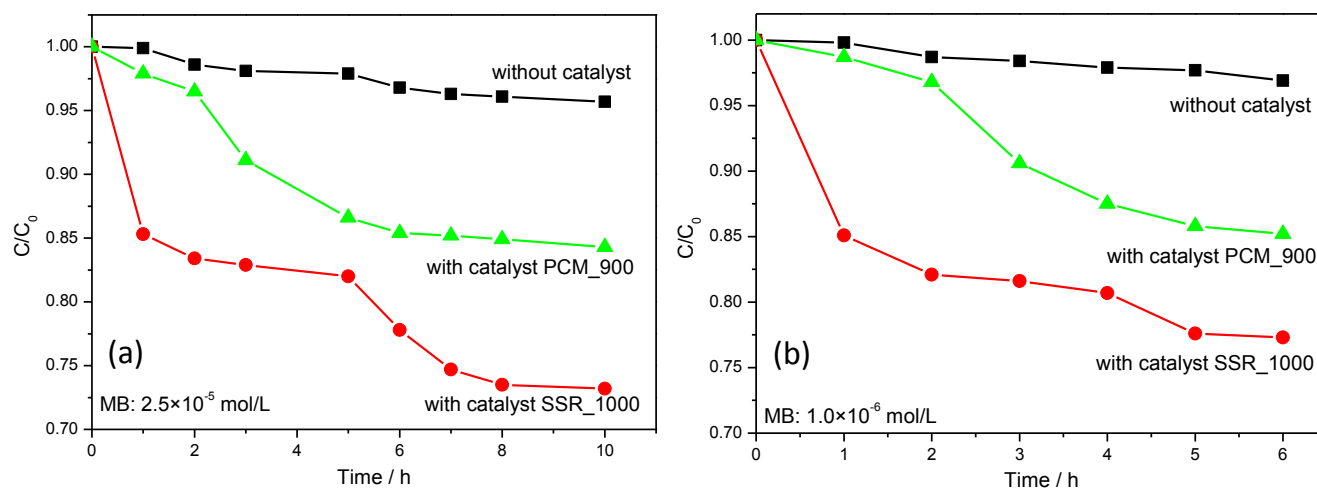


Figure 3.10 Degradation profile of (a) MB (2.5×10^{-5} mol/L) under visible light irradiation: without catalyst (black), with catalyst PCM_900 (green), with catalyst SSR_1000 (red); (b) MB (1.0×10^{-6} mol/L) under visible light irradiation: without catalyst (black), with catalyst PCM_900 (green), with catalyst SSR_1000 (red)

The photodegradation kinetics of the dyes on the different catalyst can be described as pseudo-first-order, given by Langmuir-Hinshelwood expression^[216], $\ln(C_0/C) = k_{obs}t$, where C_0 is the initial concentration of dye, C is the concentration of dye at time t , and k_{obs} is the limiting rate constant of the reaction. A plot of $\ln(C_0/C)$ vs. time leads to a linear diagram so that its slope equals the observed first-order rate constant of photodegradation k_{obs} . Figure 3.11 illustrates that SSR_1000 compound degrades MB at the fastest rate of 0.047 h^{-1} (10^{-6} mol/L of MB) and 0.041 h^{-1} (2.5×10^{-5} mol/L of MB); while it exhibits faster degradation rate in lower concentration of MB, which implies that larger amount of catalyst is necessary to enhance photocatalytic activity. Moreover, the degradation rate of PCM_900 compound is smaller than that of SSR_1000 compound (*i.e.* $0.028 \text{ h}^{-1} < 0.047 \text{ h}^{-1}$ and $0.02 \text{ h}^{-1} < 0.041 \text{ h}^{-1}$), which is in support of our hypothesis that a higher band gap leads to lower degradation effect.

Physical parameters that affect the kinetics of the dye degradation include mass of catalyst, wavelength of irradiated light, initial dye concentration, and temperature^[217]. It is very difficult to compare the results directly since physical parameters vary for each experimental setup. However, the degradation rate constant for our materials is still rather low compared to other recently reported results^[162, 167, 169, 216]. There are several possible factors may result in low degradation rate: (1) low mass of catalyst; (2) low surface area; (3) lattice defects that may act as recombination centers for photoinduced electrons and holes; (4) higher band gap due to the existence of impurity phases. Nevertheless, more experiments are needed to investigate the relation between microstructure and photocatalytic performance.

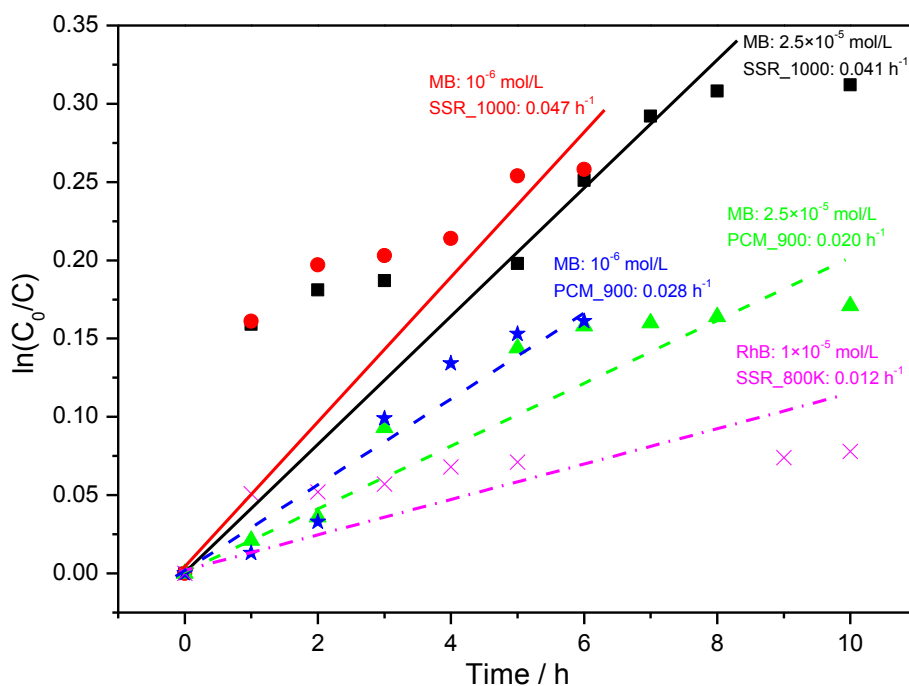


Figure 3.11 Pseudo-first-order kinetics for as-synthesized BaTaO₂N photocatalyst at various concentration of dyes: 10⁻⁶ mol/L of MB for SSR_1000 (red solid line), 2.5×10⁻⁵ mol/L of MB for SSR_1000 (black solid line), 10⁻⁶ mol/L of MB for PCM_900 (blue dash line), 2.5×10⁻⁵ mol/L of MB for PCM_900 (green dash line), and 1×10⁻⁵ mol/L of RhB for SSR_800K (magenta dash dot line). The values indicate the pseudo-first-order rate constant of photodegradation.

The chemical stability of the as-synthesized BaTaO₂N catalyst was also investigated. XRD patterns (Figure 3.12) show that no changes for SSR_1000 and SSR_800K compounds after react with MB and RhB, which indicate that these oxynitrides are quite stable in organic dyes after long time reaction. As shown in Figure 3.13, no significant morphology changes were observed for SSR_1000 and SSR_800K compounds after photocatalytic reaction as well, compared to Figure 3.5. However, we do observed the coating of organic component after photocatalytic reaction. This is because the degraded small molecular species absorbed on the surface of powder during reaction, which is probably another reason resulting in low degradation rate.

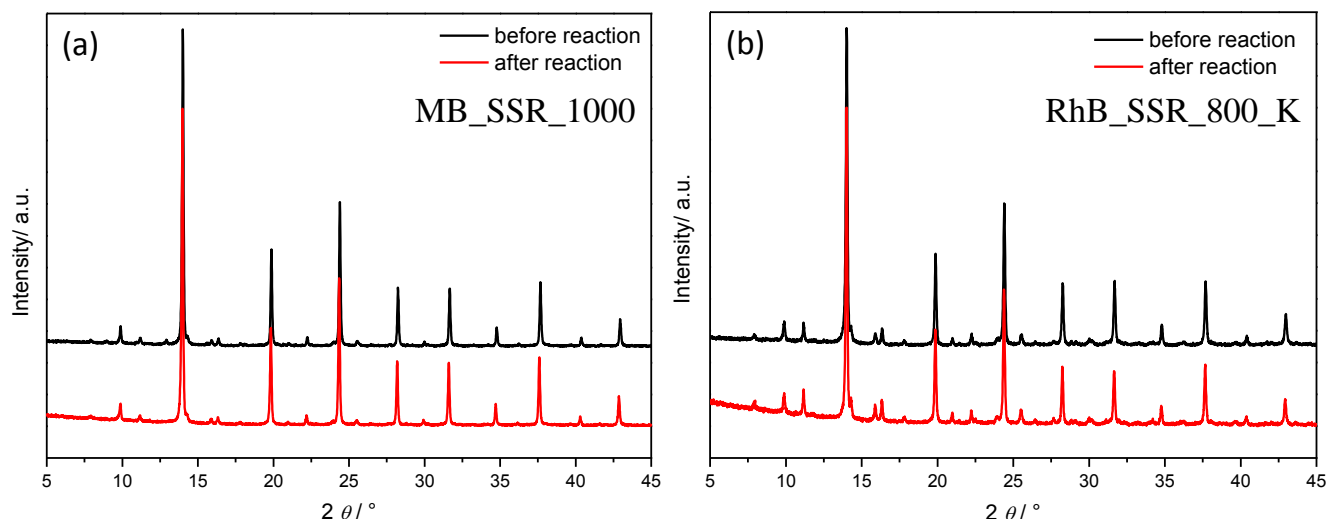


Figure 3.12 X-ray diffraction patterns of as-synthesized BaTaO₂N catalyst before and after photocatalytic reaction (a) SSR_1000 reacts with 2.5×10^{-5} mol/L of MB, (b) SSR_800K reacts with 1×10^{-5} mol/L of RhB

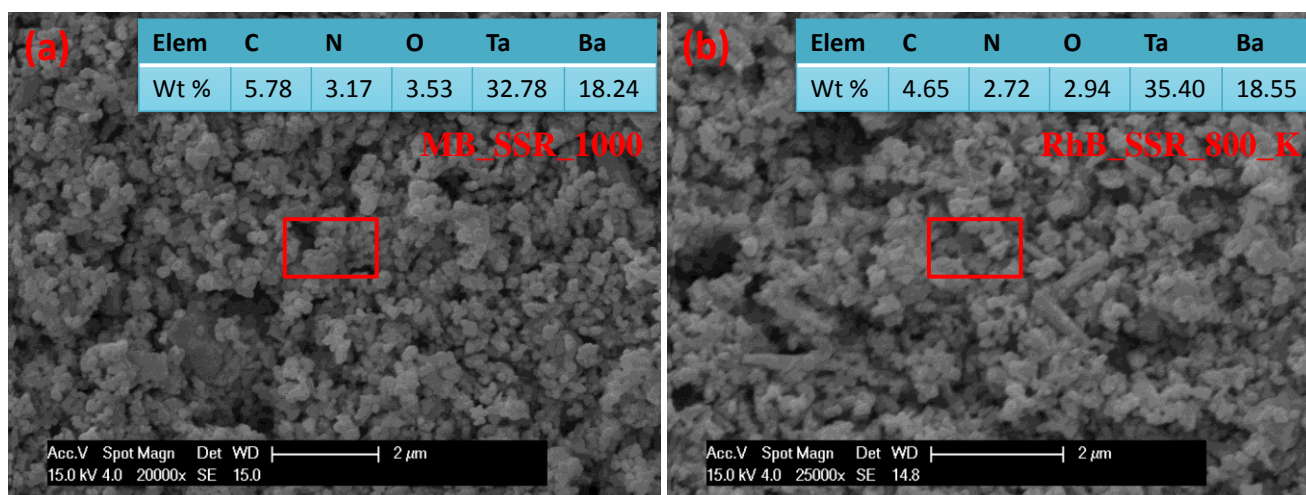


Figure 3.13 SEM images of the as-synthesized BaTaO₂N catalyst after photocatalytic reaction (a) SSR_1000 reacts with 2.5×10^{-5} mol/L of MB, (b) SSR_800K reacts with 1×10^{-5} mol/L of RhB and elemental analysis by EDX

3.4 Conclusions

In the present study, perovskite-type BaTaO₂N was prepared by thermal ammonolysis at 700 ~ 1000 °C for 16 or 40 h from PCM- and SSR-oxide precursors. The influence of mineralizers on the formation of oxynitride phase was discussed.

The purest oxynitride was obtained at 1000 °C without mineralizer (~ 97.7 wt% BaTaO₂N) and at 900 °C with KCl (~ 95.4 wt% BaTaO₂N) for PCM and SSR precursors, respectively. The mineralizer shows a rather positive impact on the formation of perovskite-type oxynitride at low ammonolysis temperature (*i.e.* 700 for PCM and 800 for SSR) instead of high thermal ammonolysis temperature. The appearance of rod-like

microstructure indicated the formation of Ta₃N₅ due to tantalum-rich phase and over-ammonolysis. The PCM mineralizer-assisted samples revealed a higher surface area because that the agglomeration was blocked to some extent via the formation of melting liquid phase at boundary; while SSR samples exhibited only a temperature-dependent effect with respect to specific surface area. The band gaps of as-synthesized oxynitride were decreased to ca. 1.9 eV depending on phase compositions.

The SSR_1000 compound exhibits the highest degradation rate ($k_{\text{obs}}=0.047 \text{ h}^{-1}$) in the 10^{-6} mol/L of MB under visible light irradiation; whereas RhB is degraded only less than 7.5% after 10 h of irradiation ($k_{\text{obs}}=0.012 \text{ h}^{-1}$) by SSR_800K compound. The as-synthesized oxynitride catalysts show high chemical stability after photocatalytic reaction.

4. Summary and Outlook

4.1 Summary

Within the scope of the present work, several aspects of perovskite-type oxynitrides were elaborated. A simple approach to predict the formability of perovskite-type oxynitrides has been addressed. The synthesis studies include different approaches from oxidic precursors. Besides, novel solid-solution compounds and mineralizer modified thermal ammonolysis techniques have been presented. A study on the structure evolution from scheelite ABO_4 to perovskite $AB(O,N)_3$ ($a=Ca, Sr, Ba$; $B=Mo, W$) via conventional thermal ammonolysis has been derived. Rapid sintering of dense oxynitride ceramics by SPS has been studied based on three oxynitrides, $SrMo(O,N)_3$, $SrW(O,N)_3$ and $LaTiO_2N$. A variety of properties including magnetic, electrical conductivity and photocatalytic properties have been illustrated.

In the first part of this work, a new model that utilizes the tolerance and octahedral factors has been developed for assessing the formability of the perovskite structure in oxynitrides and for predicting new perovskite-type oxynitrides that have not been synthesized so far. Therefore, we predict that among potentially piezoelectric oxynitrides, $YSiO_2N$ and $YGeO_2N$ are not stable in the perovskite-type structure; $YZrO_2N$ and $YSnO_2N$ are in turn formable, whereas for the possible candidate of photocatalytic oxynitrides according to DFT calculations $MgTaO_2N$ is not formable in perovskite structure; $YTiO_2N$, $CdTaO_2N$ and $CdNbO_2N$ appear to be feasible. Moreover, we predict the formability of perovskite structures for Zn^{2+} , Cd^{2+} , Y^{3+} , Hf^{4+} , Fe^{4+} and Sn^{4+} , as well as Pr^{3+} , Nd^{3+} , and Sm^{3+} oxynitrides. Our prediction results have been accepted and successfully applied into guiding synthesis work already [80, 218, 219]. In particular, based on our model, Kim et. al. [55] have succeeded to synthesize a novel perovskite oxynitride compound, $AM_{0.2}Ta_{0.8}O_{2.8}N_{0.2}$ ($A=Sr, Ba$; $M=Li, Na$). The results from this study were presented to the scientific community in publication [1].

The second part of the thesis was devoted to the understanding of the structure evolution from scheelite-type ABO_4 to perovskite-type $AB(O,N)_3$ under ammonia atmosphere; The results of the as-synthesized perovskite-oxynitrides $AM(O,N)_3$ ($A=Ba, Sr, Ca$; $B=Mo, W$) are consistent with our previous prediction in general. A new oxynitride $SrMO_{4-x}N_x$ ($M=Mo, W$) with the scheelite structure has been discovered as an intermediate phase, which subsequently converts fast into perovskite-type $SrM(O,N)_3$ at temperatures above 600 °C. The experimental results are in agreement with the high temperature oxide melt solution calorimetry experiments which indicate that the conversion of scheelite $SrMO_4$ into perovskite $SrM(O,N)_3$ is thermodynamically favorable at the used ammonolysis temperatures. Moreover, the formability of the perovskite-type oxynitrides with the structure of the used oxide precursor and the structural distortion described by the tolerance factor has been determined. The results from this study were presented to the scientific community in publication [2].

The third aspect of the thesis was concerned with the studies of densification behavior of selected perovskite-type oxynitride ceramics by SPS. The phase pure $SrMo(O,N)_3$ and $SrW(O,N)_3$ samples were densified by spark plasma sintering with heating rates of 300~400 °C/min and a uniaxial pressure of 100 MPa.

For the $\text{SrW}(\text{O},\text{N})_3$ samples decomposition occurred during sintering, since their densification needs temperatures higher than the decomposition temperature, as suggested by the TGA/MS study and the recorded SPS curves. Interestingly, $\text{SrMo}(\text{O},\text{N})_3$ was found to be significantly more resistant with respect to decomposition and thus monoliths with near full density were obtained, i.e. $\text{SrMoO}_4\text{-NH700_12H}$ (1 vol% porosity under vacuum), $\text{SrMoO}_4\text{-NH700_24H}$ (0 vol% porosity under vacuum). However, the nitrogen atmosphere fails to prevent the decomposition of oxynitride phases completely in our case, and a high porosity has been observed, i.e. $\text{SrMoO}_4\text{-NH700_12H}$ (2.3 vol% porosity under nitrogen), $\text{SrWO}_4\text{-NH900_12H}$ (12.7 vol% porosity under nitrogen). In terms of LaTiO_2N , the achieved density of 95% of the TD with 86 wt% LaTiO_2N at 1350 °C using 125 MPa sintering pressure is significantly higher than that of any counterparts prepared by conventional sintering. The results and findings from this study were reported to the scientific community in publications [3] and [4].

The fourth part of the thesis deals with the synthesis of solid-solutions of the type $\text{SrMo}_{1-x}\text{W}_x\text{O}_4$ and $\text{SrMo}_{1-x}\text{W}_x(\text{O},\text{N})_3$ as well as with their magnetic properties and electrical conductivity. Scheelite-type solid-solution $\text{SrMo}_{1-x}\text{W}_x\text{O}_4$ oxide precursors were synthesized by using a solvothermal method within the full compositional range (i.e., x from 0 to 1). The corresponding perovskite-type oxynitrides are formable upon thermal treatment of the scheelite-type solid-solution oxides in ammonia atmosphere only in a limited compositional range, i.e., for $x \leq 0.25$ and $x \geq 0.6$; whereas for $0.25 \leq x \leq 0.6$ decomposition processes occur and furnish different oxides and nitrides. A Pauli paramagnetic behavior was found for the solid-solution oxynitrides above 70 K. The magnetic susceptibility increased with increasing tungsten content. An anomalous hyperbolic crest at ~ 45.5 K is considered to likely relate to the presence of molecular oxygen in the measured materials, which is similar with the case of SrMoO_2N and $\text{SrWO}_{1.5}\text{N}_{1.5}$. The preliminary results indicate that higher amount of oxynitride, molybdenum and nitrogen content in the reaction products tends to increase the electrical conductivity of these solid-solution oxynitride. The results and findings from this study were reported to the scientific community in publications [5].

At the end, a preliminary study on the synthesis and photocatalytic properties of BaTaO_2N was carried out. Perovskite-type BaTaO_2N was prepared by thermal ammonolysis at 700 ~ 1000 °C for 16 or 40 h from PCM- and SSR-oxide precursors. The purest oxynitride was achieved at 1000 °C without mineralizer (~ 97.7 wt% BaTaO_2N) and 900 °C with KCl (~ 95.4 wt% BaTaO_2N) for PCM and SSR precursors, respectively. The band gap of the as-synthesized oxynitride was decreased to ca. 1.9 eV depending on the chemical/phase compositions. The mineralizer shows a positive impact on the formation of perovskite-type oxynitrides at low nitridation temperature (i.e. 700 °C for PCM and 800 °C for SSR). A Ta_3N_5 impurity phase was found almost in all samples due to the tantalum-rich phase and over-ammonolysis behavior. The oxynitrides ammonolyzed from PCM precursor revealed a mineralizer-dependent effect with respect to the specific surface area; while the SSR samples exhibited only a temperature-dependent effect. As-synthesized BaTaO_2N exhibits the ability to degrade MB dye (10^{-6} mol/L) with a maximum degradation rate at ca. 0.047 h^{-1} at the moment, and a great chemical stability is observed after the photocatalytic reaction. Low mass of catalyst, low surface area, lattice defect and

degraded small molecule absorbed on the surface of the oxynitride materials probably led to the poor photocatalytic performance of our as-synthesized oxynitrides.

4.2 Outlook

According to our prediction, the first challenge will be the exploration of novel perovskite-type oxynitrides, not synthesized so far, motivated by their potential impact as a new class of materials with diverse functionalities. Then the question arises how to overcome these challenges associated with their synthesis. Thus, the development of new synthesis routes is a crucial step to achieve a breakthrough in the synthetic methodology of novel $ABO_{3-x}N_x$ perovskite-type oxynitrides. For instance, oxide free sol-gel synthesis and nonaqueous sol-gel routes (e.g. single-source-precursor method), or direct high-pressure high-temperature synthesis (e.g. $BiTiO_2N$, in order to prevent reduction of Bi ions under ammonia atmosphere) are promising method to attain novel perovskite-type oxynitrides.

Besides the general structure evolution from scheelite ABO_4 to perovskite $AB(O,N)_3$, pyrochlore $A_2B_2O_7$ compounds are another alternative oxide precursor for the synthesis of perovskite-type oxynitrides^[61]. However, the mechanism of the structure evolution from pyrochlore to perovskite is still rarely investigated. A more systematic study in this context is needed and will be interesting and valuable for designing and guiding the selection of suitable oxide precursor as well as the synthesis of novel oxynitrides in perovskite-type structure.

Another challenging but highly interesting task is the densification process of oxynitride-based ceramic powders. SPS process has proved to be promising for the consolidation of perovskite-type oxynitrides as compared to other conventional consolidation methods. However, one serious drawback of SPS is the decomposition of the oxynitride during sintering. Vacuum atmosphere seems to be beneficial for consolidation, but not on oxynitride phase constraint, whereas nitrogen atmosphere appears quite tricky. Thus, optimum sintering atmosphere and parameters for different oxynitride compounds individually is necessary to achieve compacted and high purity oxynitrides for further properties investigation.

Both water splitting and photodegradation under visible light are still potential promising applications for perovskite-type oxynitrides. In terms of water splitting, some novel oxynitrides (e.g. $YTiO_2N$, $CdTaO_2N$ and $CdNbO_2N$ etc.) according to theoretical prediction^[23, 183] are expected to be investigated. In terms of photodegradation, more experiments are needed based on our preliminary results in order to promote the development of perovskite-type oxynitride for photodegradation, which is actually rarely reported up to now.

Considering the solid state structure of oxynitrides, anionic ordering has been a mystery and will be continuously attracting intensive attention due to its strong influence on optical, photocatalytic, dielectric properties etc. For instance, the coupling of anionic ordering to rotational or tilt ordering of octahedral, as observed for $SrNbO_2N$ and $SrTaO_2N$ ^[67, 113, 117], may result in structure arrangements that possess a net dipole,

which consequently leads to promising dielectric properties. The absence of local inversion symmetry around the B-site cations (and A cations given the disorder of surrounding anion chains) may also increase significantly the intensities of optical transitions in pigments and luminescent oxynitrides ^[113]. Nevertheless, the possible O/N ordering and the principle of it still remain a matter of debate, which actually deserves to be clarified.

Last but not least, concerning methodological aspects, some in-situ techniques under ammonia atmosphere, i.e. in-situ XRD/ND, TG/MS, TEM etc., are crucial to understand what is really occurring during the thermal ammonolysis process. However, the sensitivity and chemical causticity of ammonia gas which might cause a fatal damage on fine instruments completely hinders the development of these techniques so far. Perhaps a great effort is calling from both materials scientist and mechanical engineers in future to collaborate in order to solve this addressed problem.

5. References

- [1] R. D. Shannon, *Acta Crystallogr A* **1976**, *32*, 751-767.
- [2] W. H. Baur, *Crystall Rev* **1987**, *1*, 59-83.
- [3] R. G. Pearson, *Inorg Chem* **1991**, *30*, 2856-2858.
- [4] *Encyclopedia of Materials*, Vol. 7, Elsevier, Amsterdam, **2001**.
- [5] M. A. Pena, J. L. G. Fierro, *Chem Rev* **2001**, *101*, 1981-2017.
- [6] L. G. Tejuca, J. L. G. Fierro, *Properties and applications of perovskite-type oxides*, CRC Press, New York, **2000**.
- [7] M. S. Islam, *J Mater Chem* **2000**, *10*, 1027-1038.
- [8] A. Kumar, A. S. Verma, S. R. Bhardwaj, *The Open Applied Physics Journal* **2008**, *1*, 11-19.
- [9] D. M. Giaquinta, H. C. Zurloye, *Chem Mater* **1994**, *6*, 365-372.
- [10] C. H. Li, K. C. K. Soh, P. Wu, *J Alloy Compd* **2004**, *372*, 40-48.
- [11] M. W. Lufaso, P. M. Woodward, *Acta Crystallogr B* **2001**, *57*, 725-738.
- [12] H. Zhang, N. Li, K. Li, D. F. Xue, *Acta Crystallogr B* **2007**, *63*, 812-818.
- [13] M. Bharathy, A. H. Fox, S. J. Mugavero, H. C. zur Loye, *Solid State Sciences* **2009**, *11*, 651-654.
- [14] G. Hautier, C. Fischer, V. Ehrlacher, A. Jain, G. Ceder, *Inorg Chem* **2011**, *50*, 656-663.
- [15] I. Yamada, H. Etani, K. Tsuchida, S. Marukawa, N. Hayashi, T. Kawakami, M. Mizumaki, K. Ohgushi, Y. Kusano, J. Kim, N. Tsuji, R. Takahashi, N. Nishiyama, T. Inoue, T. Irifune, M. Takano, *Inorg Chem* **2013**, *52*, 13751-13761.
- [16] I. Pirrotta, R. Schmidt, A. J. Dos Santos-Garcia, M. Garcia-Hernandez, E. Moran, M. A. Alario-Franco, *J Solid State Chem* **2015**, *225*, 321-329.
- [17] N. C. Bristowe, J. Varignon, D. Fontaine, E. Bousquet, P. Ghosez, *Nat Commun* **2015**, *6*.
- [18] H. Mizoguchi, P. Chen, P. Boolchand, V. Ksenofontov, C. Felser, P. W. Barnes, P. M. Woodward, *Chem Mater* **2013**, *25*, 3858-3866.
- [19] A. T. Mulder, N. A. Benedek, J. M. Rondinelli, C. J. Fennie, *Adv Funct Mater* **2013**, *23*, 4810-4820.
- [20] H. Wolff, R. Dronskowski, *J Comput Chem* **2008**, *29*, 2260-2267.
- [21] P. E. D. Morgan, *J Mater Sci* **1986**, *21*, 4305-4309.
- [22] A. Fuertes, *Inorg Chem* **2006**, *45*, 9640-9642.
- [23] I. E. Castelli, T. Olsen, S. Datta, D. D. Landis, S. Dahl, K. S. Thygesen, K. W. Jacobsen, *Energ Environ Sci* **2012**, *5*, 5814-5819.
- [24] R. Caracas, R. E. Cohen, *Appl Phys Lett* **2007**, *91*.
- [25] R. Marchand, Y. Laurent, J. Guyader, P. L'Haridon, P. Verdier, *J Eur Ceram Soc* **1991**, *8*, 197-213.
- [26] I. Elphinston, A. Hendry, *Fabrication and Technology British Ceramic Proceedings*, Vol. 45, **1989**.
- [27] A. Hellwig, A. Hendry, *J Mater Sci* **1994**, *29*, 4686-4693.
- [28] D. Logvinovich, Ph.D thesis, Universität Augsburg (Empa), **2008**.
- [29] M. R. Brophy, S. M. Pilgrim, W. A. Schulze, *J Am Ceram Soc* **2011**, *94*, 4263-4268.
- [30] R. Aguiar, D. Logvinovich, A. Weidenkaff, A. Reller, S. G. Ebbinghaus, *Thermochim Acta* **2008**, *471*, 55-60.
- [31] R. Aguiar, A. Weidenkaff, C. W. Schneider, A. Reller, S. G. Ebbinghaus, *Prog Solid State Ch* **2007**, *35*, 291-298.
- [32] R. Aguiar, Ph.D thesis, Universität Augsburg **2008**.
- [33] T. Katsumata, A. Nakamura, M. Nakanishi, H. Yoshioka, Y. Inaguma, T. Ohba, T. Tsurui, *J Ceram Soc Jpn* **2009**, *117*, 1345-1348.
- [34] R. Marchand, F. Pors, Y. Laurent, *Rev Int Hautes Temp* **1986**, *23*, 11-15.
- [35] A. Kachina, E. Puzenat, S. Ould-Chikh, C. Geantet, P. Delichere, P. Afanasiev, *Chem Mater* **2012**, *24*, 636-642.
- [36] A. Gomathi, S. Reshma, C. N. R. Rao, *J Solid State Chem* **2009**, *182*, 72-76.
- [37] Y. I. Kim, P. M. Woodward, K. Z. Baba-Kishi, C. W. Tai, *Chem Mater* **2004**, *16*, 1267-1276.
- [38] Y. I. Kim, *Ceram Int* **2014**, *40*, 5275-5281.
- [39] A. Rachel, S. G. Ebbinghaus, M. Gungerich, P. J. Klar, J. Hanss, A. Weidenkaff, A. Reller, *Thermochim Acta* **2005**, *438*, 134-143.
- [40] E. Soignard, D. Machon, P. F. McMillan, J. J. Dong, B. Xu, K. Leinenweber, *Chem Mater* **2005**, *17*, 5465-5472.

- [41] I. O. Troyanchuk, N. V. Kasper, O. S. Mantyskaya, E. F. Shapovalova, *Mater Res Bull* **1995**, *30*, 421-425.
- [42] M. H. Yang, J. A. Rodgers, L. C. Middler, J. Oro-Sole, A. B. Jorge, A. Fuertes, J. P. Attfield, *Inorg Chem* **2009**, *48*, 11498-11500.
- [43] S. J. Clarke, K. A. Hardstone, C. W. Michie, M. J. Rosseinsky, *Chem Mater* **2002**, *14*, 2664-2669.
- [44] C. Tassel, Y. Kuno, Y. Goto, T. Yamamoto, C. M. Brown, J. Hester, K. Fujita, M. Higashi, R. Abe, K. Tanaka, Y. Kobayashi, H. Kageyama, *Angew Chem Int Edit* **2015**, *54*, 516-521.
- [45] S. K. Sun, T. Motohashi, Y. Masubuchi, S. Kikkawa, *J. Eur. Ceram. Soc.* **2014**, *34*, 4451-4455.
- [46] I. D. Fawcett, K. V. Ramanujachary, M. Greenblatt, *Mater. Res. Bull.* **1997**, *32*, 1565-1570.
- [47] Y. I. Kim, E. Lee, *J Ceram Soc Jpn* **2011**, *119*, 371-374.
- [48] R. M. F. Pors, Y. Laurent, P. Bacher, G. Roult, *Mat. Res. Bull.* **1988**, *23*, 1447-1450.
- [49] E. C. Pascual, V. B. Gutierrez, M. Subda, R. S. Puche, *Solid State Sci.* **2008**, *10*, 1905-1909.
- [50] T. Motohashi, Y. Hamade, Y. Masubuchi, T. Takeda, K. Murai, A. Yoshiasa, S. Kikkawa, *Mater. Res. Bull.* **2009**, *44*, 1899-1905.
- [51] R. Pastrana-Fabregas, J. Isasi-Marin, C. Cascales, R. Saez-Puche, *J. Solid State Chem.* **2007**, *180*, 92-97.
- [52] M. Yashima, U. Fumi, H. Nakano, K. Omoto, J. R. Hester, *J Phys Chem C* **2013**, *117*, 18529-18539.
- [53] F. Pors, P. Bacher, R. Marchand, Y. Laurent, G. Roult, *Rev. Int. Hautes Temp. Refract.* **1987**, *24*, 239.
- [54] W. Li, A. Gurlo, R. Riedel, E. Ionescu, *Z. Anorg. Allg. Chem.* **2015**, *641*, (8-9), 1533-1539.
- [55] Y. I. Kim, Y. Paik, M. Avdeev, *Cryst Growth Des* **2015**, *15*, 53-61.
- [56] F. Chevire, F. Tessier, R. Marchand, *Eur J Inorg Chem* **2006**, 1223-1230.
- [57] A. Maegli, S. Yoon, E. Otal, L. Karvonen, P. Mandaliev, A. Weidenkaff, *J Solid State Chem* **2011**, *184*, 929-936.
- [58] J. Grins, P. O. Kall, G. Svensson, *J Mater Chem* **1994**, *4*, 1293-1301.
- [59] D. Logvinovich, S. C. Ebbinghaus, A. Reller, I. Marozau, D. Ferri, A. Weidenkaff, *Z. Anorg. Allg. Chem.* **2010**, *636*, 905-912.
- [60] E. Günther, R. Hagenmayer, M. Jansen, *Z. Anorg. Allg. Chem.* **2000**, *626*, 1519-1525.
- [61] S. J. Clarke, B. P. Guinot, C. W. Michie, M. J. C. Calmont, M. J. Rosseinsky, *Chem Mater* **2002**, *14*, 288-294.
- [62] N. Kumar, A. Sundaresan, C. N. R. Rao, *Mater. Res. Bull.* **2011**, *46*, 2021-2024.
- [63] J. Rooke, M. Weller, *Sol St Phen* **2003**, *90-91*, 417-422.
- [64] M. Jansen, H. P. Letschert, *Nature* **2000**, *404*, 980-982.
- [65] D. Logvinovich, M. H. Aguirre, J. Hejtmanek, R. Aguiar, S. G. Ebbinghaus, A. Reller, A. Weidenkaff, *J. Solid State Chem.* **2008**, *181*, 2243-2249.
- [66] J. Oro-Solé, L. Clark, W. Bonin, J. P. Attfield, A. Fuertes, *Chem Commun* **2013**, *49*, 2430-2432.
- [67] Y. R. Zhang, T. Motohashi, Y. Masubuchi, S. Kikkawa, *J Ceram Soc Jpn* **2011**, *119*, 581-586.
- [68] P. Bacher, P. Antoine, R. Marchand, P. Lharidon, Y. Laurent, G. Roult, *J. Solid State Chem.* **1988**, *77*, 67-71.
- [69] N. Y. Park, Y. I. Kim, *J Mater Sci* **2012**, *47*, 5333-5340.
- [70] P. Antoine, R. Assabaa, P. L'Haridon, R. Marchand, Y. Laurent, C. Michel, B. Raveau, *Mater. Sci. Eng. B* **1989**, *5*, 43-46.
- [71] P. Antoine, R. Marchand, Y. Lament, C. Michel, B. Raveau, *Mat. Res. Bull.* **1988**, *23*, 953-957.
- [72] Y. I. Kim, P. M. Woodward, *J Solid State Chem* **2007**, *180*, 3224-3233.
- [73] F. Tessier, R. Marchand, *J Solid State Chem* **2003**, *171*, 143-151.
- [74] C. T. Ho, K. B. Low, P. Jash, H. Y. Shen, P. T. Snee, R. J. Meyer, *Chem Mater* **2011**, *23*, 4721-4725.
- [75] R. H. Mitchell, *Almaz Press: Ontario* **2002**.
- [76] A. M. Glazer, *Acta Crystallogr B* **1972**, *B 28*, 3384-&.
- [77] P. M. Woodward, *Acta Crystallogr B* **1997**, *53*, 44-66.
- [78] P. M. Woodward, *Acta Crystallogr B* **1997**, *53*, 32-43.
- [79] A. S. Bhalla, R. Y. Guo, R. Roy, *Mater Res Innov* **2000**, *4*, 3-26.
- [80] W. J. Li, D. Li, X. Gao, A. Gurlo, S. Zander, P. Jones, A. Navrotsky, Z. J. Shen, R. Riedel, E. Ionescu, *Dalton Trans* **2015**, *44*, 8238-8246.
- [81] G. S. Gallego, N. M. Alzate, O. Arnache, *J Alloy Compd* **2013**, *549*, 163-169.
- [82] S. Dutch, Natural and Applied Sciences, University of Wisconsin **2013**.
- [83] A. W. Sleight, *Acta Crystall B-Stru* **1972**, *B 28*, 2899-&.

- [84] F. M. Pontes, M. A. M. A. Maurera, A. G. Souza, E. Longo, E. R. Leite, R. Magnani, M. A. C. Machado, P. S. Pizani, J. A. Varela, *J Eur Ceram Soc* **2003**, *23*, 3001-3007.
- [85] X. H. Jiang, J. F. Ma, B. T. Lin, Y. Ren, J. Liu, X. Y. Zhu, J. T. Tao, Y. G. Wang, L. J. Xie, *J Am Ceram Soc* **2007**, *90*, 977-979.
- [86] E. Gurmen, E. Daniels, J. S. King, *J Chem Phys* **1971**, *55*, 1093-&.
- [87] B. C. Chakoumakos, M. M. Abraham, L. A. Boatner, *J Solid State Chem* **1994**, *109*, 197-202.
- [88] L. Jian, C. M. Wayman, *J Am Ceram Soc* **1997**, *80*, 803-806.
- [89] Y. Oka, T. Yao, N. Yamamoto, *J Solid State Chem* **2000**, *152*, 486-491.
- [90] C. T. Au, W. D. Zhang, H. L. Wan, *Catal Lett* **1996**, *37*, 241-246.
- [91] H. Takei, S. Tsunekawa, *J Cryst Growth* **1977**, *38*, 55-60.
- [92] L. H. Brixner, J. F. Whitney, F. C. Zumsteg, G. A. Jones, *Mater Res Bull* **1977**, *12*, 17-24.
- [93] R. E. Thoma, G. D. Brunton, R. A. Penneman, T. K. Keenan, *Inorg Chem* **1970**, *9*, 1096.
- [94] C. Keller, H. Schmutz, *J Inorg Nucl Chem* **1965**, *27*, 900-&.
- [95] Y. Zhang, N. A. W. Holzwarth, R. T. Williams, *Phys Rev B* **1998**, *57*, 12738-12750.
- [96] Z. L. Wang, H. B. Liang, M. L. Gong, Q. Su, *J Alloy Compd* **2007**, *432*, 308-312.
- [97] M. J. J. Lammers, G. Blasse, D. S. Robertson, *Phys Status Solidi A* **1981**, *63*, 569-572.
- [98] M. Itoh, M. Fujita, *Phys Rev B* **2000**, *62*, 12825-12830.
- [99] J. Hanuza, M. Maczka, K. Hermanowicz, P. J. Deren, W. Strek, L. Folcik, H. Drulis, *J Solid State Chem* **1999**, *148*, 468-478.
- [100] J. P. Sattler, J. Nemarich, *Phys Rev B* **1970**, *1*, 4249-&.
- [101] M. H. Yang, Ph.D thesis, University of Edinburgh **2010**.
- [102] M. A. Subramanian, G. Aravamudan, G. V. S. Rao, *Prog Solid State Chem* **1983**, *15*, 55-143.
- [103] S. T. Bramwell, M. J. P. Gingras, *Science* **2001**, *294*, 1495-1501.
- [104] J. S. Gardner, M. J. P. Gingras, J. E. Greedan, *Rev Mod Phys* **2010**, *82*, 53-107.
- [105] A. R. Cleave, Ph.D thesis, University of London **2006**.
- [106] D. J. P. Morris, D. A. Tennant, S. A. Grigera, B. Klemke, C. Castelnovo, R. Moessner, C. Czternasty, M. Meissner, K. C. Rule, J. U. Hoffmann, K. Kiefer, S. Gerischer, D. Slobinsky, R. S. Perry, *Science* **2009**, *326*, 411-414.
- [107] M. J. P. Gingras, C. V. Stager, B. D. Gaulin, N. P. Raju, J. E. Greedan, *J Appl Phys* **1996**, *79*, 6170-6172.
- [108] J. A. Labrincha, J. R. Frade, F. M. B. Marques, *J Mater Sci* **1993**, *28*, 3809-3815.
- [109] J. A. Diaz-Guillen, M. R. Diaz-Guillen, J. M. Almanza, A. F. Fuentes, J. Santamaria, C. Leon, *J Phys-Condens Mat* **2007**, *19*.
- [110] R. E. Carbonio, J. A. Alonso, J. L. Martinez, *J Phys-Condens Mat* **1999**, *11*, 361-369.
- [111] H. Sakai, K. Yoshimura, H. Ohno, H. Kato, S. Kambe, R. E. Walstedt, T. D. Matsuda, Y. Haga, *J Phys-Condens Mat* **2001**, *13*, L785-L790.
- [112] S. K. Kwon, J. H. Park, B. I. Min, *Physica B* **2000**, *281*, 528-530.
- [113] M. H. Yang, J. Oro'-Sole', J. A. Rodgers, A. B. Jorge, A. Fuentes, J. P. Attfield, *Nat Chem* **2011**, *3*, 47-52.
- [114] D. Armytage, B. E. F. Fender, *Acta. Cryst.* **1974**, *30*, 809-812.
- [115] N. Diot, R. Marchand, J. Haines, J. M. Leger, P. Macaudiere, S. Hull, *J. Solid State Chem.* **1999**, *146*, 390-393.
- [116] R. Marchand, R. Pastuszak, Y. Laurent, G. Roult, *Rev Chim Miner* **1982**, *19*, 684-689.
- [117] S. G. Ebbinghaus, A. Weidenkaff, A. Rachel, A. Reller, *Acta Crystallogr C* **2004**, *60*, I91-I93.
- [118] W. Li, E. Ionescu, R. Riedel, A. Gurlo, *J. Mater. Chem. A* **2013**, *1*, 12239-12245.
- [119] A. Fuentes, *J Mater Chem* **2012**, *22*, 3293-3299.
- [120] Y. Hinuma, H. Moriwake, Y.-R. Zhang, T. Motohashi, S. Kikkawa, I. Tanaka, *Chem Mater* **2012**, *24*, 4343-4349.
- [121] P. J. Camp, A. Fuentes, J. P. Attfield, *J Am Chem Soc* **2012**, *134*, 6762-6766.
- [122] J. P. Attfield, *Cryst Growth Des* **2013**, *13*, 4623-4629.
- [123] K. Charles, *Introduction to Solid State Physics*, 7th ed., Wiley.
- [124] C. R. R. Nave, Department of Physics and Astronomy, Georgia State University.
- [125] S. G. Ebbinghaus, H. P. Abicht, R. Dronskowski, T. Müller, A. Reller, A. Weidenkaff, *Prog. Solid State Chem.* **2009**, *37*, 173-205.
- [126] S. G. Ebbinghaus, R. Aguiar, A. Weidenkaff, S. Gsell, A. Reller, *Solid State Sciences* **2008**, *10*, 709-716.

- [127] R. Abe, *J Photoch Photobio C* **2010**, *11*, 179-209.
- [128] A. Fujishima, K. Honda, *Nature* **1972**, *238*, 37-38.
- [129] A. J. Nozik, *Appl Phys Lett* **1977**, *30*, 567-569.
- [130] F. E. Osterloh, *Chem Mater* **2008**, *20*, 35-54.
- [131] A. A. Ismail, D. W. Bahnemann, *Sol Energ Mat Sol C* **2014**, *128*, 85-101.
- [132] H. Kato, K. Asakura, A. Kudo, *J Am Chem Soc* **2003**, *125*, 3082-3089.
- [133] Z. K. Zheng, B. B. Huang, X. Y. Qin, X. Y. Zhang, Y. Dai, *J Colloid Interf Sci* **2011**, *358*, 68-72.
- [134] P. N. Kapoor, S. Uma, S. Rodriguez, K. J. Klabunde, *J Mol Catal a-Chem* **2005**, *229*, 145-150.
- [135] Z. X. Chen, A. Derking, W. Koot, M. P. vanDijk, *J Catal* **1996**, *161*, 730-741.
- [136] Y. H. Ni, X. H. Wang, J. M. Hong, *Mater Res Bull* **2009**, *44*, 1797-1801.
- [137] H. Kato, A. Kudo, *Chem Phys Lett* **1998**, *295*, 487-492.
- [138] H. Kato, K. Asakura, A. Kudo, *J Am Chem Soc* **2003**, *125*, 3082-3089.
- [139] J. R. Darwent, A. Mills, *J. Chem. Soc., Faraday Trans. 2* **1982**, *78*, 359-367.
- [140] W. Erbs, J. Desilvestro, E. Borgarello, M. Gratzel, *J Phys Chem* **1984**, *88*, 4001-4006.
- [141] K. Sayama, R. Yoshida, H. Kusama, K. Okabe, Y. Abe, H. Arakawa, *Chem Phys Lett* **1997**, *277*, 387-391.
- [142] A. Kudo, K. Ueda, H. Kato, I. Mikami, *Catal Lett* **1998**, *53*, 229-230.
- [143] A. Kudo, K. Omori, H. Kato, *J Am Chem Soc* **1999**, *121*, 11459-11467.
- [144] S. Tokunaga, H. Kato, A. Kudo, *Chem Mater* **2001**, *13*, 4624-4628.
- [145] J. Q. Yu, A. Kudo, *Adv Funct Mater* **2006**, *16*, 2163-2169.
- [146] M. Matsumura, Y. Saho, H. Tsubomura, *J Phys Chem* **1983**, *87*, 3807-3808.
- [147] A. Kudo, *Int J Hydrogen Energ* **2006**, *31*, 197-202.
- [148] A. Kudo, A. Nagane, I. Tsuji, H. Kato, *Chem Lett* **2002**, 882-883.
- [149] Z. B. Lei, W. S. You, M. Y. Liu, G. H. Zhou, T. Takata, M. Hara, K. Domen, C. Li, *Chem Commun* **2003**, 2142-2143.
- [150] N. Zheng, X. H. Bu, H. Vu, P. Y. Feng, *Angew Chem Int Edit* **2005**, *44*, 5299-5303.
- [151] D. Chen, J. H. Ye, *J Phys Chem Solids* **2007**, *68*, 2317-2320.
- [152] J. J. Ding, S. Sun, W. H. Yan, J. Bao, C. Gao, *Int J Hydrogen Energ* **2013**, *38*, 13153-13158.
- [153] G. Hitoki, A. Ishikawa, T. Takata, J. N. Kondo, M. Hara, K. Domen, *Chem Lett* **2002**, 736-737.
- [154] Y. Lee, K. Nukumizu, T. Watanabe, T. Takata, M. Hara, M. Yoshimura, K. Domen, *Chem Lett* **2006**, *35*, 352-353.
- [155] R. A. Masanobu Higashi, Tsuyoshi Takata and Kazunari Domen, *Chem. Mater.* **2009**, *21*, 1543-1549.
- [156] M. Higashi, K. Domen, R. Abe, *J Am Chem Soc* **2013**, *135*, 10238-10241.
- [157] K. Maeda, M. Higashi, B. Siritanaratkul, R. Abe, K. Domen, *J Am Chem Soc* **2011**, *133*, 12334-12337.
- [158] B. Siritanaratkul, K. Maeda, T. Hisatomi, K. Domen, *Chemosuschem* **2011**, *4*, 74-78.
- [159] F. X. Zhang, A. Yamakata, K. Maeda, Y. Moriya, T. Takata, J. Kubota, K. Teshima, S. Oishi, K. Domen, *J Am Chem Soc* **2012**, *134*, 8348-8351.
- [160] K. Ueda, T. Minegishi, J. Clune, M. Nakabayashi, T. Hisatomi, H. Nishiyama, M. Katayama, N. Shibata, J. Kubota, T. Yamada, K. Domen, *J Am Chem Soc* **2015**, *137*, 2227-2230.
- [161] S. Balaz, S. H. Porter, P. M. Woodward, L. J. Brinson, *Chem Mater* **2013**, *25*, 3337-3343.
- [162] D. R. Liu, Y. S. Jiang, G. M. Gao, *Chemosphere* **2011**, *83*, 1546-1552.
- [163] D. R. Liu, C. D. Wei, B. Xue, X. G. Zhang, Y. S. Jiang, *J Hazard Mater* **2010**, *182*, 50-54.
- [164] A. Houas, H. Lachheb, M. Ksibi, E. Elaloui, C. Guillard, J. M. Herrmann, *Appl Catal B-Environ* **2001**, *31*, 145-157.
- [165] G. R. Xu, J. N. Wang, C. J. Li, *Appl Surf Sci* **2013**, *279*, 103-108.
- [166] T. Cetinkaya, L. Neuwirthova, K. M. Kutlakova, V. Tomasek, H. Akbulut, *Appl Surf Sci* **2013**, *279*, 384-390.
- [167] T. M. Breault, B. M. Bartlett, *J Phys Chem C* **2012**, *116*, 5986-5994.
- [168] W. Yu, X. J. Liu, L. K. Pan, J. L. Li, J. Y. Liu, J. Zhang, P. Li, C. Chen, Z. Sun, *Appl Surf Sci* **2014**, *319*, 107-112.
- [169] A. Charanpahari, S. S. Umare, R. Sasikala, *Catal Commun* **2013**, *40*, 9-12.
- [170] D. Logvinovich, J. Hejtmanek, K. Knizek, M. Marysko, N. Homazava, P. Tomes, R. Aguiar, S. G. Ebbinghaus, A. Reller, A. Weidenkaff, *J Appl Phys* **2009**, *105*, 023522.
- [171] B. J. Ingram, T. O. Mason, *J Electrochem Soc* **2003**, *150*, E396-E402.
- [172] M. I. Bertoni, N. J. Kidner, T. O. Mason, T. A. Albrecht, E. M. Sorensen, K. R. Poepelmeier, *J Electroceram* **2007**, *18*, 189-195.

- [173] G. H. Chan, B. Deng, M. Bertoni, J. R. Ireland, M. C. Hersam, T. O. Mason, R. P. Van Duyne, J. A. Ibers, *Inorg Chem* **2006**, *45*, 8264-8272.
- [174] W. C. Sheets, E. S. Stampler, H. Kabbour, M. I. Bertoni, L. Cario, T. O. Mason, T. J. Marks, K. R. Poeppelmeier, *Inorg Chem* **2007**, *46*, 10741-10748.
- [175] S. Murali, S. Prasertpalichat, C. C. Huang, D. Cann, R. Yimnirun, J. F. Conley, *J Electrochem Soc* **2011**, *158*, G211-G216.
- [176] V. L. Nguyen, C. Zanella, P. Bettotti, G. D. Soraru, *J Am Ceram Soc* **2014**, *97*, 2525-2530.
- [177] P. Curie, *Ann. Chem. Phys.* **1895**, *5*, 289.
- [178] A. R. West, *Basic Solid State Magnetism*, John Wiley and Sons, Chichester, **1999**.
- [179] R. D. Shannon, C. T. Prewitt, *Acta Crystall B-Stru* **1969**, *B 25*, 925-946.
- [180] I. D. Brown, <http://www.iucr.org/data/assets/file/0018/59004/bvparam2011.cif>, **2006**.
- [181] P. Thompson, D. E. Cox, J. B. Hastings, *J Appl Crystallogr* **1987**, *20*, 79-83.
- [182] G. Liu, X. H. Zhao, H. A. Eick, *J Alloy Compd* **1992**, *187*, 145-156.
- [183] W. J. Li, E. Ionescu, R. Riedel, A. Gurlo, *J Mater Chem A* **2013**, *1*, 12239-12245.
- [184] A. Navrotsky, *Phys Chem Miner* **1977**, *2*, 89-104.
- [185] J. M. McHale, G. R. Kowach, A. Navrotsky, F. J. DiSalvo, *Chem-Eur J* **1996**, *2*, 1514-1517.
- [186] A. Navrotsky, *Phys Chem Miner* **1997**, *24*, 222-241.
- [187] A. Navrotsky, *J Alloy Compd* **2001**, *321*, 300-306.
- [188] S. H. Elder, F. J. DiSalvo, L. Topor, A. Navrotsky, *Chem Mater* **1993**, *5*, 1545-1553.
- [189] M. R. Ranade, F. Tessier, A. Navrotsky, V. J. Leppert, S. H. Risbud, F. J. DiSalvo, C. M. Balkas, *J Phys Chem B* **2000**, *104*, 4060-4063.
- [190] M. R. Ranade, F. Tessier, A. Navrotsky, R. Marchand, *J Mater Res* **2001**, *16*, 2824-2831.
- [191] J. J. Liang, A. Navrotsky, V. J. Leppert, M. J. Paskowitz, S. H. Risbud, T. Ludwig, H. J. Seifert, F. Aldinger, M. Mitomo, *J Mater Res* **1999**, *14*, 4630-4636.
- [192] F. Tessier, A. Navrotsky, *Chem Mater* **2000**, *12*, 148-154.
- [193] I. Molodetsky, A. Navrotsky, F. DiSalvo, M. Lerch, *J Mater Res* **2000**, *15*, 2558-2570.
- [194] K. Kamata, T. Nakamura, T. Sata, *Chem Lett* **1975**, 81-86.
- [195] K. Kamata, T. Nakamura, T. Sata, *Mater Res Bull* **1975**, *10*, 373-378.
- [196] Wikipedia, **2014**.
- [197] Z. J. Shen, M. Nygren, *J Mater Chem* **2001**, *11*, 204-207.
- [198] J. Ahchawarattaworn, Ph.D thesis, Newcastle University **2011**.
- [199] N. Kumar, A. Sundaresan, C. N. R. Rao, *Mater Res Bull* **2011**, *46*, 2021-2024.
- [200] J. Mizusaki, M. Yoshihiro, S. Yamauchi, K. Fueki, *J Solid State Chem* **1987**, *67*, 1-8.
- [201] C. Housecroft, A. G. Sharpe, *Inorganic Chemistry*, 4th ed., Pearson Education, Harlow, **2012**.
- [202] S. Banerjee, S. C. Pillai, P. Falaras, K. E. O'Shea, J. A. Byrne, D. D. Dionysiou, *J Phys Chem Lett* **2014**, *5*, 2543-2554.
- [203] J. W. Wang, W. Zhu, Y. Q. Zhang, S. X. Liu, *J Phys Chem C* **2007**, *111*, 1010-1014.
- [204] W. W. Zhang, J. Y. Zhang, Z. Y. Chen, T. M. Wang, *Catal Commun* **2009**, *10*, 1781-1785.
- [205] L. Z. Li, B. Yan, *J Alloy Compd* **2009**, *476*, 624-628.
- [206] L. R. Hou, C. Z. Yuan, Y. Peng, *J Hazard Mater* **2007**, *139*, 310-315.
- [207] K. Maeda, H. Terashima, K. Kase, K. Domen, *Appl Catal a-Gen* **2009**, *357*, 206-212.
- [208] K. Maeda, K. Teramura, N. Saito, Y. Inoue, K. Domen, *J Catal* **2006**, *243*, 303-308.
- [209] Y. G. Lee, K. Teramura, M. Hara, K. Domen, *Chem Mater* **2007**, *19*, 2120-2127.
- [210] T. Hisatomi, K. Hasegawa, K. Teramura, T. Takata, M. Hara, K. Domen, *Chem Lett* **2007**, *36*, 558-559.
- [211] T. Hisatomi, C. Katayama, Y. Moriya, T. Minegishi, M. Katayama, H. Nishiyama, T. Yamada, K. Domen, *Energ Environ Sci* **2013**, *6*, 3595-3599.
- [212] I. P. Shapiro, *Opt Spektrosk* **1958**, *4*, 256-260.
- [213] R. M. X. Gouin, Y. Laurent, F. Gervais, *Solid State Commun* **1995**, *93*, 857-859.
- [214] K. Maeda, D. L. Lu, K. Domen, *Angew Chem Int Edit* **2013**, *52*, 6488-6491.
- [215] K. Kaneko, *J Membrane Sci* **1994**, *96*, 59-89.
- [216] M. Montazerzohori, M. Nasr-Esfahani, S. Joohari, *Environ Prot Eng* **2012**, *38*, 45-55.
- [217] J. M. Herrmann, *Catal Today* **1999**, *53*, 115-129.
- [218] W. J. Li, D. Li, A. Gurlo, J. Shen, R. Riedel, E. Ionescu, *J. Eur. Ceram. Soc.* **2015**, *35*, 3273-3281.
- [219] A. Fuertes, *Materials Horizons* **2015**, DOI: 10.1039/c5mh00046g.



Cumulative publications



Can we predict the formability of perovskite oxynitrides from tolerance and octahedral factors?†

Cite this: *J. Mater. Chem. A*, 2013, **1**, 12239

Wenjie Li,* Emanuel Ionescu, Ralf Riedel and Aleksander Gurlo

Perovskite oxynitrides $AB(O,N)_3$ represent an emerging class of materials suitable for applications in the fields of clean energy and environmental protection. Nitrogen substitution for oxygen allows for a significant enrichment of possible perovskite structures for combinations of cations that are not achievable in perovskite oxides. A model that utilizes the tolerance and octahedral factors is developed for assessing the formability of the perovskite structure in oxynitrides and for predicting new perovskite oxynitrides that have not been synthesized so far. Our model considers the alteration of the interatomic distances and cationic radii in oxynitrides when compared to those in oxides and nitrides. In the first step we identify the stability field of the perovskite structure in oxynitrides from the crystal structure data for perovskite oxynitrides synthesized so far. In the next step we address the formability of the perovskite structure for compositions not studied yet. For instance, we predict that among potentially piezoelectric oxynitrides, $YSiO_2N$ and $YGeO_2N$ are not stable in the perovskite-type structure; $YZrO_2N$ and $YSnO_2N$ are in turn formable, whereas for possible candidate of photocatalytic oxynitrides according to DFT calculations $MgTaO_2N$ is not formable in perovskite structure; $YTiO_2N$, $CdTaO_2N$ and $CdNbO_2N$ appear to be feasible. Moreover, we predict the formability of perovskite structures for Zn^{2+} , Cd^{2+} , Y^{3+} , Hf^{4+} , Fe^{4+} and Sn^{4+} , as well as Pr^{3+} , Nd^{3+} , and Sm^{3+} oxynitrides. As none of these compounds has been yet synthesized, our model can be applied for designing and guiding the synthesis of novel perovskite structures in oxynitrides.

Received 15th January 2013
Accepted 8th August 2013

DOI: 10.1039/c3ta10216e

www.rsc.org/MaterialsA

1 Introduction

1.1 Perovskite oxynitrides

Perovskite oxynitrides $AB(O,N)_3$ (Fig. 1a) are typically synthesized by ammonolysis of oxide precursors and can be formally represented as nitrogen substituted perovskite oxides. A random nitrogen/oxygen distribution is assumed in the oxynitride structure (Fig. 1c), and the possible N/O ordering (Fig. 1b) still remains a matter of debate.^{1–3}

The larger negative charge as well as ionic radius of a nitride anion (N^{3-} , 1.50 Å (ref. 4 and 5)) with respect to an oxide anion (O^{2-} , 1.4 Å) allow for the formation of perovskite compounds with compositions which are not achievable in perovskite oxides (Table 1). However, only a limited number of perovskite oxynitrides have been synthesized so far (Table 2). These new compounds are becoming increasingly relevant for energy conversion and storage.^{1–3,6–12} For instance, the photocatalytic activity in the visible light region has been reported for $BaTaO_2N$, $SrTaO_2N$, $CaTaO_2N$ and $LaTaO_2N$.⁷ $SrBO_2N$ (B = Nb, Ta),¹ $LaNbON_2$, $EuWO_{1.5}N_{1.5}$ (ref. 2) and $BaTaO_2N$ (ref. 3 and 13) are lead-free relaxor-type ferroelectrics.

Fachbereich Material- und Geowissenschaften Technische Universität Darmstadt, 64287 Darmstadt, Germany. E-mail: w.li@materials.tu-darmstadt.de; Fax: +49 (0) 6151 16 6346; Tel: +49 (0) 6151 16 6342

† Electronic supplementary information (ESI) available. See DOI: 10.1039/c3ta10216e

Several theoretical studies suggest a significant improvement of relevant functionalities in new, not yet synthesized compounds. For example, an increased photocatalytic activity is computed for $MgTaO_2N$, $YTiO_2N$ and $CdTaO_2N$.⁷ An enhanced dielectric constant is suggested for $BaTaO_2N$, while a nonlinear optical response is expected for $YSiO_2N$ and $YGeO_2N$.¹⁴ Experimental verification of these theoretical predictions is, however, hindered due to the fact that these compounds are not yet synthesized (see Table 2). Moreover, perovskite oxynitrides are not known for magnesium, group 12 (Zn, Cd), 13 (Al, Ga, In) and

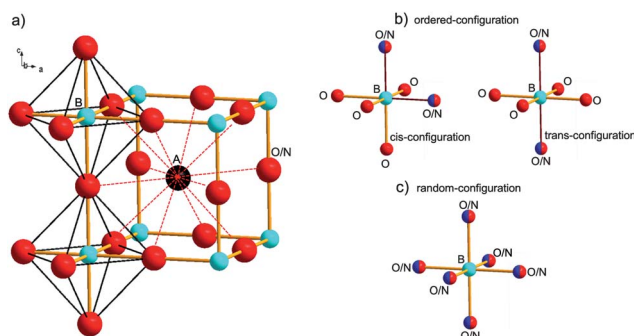


Fig. 1 (a) An undistorted ABX_3 (X = O, N) perovskite structure: a 3D network of corner-shared $[BX_6]$ octahedra incorporates the 12-fold coordinated A-cations. (b and c) Nitrogen atoms can be either randomly distributed or *cis*-/*trans*-ordered forming cross-linked –N–B–N– chains (for details, see ref. 1–3).

Table 1 Possible combinations of cations in stoichiometric perovskite-type oxides, oxynitrides and nitrides

A-site	B-site			
	ABO ₃	ABO ₂ N	ABON ₂	ABN ₃
A ⁺	B ⁵⁺	B ⁶⁺	B ⁷⁺	—
A ²⁺	B ⁴⁺	B ⁵⁺	B ⁶⁺	B ⁷⁺
A ³⁺	B ³⁺	B ⁴⁺	B ⁵⁺	B ⁶⁺
A ⁴⁺	—	B ³⁺	B ⁴⁺	B ⁵⁺
A ⁵⁺	—	—	B ³⁺	B ⁴⁺

Table 2 Perovskite oxynitrides synthesized so far (S). For all these compounds (except for LaVO_{2.1}N_{0.9} and NdWO_{0.8}N_{2.2}) the structure is confirmed and the cation–anion distances d_{A-x} and d_{B-x} are refined from the neutron and X-ray diffraction patterns (see Table S1 in the ESI for the reference list)

Site	A-site							
	Ca ²⁺	Sr ²⁺	Ba ²⁺	Eu ²⁺	La ³⁺	Pr ³⁺	Nd ³⁺	Sm ³⁺
B-site	Ti ⁴⁺				S		S	
	Zr ⁴⁺				S	S	S	S
	V ⁴⁺				S ^{a,b}		S	
	Mo ⁴⁺				S			
	Nb ⁵⁺	S	S	S	S	S ^b	S ^b	
	Ta ⁵⁺	S	S	S	S			
	Mo ⁵⁺	S ^a	S ^a					
	W ⁵⁺	S		S ^a	S ^a		S ^{a,b}	

^a Non-stoichiometric perovskites CaMoO_{1.7}N_{1.3}, SrMo_{2.5}N_{0.5}, EuWO_{1.58}N_{1.42}, LaWO_{0.6}N_{2.4}, LaVO_{2.1}N_{0.9} and NdWO_{0.8}N_{2.2}. ^b Structure is not refined and the cation–anion distances are not reported.

14 (Si, Ge, Sn) elements. The question arises whether this fact is due to instability of the perovskite structure in these compounds or is due to challenges associated with their synthesis. A simple tool that allows for the first assessment of the formability of oxynitrides with a perovskite-type structure will help in selecting suitable compositions for the synthesis.

The formability of perovskite structures in oxides,^{15,16} fluorides¹⁷ and chlorides¹⁸ is usually assessed through the tolerance (Goldschmidt)¹⁹ and octahedral^{16,20} factors. These parameters are applied for generating structure maps that reveal the stability regions of perovskite structures.^{21,22} The tolerance and octahedral factors are calculated either by applying Shannon–Prewitt ionic radii^{4,5} or by using bond-valence parameters.²³ Both approaches enable exploration and screening of possible perovskite structures.^{21,22,24}

In the present work, considering both models, we calculate and apply the octahedral and tolerance factors for predicting the formability of perovskite structures in metal oxynitrides. Our approach consists of three steps. First, we derive expressions for calculating the octahedral and tolerance factors in oxynitrides taking into account the difference in ionic radii and in interatomic distances for nitrogen and oxygen coordinated cations. In the second step we consider already synthesized, perovskite oxynitrides in the form of binary ABO_{3-x}N_x and cation-substituted A_{1-y}A_yB_{1-z}B_zO_{3-x}N_x oxynitrides and identify the region of stability of the perovskite structure in the structure

field maps. And finally, we apply the stability field, identified in the previous step, for predicting the formability of new, not yet synthesized, perovskite oxynitrides. In the following sections we discuss the main results that can guide the future synthesis of oxynitride perovskites not realized so far.

2 Tolerance and octahedral factors for perovskite oxynitrides

The expressions for tolerance and octahedral factors for perovskite oxides cannot be used for the estimation of perovskite structures in anion-substituted compounds due to the following reasons/issues:

(i) An alteration of the (experimental) cation–anion distances in oxynitrides when compared to those in oxides and nitrides; an example is represented in Table 3 for octahedrally coordinated Ta⁵⁺.

(ii) A difference and non-systematic variation in ionic radii for nitrogen and oxygen coordinated cations; an example is represented in Table 4 for the B-site cations in perovskites from Table 2.

To consider these issues, we derive new expressions for calculating tolerance and octahedral factors in perovskite oxynitrides from (i) the experimental cation–anion distances, (ii) ionic radii and (iii) bond-valence parameters. For proper consideration of a significant variation of corresponding parameters in disordered structures^{25,26} like oxynitrides, a geometric averaging of the cation–anion distances, bond-valence parameters and ionic radii is applied.

All three approaches have their specific advantages and limitations as discussed below. Despite these limitations, we inspect all three approaches for (i) confirming the clustering of perovskite oxynitrides and for (ii) verifying the stability fields of perovskite oxynitrides in structure maps.

2.1 Calculation from the experimental cation–anion distances

We consider the cation–anion distances in the perovskite oxynitrides which are confirmed in the structural refinement of

Table 3 Ta–O/N distances for 6-fold coordinated Ta⁵⁺ in perovskite oxynitride (SrTaO₂N), perovskite oxide (NaTaO₃) and nitride (Ta₃N₅)

SrTaO ₂ N		NaTaO ₃	Ta ₃ N ₅
Random ²⁵	Ordered ²⁶	$d_{Ta-O}^{27}/\text{Å}$	$d_{Ta-N}/\text{Å}$
2.0165 (O/N) [2] ^a	2.012 (N) [2] ^a	1.96 ^b	2.086 ^b
2.0184 (O/N) [4] ^a	2.025 (O) [4] ^a		2.091 ^b

^a Number of bonds. ^b Average distance.

Table 4 Ionic radii for oxygen/nitrogen 6-fold coordinated B-site cations for perovskites listed in Table 2

Anion	Ti ⁴⁺	Zr ⁴⁺	Mo ⁴⁺	Ta ⁵⁺
O ²⁻ (Å)	0.47	0.78	0.64	0.64
N ³⁻ (Å)	0.42	0.72	0.65	0.64

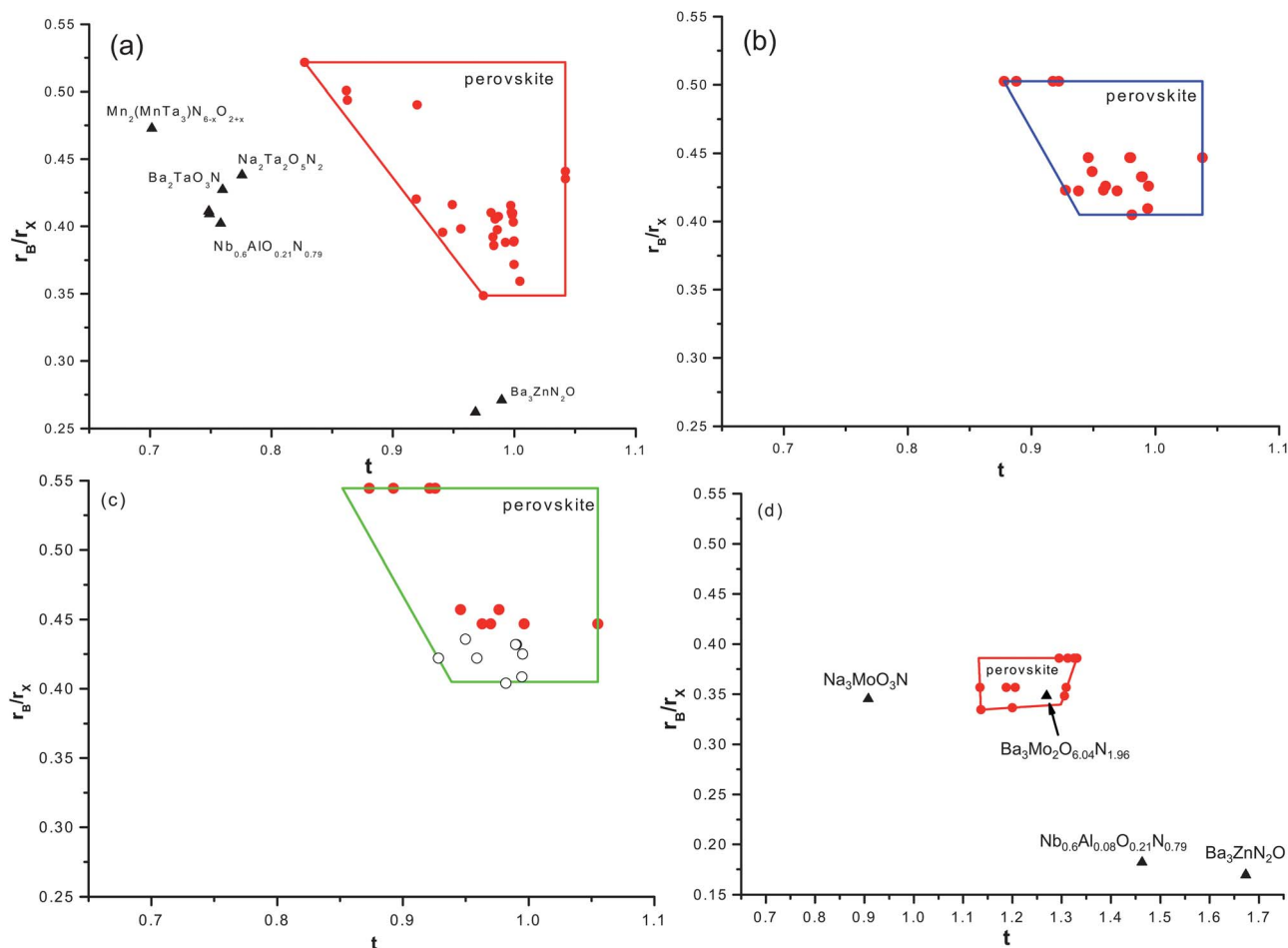


Fig. 2 Structure field maps for oxynitrides showing the octahedral versus tolerance parameter calculated from (a) the average cation–anion distances (Table 6), (b) ionic radii (Table 7) and (d) the bond-valence parameters (Table 8). Shannon–Previtt^{4,5} cationic radii in oxides are applied in (b); Baur cationic radii in nitrides³² are applied in (c); the bond-valence parameters²⁸ are applied in (d). In (c) the black squares refer to the perovskites for which Baur's radii are not available; in the calculation we applied Shannon–Previtt^{4,5} cationic radii in oxides.

experimental diffraction patterns. We express the tolerance factor t_D and the octahedral factor $(r_B/r_X)_D$ for perovskite oxynitrides as:

$$t_D = \frac{d_{A-X}^g}{\sqrt{2}d_{B-X}^g} \quad (1)$$

$$(r_B/r_X)_D = \frac{d_{B-X}^g - r_X}{r_X^g} \quad (2)$$

where X refers to the anion, *i.e.* oxide or nitride, with the radius r_O (1.4 Å) and r_N (1.5 Å), respectively. d_{A-X}^g and d_{B-X}^g are the geometric average of the cation–anion distances, d_{A-X} and d_{B-X} , respectively, calculated according to eqn (3); r_X^g is the geometric average of the anionic radii calculated according to eqn (4):

$$d_{A(B)-X}^g = \left[\prod_{i=1}^{CN} (d_{A(B)-X}) \right]^{1/CN} \quad (3)$$

$$r_X^g = \left[\prod_{i=1}^{CN} (r_X) \right]^{1/CN} \quad (4)$$

In the eqn (3) and (4) CN is the coordination number, *i.e.* 12 and 6 for A-site and B-site cations and 6 for an anion X in ABX₃ perovskite, respectively.

We consider disordered perovskite oxynitrides with a random nitrogen distribution (see Fig. 1 c). Since nitrogen and oxygen atoms are not distinguished in such structures, the average cation–anion distances $d_{A-O/N}$ and $d_{B-O/N}$ for A- and

Table 5 The stability field of the perovskite structure in oxynitrides

Calculation from	Compounds	Tolerance factor	Octahedral factor
Interatomic distances	Oxynitrides ^a	0.827–1.042	0.359–0.5217
Ionic radii	Oxides ^{20,22,29}	0.74–1.00	0.414–0.732
	Oxynitrides ^{a,b}	0.87794–1.03807	0.40487–0.50259
	Oxynitrides ^{a,c}	0.8733–1.05512	0.40487–0.54448
Bond-valence parameters	Oxides ²¹	0.822–1.139	Not calculated
	Oxynitrides ^a	1.136–1.331	0.334–0.386

^a This work. ^b Shannon–Previtt ionic radii for oxides. ^c Baur ionic radii for nitrides.

Table 6 The tolerance and octahedral factors calculated for perovskite oxynitrides in the ionic radii model (see text for details)

Perovskite	Tolerance factor t_D	Octahedral factor $(r_B/r_X)_D$
ABO ₃	$\frac{d_{A-O}}{\sqrt{2}d_{B-O}}$	$\frac{d_{B-O} - r_O}{r_O}$
ABO ₂ N	$\frac{\left[\prod_{i=1}^{12}(d_{A-O/N})\right]^{1/12}}{\sqrt{2}\left[\prod_{i=1}^6(d_{B-O/N})\right]^{1/6}}$	$\frac{\left[\prod_{i=1}^6(d_{B-O/N})\right]^{1/6} - (r_O^4 \times r_N^2)^{1/6}}{(r_O^4 \times r_N^2)^{1/6}}$
ABON ₂	$\frac{\left[\prod_{i=1}^{12}(d_{A-O/N})\right]^{1/12}}{\sqrt{2}\left[\prod_{i=1}^6(d_{B-O/N})\right]^{1/6}}$	$\frac{\left[\prod_{i=1}^6(d_{B-O/N})\right]^{1/6} - (r_O^2 \times r_N^4)^{1/6}}{(r_O^2 \times r_N^4)^{1/6}}$
ABN ₃	$\frac{d_{A-N}}{\sqrt{2}d_{B-N}}$	$\frac{d_{B-N} - r_N}{r_N}$

Table 7 The tolerance and octahedral factors calculated for perovskite oxynitrides in the ionic radii approximation

Perovskite	Tolerance factor	Octahedral factor
ABO ₃	$\frac{r_A + r_O}{\sqrt{2}(r_B + r_O)}$	r_B/r_O
ABO ₂ N	$\frac{[(r_A + r_O)^8(r_A + r_N)^4]^{1/12}}{\sqrt{2}[(r_B + r_O)^4(r_B + r_N)^2]^{1/6}}$	$r_B/(r_O^4 \times r_N^2)^{1/6}$
ABON ₂	$\frac{[(r_A + r_O)^4(r_A + r_N)^8]^{1/12}}{\sqrt{2}[(r_B + r_O)^2(r_B + r_N)^4]^{1/6}}$	$r_B/(r_O^2 \times r_N^4)^{1/6}$
ABN ₃	$\frac{r_A + r_N}{\sqrt{2}(r_B + r_N)}$	r_B/r_N

B-cations are reported in the experimental work. An example for SrTa⁵⁺O₂N is given in Table 3. In our calculation we use the geometric average as recommended for disordered structures.³⁰ Nevertheless, the difference between the arithmetic and geometric average is negligibly small (see Table S3†) indicating that both approaches can be used.

Table 6 provides the expressions used for calculation of the tolerance t_D and octahedral $(r_B/r_X)_D$ factors for ABO₃, ABO₂N, ABON₂ and ABN₃ perovskites. The numerical values are listed in Table S1 in the ESI.†

2.2 Calculation from the ionic radii

We consider the ionic radii model as the second approach. The tolerance factor t_{IR} and the octahedral factor $(r_B/r_X)_{IR}$ were expressed for perovskite oxynitrides as:

$$t_{IR} = \frac{r_A + r_X^g}{\sqrt{2}(r_B + r_X^g)} \quad (5)$$

$$(r_B/r_X)_{IR} = \frac{r_B}{r_X^g} \quad (6)$$

where X refers to the anion, r_X^g is the geometric average of the anionic radii calculated according to eqn (4), as same as that mentioned in Section 2.1; r_A and r_B are the cationic radii.

Table 7 displays the expressions used for calculating the tolerance t_{IR} and octahedral $(r_B/r_X)_{IR}$ factors for ABO₃, ABO₂N, ABON₂ and ABN₃ perovskites. The tolerance and octahedral factors calculated in this way are listed in Tables S1 and S4 in the ESI.†

3 Structure field maps

The tolerance and octahedral factors calculated in approaches of Sections 2.1 and 2.2 as described above are listed in Table S1 in the ESI† and used for the delineation of structure field maps which are shown in Fig. 2. The main result is that in all (four) cases we observe clustering of perovskite structures from which the structure field of the perovskite structure is delineated (Table 5).²⁸ This is an important finding showing that all approaches identify the same trends in the perovskite structure stability allowing in this way the search for new, unknown, perovskite oxynitrides that have not been synthesized yet.

For the prediction (see Section 4) we apply the ionic radii approach considering the Shannon–Prewitt ionic radii in oxides.^{4,5} This is due to some limitations of other approaches as discussed above.

The first issue is an increase in the covalency of metal–oxygen(nitrogen) bonds after nitrogen incorporation due to the lower electronegativity of nitrogen (3.04) compared to that of oxygen (3.44). Hence the experimental interatomic distances are shorter than those estimated from the sum of cationic and anionic radii. For instance, ionic-radii estimation for 6-fold coordinated Ta⁵⁺ gives 2.14 and 2.04 Å for Ta⁵⁺–N³⁻ and

Table 8 The tolerance and octahedral factors calculated for perovskite oxynitrides in the bond-valence model (see text for details)

Perovskite	Tolerance factor	Octahedral factor
ABO ₃	$\frac{d_{0(A-O)} - B \ln(V_A/CN_A)}{\sqrt{2}[d_{0(B-O)} - B \ln(V_B/CN_B)]}$	$\frac{d_{0(B-O)} - r_O}{r_O}$
ABO ₂ N	$\frac{[(d_{0(A-O)})^8(d_{0(A-N)})^4]^{1/12} - B \ln(V_A/CN_A)}{\sqrt{2}[(d_{0(B-O)})^4(d_{0(B-N)})^2]^{1/6} - B \ln(V_B/CN_B)}$	$\frac{[(d_{0(B-O)})^4(d_{0(B-N)})^2]^{1/6} - (r_O^4 \times r_N^2)^{1/6}}{(r_O^4 \times r_N^2)^{1/6}}$
ABON ₂	$\frac{[(d_{0(A-O)})^4(d_{0(A-N)})^8]^{1/12} - B \ln(V_A/CN_A)}{\sqrt{2}[(d_{0(B-O)})^2(d_{0(B-N)})^4]^{1/6} - B \ln(V_B/CN_B)}$	$\frac{[(d_{0(B-O)})^2(d_{0(B-N)})^4]^{1/6} - (r_O^2 \times r_N^4)^{1/6}}{(r_O^2 \times r_N^4)^{1/6}}$
ABN ₃	$\frac{d_{0(A-N)} - B \ln(V_A/CN_A)}{\sqrt{2}[d_{0(B-N)} - B \ln(V_B/CN_B)]}$	$\frac{d_{0(B-O)} - r_N}{r_N}$

Ta⁵⁺–O²⁻ distances that are significantly larger than the experimental values of 2.09 and 1.96 Å, respectively. As a result, for new, not yet synthesized compounds, the cation–anion distances cannot be calculated from the ionic radii and the structure field map delineated from the experimental cation–anion distances (Fig. 2a) cannot be applied for estimating the formability of perovskite structures in new compounds.

The applicability of the bond-valence model as well as the substitution scheme oxygen-for-nitrogen is limited and leads to poor prediction because the bond-valence parameters (d_0 , B) as well as the ionic radii in nitrides are tabulated for a limited number of cations.^{31,32} Furthermore, a similarity in the cationic radii in nitrides (*i.e.* Baur radii³¹) and oxides (*i.e.* Shannon–Prewitt radii^{4,5}) results in the almost identical structure field maps (compare Fig. 2b and c). The stability field of perovskite structures derived from bond-valence parameters (Fig. 2d) differs significantly from that determined for oxynitrides from interatomic distances/ionic radii (compare to Fig. 2a–c and Table 5), most probably, this difference is due to the limited datasets used for the delineation of the structure field map. Similar to oxides, the tolerance factors calculated from the bond-valence parameters are shifted to larger values if compared to those calculated from ionic radii. Remarkably, the tolerance factors are now larger than unity similar to oxide perovskites with B-cations in higher oxidations states (*i.e.* A²⁺B⁴⁺O₃ and A¹⁺B⁵⁺O₃, Zhang, 2007 (ref. 21)). This issue requires further, more careful examination, which is beyond the scope of the present work.

Therefore, in the following we will continue with the approach based on ionic radii in oxides.

4 Predicting new, not yet synthesized, perovskite oxynitrides

As stressed above, we follow the approach based on ionic radii in oxides. The stability field of the perovskite structure is delineated according to the parameters taken from Table 5. The main conclusion of our calculation is the identification of several oxynitrides that may exist in the perovskite structure and have not been synthesized so far. These compounds are marked as “P” in Table 9. Now we discuss the formability of perovskite oxynitrides that are computed to exhibit promising functionalities but have not been synthesized so far. Among the potentially piezoelectric oxynitrides, YSiO₂N and YGeO₂N are not stable in the perovskite-type structure; YZrO₂N and YSnO₂N are in turn formable, whereas for a possible candidate of photocatalytic oxynitrides MgTaO₂N is not formable; YTiO₂N, CdTaO₂N and CdNbO₂N appear to be feasible. Interestingly, Zn²⁺, Cd²⁺, Y³⁺, Hf⁴⁺, Fe⁴⁺ and Sn⁴⁺, as well as Pr³⁺, Nd³⁺, and Sm³⁺ should form a number of oxynitrides with a perovskite structure (Fig. 3). However, none of these compounds has been synthesized yet.

5 Conclusions

In summary, we have presented a model that utilizes the tolerance and octahedral factors for assessing the formability of oxynitrides crystallizing in the perovskite-type structure. These factors are used for drawing structure field maps that allow the prediction of new perovskite oxynitrides possessing intriguing

Table 9 The formability of perovskite oxynitrides for ABO₂N (A¹⁺–B⁶⁺, A²⁺–B⁵⁺ and A³⁺–B⁴⁺) and ABON₂ (A²⁺–B⁶⁺ and A³⁺–B⁵⁺) compositions^a

Site	A-site																	
	Li ⁺	Na ⁺	K ⁺	Mg ²⁺	Ca ²⁺	Sr ²⁺	Ba ²⁺	Zn ²⁺	Cd ²⁺	Eu ²⁺	Sc ³⁺	Y ³⁺	Ga ³⁺	In ³⁺	La ³⁺	Pr ³⁺	Nd ³⁺	Sm ³⁺
B-site	Si ⁴⁺										N	N	N	N	N	N	N	N
	Ge ⁴⁺										N	N	N	N	N	N	N	N
	Sn ⁴⁺										N	P	N	N	P	P	P	N
	Ti ⁴⁺										N	P	N	N	S/P	P	S/P	N
	Zr ⁴⁺										N	P	N	N	S/P	S/P	S/P	S/P
	Hf ⁴⁺										N	P	N	N	P	P	P	N
	Mn ⁴⁺										N	N	N	N	N	N	N	N
	Fe ⁴⁺										N	P	N	N	P	P	P	P
	Co ⁴⁺										N	N	N	N	N	N	N	N
	V ⁴⁺										N	P	N	N	S ^b /P	P	S/P	P
	Nb ⁴⁺										N	P	N	N	P	P	P	N
	Ta ⁴⁺										N	P	N	N	P	P	P	N
	Mo ⁴⁺										N	P	N	N	P	P	P	N
	W ⁴⁺										N	P	N	N	P	P	P	N
	V ⁵⁺				N	N	N	N	N	N	N	N	N	N	N	N	N	N
	Nb ⁵⁺				N	S/P	S/P	S/P	N	P	S/P	N	N	N	S/P	S/P	N	N
	Ta ⁵⁺				N	S/P	S/P	S/P	N	P	S/P	N	N	N	S/P	P	N	N
	Mo ⁵⁺				N	S ^b /P	S ^b /P	N	N	P	P	N	N	N	P	P	P	N
	W ⁵⁺				N	P	S/P	N	N	P	S ^b /P	N	N	N	S ^b /P	P	S ^b /P	N
	Mo ⁶⁺	P	P	N	N	N	N	N	N	N								
	W ⁶⁺	P	P	N	N	P	P	N	N	P	P							

^a S – perovskite oxynitrides synthesized so far, P – perovskite oxynitrides predicted in our model, N – perovskite structure is not stable. ^b Non-stoichiometric perovskites CaMoO_{1.7}N_{1.3}, SrMo_{2.5}N_{0.5}, EuWO_{1.58}N_{1.42}, LaWO_{0.6}N_{2.4}, LaVO_{2.1}N_{0.9} and NdWO_{0.8}N_{2.2}.

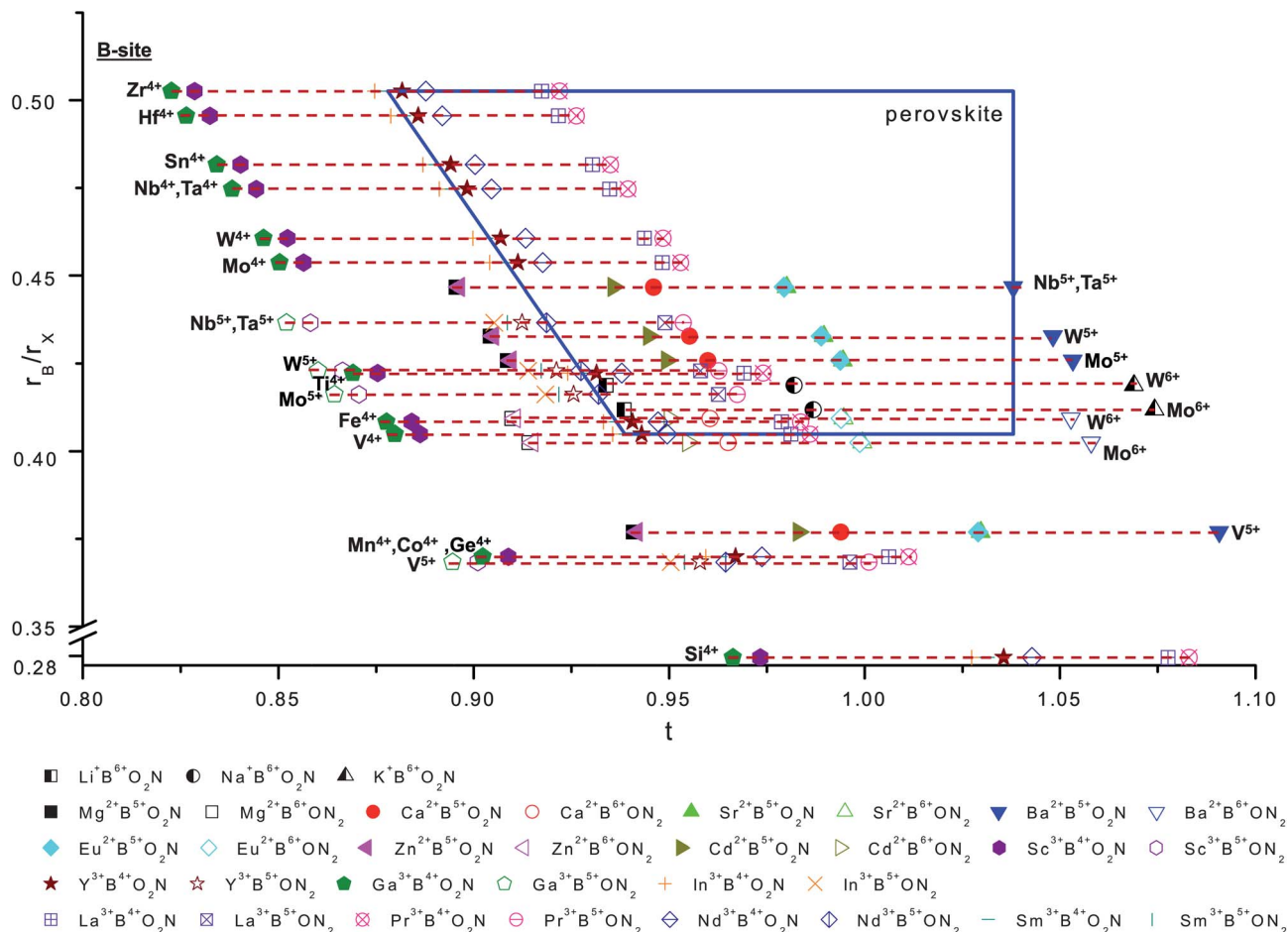


Fig. 3 Structure field map for perovskite oxynitrides showing the octahedral versus tolerance parameter calculated according to Table 7 by applying the Shannon-Prewitt radii.^{4,5}

structural and functional properties, which have not been synthesized so far.

Acknowledgements

This research has been funded by the European Union Seventh Framework Programme (FP7/2007–2013) under the grant agreement FUNEA-Functional Nitrides for Energy Applications.

Notes and references

- M. H. Yang, J. Oro-Sole, J. A. Rodgers, A. B. Jorge, A. Fuertes and J. P. Attfield, *Nat. Chem.*, 2011, **3**, 47–52.
- P. J. Camp, A. Fuertes and J. P. Attfield, *J. Am. Chem. Soc.*, 2012, **134**, 6762–6766.
- Y. Hinuma, H. Moriwake, Y.-R. Zhang, T. Motohashi, S. Kikkawa and I. Tanaka, *Chem. Mater.*, 2012, **24**, 4343–4349.
- R. D. Shannon, *Acta Crystallogr., Sect. A: Cryst. Phys., Diffr., Theor. Gen. Crystallogr.*, 1976, **32**, 751–767.
- R. D. Shannon and C. T. Prewitt, *Acta Crystallogr., Sect. B: Struct. Crystallogr. Cryst. Chem.*, 1969, **25**, 925–946.
- A. Fuertes, *J. Mater. Chem.*, 2012, **22**, 3293–3299.
- I. E. Castelli, T. Olsen, S. Datta, D. D. Landis, S. Dahl, K. S. Thygesen and K. W. Jacobsen, *Energy Environ. Sci.*, 2012, **5**, 5814–5819.
- R. Caracas and R. E. Cohen, *Appl. Phys. Lett.*, 2007, **91**, 092902.
- Y. I. Kim, P. M. Woodward, K. Z. Baba-Kishi and C. W. Tai, *Chem. Mater.*, 2004, **16**, 1267–1276.
- S. G. Ebbinghaus, H. P. Abicht, R. Dronskowski, T. Müller, A. Reller and A. Weidenkaff, *Prog. Solid State Chem.*, 2009, **37**, 173–205.
- R. Marchand, F. Tessier, A. Le Sauze and N. Diot, *Int. J. Inorg. Mater.*, 2001, **3**, 1143–1146.
- B. Siritanaratkul, K. Maeda, T. Hisatomi and K. Domen, *ChemSusChem*, 2011, **4**, 74–78.
- R. L. Withers, Y. Liu, P. Woodward and Y. I. Kim, *Appl. Phys. Lett.*, 2008, **92**, 102907.
- R. Caracas and R. E. Cohen, *Appl. Phys. Lett.*, 2007, **91**, 092902.
- H. Mullerbu and C. Teske, *Z. Anorg. Allg. Chem.*, 1969, **369**, 249–254.
- Z. L. Wang and Z. C. Kang, *Functional and smart materials structural evolution and structure analysis*, Plenum Press, New York, 1998.

- 17 D. Babel, *Z. Anorg. Allg. Chem.*, 1969, **369**, 117.
- 18 H. F. McMurdie, J. D. Groot, M. Morris and H. E. Swanson, *J. Res. Natl. Bur. Stand., Sect. A*, 1969, **73**, 621–626.
- 19 V. M. Goldschmidt, *Skrifter Norske Videnskaps-Akad, I. Mat. Naturv.*, Oslo, 1926.
- 20 R. C. Buchanan, *Materials Crystal Chemistry*, Marcel Dekker, New York, 1997.
- 21 H. Zhang, N. Li, K. Li and D. F. Xue, *Acta Crystallogr., Sect. B: Struct. Sci.*, 2007, **63**, 812–818.
- 22 C. H. Li, K. C. K. Soh and P. Wu, *J. Alloys Compd.*, 2004, **372**, 40–48.
- 23 N. E. Brese and M. Okeeffe, *Acta Crystallogr., Sect. B: Struct. Sci.*, 1991, **47**, 192–197.
- 24 I. D. Brown, *Chem. Rev.*, 2009, **109**, 6858–6919.
- 25 S. J. Clarke, K. A. Hardstone, C. W. Michie and M. J. Rosseinsky, *Chem. Mater.*, 2002, **14**, 2664–2669.
- 26 E. Günther, R. Hagenmayer and M. Jansen, *Z. Anorg. Allg. Chem.*, 2000, **626**, 1519–1525.
- 27 M. Ahtee and L. Unonius, *Acta Crystallogr., Sect. A: Cryst. Phys., Diffr., Theor. Gen. Crystallogr.*, 1977, **33**, 150–154.
- 28 In addition to that we observe a trend in clustering of compounds with similar crystal symmetry (see Fig. S1 in the ESI†). However, the limited experiment data do not allow for drawing a conclusion.
- 29 G. S. Roher, *Structure and Bonding in Crystalline Materials*, Cambridge University Press, New York, 2001.
- 30 B. Dabrowski, O. Chmaissem, J. Mais, S. Kolesnik, J. D. Jorgensen and S. Short, *J. Solid State Chem.*, 2003, **170**, 154–164.
- 31 W. H. Baur, *Crystallogr. Rev.*, 1987, **1**, 59–83.
- 32 I. D. Brown, http://www.iucr.org/__data/assets/file/0018/59004/bvparam2011.cif, 2006.

Supplementary material

Can we predict the formability of perovskite oxynitrides from tolerance and octahedral factors?

Wenjie Li, Emanuel Ionescu, Ralf Riedel and Aleksander Gurlo

Fachbereich Material- und Geowissenschaften, Technische Universität Darmstadt, 64287 Darmstadt, Germany. E-mail: W.Li@materials.tu-darmstadt.de, Fax: +49(0)6151-16-6346, Tel: +49(0)6151-16-75318

Structure field map

Table S 1. Tolerance and octahedral factors of perovskite oxynitrides synthesized so far. The tolerance and octahedral factors are calculated according to the eqs. 1 and 2 and Table 3 (see main text).

Material/Ref	Structure	Parameters calculated from interatomic distance ^a		Ref	Parameters calculated from ionic radii for oxides ^b	
		Tolerance factor	Octahedral factor		Tolerance factor	Octahedral factor
SrWO ₂ N	<i>Pm-3m</i>	0.9998	0.3891	1	0.989616	0.432789
SrMoO _{2.5} N _{0.5}	<i>Pm-3m</i>	0.9996	0.3884	2	0.994462	0.425808
BaTaO ₂ N	<i>Pm-3m</i>	1.0420	0.4354	3	1.038066	0.446750
BaNbO ₂ N	<i>Pm-3m</i>	1.0420	0.4409	4	1.038066	0.446750
EuNbO ₂ N	<i>Pm-3m</i>	0.9870	0.4073	5	0.979383	0.44674963
EuTaO ₂ N	<i>Pm-3m</i>	0.9991	0.4031	6	0.979383	0.44674963
EuWO _{1.58} N _{1.42}	<i>Pm-3m</i>	0.9998	0.3718	7	0.988927	0.4327887
LaNbON ₂	<i>Pnma</i>	0.9842	0.4054	8	0.948883	0.436593
CaTaO ₂ N	<i>Pnma</i>	0.9490	0.4161	9	0.945947	0.446750
	<i>Pnma</i>	0.9808	0.4100	6		
NdTiO ₂ N	<i>Pnma</i>	0.9410	0.3955	10	0.937905	0.422318
LaZrO ₂ N	<i>Pnma</i>	0.9200	0.4903	9	0.917357	0.502593
SrNbO ₂ N	<i>Pnma</i>	0.9969	0.4155	11	0.980065	0.446750
PrZrO ₂ N	<i>Pmna</i>	0.8618	0.5008	2	0.921956	0.502593
NdZrO ₂ N	<i>Pmna</i>	0.8625	0.4938	12	0.887791	0.502593
SmZrO ₂ N	<i>Pmna</i>	0.8272	0.5217	12	0.877936	0.50259333
CaMoO _{1.7} N _{1.3}	<i>Pbnm</i>	0.9823	0.3921	13	0.959842	0.425808
NdVO ₂ N ^{*1}	<i>Pbnm</i>	0.9745	0.3486	14	0.949557	0.40486685
CaNbO ₂ N	<i>I4/mcm</i>	0.9191	0.4203	15	0.945947	0.446750
SrTaO ₂ N	<i>I4/mcm</i>	0.9986	0.4098	16	0.980065	0.446750
		0.9982	0.4085	17		
		0.9973	0.4105	9		
LaWO _{0.6} N _{2.4}	<i>I-4</i>	1.0046	0.3593	18	0.957983	0.422949
LaTiO ₂ N	<i>Imma</i>	0.9860	0.3974	10	0.969139	0.422318
LaTaON ₂	<i>C2/m</i>	0.9560	0.3982	16	0.948883	0.436593
LaVO _{2.1} N _{0.9} ^{*2}	-	-	-	19	0.981180	0.404867
NdWO _{0.8} N _{2.2} ^{*2}	-	-	-	20	0.927472	0.42294916
NdNbON ₂ ^{*2}	<i>Pnma</i>	-	-	21	0.918663	0.43659269
PrNbON ₂ ^{*2}	<i>Pnma</i>	-	-	21	0.953584	0.436593

*1: structure refinement is performed; the cation-anion distances d_{A-X} is not available

*2: structure refinement is not performed; the cation-anion distances d_{A-X} and d_{B-X} are not available

^a: calculated based on average cation-anion distances from refinement results of neutron diffraction (see main text Table 5 and 8)

^b: calculated based on ionic radii for oxides (see main text Table 6 and 8)

Table S 2. Tolerance and octahedral factors of non-perovskite oxynitrides. The tolerance and octahedral factors are calculated according to the eqs. 1 and 2 and Table 3(see main text).

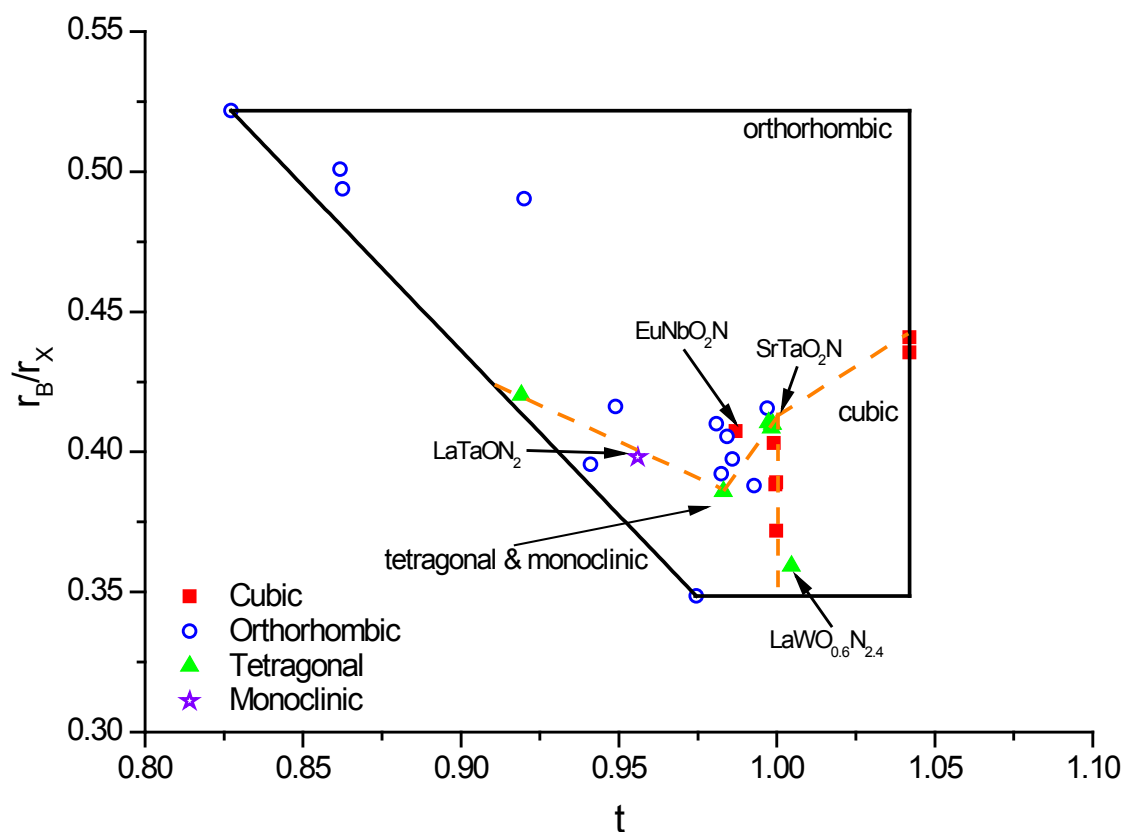
Material/Ref	Structure Space Group	Parameters under room temperature		Ref
		Tolerance factor	Octahedral factor	
Mn ₂ (MnTa ₃)N _{6-x} O _{2+x}	Spinel <i>Fd3m</i>	0.7015	0.4728	22
NdWO _{3.05} N _{0.95}	Scheelite <i>I41/a</i>	0.9679	0.2621	7
KOsO ₃ N	Scheelite <i>I41/a</i>	1.1641	0.2020	23
RbOsO ₃ N	Scheelite <i>I41/a</i>	1.7936	0.1921	24
Sr ₂ TaO ₃ N	K ₂ NiF ₄ <i>I4/mmm</i>	0.7489	0.4090	25, 26
Ba ₂ TaO ₃ N	K ₂ NiF ₄ <i>I4/mmm</i>	0.7598	0.4272	13, 27
Sr ₂ NbO _{2.8} N	K ₂ NiF ₄ <i>I4/mmm</i>	0.7484	0.4112	28
Nb _{0.6} Al _{0.08} O _{0.21} N _{0.79}	Rock-salt <i>I4/m</i>	0.7581	0.4020	29
Nd ₂ Ta ₂ O ₅ N ₂	Pyrochlore	0.7757	0.4380	30
Na ₃ WO ₃ N	Others <i>Pmn21</i>	0.8457	0.0332	31
Na ₃ MoO ₃ N	Others <i>Pmn21</i>	0.8404	0.0379	32
Ba ₃ ZnN ₂ O	Others <i>P4/mmm</i>	0.9897	0.2709	33
Ba ₃ W ₂ O _{6.27} N _{1.73}	Others <i>R-3m</i>	3.6632	0.0325	34
Ba ₃ Mo ₂ O _{6.04} N _{1.96}	Others <i>R-3m</i>	3.6589	0.0255	32
Ba ₂ VO ₃ N	Others <i>Pnma</i>	1.0354	0.2076	25

Table S 3 The bond distance A-X, B-X, tolerance and octahedral factors based on geometric and arithmetic means

Composition		LaNbON ₂	CaTaO ₂ N	SrTaO ₂ N	LaTiO ₂ N	CaMoO _{1.7} N _{1.3}	LaWO _{0.6} N _{2.4}	CaNbO ₂ N	SrNbO ₂ N	NdVO ₂ N	
Experimental data by Neutron diffraction	Geometric mean	A-X	2.8677	2.802	2.8523	2.7915	2.7707	2.8311	2.6446	2.8591	2.7245
		B-X	2.0602	2.02	2.0197	2.002	1.9943	1.9927	2.0346	2.0278	1.9769
		t	0.9842	0.9809	0.9986	0.986	0.9824	1.0046	0.9191	0.9970	0.9745
		O _t	0.4054	0.4100	0.4098	0.3974	0.3921	0.3593	0.4203	0.4155	0.3486
	Arithmetic mean	A-X	2.8798	2.8167	2.8533	2.7991	2.7862	2.834	2.6556	2.8615	2.7373
		B-X	2.0602	2.02	2.0197	2.002	1.9943	1.9927	2.0347	2.0278	1.977
		t	0.9886	0.9861	0.9991	0.9888	0.9880	1.0058	0.9230	0.9980	0.9792
		O _t	0.4054	0.4100	0.4098	0.3975	0.3921	0.3594	0.4203	0.4154	0.3800
Prediction by ionic radii	Geometric mean	A-X	2.8263	2.7729	2.8729	2.7929	2.7729	2.8263	2.7729	2.8729	2.7029
		B-X	2.1061	2.0728	2.0728	2.0378	2.0428	2.0861	2.0728	2.0728	2.0128
	Arithmetic mean	A-X	2.8267	2.7733	2.8733	2.7933	2.7733	2.8267	2.7733	2.8733	2.7033
		B-X	2.1067	2.0733	2.0733	2.0383	2.0433	2.0867	2.0733	2.0733	2.0133

t: tolerance factor; O_t: Octahedral factor

Figure S1. Location of perovskite oxynitrides with different crystal symmetry in the structure field map from Figure 2.



Prediction

Table S 4. Combination of A and B cations in $\text{AB}(\text{O},\text{N})_3$ perovskites applied for the calculation of the tolerance and octahedral factors listed in the Table S4 and displayed in the Figure 3.

$\text{AB}(\text{O},\text{N})_3$ perovskites	A-site	B-site
$\text{A}^+\text{B}^{6+}\text{O}_2\text{N}$	$\text{Li}^+, \text{Na}^+, \text{K}^+$	$\text{Mo}^{6+}, \text{W}^{6+}$
$\text{A}^{2+}\text{B}^{5+}\text{O}_2\text{N}$	$\text{Mg}^{2+}, \text{Ca}^{2+}, \text{Sr}^{2+}, \text{Ba}^{2+}, \text{Zn}^{2+}, \text{Cd}^{2+}, \text{Eu}^{2+}$	$\text{V}^{5+}, \text{Nb}^{5+}, \text{Ta}^{5+}, \text{Mo}^{5+}, \text{W}^{5+}$
$\text{A}^{2+}\text{B}^{6+}\text{ON}_2$	$\text{Mg}^{2+}, \text{Ca}^{2+}, \text{Sr}^{2+}, \text{Ba}^{2+}, \text{Zn}^{2+}, \text{Cd}^{2+}, \text{Eu}^{2+}$	$\text{Mo}^{6+}, \text{W}^{6+}$
$\text{A}^{3+}\text{B}^{4+}\text{O}_2\text{N}$	$\text{Sc}^{3+}, \text{Y}^{3+}, \text{Ga}^{3+}, \text{In}^{3+}, \text{La}^{3+}, \text{Pr}^{3+}, \text{Nd}^{3+}, \text{Sm}^{3+}$	$\text{Si}^{4+}, \text{Ge}^{4+}, \text{Sn}^{4+}, \text{Ti}^{4+}, \text{Zr}^{4+}, \text{Hf}^{4+}, \text{Mn}^{4+}, \text{Fe}^{4+}, \text{Co}^{4+}, \text{V}^{4+}, \text{Nb}^{4+}, \text{Ta}^{4+}, \text{Mo}^{4+}, \text{W}^{4+}$
$\text{A}^{3+}\text{B}^{5+}\text{ON}_2$	$\text{Sc}^{3+}, \text{Y}^{3+}, \text{Ga}^{3+}, \text{In}^{3+}, \text{La}^{3+}, \text{Pr}^{3+}, \text{Nd}^{3+}, \text{Sm}^{3+}$	$\text{V}^{5+}, \text{Nb}^{5+}, \text{Ta}^{5+}, \text{Mo}^{5+}, \text{W}^{5+}$

Table S 5. Tolerance and octahedral factors of metal oxynitrides calculated according to the Table 6 (see main text). These factors are applied in the Figure 3 (see main text). “S” refers for perovskite oxynitrides synthesized so far, “P” stays for the perovskite oxynitrides predicted in our model, N - for perovskite structure is not stable, non-stoichiometric perovskite

Compounds	t	r _B /r _X	Formability
ABO₂N A¹⁺B⁶⁺			
LiMoO ₂ N	0.938464	0.41184731	P
LiWO ₂ N	0.933846	0.41882777	P
NaMoO ₂ N	0.986816	0.41184731	P
NaWO ₂ N	0.98196	0.41882777	P
KMoO ₂ N	1.07422	0.41184731	N
KWO ₂ N	1.068934	0.41882777	N
A²⁺B⁵⁺			
MgVO ₂ N	0.940854	0.376945	N
MgNbO ₂ N	0.895451	0.44674963	N
MgTaO ₂ N	0.895451	0.44674963	N
MgMoO ₂ N	0.908605	0.42580824	N
MgWO ₂ N	0.904178	0.4327887	N
CaVO ₂ N	0.993910	0.376945	N
CaNbO ₂ N	0.945947	0.446750	S/P
CaTaO ₂ N	0.945947	0.446750	S/P
CaMoO ₂ N	0.959842	0.425808	S ³ /P
CaWO ₂ N	0.955165	0.432789	P
SrVO ₂ N	1.029758	0.376945	N
SrNbO ₂ N	0.980065	0.446750	S/P
SrTaO ₂ N	0.980065	0.446750	S/P
SrMoO ₂ N	0.994462	0.425808	S ³ /P
SrWO ₂ N	0.989616	0.432789	S/P
BaVO ₂ N	1.090699	0.376945	N
BaNbO ₂ N	1.038066	0.446750	S/P
BaTaO ₂ N	1.038066	0.446750	S/P
BaMoO ₂ N	1.053314	0.425808	N
BaWO ₂ N	1.048182	0.432789	N
ZnVO ₂ N	0.941693	0.376945	N
ZnNbO ₂ N	0.89625	0.44674963	N
ZnTaO ₂ N	0.89625	0.44674963	N
ZnMoO ₂ N	0.909415	0.42580824	N
ZnWO ₂ N	0.904984	0.4327887	N
CdVO ₂ N	0.983155	0.376945	N
CdNbO ₂ N	0.935711	0.44674963	P
CdTaO ₂ N	0.935711	0.44674963	P
CdMoO ₂ N	0.949457	0.42580824	P
CdWO ₂ N	0.94483	0.4327887	P
EuVO ₂ N	1.029041	0.376945	N
EuNbO ₂ N	0.979383	0.44674963	S/P
EuTaO ₂ N	0.979383	0.44674963	S/P
EuMoO ₂ N	0.99377	0.42580824	P
EuWO ₂ N	0.988927	0.4327887	S ³ /P
A³⁺B⁴⁺			
ScSiO ₂ N	0.973386	0.27921852	N
ScGeO ₂ N	0.908896	0.36996453	N
ScSnO ₂ N	0.840373	0.48165194	N
ScTiO ₂ N	0.875436	0.42231801	N
ScZrO ₂ N	0.82866	0.50259333	N
ScHfO ₂ N	0.832528	0.49561287	N
ScMnO ₂ N	0.908896	0.36996453	N
ScFeO ₂ N	0.884115	0.40835708	N
ScCoO ₂ N	0.908896	0.36996453	N
ScVO ₂ N	0.886312	0.40486685	N
ScNbO ₂ N	0.844352	0.47467148	N
ScTaO ₂ N	0.844352	0.47467148	N
ScMoO ₂ N	0.856517	0.45373009	N
ScWO ₂ N	0.852423	0.46071055	N
YSiO ₂ N	1.035629	0.27921852	N
YGeO ₂ N	0.967015	0.36996453	N
YSnO ₂ N	0.894111	0.48165194	P
YTiO ₂ N	0.931415	0.42231801	P
YZrO ₂ N	0.881648	0.50259333	P
YHfO ₂ N	0.885764	0.49561287	P
YMnO ₂ N	0.967015	0.36996453	N
YFeO ₂ N	0.94065	0.40835708	P
YCoO ₂ N	0.967015	0.36996453	N
YVO ₂ N	0.942987	0.40486685	P
YNbO ₂ N	0.898344	0.47467148	P
YTaO ₂ N	0.898344	0.47467148	P
YMoO ₂ N	0.911286	0.45373009	P
YWO ₂ N	0.906931	0.46071055	P
GaSiO ₂ N	0.966324	0.27921852	N
GaGeO ₂ N	0.902302	0.36996453	N
GaSnO ₂ N	0.834277	0.48165194	N
GaTiO ₂ N	0.869074	0.42231801	N
GaZrO ₂ N	0.822638	0.50259333	N
GaHfO ₂ N	0.826488	0.49561287	N
GaMnO ₂ N	0.902291	0.36996453	N
GaFeO ₂ N	0.87769	0.40835708	N
GaCoO ₂ N	0.902291	0.36996453	N
GaVO ₂ N	0.879871	0.40486685	N
GaNbO ₂ N	0.838216	0.47467148	N
GaTaO ₂ N	0.838216	0.47467148	N
GaMoO ₂ N	0.850292	0.45373009	N
GaWO ₂ N	0.846229	0.46071055	N
InSiO ₂ N	1.027409	0.27921852	N
InGeO ₂ N	0.959341	0.36996453	N
InSnO ₂ N	0.887015	0.48165194	N
InTiO ₂ N	0.924023	0.42231801	N
InZrO ₂ N	0.874651	0.50259333	N
InHfO ₂ N	0.878734	0.49561287	N
InMnO ₂ N	0.959341	0.36996453	N
InFeO ₂ N	0.933184	0.40835708	N
InCoO ₂ N	0.959341	0.36996453	N
InVO ₂ N	0.935503	0.40486685	N
InNbO ₂ N	0.891214	0.47467148	N
InTaO ₂ N	0.891214	0.47467148	N
InMoO ₂ N	0.904054	0.45373009	N
InWO ₂ N	0.899733	0.46071055	N
LaSiO ₂ N	1.077573	0.27921852	N
LaGeO ₂ N	1.006181	0.36996453	N
LaSnO ₂ N	0.930324	0.48165194	P
LaTiO ₂ N	0.969139	0.422318	S/P
LaZrO ₂ N	0.917357	0.502593	S/P
LaHfO ₂ N	0.921639	0.49561287	P
LaMnO ₂ N	1.006181	0.36996453	N
LaFeO ₂ N	0.978748	0.40835708	P
LaCoO ₂ N	1.006181	0.36996453	N
LaVO ₂ N	0.981180	0.404867	S ³ /P
LaNbO ₂ N	0.934728	0.474671	P
LaTaO ₂ N	0.934728	0.474671	P
LaMoO ₂ N	0.948195	0.453730	P
LaWO ₂ N	0.943663	0.460711	P
PrSiO ₂ N	1.082976	0.27921852	N
PrGeO ₂ N	1.011225	0.36996453	N
PrSnO ₂ N	0.934988	0.48165194	P
PrTiO ₂ N	0.973998	0.422318	P
PrZrO ₂ N	0.921956	0.502593	S/P
PrHfO ₂ N	0.926259	0.49561287	P
PrMnO ₂ N	1.011225	0.36996453	N
PrFeO ₂ N	0.983654	0.40835708	P
PrCoO ₂ N	1.011225	0.36996453	N
PrVO ₂ N	0.986099	0.404867	P
PrNbO ₂ N	0.939414	0.474671	P
PrTaO ₂ N	0.939414	0.474671	P
PrMoO ₂ N	0.952949	0.453730	P
PrWO ₂ N	0.948394	0.460711	P
NdSiO ₂ N	1.042845	0.27921852	N
NdGeO ₂ N	0.973753	0.36996453	N
NdSnO ₂ N	0.900341	0.48165194	P
NdTiO ₂ N	0.937905	0.422318	S/P
NdZrO ₂ N	0.887791	0.502593	S/P
NdHfO ₂ N	0.891935	0.49561287	P
NdMnO ₂ N	0.973753	0.36996453	N
NdFeO ₂ N	0.947204	0.40835708	P
NdCoO ₂ N	0.973753	0.36996453	N
NdVO ₂ N	0.949557	0.40486685	S/P
NdNbO ₂ N	0.904603	0.47467148	P
NdTaO ₂ N	0.904603	0.47467148	P
NdMoO ₂ N	0.917636	0.45373009	P
NdWO ₂ N	0.91325	0.46071055	P
SmSiO ₂ N	1.031268	0.27921852	N

Electronic Supplementary Material (ESI) for Journal of Materials Chemistry A
This journal is © The Royal Society of Chemistry 2013

SmGeO ₂ N	0.962944	0.36996453	N
SmSnO ₂ N	0.890346	0.48165194	N
SmTiO ₂ N	0.927493	0.42231801	N
SmZrO ₂ N	0.877936	0.50259333	S/P
SmHfO ₂ N	0.882034	0.49561287	N
SmMnO ₂ N	0.962944	0.36996453	N
SmFeO ₂ N	0.936689	0.40835708	P
SmCoO ₂ N	0.962944	0.36996453	N
SmVO ₂ N	0.939017	0.40486685	P
SmNbO ₂ N	0.894561	0.47467148	N
SmTaO ₂ N	0.894561	0.47467148	N
SmMoO ₂ N	0.907449	0.45373009	N
SmWO ₂ N	0.903112	0.46071055	N
ABON₂ A²⁺B⁶⁺			
MgMoON ₂	0.91418	0.40248388	N
MgWON ₂	0.909754	0.40930564	N
CaMoON ₂	0.965085	0.402484	N
CaWON ₂	0.960413	0.409306	P
SrMoON ₂	0.999480	0.402484	N
SrWON ₂	0.994641	0.409306	P
BaMoON ₂	1.057951	0.402484	N
BaWON ₂	1.052829	0.409306	N
ZnMoON ₂	0.914984	0.40248388	N
ZnWON ₂	0.910555	0.40930564	N
CdMoON ₂	0.954766	0.40248388	N
CdWON ₂	0.950144	0.40930564	P
EuMoON ₂	0.998792	0.40248388	N
EuWON ₂	0.993957	0.40930564	P
A³⁺B⁵⁺			
ScVON ₂	0.901012	0.36837508	N
ScNbON ₂	0.85822	0.43659269	N
ScTaON ₂	0.85822	0.43659269	N
ScMoON ₂	0.870625	0.4161274	N
ScWON ₂	0.86645	0.42294916	N
YVON ₂	0.957876	0.36837508	N
YNbON ₂	0.912383	0.43659269	N
YTaON ₂	0.912383	0.43659269	N
YMoON ₂	0.925571	0.4161274	N
YWON ₂	0.921133	0.42294916	N
GaVON ₂	0.89455	0.36837508	N
GaNbON ₂	0.852065	0.43659269	N
GaTaON ₂	0.852065	0.43659269	N
GaMoON ₂	0.864381	0.4161274	N
GaWON ₂	0.860236	0.42294916	N
InVON ₂	0.950367	0.36837508	N
InNbON ₂	0.905231	0.43659269	N
InTaON ₂	0.905231	0.43659269	N
InMoON ₂	0.918315	0.4161274	N
InWON ₂	0.913912	0.42294916	N
LaVON ₂	0.996196	0.368375	N
LaNbON ₂	0.948883	0.436593	S/P
LaTaON ₂	0.948883	0.436593	S/P
LaMoON ₂	0.962598	0.416127	P
LaWON ₂	0.957983	0.422949	S ² /P
PrVON ₂	1.001131	0.368375	N
PrNbON ₂	0.953584	0.436593	S/P
PrTaON ₂	0.953584	0.436593	P
PrMoON ₂	0.967367	0.416127	P
PrWON ₂	0.962729	0.422949	P
NdVON ₂	0.964468	0.36837508	N
NdNbON ₂	0.918663	0.43659269	N
NdTaON ₂	0.918663	0.43659269	N
NdMoON ₂	0.931941	0.4161274	P
NdWON ₂	0.927472	0.42294916	S ² /P
SmVON ₂	0.953892	0.36837508	N
SmNbON ₂	0.908589	0.43659269	N
SmTaON ₂	0.908589	0.43659269	N
SmMoON ₂	0.921721	0.4161274	N
SmWON ₂	0.917302	0.42294916	N

References

1. I. D. Fawcett, K. V. Ramanujachary and M. Greenblatt, *Mater. Res. Bull.*, 1997, **32**, 1565-1570.
2. M. H. Yang, J. A. Rodgers, L. C. Middler, J. Oro-Sole, A. B. Jorge, A. Fuertes and J. P. Attfield, *Inorg Chem*, 2009, **48**, 11498-11500.
3. Y. I. Kim and E. Lee, *J Ceram Soc Jpn*, 2011, **119**, 371-374.
4. R. M. F. Pors, Y. Laurent, P. Bacher, G. Roult, *Mat. Res. Bull.*, 1988, **23**, 1447-1450.
5. E. C. Pascual, V. B. Gutierrez, M. Subda and R. S. Puche, *Solid State Sci.*, 2008, **10**, 1905-1909.
6. T. Motohashi, Y. Hamade, Y. Masubuchi, T. Takeda, K. Murai, A. Yoshiasa and S. Kikkawa, *Mater. Res. Bull.*, 2009, **44**, 1899-1905.
7. R. Pastrana-Fabregas, J. Isasi-Marin, C. Cascales and R. Saez-Puche, *J. Solid State Chem.*, 2007, **180**, 92-97.
8. D. Logvinovich, S. C. Ebbinghaus, A. Reller, I. Marozau, D. Ferri and A. Weidenkaff, *Z. Anorg. Allg. Chem.*, 2010, **636**, 905-912.
9. E. Günther, R. Hagenmayer and M. Jansen, *Z. Anorg. Allg. Chem.*, 2000, **626**, 1519-1525.
10. S. J. Clarke, B. P. Guinot, C. W. Michie, M. J. C. Calmont and M. J. Rosseinsky, *Chem Mater*, 2002, **14**, 288-294.
11. A. Rachel, S. G. Ebbinghaus, M. Güngerich, P. J. Klar, J. Hanss, A. Weidenkaff and A. Reller, *Thermochim Acta*, 2005, **438**, 134-143.
12. M. H. Yang, J. Oro-Sole, J. A. Rodgers, A. B. Jorge, A. Fuertes and J. P. Attfield, *Nat Chem*, 2011, **3**, 47-52.
13. D. Logvinovich, M. H. Aguirre, J. Hejtmanek, R. Aguiar, S. G. Ebbinghaus, A. Reller and A. Weidenkaff, *J. Solid State Chem.*, 2008, **181**, 2243-2249.
14. J. Oro-Solé, L. Clark, W. Bonin, J. P. Attfield and A. Fuertes, *Chem Commun*, 2013, **49**, 2430-2432.
15. Y. I. Kim, P. M. Woodward, K. Z. Baba-Kishi and C. W. Tai, *Chem Mater*, 2004, **16**, 1267-1276.
16. Y. R. Zhang, T. Motohashi, Y. Masubuchi and S. Kikkawa, *J Ceram Soc Jpn*, 2011, **119**, 581-586.
17. S. J. Clarke, K. A. Hardstone, C. W. Michie and M. J. Rosseinsky, *Chem Mater*, 2002, **14**, 2664-2669.
18. P. Bacher, P. Antoine, R. Marchand, P. Lharidon, Y. Laurent and G. Roult, *J. Solid State Chem.*, 1988, **77**, 67-71.
19. P. Antoine, R. Assabaa, P. L'Haridon, R. Marchand, Y. Laurent, C. Michel and B. Raveau, *Mater. Sci. Eng., B* 1989, **5**, 43-46.
20. R. M. Po Antoine, Y. Lament, C. Michel and B. Raveau, *Mat. Res. Bull.*, 1988, **23**, 953-957.
21. N. Kumar, A. Sundaresan and C. N. R. Rao, *Mater. Res. Bull.*, 2011, **46**, 2021-2024.
22. J. Grins, P. O. Kall and G. Svensson, *J. Solid State Chem.*, 1995, **117**, 48-54.
23. P. Y. Laurent, R. Pastuszak, P. L'Haridon and R. Marchand, *Acta Cryst. B*, 1984, **38**, 914-916.
24. P. Lharidon, R. Pastuszak and Y. Laurent, *J. Solid State Chem.*, 1982, **43**, 29-32.
25. S. J. Clarke, P. R. Chalker, J. Holman, C. W. Michie, M. Puyet and M. J. Rosseinsky, *J Am Chem Soc*, 2002, **124**, 3337-3342.
26. N. Diot, R. Marchand, J. Haines, J. M. Leger, P. Macaudiere and S. Hull, *J. Solid State Chem.*, 1999, **146**, 390-393.
27. C. Z. Ye, J. Yang, L. X. Yao and N. Y. Chen, *Chinese Sci Bull*, 2002, **47**, 458-460.
28. G. Tobias, J. Oro-Sole, D. Beltran-Porter and A. Fuertes, *Inorg Chem*, 2001, **40**, 6867.
29. Y. Ohashi, T. Motohashi, Y. Masubuchi and S. Kikkawa, *J. Solid State Chem.*, 2010, **183**, 1710-1714.
30. S. Kikkawa, T. Takeda, A. Yoshiasa, P. Maillard and F. Tessier, *Mater. Res. Bull.*, 2008, **43**, 811-818.
31. S. H. Elder, F. J. DiSalvo, J. B. Parise, J. A. Hriljac and J. W. Richardson, *J. Solid State Chem.*, 1994, **108**, 73-79.
32. N. Arumugam, A. Honnorscheid and M. Jansen, *Z. Anorg. Allg. Chem.*, 2003, **629**, 939-941.
33. H. Yamane and F. J. DiSalvo, *J Alloy Compd*, 1996, **234**, 203-206.
34. M. T. Weller and S. J. Skinner, *Int J Inorg Mater*, 2000, **2**, 463-467.

Cite this: *Dalton Trans.*, 2015, **44**,
8238

A study on the thermal conversion of scheelite-type ABO_4 into perovskite-type $AB(O,N)_3$ †

Wenjie Li,^a Duan Li,^b Xin Gao,^b Aleksander Gurlo,^c Stefan Zander,^d Philip Jones,^e Alexandra Navrotsky,^e Zhijian Shen,^b Ralf Riedel^a and Emanuel Ionescu^{*a}

Phase-pure scheelite $AMoO_4$ and AWO_4 ($A = Ba, Sr, Ca$) were thermally treated under an ammonia atmosphere at 400 to 900 °C. $SrMoO_4$ and $SrWO_4$ were shown to convert into cubic perovskite $SrMoO_2N$ and $SrWO_{1.5}N_{1.5}$, at 700 °C and 900 °C respectively, and to form metastable intermediate phases (scheelite $SrMoO_{4-x}N_x$ and $SrWO_{4-x}N_x$), as revealed by X-ray diffraction (XRD), elemental analysis and FTIR spectroscopy. High-temperature oxide melt solution calorimetry reveals that the enthalpy of formation for $SrM(O,N)_3$ ($M = Mo, W$) perovskites is less negative than that of the corresponding scheelite oxides, though the conversion of the scheelite oxides into perovskite oxynitrides is thermodynamically favorable at moderate temperatures. The reaction of $BaMoO_4$ with ammonia leads to the formation of rhombohedral $Ba_3M_2(O,N)_8$ and the corresponding binary metal nitrides Mo_3N_2 and $W_{4.6}N_4$; similar behavior was observed for $CaMoO_4$, which converted upon ammonolysis into individual oxides and nitrides. Thus, $BaMoO_4$ and $CaMoO_4$ were shown to not provide access to perovskite oxynitrides. The influence of the starting scheelite oxide precursor, the structure distortion and the degree of covalency of the B-site-N bond are discussed within the context of the formability of perovskite oxynitrides.

Received 17th February 2015,
Accepted 27th March 2015

DOI: 10.1039/c5dt00711a

www.rsc.org/dalton

1 Introduction

Perovskite oxynitrides $AB(O,N)_3$ are typically synthesized *via* ammonolysis of oxide precursors; thus they can be formally represented as nitrogen-substituted perovskite-type oxides,^{1,2} which are an emerging class of materials suitable for novel applications in the fields of energy conversion, storage, non-toxic pigments, dielectrics, *etc.*³

Most perovskite-type oxynitrides are synthesized *via* conversion of scheelite-type ABO_4 and pyrochlore-type $A_2B_2O_7$ upon thermal treatment under an ammonia atmosphere. However, not all scheelite- and pyrochlore-type oxides are able to afford

perovskite oxynitrides. For example, pyrochlore-type $La_2Zr_2O_7$ as well as scheelite-type $EuMO_4$ ($M = Nb$ and Ta) and $SrMoO_4$ provide perovskite-type $LaZrO_2N^4$ as well as $EuMO_2N^5$ and $SrMoO_2N^6$, respectively, whereas other precursor oxides such as scheelite-type $ATaO_4$ ($A = Nd, Sm, Gd, Dy$) and $A_2W_2O_9$ ($A = Pr, Nd, Sm, Gd, Dy$) convert upon ammonolysis into pyrochlore-type $A_2Ta_2O_5N_2^7$ and scheelite-type AWO_3N^8 , respectively.

According to our previous work, only a limited number of perovskite-type oxynitrides are formable.⁹ For instance, $SrMoO_2N$, $SrWO_2N$, $CaMoO_2N$ and $CaWO_2N$ appear to be feasible, while $BaMoO_2N$ and $BaWO_2N$ are not stable in the perovskite-type structure. Although perovskite-type $SrMo(O,N)_3$, $SrW(O,N)_3$ and $CaMo(O,N)_3$ ^{6,10–14} have been reported in the literature (consistent with our prediction based on tolerance and octahedral factors),⁹ details of the structure evolution of the oxides into perovskite-type oxynitrides are scarce. Furthermore, the existence of perovskite-type $BaMo(O,N)_3$ is questionable;^{11,12} whereas perovskite-type $BaW(O,N)_3$ and $CaW(O,N)_3$ have not yet been synthesized.

2 Experimental methods

2.1 Synthesis

Scheelite-type oxide precursors (*i.e.*, $SrMoO_4$, $SrWO_4$, $BaMoO_4$, $BaWO_4$, $CaMoO_4$ and $CaWO_4$) were synthesized *via* solvo-thermal methods. Thus, $Sr(NO_3)_2$ (Sigma-Aldrich, >99.0%),

^aFachbereich Material- und Geowissenschaften Technische Universität Darmstadt, 64287 Darmstadt, Germany. E-mail: ionescu@materials.tu-darmstadt.de; Fax: +49 (0)6151 16 6346; Tel: +49 (0)6151 16 6342

^bDepartment of Materials and Environmental Chemistry, Arrhenius Laboratory, Stockholm University, S-106 91 Stockholm, Sweden

^cFachgebiet Keramische Werkstoffe, Institut für Werkstoffwissenschaften und –technologien Fakultät III Prozesswissenschaften, Technische Universität Berlin, Hardenbergstraße 40, 10623 Berlin, Germany

^dHelmholtz-Zentrum Berlin für Materialien und Energie, Department of Crystallography, Hahn-Meitner-Platz 1, 14109 Berlin, Germany

^ePeter A. Rock Thermochemistry Laboratory and NEATORU, University of California Davis, Davis, CA 95616-8779, USA

† Electronic supplementary information (ESI) available: XRD, FTIR, lattice parameters and the phase composition obtained by Rietveld refinement, elemental analysis and the enthalpies of formation results as well as Gibbs free energy calculation. See DOI: 10.1039/c5dt00711a

Ba(NO₃)₂ (Sigma-Aldrich, >99.0%) or Ca(NO₃)₂·4H₂O (Sigma-Aldrich, >99.0%) was mixed in an equimolar ratio with Na₂MoO₄·4H₂O (Sigma-Aldrich, >99.5%) or Na₂WO₄·4H₂O (Sigma-Aldrich, >99.5%) in ethylenediamine (FLUKA, >99.5%) under vigorous stirring. Subsequently, the reaction mixture was transferred into an autoclave with Teflon lining and heated at 200 °C for 24 h. The resulting mixture was rinsed 5 times with deionized water and ethanol alternately. Centrifugation and drying at 60 °C overnight led to the powdered scheelite-type oxides.

The resulting oxides were ground to fine powders (grain size < 500 nm) and placed in a silica crucible. The thermal treatments were carried out in flowing ammonia at temperatures between 400 and 900 °C for 4–24 h. The Schlenk system used for thermal ammonolysis is specifically limited to small batch sizes (about 0.3–0.5 g) to maximize exposure to flowing NH₃ and thus the product homogeneity.

2.2 Sample characterization

The crystalline phase composition of the as-synthesized samples was analyzed by using powder X-ray diffraction (XRD, STOE STADI P) with Mo K α radiation (wavelength of 0.7093 Å). The oxygen and nitrogen contents of the synthesized samples were determined by hot gas extraction using a Leco TC436 analyzer. Fourier Transform Infrared (FT-IR) spectroscopy was performed on a Varian 670-IR spectrometer. Thermogravimetric analysis (TGA 92, SETARAM) under an ammonia atmosphere was performed to obtain the weight change of samples. A high resolution transmission electron microscope (HRTEM, JEOL JEM-2100F) was used to assess the morphology and the local crystallinity of the samples.

High temperature oxidative-solution calorimetry was used to determine the enthalpies of formation of the prepared oxynitride samples. This method is well developed^{15–18} and has been applied previously to study nitrides^{19–21} and oxynitrides.^{22–24} Using this technique, ~5 mg pellets, prepared by pressing the powders into a die with a diameter of 1 mm, were dropped from room temperature into molten sodium molybdate (3Na₂O·4MoO₃) solvent at 701 °C using a custom made Tian–Calvet twin microcalorimeter.^{15,17}

Neutron diffraction (ND) experiments were performed using a high resolution powder diffractometer for thermal neutrons (HRPT)²⁵ located at the Swiss Spallation Neutron Source (SINQ) of the Paul Scherrer Institute in Switzerland and the Fine Resolution Powder Diffractometer (FIREPOD, E9)²⁶ at the BERII of the Helmholtz-Zentrum Berlin (HZB), Germany. The measurements were performed using a neutron wavelength of $\lambda = 1.494$ Å at SINQ and $\lambda = 1.308$ Å at HZB. Crystallographic parameters were confirmed by the individual Rietveld refinements of the XRD and ND patterns. The peak shapes were modeled with the pseudo-Voigt function for XRD and the Thompson-Cox-Hastings pseudo-Voigt function²⁷ for ND patterns. Isotropic thermal parameters of O/N were constrained to the same value for the anions. All refinements were performed with the Fullprof software.²⁸

3 Results and discussion

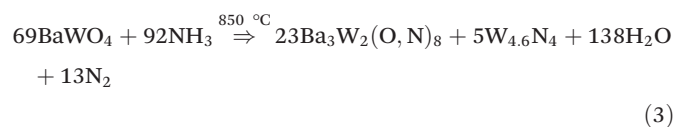
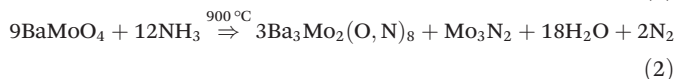
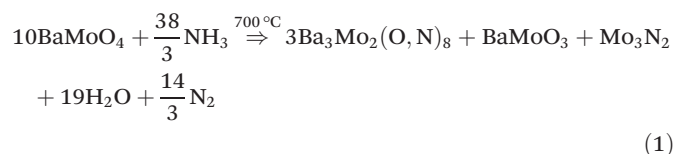
3.1 Ammonolysis of scheelite-type oxides

3.1.1 BaMoO₄ and BaWO₄. The ammonolysis of the scheelite-type BaMoO₄ was performed at 600, 700 and 900 °C for 6 h. The sample treated at 600 °C already formed small amounts of the Ba₃Mo₂(O,N)₈ oxynitride phase (structure identical to Ba₃Mo₂N₆N₂^{29,30}), as shown in Fig. S1†. At 700 °C, Mo₃N₂³¹ and BaMoO₃³² were observed. Up to 900 °C, only small amounts of Mo₃N₂ were detected besides the main phase Ba₃Mo₂(O,N)₈. The absence of the perovskite-type BaMo(O,N)₃ is consistent with the experimental work of Liu *et al.*¹² and our previous prediction.⁹ The crystallographic data and phase compositions of the samples obtained at 700 and 900 °C were analyzed by Rietveld refinement (Fig. S2a and b†). The refined lattice parameter of BaMoO₃ was 4.0489 (6) Å, which is similar to reported values.^{11,33} No cubic perovskite BaMo(O,N)₃ was formed. The lattice parameters of the rhombohedral Ba₃Mo₂(O,N)₈ were 5.9670 (3) and 21.4812 (10) Å (Table S1†); these values are smaller than those of Ba₃Mo₂O₆N₂ (5.9706 (5) and 21.5020 (6) Å)³⁴ probably because of the lower nitrogen content in our as-synthesized oxynitrides (however, we balanced eqn (1)–(3) based on Ba₃Mo₂O₆N₂ and Ba₃W₂O₆N₂).

A noticeable reaction between BaWO₄ and NH₃ occurs at 700 °C (Fig. S3†). Compared to BaMoO₄, BaWO₄ seems to be rather more inert against ammonia, thus more than 50 wt% of BaWO₄ still remained after ammonolysis at temperatures up to 850 °C (Table S2†). Hence, the ammonolysis of BaWO₄ at 700 and 850 °C leads to a mixture consisting of BaWO₄, Ba₃W₂(O,N)₈ and W_{4.6}N₄. The lattice parameters of Ba₃W₂(O,N)₈ and W_{4.6}N₄ assessed by Rietveld refinement of the XRD patterns (Fig. S4†) are close to those reported in ref. 29 and 34 (see also the ESI, Tables S2 and S4†). As we recently predicted,⁹ the perovskite-type BaWO₂N cannot be formed.

The samples obtained upon ammonolysis of BaMoO₄ and BaWO₄ were also investigated by FTIR spectroscopy; both show an absorption band around 975 cm⁻¹ for oxynitride (Fig. S5†), which was assigned to a stretching mode ($\nu(\text{M-N})$) in (WO₃N)³⁻/(MoO₃N)³⁻, having W⁶⁺/Mo⁶⁺ in tetrahedral coordination, as reported by Herle *et al.*³⁰

Thus ammonolysis of the scheelite-type oxides BaWO₄ and BaMoO₄ leads to non-perovskite oxynitride products following the paths proposed in eqn (1)–(3):



3.1.2 SrMoO₄ and SrWO₄. A similar ammonolysis procedure was applied to the scheelite-type SrMoO₄ and SrWO₄.

XRD measurements confirm that the ammonolysis of SrMoO₄ at 700 °C for 4 h leads to the formation of SrMoO₂N (Fig. 1). The change of the O/N ratio with annealing time in SrMoO₂N was shown to decrease from 2.3 upon annealing time of 4 h (the empirical chemical composition of the oxynitride SrMoO_{2.09(1)}N_{0.91(1)}) to 1.89 after 12 h (SrMoO_{1.96(1)}N_{1.04(1)}) and to 1.54 after 24 h of ammonolysis (SrMoO_{1.82(1)}N_{1.18(1)}). However, the nitrogen incorporation seems to have limitations under the conditions used, thus nitrogen-rich compositions (*e.g.*, SrMoON₂, with an O/N ratio of 0.5) are not accessible in this way.

The ammonolysis of scheelite-type SrWO₄ at 900 °C leads to the corresponding perovskite-type oxynitride as well (Fig. 2). However, the temperature required to obtain phase-pure Sr,W-based oxynitrides was higher than that used for SrMoO₄. The nitrogen content of the SrW(O,N)₃ increases slightly with the increasing temperature and holding time. Moreover, the O/N ratio in SrW(O,N)₃ seems to be more constant than that in SrMo(O,N)₃ and appears to be independent of the annealing time. Thus, the O/N ratio decreases only slightly as the annealing time was extended from 4 h (SrWO_{1.50(6)}N_{1.50(6)}; O/N ratio 1.08) to 12 h (SrWO_{1.42(2)}N_{1.58(2)}; O/N ratio 0.98) and to 24 h (SrWO_{1.39(2)}N_{1.61(2)}; O/N ratio 0.86). Interestingly, the Sr,W-based system can accommodate more nitrogen than its analogous Sr,Mo-based system. Nevertheless the O/N ratio still cannot be pushed down to 0.5.

3.1.3 CaMoO₄ and CaWO₄. The ammonolysis of CaMoO₄ was found to proceed in a different way, leading to the formation of CaO and various molybdenum nitrides (including Mo₂N, Mo₃N₂ and MoN, depending on the temperature, time and ammonia flow) (Fig. S6†) and consequently CaMoO₄ was not considered further as a precursor for the corresponding perovskite-type oxynitrides.

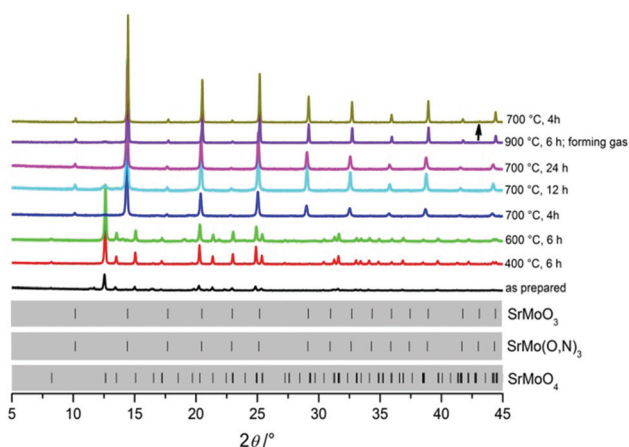


Fig. 1 XRD patterns of SrMoO₄ after heating at 400, 600 and 700 °C for different times under an ammonia flow in forming gas (a mixture of 5 vol% H₂ and 95 vol% N₂). The arrow indicates the diffraction pattern of the oxynitride obtained upon ammonolysis of SrMoO₃ which was synthesized by reducing SrMoO₄ under an ammonia flow at 700 °C.

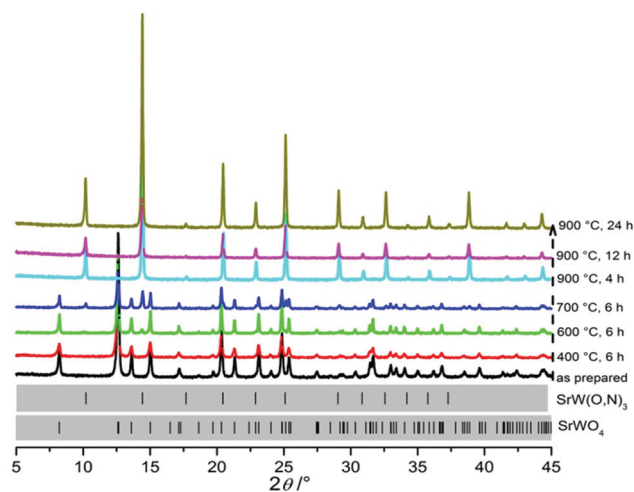
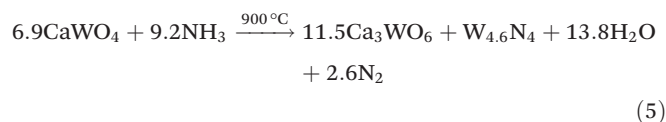
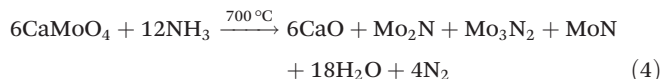


Fig. 2 XRD patterns of SrWO₄ after heating at 400, 600, 700 and 900 °C for different times under an ammonia flow.

Ammonolysis of CaWO₄ at 900 °C for 6 h leads to complete decomposition into Ca₃WO₆ and W_{4,6}N₄ and no oxynitride phase was observed (Fig. S6†). For both CaMoO₄ and CaWO₄, the corresponding perovskite oxynitrides did not form and thus their conversion into an oxide/nitride mixture is assumed to occur as follows:



3.2 Intermediate oxynitride phase during the conversion of SrMoO₄ into perovskite-type SrMoO₂N

An interesting phenomenon during the ammonolysis of SrMoO₄ at 600 °C relates to the incorporation of 2.23 wt% nitrogen without the formation of any new crystalline phase; thus, the color of the sample changed from white to light-grayish and the FTIR spectrum showed a new absorption band at 978 cm⁻¹ related to (MoO₃N)³⁻ units in tetrahedral coordination (Fig. 3a),³⁰ as also observed in Ba₃Mo₂(O,N)₈. Tetra-coordinated Mo⁶⁺ in scheelite-type SrMoO₄ can be identified by FTIR spectroscopy *via* a very broad band around 822 cm⁻¹ representing the antisymmetric stretching vibrations of Mo–O in (MoO₄)²⁻ tetrahedral units.³⁵ Thus, the formation of (MoO₃N)³⁻ is considered to be a result of the substitution of one oxygen with nitrogen in (MoO₄)²⁻ tetrahedra. Therefore, we assume that an intermediate scheelite-type oxynitride phase SrMoO_{4-x}N_x (*x* = 0.39 in our experiment, as obtained from elemental analysis and Rietveld refinement, Fig. 4) forms at 600 °C, which subsequently rearranges into the perovskite structure while taking up more nitrogen. The absence of the absorption band of (MoO₃N)³⁻ in the samples obtained upon

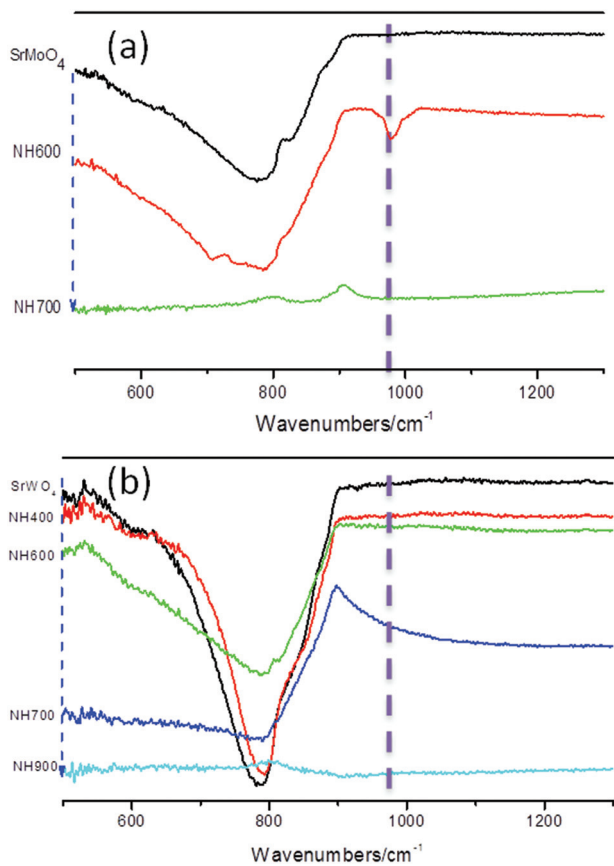


Fig. 3 FTIR spectrum of the as-synthesized scheelite oxide: (a) SrMoO_4 , (b) SrWO_4 and the resulting oxynitrides from ammonolysis at different temperatures (400, 600, 700 and 900 °C) for 6 h.

ammonolysis at temperatures above 700 °C might be related to the strong absorption of the black sample.

Yang *et al.*³⁶ reported the formation of analogous scheelite-type $\text{EuWO}_{4-y}\text{N}_y$ oxynitride as the intermediate phase during the nitridation from $\text{Eu}_2\text{W}_2\text{O}_9$ to $\text{EuWO}_{1+x}\text{N}_{2-x}$. However, in their case, the nitrogen substitution is compensated by the partial oxidation of Eu^{2+} to Eu^{3+} ($y = 0.04$ in $\text{EuWO}_{4-y}\text{N}_y$; *i.e.*, $\text{Eu}^{2+}_{1-y}\text{Eu}^{3+}_y\text{WO}_{4-y}\text{N}_y$ ^{36,37}). In our system, Sr^{2+} is not able to be oxidized to Sr^{3+} , so a different mechanism must be responsible for the formation of the nitrogen-containing scheelite-based phase. A likely explanation is that the generation of oxygen vacancies compensates the extra negative charge due to the replacement of oxygen by nitrogen within the pre-formed crystallites, which usually occurs for nitrogen-doped TiO_2 ^{38,39} or HfO_2 .⁴⁰ As shown in the HRTEM image within the FFT pattern (Fig. 5), the crystalline phase in the sample obtained after ammonolysis of SrMoO_4 at 600 °C for 4 h was indexed as tetragonal ($I41/a$, *i.e.* the same as scheelite-type SrMoO_4) and exhibited the presence of pores. Some defect regions with different fringe distances were observed as well probably due to the distortion of the lattice. Interestingly, thermogravimetric analysis of the SrMoO_4 in ammonia revealed a slight mass increase of the sample at temperatures up to 600 °C (Fig. 6), indicating that the oxygen, which is expected to be released

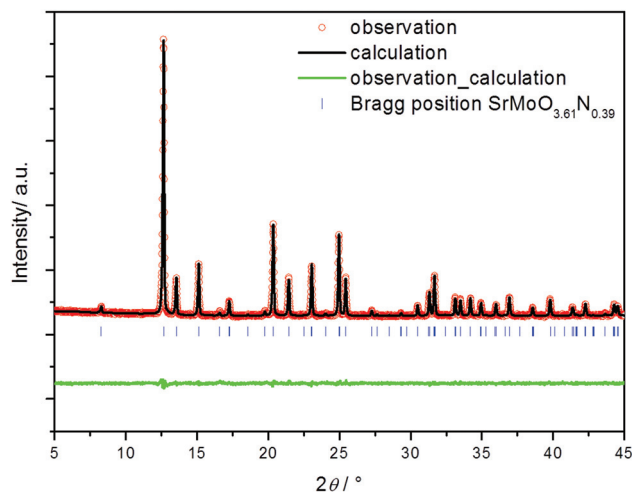
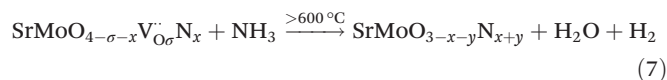
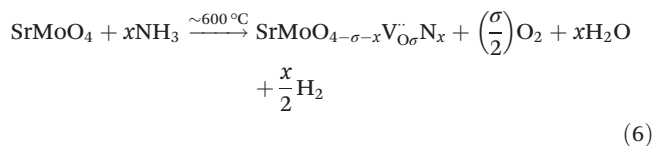


Fig. 4 Rietveld patterns of the X-ray powder diffraction data of the sample obtained upon ammonolysis of SrMoO_4 at 600 °C for 4 h. Blue tick marks are Bragg peak positions of the related phase $\text{SrMoO}_{3.61(3)}\text{N}_{0.39(3)}$ (the ratio of O/N was fixed based on the results of the elemental analysis). The green line at the bottom denotes the difference in intensities between the observed and calculated profiles. Table S3† summarizes the results of the structure refinement.

from SrMoO_4 upon ammonolysis, might be stored at intermediate temperatures in the pores or interstitially in the structure as molecular oxygen¹³ before being released (as shown by the mass loss of SrMoO_4 at temperatures beyond 700 °C, see Fig. 6). This was shown to be the reason for anomalous magnetic behavior at $T = -219$ °C (54 K) as reported by Logvinovich *et al.* The sharp weight loss above 650 °C is attributed to the complete conversion from scheelite to perovskite resulting in 1 mol oxygen release. Elemental analyses confirm the expected oxygen loss for samples heated in NH_3 between 600 and 700 °C and are in agreement with the measured mass loss, indicating that nitrogen is already incorporated into the sample at 600 °C. (Tables 1 and S6†).

Based on all these observations, we conclude that the nitridation of SrMoO_4 occurs prior to the reduction of W^{6+} during ammonolysis, thus scheelite-type $\text{SrMoO}_{4-x}\text{N}_x$ forms as an intermediate phase and decomposes fast according to the following paths (σ stands for the amount of oxygen vacancies):



3.3 Ammonolysis of SrMoO_4 vs. SrMoO_3

In order to investigate the influence of the oxide precursor on the final oxynitride, we converted the scheelite-type SrMoO_4

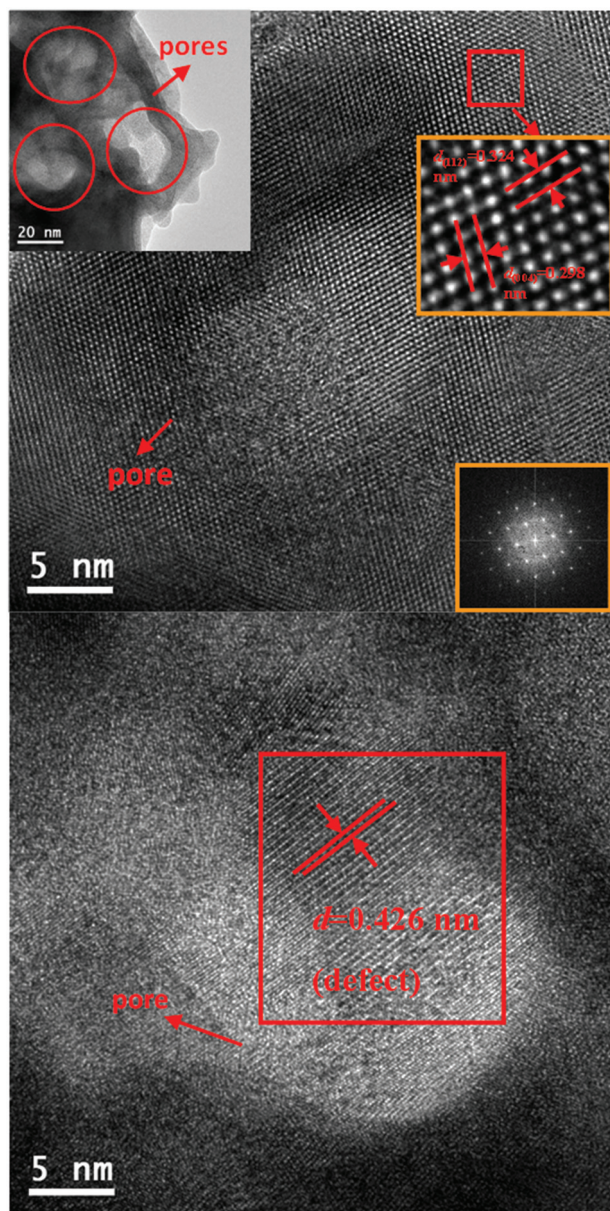


Fig. 5 HRTEM micrographs of SrMoO₄ after heating at 600 °C for 4 h.

into SrMo(O,N)₃ via a two-step process as well. In the first step, the scheelite-type oxide SrMoO₄ was easily reduced to the perovskite-type SrMoO₃ (Fig. S7†) upon thermal annealing at 900 °C for 6 h under forming gas (a mixture of 5 vol% H₂ and 95 vol% N₂). In the subsequent step, SrMoO₃ underwent ammonolysis at 700 °C for 4 h (the same conditions as for SrMoO₄) to obtain SrMo(O,N)₃. Interestingly, the nitrogen content of the phase-pure perovskite-type oxynitride (empirical formula SrMoO_{2.77(3)}N_{0.23(3)}, see the Rietveld refinement data of the neutron diffraction pattern shown in Fig. 7a) obtained from perovskite-type SrMoO₃ was significantly lower than that of the oxynitride obtained under the same conditions from SrMoO₄ (SrMoO_{2.19(2)}O_{0.81(2)}). This obviously relates to the ox-

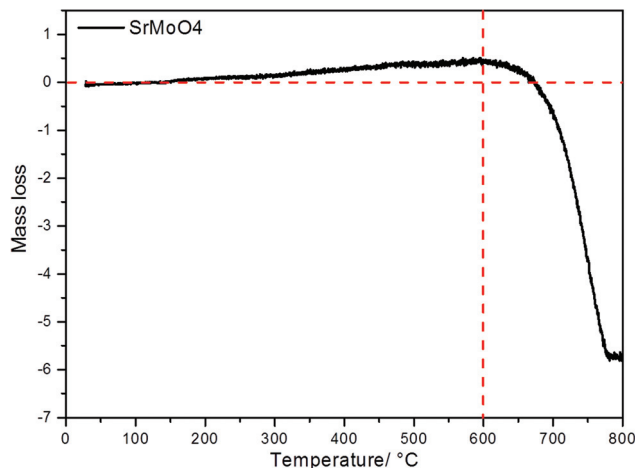


Fig. 6 TG curve of SrMoO₄ under an ammonia atmosphere from room temperature to 800 °C.

Table 1 Experimental and calculated mass loss of SrMoO₄ upon ammonolysis at 600 and 700 °C. The calculated mass loss relies on the evolution of the chemical composition of the sample upon ammonolysis

Specimens	Experiment	Empirical formula	Calculated
SrMoO ₄ _NH600_4H	0.4218 g	SrMoO _{3.61} N _{0.39}	
SrMoO ₄ _NH700_12H	0.3925 g	SrMoO _{1.96} N _{1.04}	
Mass loss (wt %)	6.95		6.97

dation state of Mo in SrMoO₄ and SrMoO₃ and its evolution under an ammonia atmosphere which will be discussed later.

Moreover, the attempt to synthesize perovskite-type SrWO₃ upon reducing SrWO₄ at high temperatures was unsuccessful.

3.4 Structural verification of perovskite oxynitrides

The neutron powder diffraction data measured at room temperature for SrMo(O,N)₃ and SrW(O,N)₃ were refined by the Rietveld method on the basis of the cubic *Pm* $\bar{3}$ *m* perovskite-type structure (Fig. 7 and Table 2). The refined O/N content of SrMoO_{2.19(2)}N_{0.81(2)} (700 °C for 4 h) and SrWO_{1.50(6)}N_{1.50(6)} (900 °C for 4 h) is consistent with the results of elemental analysis (ESI, see Table S6†).

The enthalpies of dissolution (ΔH_{ds}) and formation (ΔH_f) of scheelite-type SrMoO₄ and SrWO₄ and the corresponding perovskite-type oxynitride samples measured by high temperature oxide melt solution calorimetry are listed in Table 3.

The enthalpies of formation of the oxides and oxynitrides from the elements were calculated using the thermodynamic cycles shown in Tables S7 and S8† and are given in Table 3. The enthalpy of formation of SrMoO₄ (-260.2 ± 0.5 kJ per g-atom) is ~ 36 kJ per g-atom more exothermic than that of SrMoO_{1.96}N_{1.04} (-223.8 ± 0.7 kJ per g-atom). Likewise, the enthalpy of formation of SrWO₄ (-273.4 ± 0.5 kJ per g-atom) is ~ 83 kJ per g-atom more exothermic than that of SrWO_{1.5}N_{1.5}

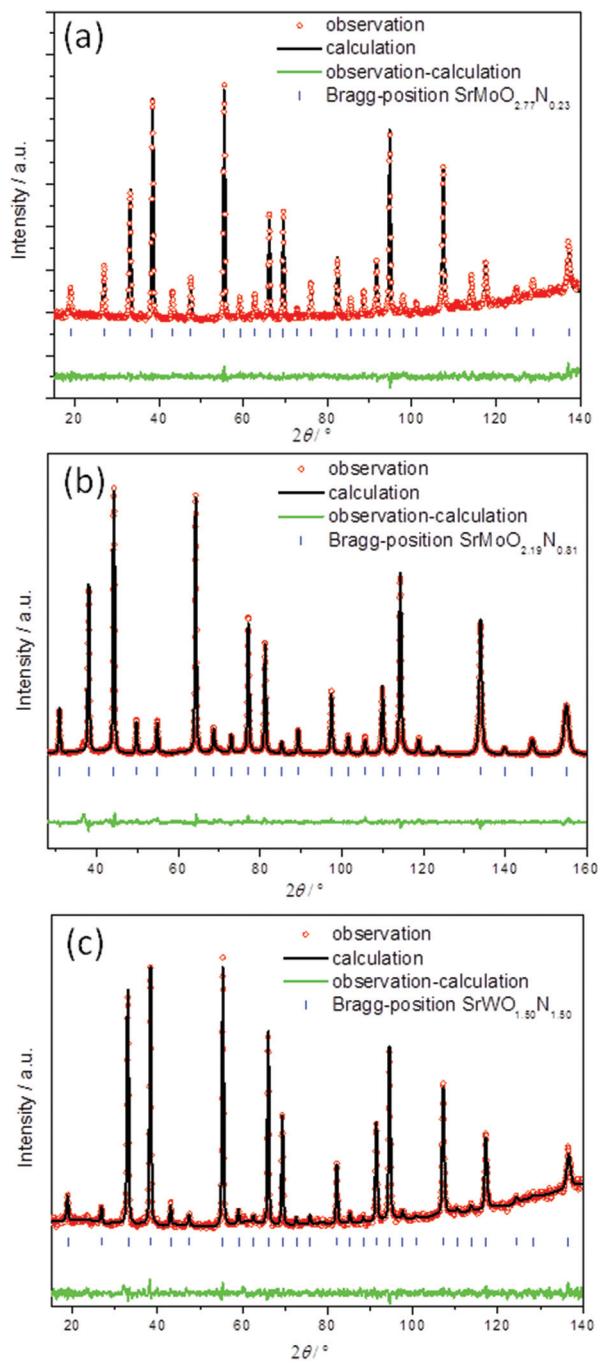
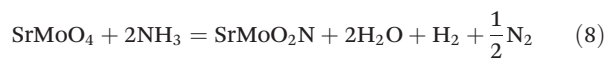


Fig. 7 Rietveld patterns of the neutron powder diffraction data of the sample obtained upon ammonolysis of (a) SrMoO_3 at 700 °C for 4 h (FIREPOD, E9); (b) SrMoO_4 at 700 °C for 4 h (HRPT, SINQ) and (c) SrWO_4 at 900 °C for 4 h (FIREPOD, E9). Blue tick marks are Bragg peak positions of related phases (a) $\text{SrMoO}_{2.77(3)}\text{N}_{0.23(3)}$; (b) $\text{SrMoO}_{2.19(2)}\text{N}_{0.81(2)}$ and (c) $\text{SrWO}_{1.50(6)}\text{N}_{1.50(6)}$. The green line at the bottom denotes the difference in intensities between the observed and calculated profiles.

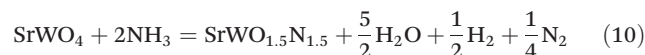
(-190.4 ± 0.7 kJ per g-atom). Thus, perovskite-type oxynitrides show less favorable enthalpies of formation than their corresponding scheelite-type oxides. Furthermore, the difference of the enthalpy of formation for Sr–W is larger than that of Sr–Mo. This suggests that the formation of Sr–W oxynitrides is

less favorable and requires higher temperatures (as observed), probably for both thermodynamic and kinetic reasons.

In order to gain further insights into the energetics of the conversion of SrMO_4 into $\text{SrM}(\text{O},\text{N})_3$ ($\text{M} = \text{Mo}, \text{W}$) under an ammonia atmosphere, the Gibbs free energy (ΔG) of reactions (8) and (9) was calculated (Tables S9 and S10†). Since the entropies of SrMoO_2N and $\text{SrWO}_{1.5}\text{N}_{1.5}$ are not available, we estimated them as 5/6 of the entropy of the corresponding scheelite-type oxide. Eqn (9) and (11) describe the temperature evolution of the Gibbs free energy of the reaction of SrMO_4 with NH_3 to give $\text{SrM}(\text{O},\text{N})_3$, indicating that the reaction is spontaneous at temperatures exceeding 992 K (*i.e.*, 719 °C) for SrWO_4 , whereas for SrMoO_4 the reaction seems to be thermodynamically favorable at any of the temperatures used for its ammonolysis (Fig. 8). It is worth pointing out that only a thermodynamic consideration might not be enough to describe the ammonolysis processes of the scheelite oxides. The kinetics (*e.g.*, activation energy) of the ammonolysis probably also play an important role and thus might explain why the conversion of SrMoO_4 into the perovskite oxynitride needs temperatures exceeding 600 °C and proceeds through an intermediate phase.



$$\Delta G_{\text{Sr-Mo}} \text{ (kJ mol}^{-1}\text{)} = 50.404 - 0.197T \quad (9)$$



$$\Delta G_{\text{Sr-W}} \text{ (kJ mol}^{-1}\text{)} = 175.615 - 0.177T \quad (11)$$

The negative temperature dependence of the free energy reflects positive entropy of the reaction because 1.5 moles of gas are produced.

3.5 Factors affecting the formation of perovskite-type oxynitrides

As addressed above, the experimental results related to the conversion of BaMoO_4 , BaWO_4 , SrMoO_4 and SrWO_4 into perovskite-type oxynitrides are consistent with our prediction.⁹ However, CaMoO_4 and CaWO_4 do not appear to be converted to oxynitrides.

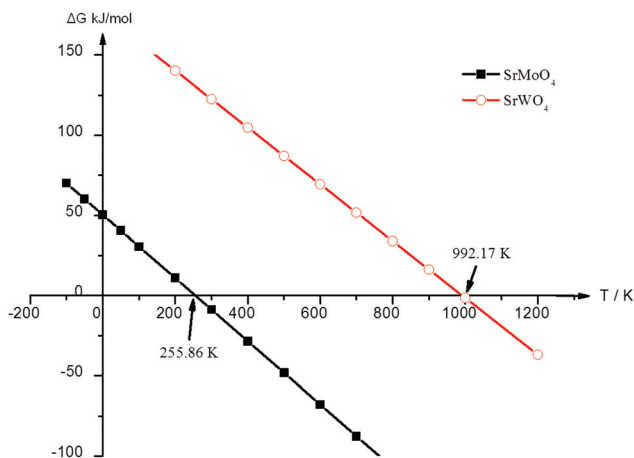
Scheelite-type ABO_4 oxides are rather common precursors for the synthesis of perovskite oxynitrides, *e.g.* $\text{Nd}^{3+}\text{V}^{4+}\text{O}_2\text{N}$,⁴¹ $\text{Eu}^{2+}\text{Nb}^{5+}\text{O}_2\text{N}^5$, $\text{La}^{3+}\text{Nb}^{4+}\text{O}_2\text{N}$,⁴² $\text{Ca}^{2+}_x\text{Sr}^{2+}_{1-x}\text{W}^{5+}\text{O}_2\text{N}$ ⁴³ and so on. The formation of hydrogen due to the dissociation of ammonia at high temperatures is beneficial for the reduction of the B-site cation in scheelite-type oxides (*e.g.* from $\text{A}^{2+}\text{B}^{6+}\text{O}_4$ to $\text{A}^{2+}\text{B}^{5+}\text{O}_2\text{N}$ or from $\text{A}^{3+}\text{B}^{5+}\text{O}_4$ to $\text{A}^{3+}\text{B}^{4+}\text{O}_2\text{N}$). In the case of using perovskite oxides as precursors for perovskite-type oxynitrides, the B-site cation has to be oxidized in order to compensate for the increase of the negative charge resulting from nitrogen incorporation (*e.g.* from $\text{Sr}^{2+}\text{Mo}^{4+}\text{O}_3$ to $\text{Sr}^{2+}\text{Mo}^{5+}\text{O}_2\text{N}$). Thus, it seems that scheelite-type oxide precursors are more favorable for the synthesis of perovskite-type oxynitrides.

Table 2 Crystal structure data of AB(O,N)₃ perovskite oxynitrides

Specimens and parameters	SrMoO _{2.77(3)} N _{0.23(3)}	SrMoO _{2.19(2)} N _{0.81(2)}	SrWO _{1.50(6)} N _{1.50(6)}
S.G.	<i>Pm</i> $\bar{3}$ <i>m</i> , Nr. 221	<i>Pm</i> $\bar{3}$ <i>m</i> , Nr. 221	<i>Pm</i> $\bar{3}$ <i>m</i> , Nr. 221
Z	1	1	1
<i>a</i> , <i>b</i> , <i>c</i> (Å)	3.9744(3)	3.9756(1)	3.9856(2)
Sr	<i>x</i> , <i>y</i> , <i>z</i> <i>B</i> _{iso} (Å ²) Occ.	0.5, 0.5, 0.5 0.666(25) 1	0.5, 0.5, 0.5 0.879(21) 1
Mo/W	<i>x</i> , <i>y</i> , <i>z</i> <i>B</i> _{iso} (Å ²) Occ.	0.0, 0.0, 0.0 0.298(23) 1	0.0, 0.0, 0.0 0.693(18) 1
O/N	<i>x</i> , <i>y</i> , <i>z</i> <i>B</i> _{iso} (Å ²) Occ.	0.5, 0.0, 0.0 0.748(18) 2.77(3)/0.23(3)	0.5, 0.0, 0.0 0.799(12) 2.19(2)/0.81(2)
			1.50(6)/1.50(6)

Table 3 Thermochemical data obtained by drop-solution calorimetry of scheelite-type oxides and their corresponding perovskite-type oxynitrides

Composition	Crystal structure	ΔH_{ds} (kJ mol ⁻¹)	ΔH_f (kJ mol ⁻¹)	ΔH_f (kJ per g-atom)
SrMoO ₄	Tetragonal/scheelite	161.8 ± 1.5	-1561.3 ± 3.1	-260.2 ± 0.5
SrMoO _{1.96} N _{1.04}	Cubic/perovskite	-291.9 ± 2.3	-1119.1 ± 3.6	-223.8 ± 0.7
SrWO ₄	Tetragonal/scheelite	-162.8 ± 1.5	-1641.2 ± 3.1	-273.4 ± 0.5
SrWO _{1.5} N _{1.5}	Cubic/perovskite	-537.2 ± 1.9	-952.9 ± 3.6	-190.4 ± 0.7

Fig. 8 Gibbs free energy (ΔG) for the ammonolysis of SrMoO₄ and SrWO₄ (eqn (8) and (10), respectively) as a function of temperature.

Moreover, parameters such as the tolerance factor (describing the distortion of the cubic perovskite structure) were shown to be crucial for the formability of perovskite-type oxynitrides.⁹ As defined by Goldschmidt,⁴⁴ the tolerance factor (t) in ABX₃ is expressed as:

$$t = \frac{(r_A - r_X)}{\sqrt{2}(r_B - r_X)} \quad (12)$$

r_A , r_B and r_X being the ionic radii of A, B and X atoms, respectively.

In our previous work,⁹ the formability of perovskite-type oxynitrides was also rationalized upon assessing the values of the tolerance factor, defined as in eqn (13) (see Table 4, as for the O/N ratio 2, *i.e.* ABO₂N):

$$t_{\text{oxy}} = \frac{[(r_A + r_O)^8 \times (r_A + r_N)^4]^{1/12}}{\sqrt{2}[(r_B + r_O)^4 \times (r_B + r_N)^2]^{1/6}} \quad (13)$$

For a general consideration of the formability of perovskite-type oxynitrides, we compared their tolerance factors with those of the corresponding perovskite-type oxides. The values of the tolerance factors t_o and t_{oxy} calculated from the ionic radii⁴⁵ are shown in Table 4 and indicate that the formal substitution of O²⁻ with N³⁻ in SrMoO₃, SrWO₃, CaMoO₃ and CaWO₃ reduces the structural distortion (*i.e.*, the tolerance factor becomes closer to unity), which suggests that the formation of the corresponding perovskite-type oxynitrides is favorable. This is in agreement with the experiment for Sr-Mo/Sr-W compounds and does not fit the experimental observations for Ca-Mo/Ca-W compositions. Large basic cations like Ca typically stabilize higher oxidation states of the transition metals (Mo, W as in our case),^{46,47} thus this may explain why the Ca scheelite-type oxides cannot be converted into oxynitrides.

In contrast, incorporation of nitrogen into BaMoO₃ and BaWO₃ increases the structural distortion; thus, the formation of BaMoO₂N and BaWO₂N would be less favorable. This is in agreement with our synthetic observation.

Moreover, the higher covalent character of the B-site-N bond than that of the B-site-O bond might also induce structural distortion into the perovskite structure of oxynitrides as

Table 4 The tolerance factors for ABO₃ and ABO₂N calculated with eqn (12) and (13), respectively^a

Oxide	BaMoO ₃	BaWO ₃	SrMoO ₃	SrWO ₃	CaMoO ₃	CaWO ₃
t_{O}	1.03	1.027	0.98	0.975	0.945	0.941
t_{oxy}	1.053	1.048	0.995	0.989	0.959	0.955
Oxynitride	BaMoO ₂ N	BaWO ₂ N	SrMoO ₂ N	SrWO ₂ N	CaMoO ₂ N	CaWO ₂ N
Predicted ^{b,9}	N	N	P	P	P	P
Experiment ^c	N	N	P	P	P ¹¹	N

^a P: perovskite; N: non-perovskite. ^b The predicted formability of oxynitrides. ^c The formability of oxynitrides for this work.

compared to their analogous perovskite oxides, *i.e.* B(O,N)₆ octahedra are expected to be more distorted than their analogous BO₆ octahedra. This structural distortion might be quite pronounced, as for compounds which exhibit so-called second-order Jahn–Teller distortion⁴⁸ (*i.e.* d⁰ B-site octahedra such as in LaZrO₂N, NdTiO₂N or LaTiO₂N).⁴ However, we consider in our compound SrM(O,N)₃ the first-order Jahn–Teller effect is relevant and thus the contribution of the B-site-N covalency to the distortion might not be significant.

4 Conclusions

In the present study, preparative possibilities to access perovskite-type oxynitrides AM(O,N)₃ (A = Ba, Sr, Ca; B = Mo, W) phases upon thermal ammonolysis of scheelite-type AMO₄ oxide precursors were investigated. The as-synthesized results of perovskite-oxynitrides are consistent with our previous prediction in general.

The experimental data reveal that both scheelite-type SrMoO₄ and SrWO₄ transform into a scheelite-type oxynitride intermediate phase, SrMO_{4-x}N_x (M = Mo, W), which subsequently converts fast into perovskite-type SrM(O,N)₃ at temperatures above 600 °C and are in agreement with the high temperature oxide melt solution calorimetry experiments which indicate that the conversion of scheelite SrMO₄ into perovskite SrM(O,N)₃ is thermodynamically favorable at the ammonolysis temperatures used.

Furthermore, the formability of the perovskite-type oxynitrides depends on the structure of the oxide precursor used (scheelite seems to be favorable, except for large basic A cations) and on the structural distortion described by the tolerance factor.

Acknowledgements

The authors acknowledge Dr Samuel Bernard (IEM, University Montpellier 2) for the TGA of SrMoO₄ under an ammonia atmosphere. This work was supported by Dr Denis Sheptyakov and based on experiments performed at the Swiss Spallation Neutron Source (SINQ), Paul Scherrer Institute, Villigen, Switzerland. This research was funded by the European Union Seventh Framework Programme (FP7/2007–2013) under the

grant agreement FUNEA – Functional Nitrides for Energy Applications. The calorimetry at UC Davis was supported by the U.S. Dept. of Energy, Office of Basic Energy Sciences, grant DE-FG02-03ER46053.

Notes and references

- 1 A. Fuertes, *J. Mater. Chem.*, 2012, **22**, 3293–3299.
- 2 Y. I. Kim and P. M. Woodward, *J. Solid State Chem.*, 2007, **180**, 3224–3233.
- 3 S. G. Ebbinghaus, H. P. Abicht, R. Dronskowski, T. Müller, A. Reller and A. Weidenkaff, *Prog. Solid State Chem.*, 2009, **37**, 173–205.
- 4 S. J. Clarke, B. P. Guinot, C. W. Michie, M. J. C. Calmont and M. J. Rosseinsky, *Chem. Mater.*, 2002, **14**, 288–294.
- 5 A. B. Jorge, J. Oró-Solé, A. M. Bea, N. Mufti, T. T. M. Palstra, J. A. Rodgers, J. P. Attfield and A. Fuertes, *J. Am. Chem. Soc.*, 2008, **130**, 12572–12573.
- 6 D. Logvinovich, R. Aguiar, R. Robert, M. Trottman, S. G. Ebbinghaus, A. Reller and A. Weidenkaff, *J. Solid State Chem.*, 2007, **180**, 2649–2654.
- 7 P. Maillard, F. Tessier, E. Orhan, F. Chevre and R. Marchand, *Chem. Mater.*, 2005, **17**, 152–156.
- 8 F. Chevre, F. Tessier and R. Marchand, *Mater. Res. Bull.*, 2004, **39**, 1091–1101.
- 9 W. J. Li, E. Ionescu, R. Riedel and A. Gurlo, *J. Mater. Chem. A*, 2013, **1**, 12239–12245.
- 10 Y. I. Kim, P. M. Woodward, K. Z. Baba-Kishi and C. W. Tai, *Chem. Mater.*, 2004, **16**, 1267–1276.
- 11 D. Logvinovich, M. H. Aguirre, J. Hejtmanek, R. Aguiar, S. G. Ebbinghaus, A. Reller and A. Weidenkaff, *J. Solid State Chem.*, 2008, **181**, 2243–2249.
- 12 G. Liu, X. H. Zhao and H. A. Eick, *J. Alloys Compd.*, 1992, **187**, 145–156.
- 13 D. Logvinovich, J. Hejtmanek, K. Knizek, M. Marysko, N. Homazava, P. Tomes, R. Aguiar, S. G. Ebbinghaus, A. Reller and A. Weidenkaff, *J. Appl. Phys.*, 2009, **105**, 023522.
- 14 R. M. Po Antoine, Y. Lament, C. Michel and B. Raveau, *Mater. Res. Bull.*, 1988, **23**, 953–957.
- 15 A. Navrotsky, *Phys. Chem. Miner.*, 1977, **2**, 89–104.
- 16 J. M. McHale, G. R. Kowach, A. Navrotsky and F. J. DiSalvo, *Chem. – Eur. J.*, 1996, **2**, 1514–1517.

- 17 A. Navrotsky, *Phys. Chem. Miner.*, 1997, **24**, 222–241.
- 18 A. Navrotsky, *J. Alloys Compd.*, 2001, **321**, 300–306.
- 19 S. H. Elder, F. J. DiSalvo, L. Topor and A. Navrotsky, *Chem. Mater.*, 1993, **5**, 1545–1553.
- 20 M. R. Ranade, F. Tessier, A. Navrotsky, V. J. Leppert, S. H. Risbud, F. J. DiSalvo and C. M. Balkas, *J. Phys. Chem. B*, 2000, **104**, 4060–4063.
- 21 M. R. Ranade, F. Tessier, A. Navrotsky and R. Marchand, *J. Mater. Res.*, 2001, **16**, 2824–2831.
- 22 J. J. Liang, A. Navrotsky, V. J. Leppert, M. J. Paskowitz, S. H. Risbud, T. Ludwig, H. J. Seifert, F. Aldinger and M. Mitomo, *J. Mater. Res.*, 1999, **14**, 4630–4636.
- 23 F. Tessier and A. Navrotsky, *Chem. Mater.*, 2000, **12**, 148–154.
- 24 I. Molodetsky, A. Navrotsky, F. DiSalvo and M. Lerch, *J. Mater. Res.*, 2000, **15**, 2558–2570.
- 25 P. Fischer, G. Frey, M. Koch, M. Konnecke, V. Pomjakushin, J. Schefer, R. Thut, N. Schlumpf, R. Burge, U. Greuter, S. Bondt and E. Berruyer, *Physica B*, 2000, **276**, 146–147.
- 26 D. M. Tobbens, N. Stusser, K. Knorr, H. M. Mayer and G. Lampert, *Epdic 7: European Powder Diffraction, Pts 1 and 2*, 2001, **378–3**, 288–293.
- 27 P. Thompson, D. E. Cox and J. B. Hastings, *J. Appl. Crystallogr.*, 1987, **20**, 79–83.
- 28 J. Rodriguezcarvajal, *Physica B*, 1993, **192**, 55–69.
- 29 Z. G. Pinsker, *Acta Crystallogr.*, 1957, **10**, 775–775.
- 30 P. S. Herle, M. S. Hegde and G. N. Subbanna, *J. Mater. Chem.*, 1997, **7**, 2121–2125.
- 31 V. V. Klechkovskaya, N. V. Troitskaya and Z. G. Pinsker, *Sov. Phys. Crystallogr. (Engl. Transl.)*, 1965, **10**, 28–35.
- 32 R. Scholder and L. Brixner, *Z. Naturforsch., B: Chem. Sci.*, 1955, **10**, 178–179.
- 33 L. H. Brixner, *J. Inorg. Nucl. Chem.*, 1960, **14**, 225–230.
- 34 M. T. Weller and S. J. Skinner, *Int. J. Inorg. Mater.*, 2000, **2**, 463–467.
- 35 A. P. A. Marques, M. T. S. Tanaka, E. Longo, E. R. Leite and I. L. V. Rosa, *J. Fluoresc.*, 2011, **21**, 893–899.
- 36 M. Yang, J. Oro-Sole, A. Kusmartseva, A. Fuertes and J. P. Attfield, *J. Am. Chem. Soc.*, 2010, **132**, 4822–4829.
- 37 A. Kusmartseva, M. Yang, J. Oró-Solé, A. M. Bea, A. Fuertes and J. P. Attfield, *Appl. Phys. Lett.*, 2009, **95**, 02210.
- 38 J. B. Varley, A. Janotti and C. G. Van de Walle, *Adv. Mater.*, 2011, **23**, 2343–2347.
- 39 A. K. Rumaiz, J. C. Woicik, E. Cockayne, H. Y. Lin, G. H. Jaffari and S. I. Shah, *Appl. Phys. Lett.*, 2009, **95**, 95.
- 40 M. Yang, J. H. Bae, C. W. Yang, A. Benayad and H. Baik, *J. Anal. Atom. Spectrom.*, 2013, **28**, 482–487.
- 41 J. Oró-Solé, L. Clark, W. Bonin, J. P. Attfield and A. Fuertes, *Chem. Commun.*, 2013, **49**, 2430–2432.
- 42 D. Logvinovich, S. C. Ebbinghaus, A. Reller, I. Marozau, D. Ferri and A. Weidenkaff, *Z. Anorg. Allg. Chem.*, 2010, **636**, 905–912.
- 43 Y. Masatomo, F. Uhi, N. Hiromi, O. Kazuki and R. H. James, *J. Phys. Chem. C*, 2013, **117**, 18529–18539.
- 44 V. M. Goldschmidt, *Skrifter Norske Videnskaps-Akad.*, I. Mat. Naturv., Oslo, 1926.
- 45 R. D. Shannon and C. T. Prewitt, *Acta Crystallogr., Sect. B: Struct. Crystallogr. Cryst. Chem.*, 1969, **25**, 925–946.
- 46 K. Kamata, T. Nakamura and T. Sata, *Chem. Lett.*, 1975, 81–86.
- 47 K. Kamata, T. Nakamura and T. Sata, *Mater. Res. Bull.*, 1975, **10**, 373–378.
- 48 R. G. Pearson, *Proc. Natl. Acad. Sci. U. S. A.*, 1975, **72**, 2104–2106.

Supplementary material

Study on the thermal conversion of scheelite-type ABO_4 into perovskite-type $AB(O,N)_3$

Wenjie Li,^a Duan Li,^b Xin Gao,^b Aleksander Gurlo,^c Stefan Zander,^e Philip Jones,^d Alexandra Navrotsky,^d Zhijian Shen,^b Ralf Riedel,^a and Emanuel Ionescu

[a] Fachbereich Material- und Geowissenschaften, Technische Universität Darmstadt, Jovanka-Bontschits-Strasse 2, 64287 Darmstadt, Hessen, Germany

[b] Department of Materials and Environmental Chemistry, Arrhenius Laboratory, Stockholm University, S-106 91 Stockholm, Sweden

[c] Fachgebiet Keramische Werkstoffe, Institut für Werkstoffwissenschaften und -technologien Fakultät III Prozesswissenschaften, Technische Universität Berlin, Hardenbergstraße 40, 10623 Berlin

[d] Peter A. Rock Thermochemistry Laboratory and NEATORU, University of California Davis, Davis, CA 95616-8779, USA

[e] Helmholtz-Zentrum Berlin für Materialien und Energie, Department of Crystallography, Hahn-Meitner-Platz 1, 14109 Berlin, Germany

Figures

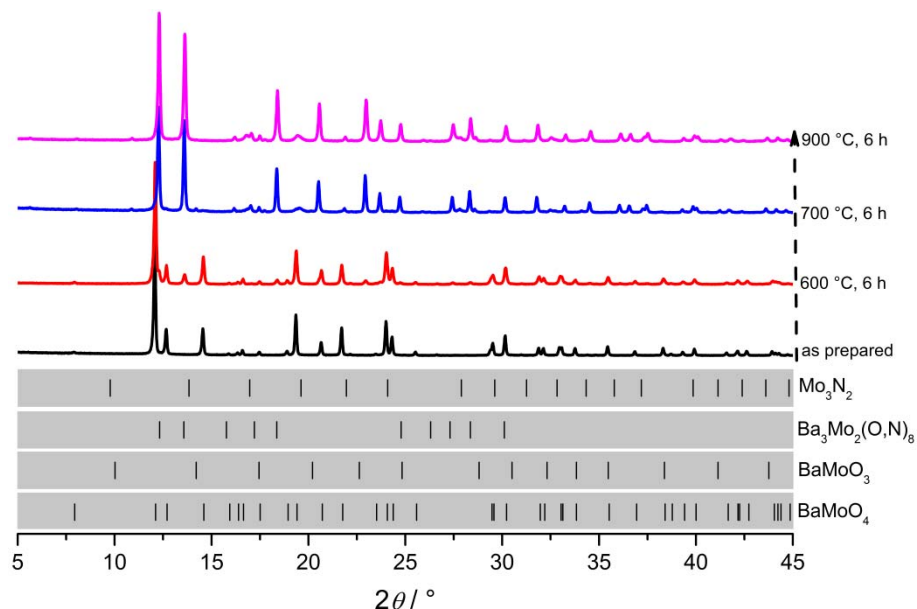


Figure S 1 XRD patterns of BaMoO₄ after heating at 600, 700 and 900 °C under an ammonia flow for 6 hours.

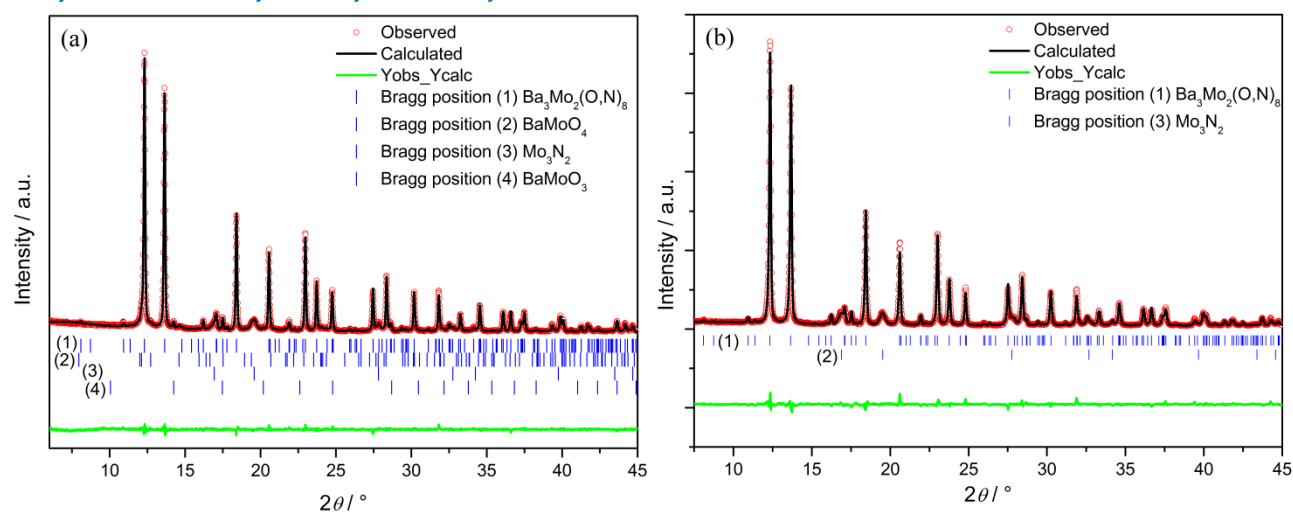


Figure S 2 Rietveld refinement of the X-ray powder diffraction patterns of the samples obtained from the ammonolysis of BaMoO_4 (a) 700 °C for 6 hours and (b) 900 °C for 6 hours. Blue tick marks are Bragg peak positions of related phase (bottom); (a) (1) $\text{Ba}_3\text{Mo}_2(\text{O},\text{N})_8$, (2) BaMoO_4 , (3) Mo_3N_2 and (4) BaMoO_3 ; (b) (1) $\text{Ba}_3\text{Mo}_2(\text{O},\text{N})_8$ and (2) Mo_3N_2 . Green line at the bottom denotes the difference intensities between the observed and calculated profiles. Table S1 summarizes the results of the structure refinement.

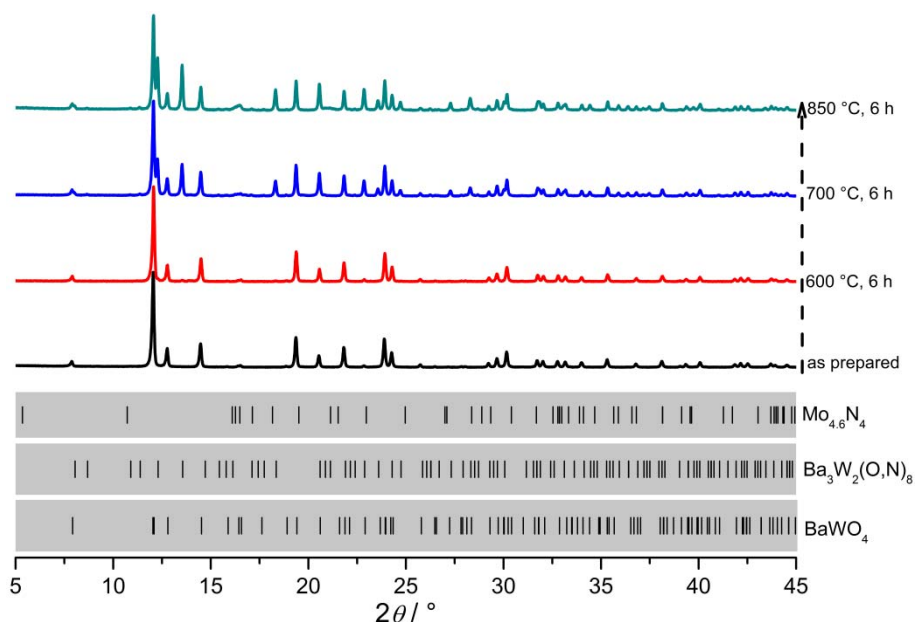


Figure S 3 XRD patterns of BaWO_4 after heating at 600, 700 and 850 °C under an ammonia flow for 6 hours.

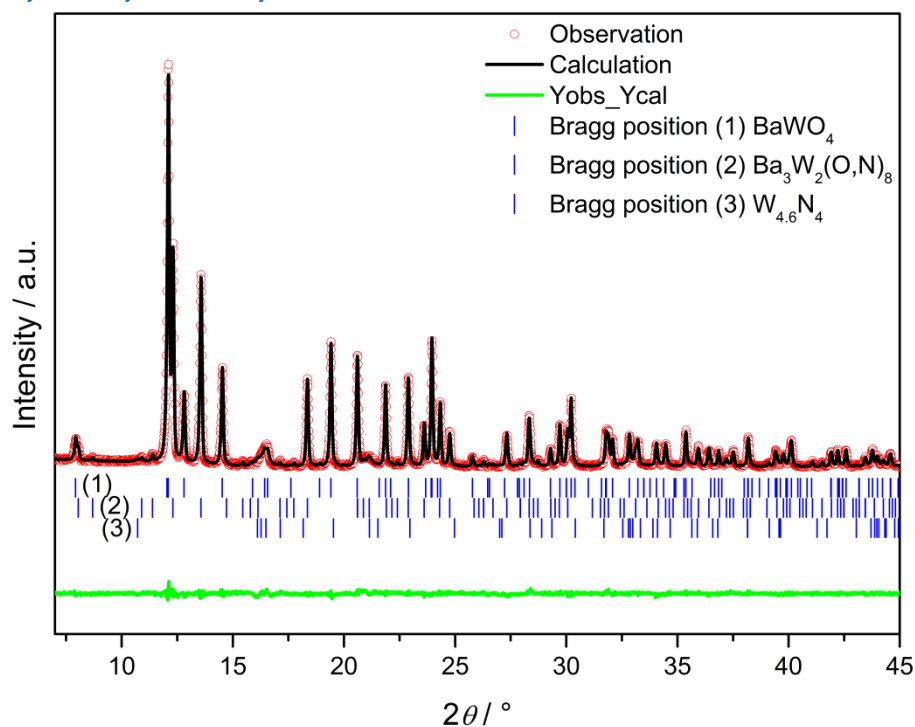


Figure S 4 Rietveld refinement of the X-ray powder diffraction pattern of the sample obtained from the ammonolysis of BaWO_4 at 850°C for 6 hours. Blue tick marks are Bragg peak positions of related phase (bottom) as (1) BaWO_4 , (2) $\text{Ba}_3\text{W}_2(\text{O},\text{N})_8$ and (3) $\text{W}_{4.6}\text{N}_4$. Green line at the bottom denotes the difference intensities between the observed and calculated profiles. Error! Reference source not found. summarizes the results of the structure refinement.

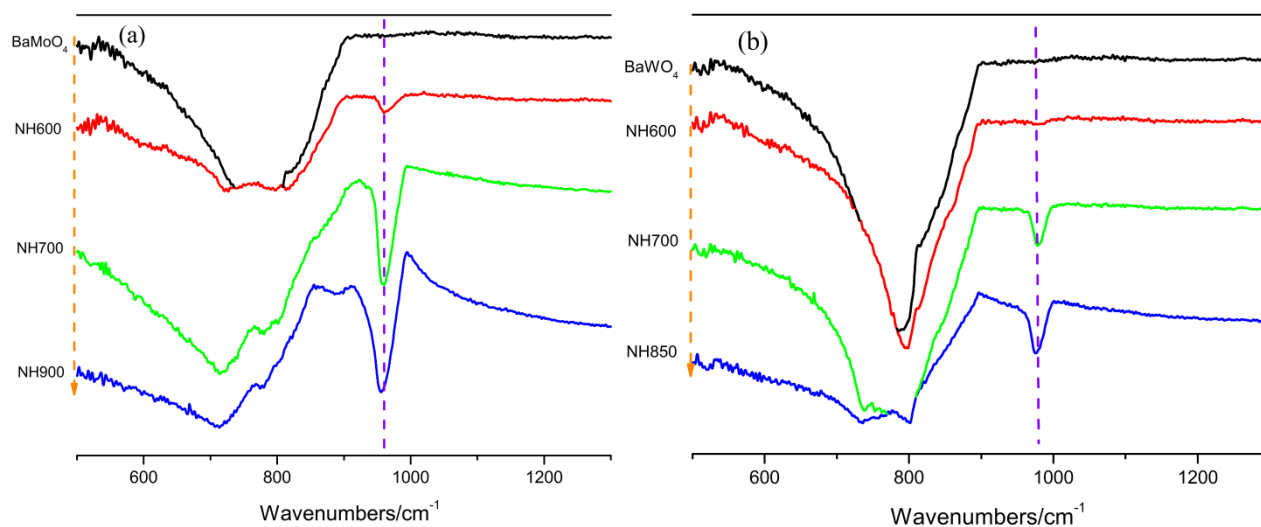


Figure S 5 FTIR spectra of the as-synthesized scheelite oxides and the corresponding materials after their ammonolysis at different temperatures: (a) BaMoO_4 ; (b) BaWO_4 . NHx00 denotes the thermal treatment at different temperatures under ammonia flow for 6 hours.

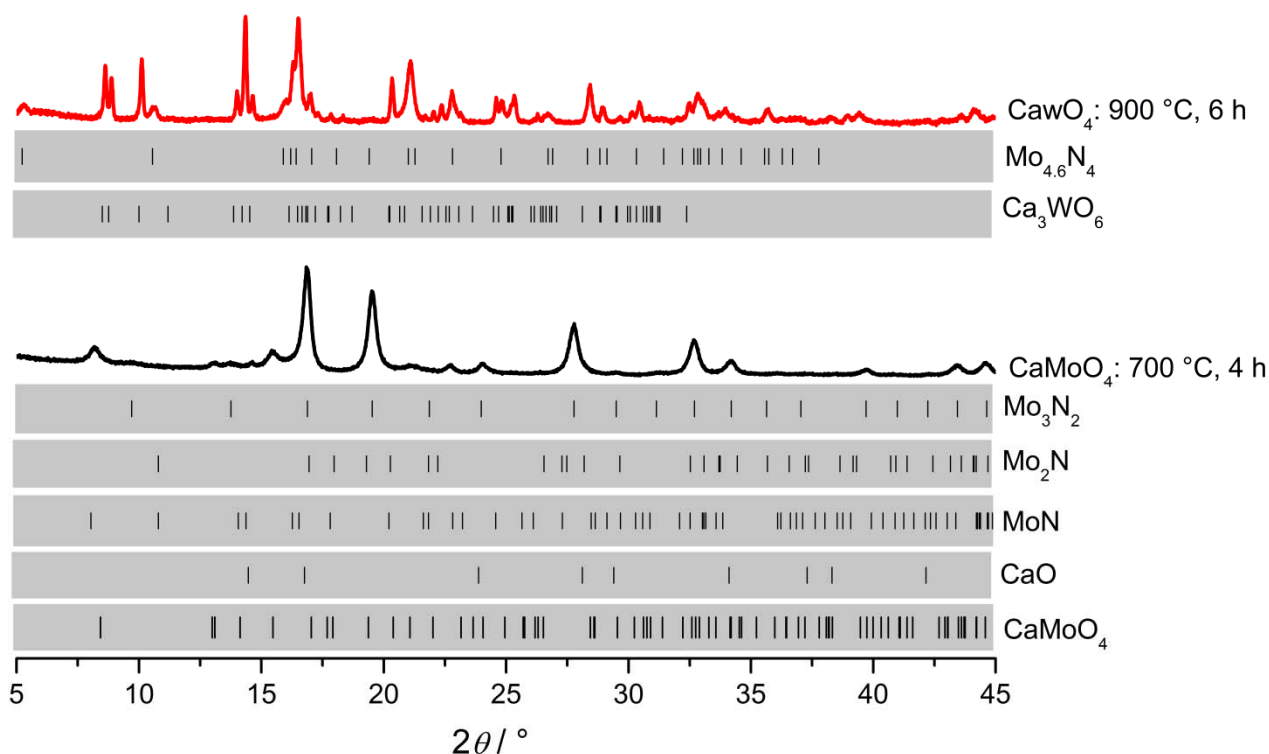


Figure S 6 XRD patterns of CaMoO_4 and CaWO_4 after ammonolysis at $700\text{ }^\circ\text{C}$ for 4 h (bottom) and $900\text{ }^\circ\text{C}$ for 6 h (top).

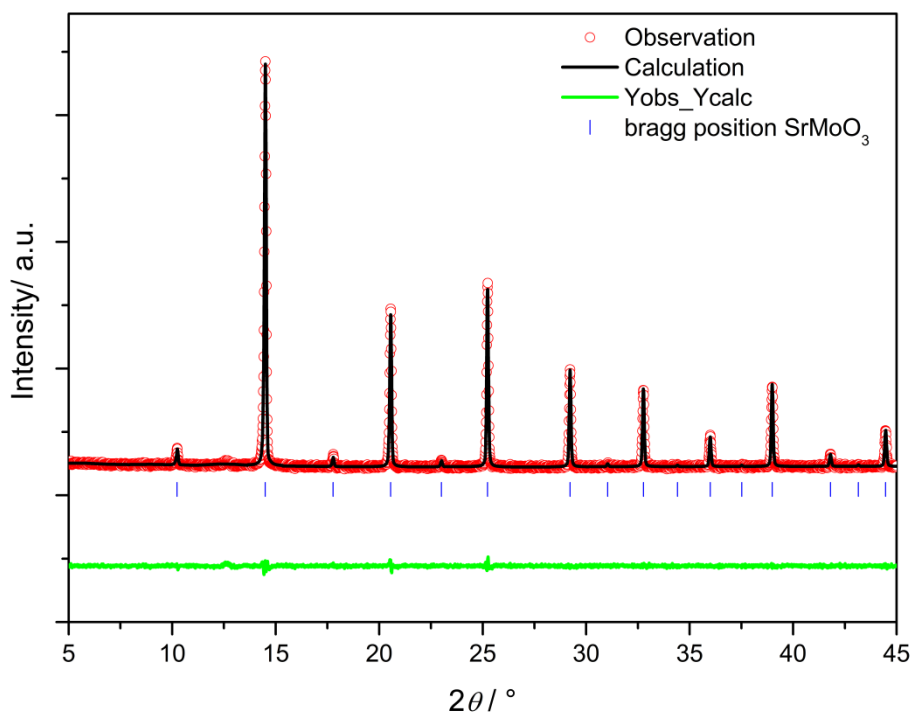


Figure S 7 Rietveld patterns of the X-ray powder diffraction data of the sample obtained upon reduction of the SrMoO_4 at $900\text{ }^\circ\text{C}$ for 6 h. Blue tick marks are Bragg peak positions of related phase as SrMoO_3 . Green line at the bottom denotes the difference intensities between the observed and calculated profiles. Error! Reference source not found. summarizes the results of the structure refinement.

Tables

Table S 1 Phase composition of the samples obtained via ammonolysis of BaMoO₄ at 700 and 900 °C for 6 hours from Rietveld refinement of the XRD patterns. ^[a]

Specimen	Ba ₃ Mo ₂ (O,N) ₈ (<i>R-3m</i> , Nr. 166, <i>Z</i> =3)	BaMoO ₄ (<i>I 41/a</i> , Nr. 88, <i>Z</i> =4)	Mo ₃ N ₂ (<i>Pm-3m</i> , Nr. 221, <i>Z</i> =1)	BaMoO ₃ (<i>Pm-3m</i> , Nr. 221, <i>Z</i> =1)
NH700 (Figure S 2 a)	79.93 a=5.9579(2) c=21.4662(6)	10.72 a=5.5830(14) c=12.8117(59)	9.35 a=4.1708(6)	0.01 a=4.0489(6)
NH900 (Figure S 2 b)	85.94 a=5.9670(3) c=21.4812(10)	/	14.06 a=4.1839(6)	/

[a] Fraction (wt%) and lattice parameter a,b,c [Å]

Table S 2 Phase composition of the samples obtained via ammonolysis of BaWO₄ at 850 °C for 6 hours from Rietveld refinement of the XRD patterns. ^[a]

Specimen	BaWO ₄ (<i>I 41/a</i> , Nr. 88, <i>Z</i> =4)	Ba ₃ W ₂ (O,N) ₈ (<i>R-3m</i> , Nr. 166, <i>Z</i> =3)	W _{4,6} N ₄ (<i>P63/mmc</i> , Nr. 194, <i>Z</i> =1)
NH850 (Figure S 4)	54.79 a=5.6111(2) c=12.7188(5)	34.24 a=6.0057(2) c=21.4469(9)	10.97 a=2.8943(7) c=15.1899(55)

[a] Fraction (wt%) and lattice parameter a,b,c [Å]

Table S 3 Crystal structure data of SrMoO_{3.61}N_{0.39}, SrMoO₄ and SrMoO₃

Specimens and parameters		SrMoO _{3.61(3)} N _{0.39(3)}	SrMoO ₄	SrMoO ₃
S.G.		<i>I 41/a</i> , Nr. 88	<i>I 41/a</i> , Nr. 88	<i>P m-3m</i> , Nr. 221
<i>Z</i>		4	4	1
a,b, Å		5.3947(2)	5.4032(2)	3.9763(1)
c, Å		12.0367(5)	12.0412(4)	/
Sr	x, y, z	0.0,0.25,0.625	0.0,0.25,0.625	0.5, 0.5, 0.5
	Biso, Å ²	0.210(70)	0.461(100)	0.472(47)
	Occ.	1	1	1
Mo	x, y, z	0.0,0.25,0.125	0.0,0.25,0.125	0.0, 0.0, 0.0
	Biso, Å ²	0.383(68)	0.587(95)	0.148(42)
	Occ.	1	1	1
O/N	x	0.24078(78)	0.24042(105)	0.5
	y	0.11411(69)	0.11602(88)	0.0
	z	0.04267(29)	0.04162(38)	0.0
	Biso, Å ²	-0.369(111)	0.380(161)	0.578(102)
	Occ.	3.61/0.39 ^a	4	3

^a: Not refined

Table S 4 The lattice parameters of $\text{Ba}_3\text{W}_2\text{O}_6\text{N}_2$ and $\text{W}_{4.6}\text{N}_4$ based on our as-synthesized sample via ammonolysis of BaWO_4 at 850 °C for 6 hours and Reference obtained by Rietveld refinement

	Lattice parameter based on our experiments		Lattice parameter from Reference	
	a=b	c	a=b	c
$\text{Ba}_3\text{W}_2\text{O}_6\text{N}_2$	6.0057 (2)	21.4469 (9)	6.0083 (6) ¹	21.4637 (6) ¹
$\text{W}_{4.6}\text{N}_4$	2.8943 (7)	15.1899 (55)	2.89 ²	15.3 ²

Table S 5 The oxygen and nitrogen content in weight percent of BaMoO_4 and BaWO_4 after thermal ammonolysis under different temperature. NHx00 denotes the different thermal ammonolysis temperatures.

Samples	BaMoO_4 NH600	BaMoO_4 NH700	BaMoO_4 NH900	BaWO_4 NH600	BaWO_4 NH700	BaWO_4 NH850
Oxygen wt%	18.3(0.166)	12.77(0.153)	11.54(0.174)	15.88(0.33)	13.58(0.276)	12.17(0.257)
Nitrogen wt%	0.788(0.002)	5.014(0.033)	5.476(0.021)	0.045(0.01)	8.74(0.297)	9.435(0.64)

Table S 6 The oxygen and nitrogen content in weight percent of SrMoO_4 and SrWO_4 after thermal ammonolysis under different temperature and holding time

Sample	Oxygen wt%	Nitrogen wt%
SrMoO_4 _NH400_4H	24.830(24)	0
SrMoO_4 _NH600_4H	22.260(25)	2.230(3)
SrMoO_4 _NH700_4H	14.790(18)	5.542(10)
SrMoO_4 _NH700_12H	13.940(270)	6.318(104)
SrMoO_4 _NH700_24H	12.750(215)	7.187(83)
SrMoO_3 _NH700_4H	19.180(178)	1.386(25)
SrWO_4 _NH400_4H	18.310(220)	0.017(15)
SrWO_4 _NH600_4H	18.740(123)	0.095(11)
SrWO_4 _NH700_4H	17.130(153)	1.002(6)
SrWO_4 _NH900_6H	8.547(375)	6.373(130)
SrWO_4 _NH900_12H	8.114(170)	7.006(110)
SrWO_4 _NH900_24H	7.977(25)	7.148(70)

Table S 7 Thermodynamic cycles for the determination of the enthalpies of formation of SrMoO₄ and SrMoO_{1.96}N_{1.04} relative to elementary components

Reaction	Enthalpy (kJ/mol)
(1) SrMoO ₄ (s, 25 C) = SrO (soln, 701 C) + MoO ₃ (soln, 701 C)	161.8 ± 1.5
(2) SrMoO _{1.96} N _{1.04} (s, 25 C) + 1.02O ₂ (g, 701 C) = SrO (soln, 701 C) + MoO ₃ (soln, 701 C) + 0.52N ₂ (g, 701 C)	-291.9 ± 2.3
(3) SrO (s, 25 C) = SrO (soln, 701 C)	-135.8 ± 2.5
(4) MoO ₃ (s, 25 C) = MoO ₃ (soln, 701 C)	72.8 ± 0.6
(5) O ₂ (g, 25 C) = O ₂ (g, 701 C)	21.8 ± 0
(6) N ₂ (g, 25 C) = N ₂ (g, 701 C)	20.6 ± 0
(7) Sr (s, 25 C) + 0.5 O ₂ (g, 25 C) = SrO (s, 25 C)	-591.3 ± 1
(8) Mo (s, 25 C) + 1.5O ₂ (g, 25 C) = MoO ₃ (s, 25 C)	-745.2 ± 0.4
(9) Sr (s, 25 C) + Mo (s, 25 C)+ 2O ₂ (g, 25 C) = SrMoO ₄ (s, 25 C)	
$\Delta H_9 = -\Delta H_1 + \Delta H_3 + \Delta H_4 + \Delta H_7 + \Delta H_8$	-1561.3 ± 3.1
(10) Sr (s, 25 C) + Mo (s, 25 C)+ 0.98O ₂ (g, 25 C) + 0.52N ₂ (g, 25 C) = SrMoO _{1.96} N _{1.04} (s, 25 C)	
$\Delta H_{10} = -\Delta H_2 + \Delta H_3 + \Delta H_4 - 1.02 \Delta H_5 + 0.52\Delta H_6 + \Delta H_7 + \Delta H_8$	-1119.124 ± 3.6

Table S 8 Thermodynamic cycles for the determination of the enthalpies of formation of SrWO₄ and SrWO_{1.5}N_{1.5} relative to elementary components

Reaction	Enthalpy		
	(kJ/mol)		
(1) SrWO ₄ (s, 25 C) = SrO (soln, 701 C) + WO ₃ (soln, 701 C)	162.8	±	1.5
(2) SrWO _{1.5} N _{1.5} (s, 25 C) + 1.25O ₂ (g, 701 C) = SrO (soln, 701 C) + WO ₃ (soln, 701 C) + 0.75N ₂ (g, 701 C)	-537.2	±	1.9
(3) SrO (s, 25 C) = SrO (soln, 701 C)	-135.8	±	2.5
(4) WO ₃ (s, 25 C) = WO ₃ (soln, 701 C)	91.7	±	1.3
(5) O ₂ (g, 25 C) = O ₂ (g, 701 C)	21.8	±	0
(6) N ₂ (g, 25 C) = N ₂ (g, 701 C)	20.6	±	0
(7) Sr (s, 25 C) + 0.5 O ₂ (g, 25 C) = SrO (s, 25 C)	-591.3	±	1
(8) W (s, 25 C) + 1.5O ₂ (g, 25 C) = WO ₃ (s, 25 C)	-842.9	±	0.8
(9) Sr (s, 25 C) + W (s, 25 C) + 2O ₂ (g, 25 C) = SrWO ₄ (s, 25 C)			
$\Delta H_9 = -\Delta H_1 + \Delta H_3 + \Delta H_4 + \Delta H_7 + \Delta H_8$	-1641.2	±	3.8
(10) Sr (s, 25 C) + W (s, 25 C) + 0.75O ₂ (g, 25 C) + 0.75N ₂ (g, 25 C) = SrWO _{1.5} N _{1.5} (s, 25 C)			
$\Delta H_{10} = -\Delta H_2 + \Delta H_3 + \Delta H_4 - 1.25 \Delta H_5 + 0.75 \Delta H_6 + \Delta H_7 + \Delta H_8$	-952.9	±	4.3

Table S 9 The enthalpies of formation and standard entropies of SrMoO₄ nitridation reaction for Gibbs free energy calculation

	SrMoO ₄	NH ₃	SrMoO ₂ N	H ₂ O	H ₂	N ₂
$\Delta_f H$ (kJ/mol)	-1561.3*	-45.94	-1119.124*	-241.826	0	0
S^0 (J/mol·K) ³	128.9	192.776	107.417 ^a	188.835	130.68	191.609

*: from our own calorimetric experiment results

^a: estimated as the value of 5/6 SrMoO₄

Table S 10 The enthalpies of formation and standard entropies of SrWO₄ nitridation reaction for Gibbs free energy calculation

	SrWO ₄	NH ₃	SrWO _{1.5} N _{1.5}	H ₂ O	H ₂	N ₂
$\Delta_f H$ (kJ/mol)	-1641.2*	-45.94	-952.9*	-241.826	0	0
S^0 (J/mol·K) ^{3,4}	138.07	192.776	115.06 ^a	188.835	130.68	191.609

*: from our own calorimetric experiment results

^a: estimated as the value of 5/6 SrWO₄

References

1. Weller, M. T.; Skinner, S. J., Neutron and X-ray powder diffraction studies of the oxynitrides SrW(O,N)(3), Ba₃W₂(O,N)(8) and Ba₃Mo₂(O,N)(8). *Int J Inorg Mater* **2000**, 2, (5), 463-467.
2. Pinsker, Z. G., The Investigation of Some Carbides and Nitrides of Chrome, Iron, Tungsten and Molybdenum by Electron Diffraction. *Acta Crystallogr* **1957**, 10, (12), 775-775.
3. Dean, J. A.; Lange, N. A., *Lange's handbook of chemistry*. McGraw-Hill: 1992.
4. R, L. D., *CRC Handbook*. 84th edition ed.; CRC Press: Boca Raton, Florida, 2003.



Synthesis and rapid sintering of dense SrA(O,N)₃ (A = Mo, W) oxynitride ceramics

Wenjie Li^{a,1}, Duan Li^{b,1}, Aleksander Gurlo^c, Zhijian Shen^b, Ralf Riedel^a, Emanuel Ionescu^{a,*}

^a *Fachbereich Material- und Geowissenschaften, Technische Universität Darmstadt, Jovanka-Bontschits-Str. 02, D-64287 Darmstadt, Hessen, Germany*

^b *Department of Materials and Environmental Chemistry, Arrhenius Laboratory, Stockholm University, S-106 91 Stockholm, Sweden*

^c *Fachgebiet Keramische Werkstoffe, Institut für Werkstoffwissenschaften und -technologien, Fakultät III Prozesswissenschaften, Technische Universität Berlin, Hardenbergstraße 40, 10623 Berlin, Germany*

Received 23 October 2014; received in revised form 11 December 2014; accepted 12 December 2014

Available online 23 January 2015

Abstract

SrMo(O,N)₃ and SrW(O,N)₃ oxynitride powders were synthesized via a solvothermal route followed by ammonolysis. Their rapid densification by spark plasma sintering with a heating rate of 300–400 °C/min under a uniaxial pressure of 100 MPa yielded dense monoliths. The lowest open porosity achieved was 0 vol% for SrMo(O,N)₃ and 7.6 vol% for SrW(O,N)₃. The compacted monoliths were characterized by elemental analysis, electron microscopy (SEM, TEM) coupled with energy dispersive X-ray spectroscopy (EDX), as well as X-ray diffraction (XRD). Rietveld refinement of the XRD patterns revealed in the case of the compacted SrMo(O,N)₃ the formation of small amount of ternary oxides (Sr₃Mo₂O₇/SrMoO₄/Sr₃MoO₆), molybdenum nitride (Mo₂N), as well as metallic Mo. On the contrary, SrW(O,N)₃ exhibited significant decomposition after consolidation, with SrWO₄/Sr₃WO₆ being main components beside SrMo(O,N)₃, accompanied by tungsten nitride (WN) and metallic W. Thus, rapid SPS enables the densification of oxynitrides with high density and acceptable purity that were hardly achieved earlier.

© 2014 Elsevier Ltd. All rights reserved.

Keywords: Perovskite; Oxynitride; Spark plasma sintering; Densification; Microstructure

1. Introduction

Perovskite-type oxynitrides have attracted considerable attention over the last thirty years, especially during the last decade.^{1–5} The incorporation of nitrogen atoms into their crystal structure results in multifunctional properties due to the reduction of the band gap. Various crystalline structures can thus be tailored, and consequently perovskite oxynitrides represent an emerging class of materials suitable for novel applications in the fields of photocatalysts,^{6–13} non-toxic pigments,^{14–16} colossal magnetoresistance^{17,18} or dielectrics^{19–22}.

Most of the known perovskite-type oxynitrides contain early transition metals such as Ti, V,^{23,24} Zr, Nb and Ta, as well

as Mo and W and exhibit intriguing thermoelectric, electrical conductivity and magnetic properties.^{25–29} Mixed-valence molybdenum and tungsten oxynitride perovskites (SrA(O,N)₃ (A = Mo, W)) are expected to have good electronic conductivity. This group of materials has been, however, rather poorly investigated as dense monoliths so far.

The synthesis of perovskite-type oxynitride powders is usually conducted via a soft chemical route followed by ammonolysis. Sintering is a critical step for obtaining dense oxynitride monoliths suitable for characterization and demanded applications.^{30–32} Previous thermodynamic studies indicated that perovskite-type oxynitrides such as LaTiO₂N, SrTaO₂N, NdTiO₂N and CaTaO₂N encountered severe decomposition at 800–1300 °C.^{32–35} This evidence raised challenges for the sintering practice, as the densification processes of these compounds normally start at temperatures beyond 1100 °C^{32,35}. Therefore, oxynitride-based monoliths prepared so far by conventional sintering methods often revealed relatively low density and purity, as long dwelling time are needed for the entire

* Corresponding author. Tel.: +49 6151 166344; fax: +49 6151 166346.

E-mail address: ionescu@materials.tu-darmstadt.de (E. Ionescu).

¹ These authors contributed equally to the work and should be regarded as co-first authors.

sintering cycle. Spark plasma sintering (SPS) enables the rapid consolidation of materials with high densities due to two main advantages: (i) very high heating rates (up to $>1000^\circ\text{C}/\text{min}$) are applicable; (ii) high external pressures can be uniaxially applied ($>100\text{ MPa}$).^{36–39} Moreover, in the case of sintering conductive materials, the ‘field effect’ can facilitate the densification process.^{37,38,40} In our previous work, LaTiO_2N ceramic with a relative density of 94% and a purity of 86% was prepared by SPS at 1350°C under 125 MPa.³² Thus, it seems worthy to densify $\text{SrA}(\text{O},\text{N})_3$ ($\text{A} = \text{Mo}, \text{W}$) oxynitrides by SPS, again upon using high heating rates and uniaxial pressures in order to promote densification and at the same time to suppress possible degradation of the oxynitride materials.

In this study, we implemented a solvothermal route with subsequently ammonolysis to synthesize $\text{SrMo}(\text{O},\text{N})_3$ and $\text{SrW}(\text{O},\text{N})_3$ oxynitride powders. Both powders were then consolidated by SPS using high heating rates under uniaxial pressures. The compositional and structural changes of the compounds prior to and post sintering were examined with the aim of optimizing the SPS conditions to obtain oxynitride monoliths with high purities and reasonable low skeletal densities for further physical property characterization.

2. Experimental procedure

Scheelite-type oxide precursors, i.e., SrMoO_4 and SrWO_4 , were synthesized by using the following solvothermal method: $\text{Sr}(\text{NO}_3)_2$ (Sigma-Aldrich, 99.0%) was mixed in an equimolar ratio with $\text{Na}_2\text{MoO}_4 \cdot 4\text{H}_2\text{O}$ (or $\text{Na}_2\text{WO}_4 \cdot 4\text{H}_2\text{O}$) (Sigma-Aldrich, $>99.5\%$) in ethylenediamine (FLUKA, $>99.5\%$) under vigorous stirring. Subsequently, the precursor mixture was transferred into an autoclave with Teflon lining and heated at 200°C for 24 h. The resulting mixture was rinsed repeatedly with de-ionized water and ethanol (5 times each). After centrifugation and drying at 60°C overnight, scheelite-type oxide powders were produced.⁴¹ The resulting oxide powders were further ground to reduce the particle size down to $<500\text{ nm}$. The oxide powders were placed in a quartz crucible for nitridation in flowing ammonia at temperatures between 700 and 900°C for 6–24 h. The Schlenk system used for thermal ammonolysis is specifically limited to small batch sizes (about 0.3–0.5 g) in order to maximize the exposure to flowing NH_3 and guarantee the homogeneity of the resulting oxynitrides. Four groups of samples, labeled as $\text{SrMoO}_4\text{-NH700-12H}$, $\text{SrMoO}_4\text{-NH700-24H}$, $\text{SrWO}_4\text{-NH900-12H}$ and $\text{SrWO}_4\text{-NH900-24H}$, respectively, were selected for further SPS consolidation study.

The SPS compaction experiments were performed in vacuum in a SPS apparatus (Dr. Sinter 2050, Sumitomo Coal Mining Co. Ltd., Tokyo, Japan). For each test $\sim 1\text{ g}$ powder was loaded into a cylindrical graphite die with an inner diameter of 12 mm. The temperature was automatically raised to 600°C over a period of 3 min, above which it was monitored and regulated by a radiation pyrometer focused on the outer surface of the die. Table 1 summarizes the sintering parameters applied. Different heating rates (300 or $400^\circ\text{C}/\text{min}$) and sintering temperatures (1200 or 1250°C) were tested while a uniaxial pressure of 100 MPa was applied at 600°C until the end of the sintering cycle with 1 min

Table 1
Sintering parameters, density, and O/N content of the as-synthesized powders and as-sintered samples.

Sample	Sintering parameters				Density			O/N content (wt%)	
	Heating rate ($^\circ\text{C}/\text{min}$)	Temperature ($^\circ\text{C}$)	Dwell time (min)	Pressure (MPa)	Geometrical (g/cm^3)	Skeletal (g/cm^3)	Open Porosity (vol%)	As-synthesized	As-sintered
$\text{SrMoO}_4\text{-NH700-12H}$ ($\text{SrMoO}_{2.09}\text{N}_{0.91}$)	400	1200	1	100	5.67	5.73	1.0	13.94 (O) 6.318 (N)	14.820 (O) 1.214 (N)
$\text{SrMoO}_4\text{-NH700-24H}$ ($\text{SrMoO}_{1.96}\text{N}_{1.04}$)	400	1200	1	100	6.03	6.03	0	12.75 (O) 7.187 (N)	16.110 (O) 1.662 (N)
$\text{SrWO}_4\text{-NH900-12H}$ ($\text{SrWO}_{1.42}\text{N}_{1.58}$)	300	1250	1	100	6.81	7.36	7.6	8.114 (O) 7.006 (N)	11.060 (O) 0.9193 (N)
$\text{SrWO}_4\text{-NH900-24H}$ ($\text{SrWO}_{1.39}\text{N}_{1.61}$)	300	1250	1	100	5.87	6.44	8.7	7.977 (O) 7.148 (N)	13.890 (O) 0.8707 (N)

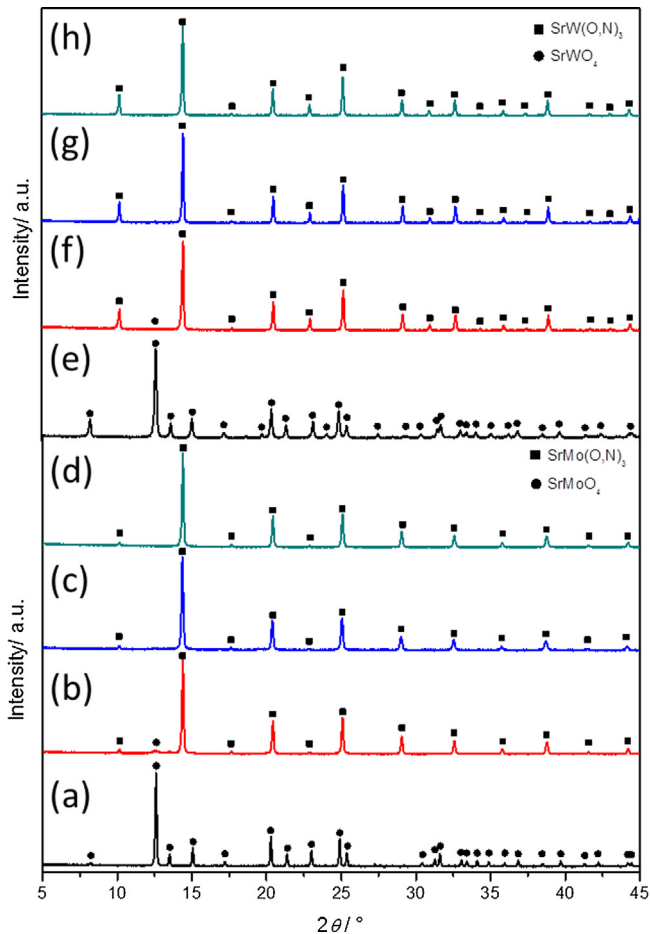


Fig. 1. XRD patterns of SrMoO₄ (a) and SrMo(O,N)₃ powders synthesized under ammonia at 700 °C for 6 h (b), 12 h (c), 24 h (d) as well as of SrWO₄ (e) and SrW(O,N)₃ powder synthesized under ammonia at 900 °C for 6 h (f), 12 h (g), 24 h (h).

dwelling in all cases. The shrinkage (ΔL) and linear shrinkage rate (defined as $-\text{d}(\Delta L/L_0)/\text{d}t$, with L_0 being the thickness of the green body at room temperature) were recorded in one second intervals in real time. The densities of the sintered samples were determined by the Archimedes' method (water immersion) and compared to the geometrical densities of the corresponding oxynitrides (see Table 1).

The weight change of the samples was studied by means of thermal gravimetric analysis (TGA) and simultaneous differential thermal analysis (DTA) device (STA 449C Jupiter, Netzsch, Germany) coupled with a quadrupole mass spectrometer (QMS 403C Aeolus, Netzsch, Germany). The measurements were done under flowing argon at ambient pressure, with a heating rate of 10 °C/min up to 1400 °C. Elemental analyses for nitrogen and oxygen were performed by means of hot gas extraction techniques using a LECO TC-436 analyzer (LECO Corporation, Michigan, USA). Five analyses were performed of each specimen in order to get an appropriate accuracy of the determined chemical composition. To identify the phase assemblage, X-ray diffraction (XRD) patterns of the as-synthesized powders and the SPS consolidated ceramic samples were recorded by using powder diffractometers STOE STADI

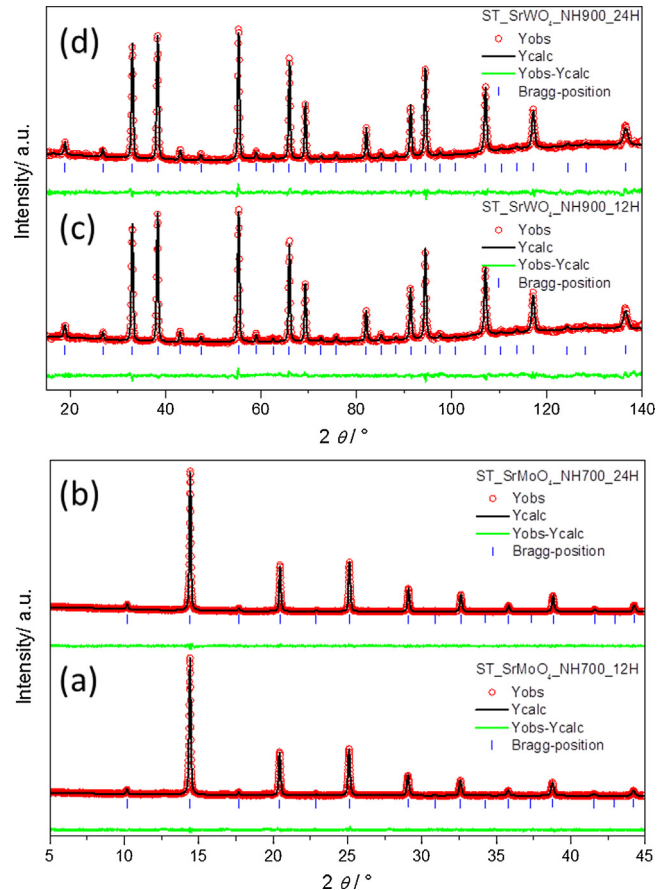


Fig. 2. Rietveld refinement of X-ray diffraction and Neutron diffraction patterns of the sample obtained from the ammonolysis of SrMoO₄ at 700 °C for 12 (a) and 24 h (b) as well as SrWO₄ at 900 °C for 12 (c) and 24 h (d). Blue tick marks are Bragg peak positions of SrMo(O,N)₃ and SrW(O,N)₃, respectively. The green lines at the bottom denote the different intensities between the observed and calculated profiles. (For interpretation of the references to color in this figure legend, the reader is referred to the web version of this article.)

P (STOE & Cie GmbH, Darmstadt, Germany) with Mo $K\alpha$ radiation ($\lambda = 0.7093 \text{ \AA}$) operating over a 2θ range of 5–45° and XPERTPRO (PANalytical, Almelo, the Netherlands) with Cu $K\alpha$ radiation ($\lambda = 1.5418 \text{ \AA}$) operating over a 2θ range of 15–80°, respectively. Prior to the XRD measurements, the surfaces of the sintered samples were well polished to assure that the surface layer contaminated by graphite was removed. The Fine Resolution Powder Diffractometer (FIREPOD, E9)⁴² were performed at the BERII of the Helmholtz-Zentrum Berlin (HZB), Germany. The measurements were carried out by using a neutron wavelength of $\lambda = 1.3084 \text{ \AA}$. Crystallographic parameters were confirmed by the individual Rietveld refinements of the XRD and ND patterns. The reflection shapes were modeled with pseudo-Voigt function for XRD and Thompson–Cox–Hastings pseudo-Voigt function⁴³ for ND patterns. Isotropic thermal parameters of O/N were constrained to the same value for the anions. All refinements were performed using the Fullprof software.⁴⁴ Field emission scanning electron microscopes (FE-SEM, JSM-7000F, JEOL Ltd., Tokyo, Japan; XL30 FEG, Philips Ltd., The Netherlands) and a Schottky-type field emission transmission electron microscope

Table 2
Crystal structure data for SrMo(O,N)₃ and SrW(O,N)₃ powder samples.

Parameters		SrMoO ₄ _NH700_12H	SrMoO ₄ _NH700_24H	SrWO ₄ _NH900_12H	SrWO ₄ _NH900_24H
Radiation		X-ray Mo K α	X-ray Mo K α	Neutron (HRPT, PSI)	Neutron (HRPT, PSI)
λ (Å)		0.7093	0.7093	1.494	1.494
S.G.		<i>Pmm</i> , Nr. 221	<i>Pmm</i> , Nr. 221	<i>Pmm</i> , Nr. 221	<i>Pmm</i> , Nr. 221
Z		1	1	1	1
a,b, c (Å)		3.99851(20)	3.99427(13)	3.98451(6)	3.98379(8)
Sr	x, y, z	0.5, 0.5, 0.5	0.5, 0.5, 0.5	0.5, 0.5, 0.5	0.5, 0.5, 0.5
	B _{iso} (Å ²)	0.926(67)	0.761(46)	0.577(44)	0.601(46)
	Occ.	1.0	1.0	1.0	1.0
Mo	x, y, z	0.0, 0.0, 0.0	0.0, 0.0, 0.0	0.0, 0.0, 0.0	0.0, 0.0, 0.0
	B _{iso} (Å ²)	1.148(69)	0.965(47)	0.693(46)	0.853(49)
	Occ.	1.0	1.0	1.0	1.0
O/N	x, y, z	0.5, 0.0, 0.0	0.5, 0.0, 0.0	0.5, 0.0, 0.0	0.5, 0.0, 0.0
	B _{iso} (Å ²)	1.498(120)	0.857(88)	0.725(21)	0.693(23)
	Occ.	1.96/1.04 ^a	1.82/1.18 ^a	1.449/1.551	1.364/1.636
χ^2		1.069	1.079	1.152	1.152
R_p		2.06	1.93	2.11	2.26
wR_p		2.64	2.43	2.65	2.85
χ^2		1.38	1.42	1.39	1.61

^a Fixed by elemental analysis results without refinement.

(TEM, JEM-2100F, JEOL Ltd., Tokyo, Japan) were used for microstructural characterization. For TEM study, the bulk samples were crushed into powders (average grain size ~60 nm) and dispersed in absolute ethanol with ultrasonication for 15 min. A droplet of the suspension was transferred onto a copper grid.

3. Results and discussion

3.1. Synthesis of SrA(O,N)₃ (A = Mo, W)

Ammonolysis of the scheelite-type SrMoO₄ and SrWO₄ oxide precursors at 700–900 °C resulted in the formation of

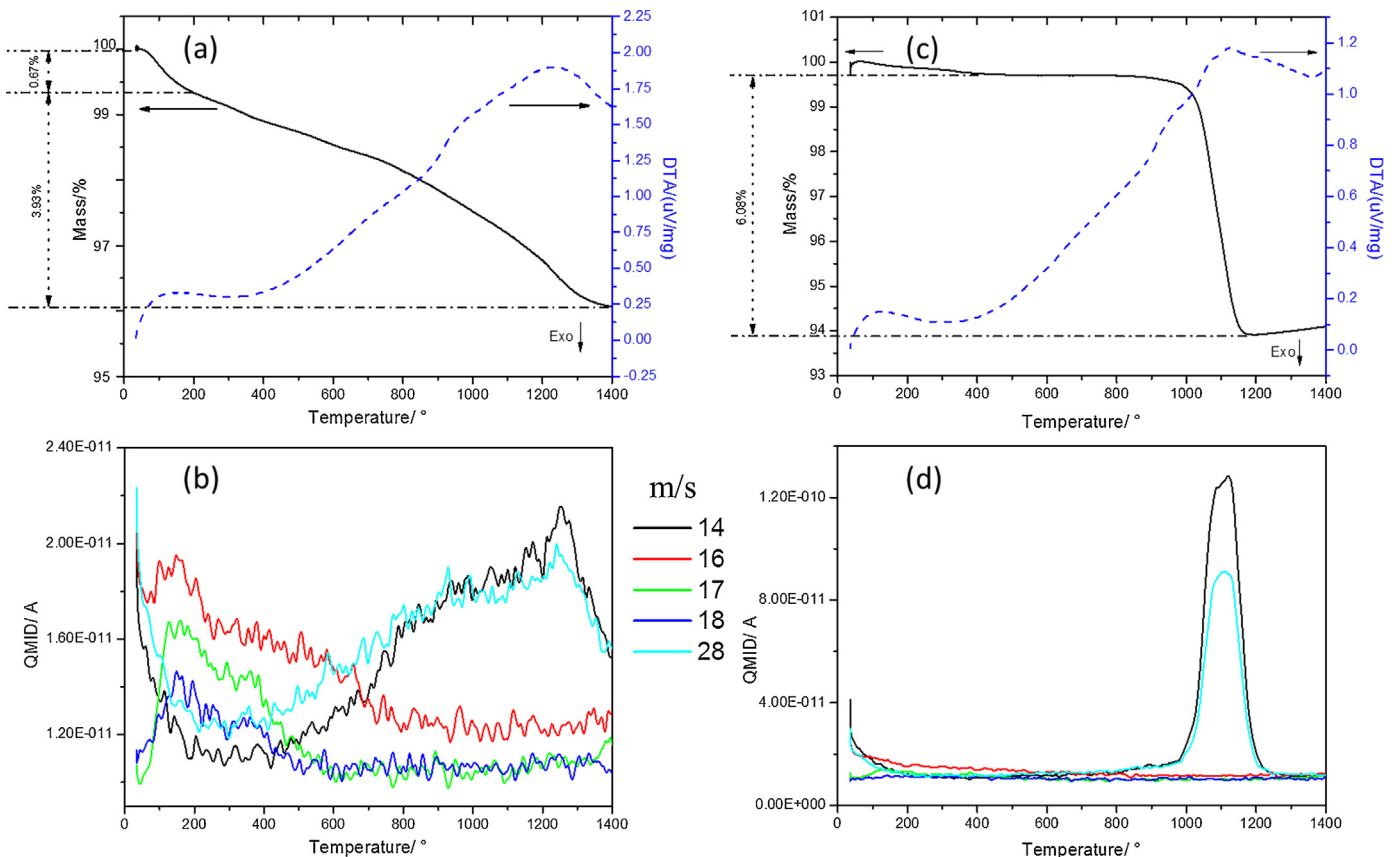


Fig. 3. TGA/DTA curves and corresponding QMID (quasi multiple ion detection) ion current curves under argon for SrMoO₄.NH700.12H (a and b) and SrWO₄.NH900.12H (c and d), respectively.

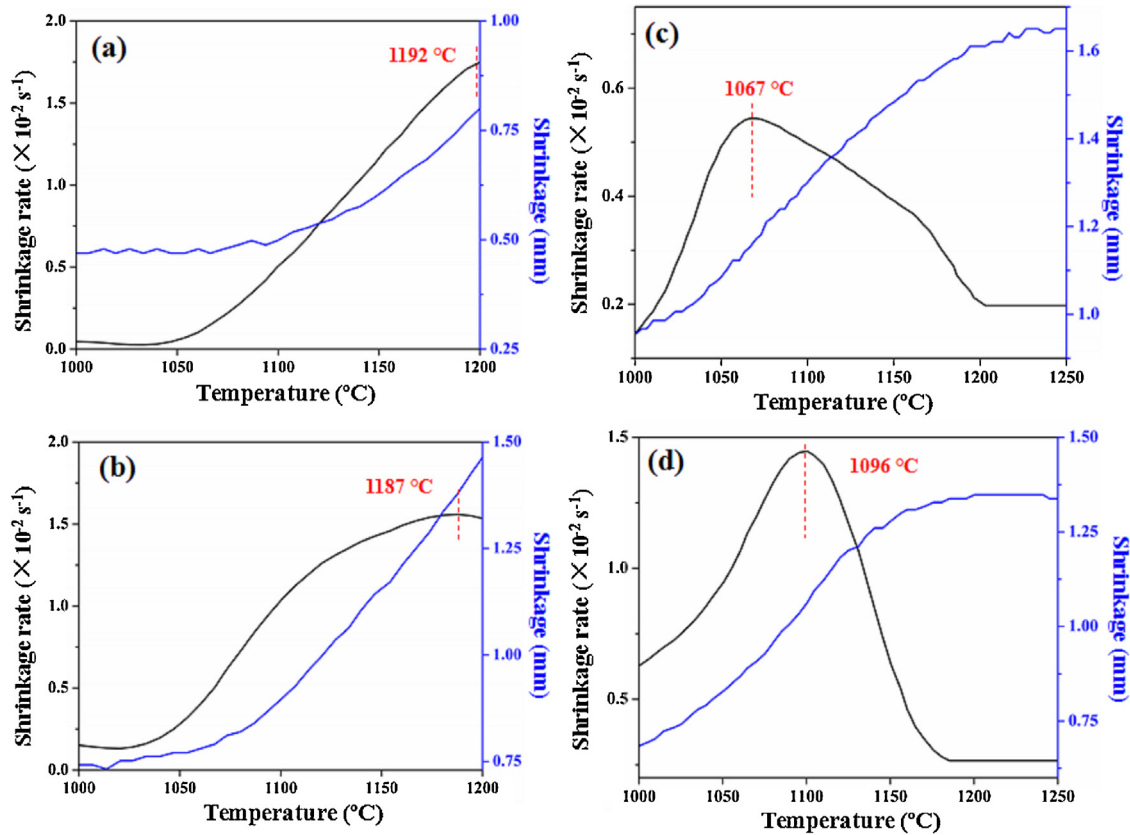


Fig. 4. Shrinkage and shrinkage rate for SrMoO₄_NH700_12H (a), SrMoO₄_NH700_24H (b), SrWO₄_NH900_12H (c) and SrWO₄_NH900_24H (d) as functions of the temperature.

single-phase perovskite-type oxynitride upon 12 h, as shown in Fig. 1, whereas a tiny amount of initial oxide phases still remained in both cases after 6 h holding. Thus, only 4 phase-pure samples treated for 12 and 24 h were selected for further Rietveld analysis and SPS experiments, i.e. SrMoO₄_NH700_12H, SrMoO₄_NH700_24H, SrWO₄_NH900_12H, and SrWO₄_NH900_24H.

The O/N content of the prepared oxynitride powders (listed in Table 1) shows a slight increasing of the nitrogen content with prolonging the ammonolysis time. Moreover, no carbon content was detected in the prepared materials, even after the SPS processes.

Rietveld refinements of selected samples were performed in the space group *Pm-3m*, as shown in Fig. 2. The single phase was confirmed. The refined O/N content of SrW(O,N)₃ based on neutron powder diffraction (Table 2) corresponds to the composition SrWO_{1.45}N_{1.55} and SrWO_{1.36}N_{1.64}, which are in a reasonable agreement with the result obtained from the elemental analysis.

It is necessary to understand the thermal stability of materials since during the densification process at high temperature decomposition may occur. Thus, the thermal behavior of SrMo(O,N)₃ and SrW(O,N)₃ in argon atmosphere was assessed, in order to find suitable sintering parameters. The results obtained from thermogravimetric analysis (TGA) coupled with differential thermal analysis (DTA) and evolved gas analysis (i.e. mass spectrometry, MS) are summarized in Fig. 3. A continuous weight loss is observed during heating the samples up to 1400 °C, with a total mass loss of 4.6 wt% for SrMo(O,N)₃. The relatively small mass loss of ~0.67 wt% (Fig. 3a) in the temperature range from RT to 200 °C relies on the removal of absorbed water, as well as the absorbed ammonia on the surface of oxynitrides, as confirmed by MS (Fig. 3b). The mass loss at temperatures beyond 200 °C is due to a continuing removal of N₂ which was also confirmed by *in situ* MS and suggested for analogous perovskite-type oxynitrides.^{34,45}

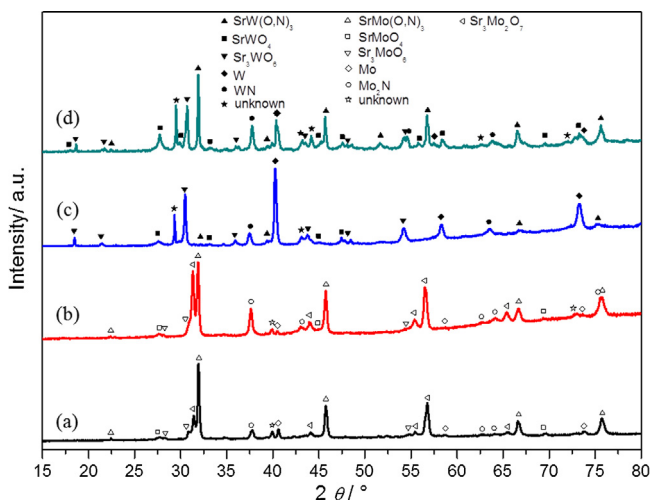


Fig. 5. X-ray diffraction patterns for the as-sintered samples SrMoO₄_NH700_12H (a), SrMoO₄_NH700_24H (b), SrWO₄_NH900_12H (c) and SrWO₄_NH900_24H (d).

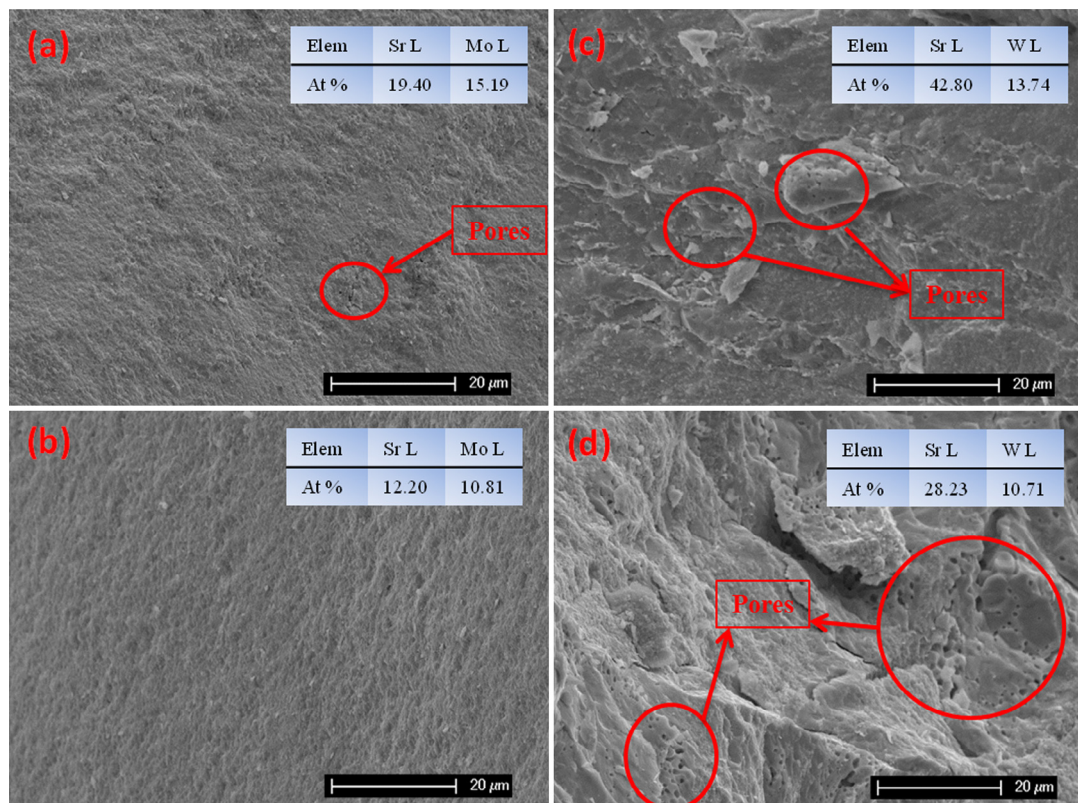


Fig. 6. SEM images for the cross-section of the sintered monolith samples: SrMoO₄_NH700_12H (a); SrMoO₄_NH700_24H (b); SrWO₄_NH900_12H (c) and SrWO₄_NH900_24H (d).

The thermal stability of SrW(O,N)₃ under argon flow seems different, and thus the mass loss occur in three distinct stages, as shown in Fig. 3c and d. As mentioned above, a small mass loss of ~0.35 wt% occurring below 400 °C corresponds to the removal of absorbed and chemically bonded water. Between ~400 °C and 1000 °C, almost no mass loss is observed. In the third stage, a sharp mass loss (~6.08 wt%) happens from 1000 °C to 1150 °C, related to the release of N₂ (as shown by *in situ* MS). This result implies that significant decomposition of the oxynitride takes place at temperatures above 1000 °C.

3.2. Sintering process and structural evolution

The applied SPS parameters as well as the skeletal densities and open porosities achieved in the consolidated samples are summarized in Table 1. Sintering curves in terms of the recorded shrinkage and shrinkage rate plotted versus temperature are shown in Fig. 4 for all samples. As can be seen, a high heating rate of 400 °C/min was used for SrMo(O,N)₃ samples; while for SrW(O,N)₃ a rate of 300 °C/min was chosen. In both cases a uniaxial pressure of 100 MPa was applied. The total time needed for entire SPS cycle was less than 10 min. Despite a short sintering cycle, low open porosity values were observed: 1 vol% and 0 vol% for SrMo(O,N)₃ as well as 7.6 vol% and 8.7 vol% for SrW(O,N)₃. Especially the skeletal densities of SrMo(O,N)₃ were found to be significantly higher than those obtained for LaTiO₂N,⁴⁶ NdTiO₂N, CaTaO₂N and BaTaO₂N³⁵ by either pressureless sintering, hot-press sintering or SPS.

The densification behavior of both oxynitrides is revealed by the sintering curves shown in Fig. 4. For SrMo(O,N)₃, the shrinkage started at ~1050 °C and the maximum shrinkage rate was observed at 1187–1192 °C (see Fig. 4a and b); whereas the densification of SrW(O,N)₃ started at ~1000 °C with the maximum shrinkage rate being observed at 1067–1096 °C. It appears that a sintering temperature of 1200 °C is high enough for consolidating SrMo(O,N)₃ and is slightly lower than that required for consolidating SrW(O,N)₃. This difference in the sintering behavior induces the observed density difference of the two oxynitrides, and is probably also related to the difference in their thermal stability as shown in Fig. 3. For SrMo(O,N)₃, the maximum release of nitrogen due to decomposition occurred at temperatures beyond the sintering temperature (i.e., 1200 °C) and the total mass loss at 1200 °C was <3.5 wt% (see Fig. 3a and b). While SrW(O,N)₃ suffered a significant degradation already at 1100 °C and the total mass loss at the sintering temperature (i.e., 1250 °C) was >6.0 wt%. The dissociation of the oxynitrides generated pores inside the sintered bodies that further reduced the density (see later the SEM and TEM results in Figs. 6 and 7).

The decomposition of oxynitrides was observed in all as-sintered samples, as shown in Fig. 5. SrMoO₄_NH700_12H and SrMoO₄_NH700_24H samples showed similar phase compositions, i.e. SrMo(O,N)₃ as main phase and small amounts of other phases which resulted from decomposition-related nitrogen release (Fig. 5a and b). Whereas, the SrWO₄_NH900_12H sample encountered more severe decomposition, yielding Sr₃WO₆, SrWO₄, WN, metallic W as decomposition phases and

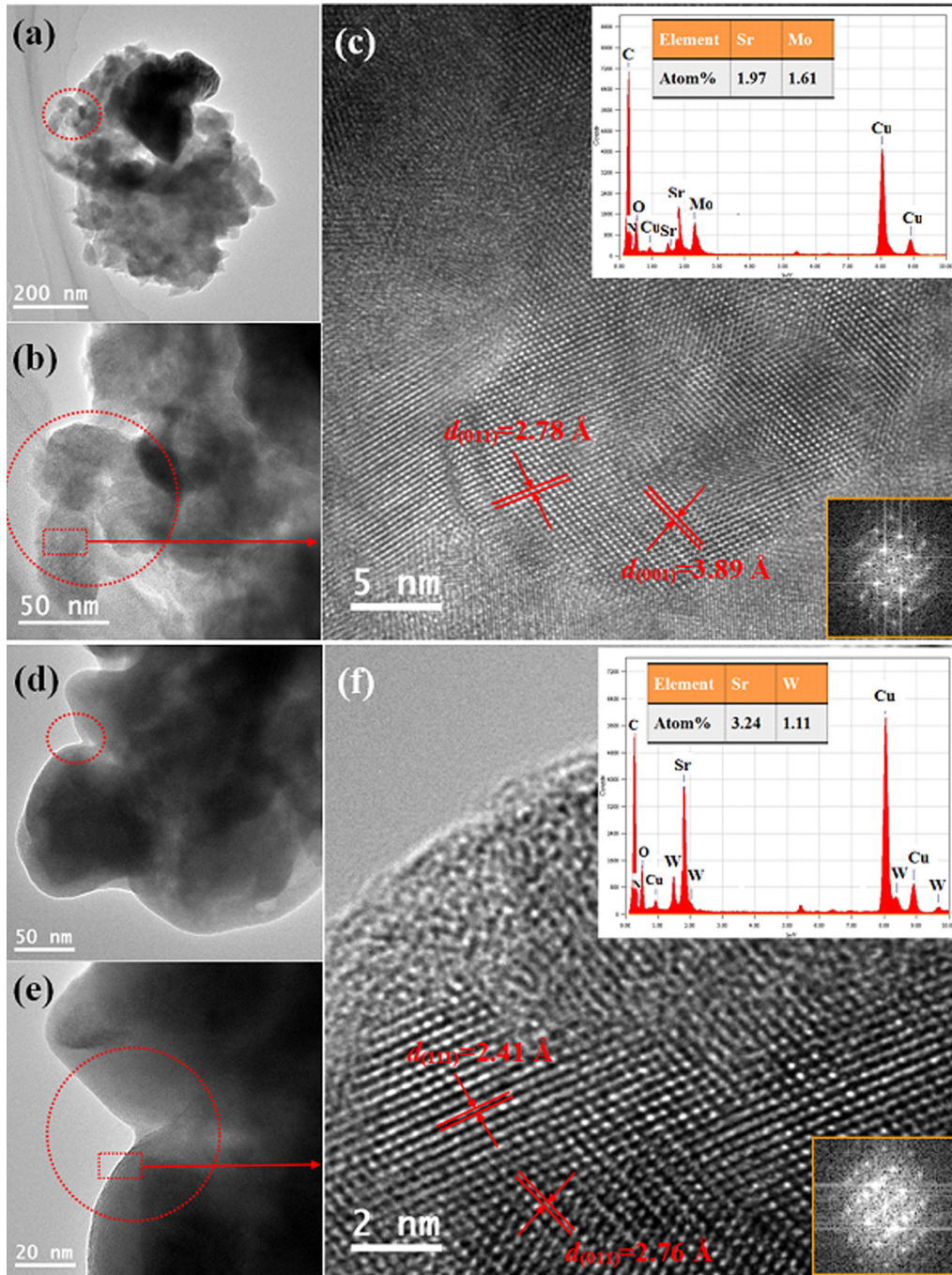


Fig. 7. HRTEM/EDX analysis for the as-sintered monolith samples SrMoO₄_NH700_24H (a–c) and SrWO₄_NH900_12H (d–f). The circles in (b), and (e) indicate the region from where the EDX data shown in (c) and (f), respectively, were collected; whereas the rectangles from (b) and (e) correspond to the regions from where the magnified HRTEM images in (c) and (e), respectively, were collected.

SrW(O,N)₃ as a minor phase. The sample SrWO₄_NH900_24H exhibited only minor amounts of decomposition phases (Fig. 5c and d).

Fig. 6 shows the SEM micrographs taken on the cross-section of the as-sintered SrMo(O,N)₃ and SrW(O,N)₃ samples. The as-sintered SrW(O,N)₃ samples exhibit large number of pores, as shown in Fig. 6c and d, indicating the presence of closed porosity in addition to the determined open porosity. On the contrary, the SrMo(O,N)₃ samples were shown to be almost fully dense, especially in the case of using SrMo(O,N)₃

powder prepared upon ammonolysis time of 24 h. The Sr/Mo and Sr/W molar ratios determined by EDX were nearly 1:1 and 3:1, respectively. Thus, a significant decomposition of SrW(O,N)₃ took place during the SPS process and led to the formation of Sr₃WO₆ as major phase (Fig. 5); whereas SrMo(O,N)₃ did not show the decomposition as strong as SrW(O,N)₃ during the SPS consolidation.

Fig. 7 illustrates the HRTEM/EDX analysis results of the monolithic samples SrMoO₄_NH700_24H and SrWO₄_NH900_12H possessing very low open porosity

of 0 and 1 vol%, respectively. For SrMoO₄-NH700_24H, a piece of sintered monolith was selected for detailed characterization (see Fig. 7a). The HRTEM images (see Fig. 7c) clearly show the lattice fringes of the (0 1 1) and (0 0 1) planes. The EDX spectrum on the top-right confirmed the existence of Sr, Mo, O, N, Cu (from the Cu grid) and C (from the carbon film). The quantitative analysis indicates an overall metallic composition of Sr_{1.97}Mo_{0.61}. The slight excess of Sr over Mo suggests that some decomposition of the SrMo(O,N)₃ occurs. When it comes to the SrWO₄-NH900_12H sample, a few pores can be observed inside the sintered monolith pieces (Fig. 7d and e), which is in good agreement with the information obtained from Table 1 and Fig. 6. The HRTEM image with FFT pattern also confirmed a good crystallinity (Fig. 7f). The molar ratio between Sr and W, as revealed by EDX, is 2.92. Thus, the Sr content is significantly larger than that of W, supporting the existence of the Sr₃WO₆ phase (as also revealed by XRD). Overall, the sintered SrMo(O,N)₃ samples have better purity and high density than the SrW(O,N)₃ samples.

4. Conclusion

Scheelite-type SrAO₄ powders (A=Mo, W) were synthesized by a solvothermal reaction and converted upon thermal treatment in flowing ammonia at 700–900 °C for 6–24 h into perovskite-type SrMo(O,N)₃ and SrW(O,N)₃ oxynitrides. Four powder samples, i.e. SrMoO₄-NH700_12H, SrMoO₄-NH700_24H, SrWO₄-NH900_12H and SrWO₄-NH900_24H, were densified by spark plasma sintering with heating rates of 300–400 °C/min and a uniaxial pressure of 100 MPa to achieve open porosity values of 1, 0, 7.6, and 8.7 vol%, respectively. For the SrW(O,N)₃ samples decomposition occurred during sintering, since their densification needs temperatures higher than the decomposition temperature, as suggested by the TGA/MS study and the recorded SPS curves. Interestingly, SrMo(O,N)₃ was found to be significantly more resistant with respect to decomposition and thus near fully dense monoliths were obtained. The rapid SPS process proved to be promising for the consolidation of perovskite-type oxynitrides compared to other conventional consolidation methods. Future work will be focused on the assessment of the physical properties of the SrMo(O,N)₃ monolithic samples.

Acknowledgements

The authors would like to thank Jia Yuan and Claudia Fasel from Technical University of Darmstadt for their help on SEM and TGA/MS measurement. We thank Dr. Stefan Zander (HZB) for the technical assistance during the neutron beamtime. Financial support of this work by European Commission through the Marie-Curie ITN project “Functional Nitrides for Energy Applications, FUNEA” (FP7-PITN-GA-2010-264873) is gratefully acknowledged.

References

- Ebbinghaus SG, Abicht HP, Dronskowski R, Müller T, Reller A, Weidenkaff A. Perovskite-related oxynitrides—recent developments in synthesis,

- characterisation and investigations of physical properties. *Prog Solid State Chem* 2009;**37**:173–205.
- Fuertes A. Chemistry and applications of oxynitride perovskites. *J Mater Chem* 2012;**22**:3293–9.
- Kim YI, Woodward PM. Syntheses and characterizations of complex perovskite oxynitrides LaMg_{1/3}Ta_{2/3}O₂N, LaMg_{1/2}Ta_{1/2}O_{5/2}N_{1/2}, and BaSc_{0.05}Ta_{0.95}O_{2.1}N_{0.9}. *J Solid State Chem* 2007;**180**:3224–33.
- Marchand R, Laurent Y, Guyader J, L'Haridon P, Verdier P. Nitrides and oxynitrides: preparation, crystal chemistry and properties. *J Eur Ceram Soc* 1991;**8**:197–213.
- Li W, Ionescu E, Riedel R, Gurlo A. Can we predict the formability of perovskite oxynitrides from tolerance and octahedral factors? *J Mater Chem A* 2013;**1**:12239–45.
- Hisatomi T, Katayama C, Moriya Y, Minegishi T, Katayama M, Nishiyama H, et al. Photocatalytic oxygen evolution using BaNbO₂N modified with cobalt oxide under photoexcitation up to 740 nm. *Energy Environ Sci* 2013;**6**:3595–9.
- Maeda K, Higashi M, Siritanaratkul B, Abe R, Domen K. SrNbO₍₂₎N as a water-splitting photoanode with a wide visible-light absorption band. *J Am Chem Soc* 2011;**133**:12334–7.
- Masanobu Higashi RA, Takata T, Domen K. Photocatalytic overall water splitting under visible light using ATaO₂N (A = Ca, Sr, Ba) and WO₃ in a IO₃⁻/I⁻ shuttle redox mediated system. *Chem Mater* 2009;**21**:1543–9.
- Siritanaratkul B, Maeda K, Hisatomi T, Domen K. Synthesis and photocatalytic activity of perovskite niobium oxynitrides with wide visible-light absorption bands. *ChemSusChem* 2011;**4**:74–8.
- Zhang FX, Yamakata A, Maeda K, Moriya Y, Takata T, Kubota J, et al. Cobalt-modified porous single-crystalline LaTiO₂N for highly efficient water oxidation under visible light. *J Am Chem Soc* 2012;**134**:8348–51.
- Kasahara A, Nukumizu K, Hitoki G, Takata T, Kondo JN, Hara M, et al. Photoreactions on LaTiO₂N under visible light irradiation. *J Phys Chem A* 2002;**106**:6750–3.
- Leroy CM, Maegli AE, Sivula K, Hisatomi T, Xanthopoulos N, Otal EH, et al. LaTiO₂N/In₂O₃ photoanodes with improved performance for solar water splitting. *Chem Commun* 2012;**48**:820–2.
- Maeda K, Lu DL, Domen K. Oxidation of water under visible-light irradiation over modified BaTaO₂N photocatalysts promoted by tungsten species. *Angew Chem Int Ed* 2013;**52**:6488–91.
- Aguirer R, Lopinovich D, Weidenkaff A, Rachel A, Reller A, Ebbinghaus SG. The vast colour spectrum of ternary metal oxynitride pigments. *Dyes Pigm* 2008;**76**:70–5.
- Jansen M, Letschert HP. Inorganic yellow–red pigments without toxic metals. *Nature* 2000;**404**:980–2.
- Tessier F, Maillard P, Chevre F, Domen K, Kikkawa S. Optical properties of oxynitride powders. *J Ceram Soc Jpn* 2009;**117**:1–5.
- Kusmartseva A, Yang M, Oró-Solé J, Bea AM, Fuertes A, Attfield JP. Large magnetoresistances and non-Ohmic conductivity in EuWO_{1+x}N_{2-x}. *Appl Phys Lett* 2009;**95**:02210.
- Yang M, Oro-Sole J, Kusmartseva A, Fuertes A, Attfield JP. Electronic tuning of two metals and colossal magnetoresistances in EuWO_{1+x}N_{2-x} perovskites. *J Am Chem Soc* 2010;**132**:4822–9.
- Chevre F, Tessier F, Marchand R. Optical properties of the perovskite solid solution LaTiO₂N-ATiO(3) (A = Sr, Ba). *Eur J Inorg Chem* 2006;**2006**:1223–30.
- Gouin RMX, Laurent Y, Gervais F. Infrared dielectric response of BaTaO₂N. *Solid State Commun* 1995;**93**:857–9.
- Lu Y, Ziani A, Le Paven-Thivet C, Benzerga R, Le Gendre L, Fasquelle D, et al. Perovskite oxynitride LaTiO_xN_y thin films: dielectric characterization in low and high frequencies. *Thin Solid Films* 2011;**520**:778–83.
- Zhang YR, Motohashi T, Masubuchi Y, Kikkawa S. Local anionic ordering and anisotropic displacement in dielectric perovskite SrTaO₍₂₎N. *J Ceram Soc Jpn* 2011;**119**:581–6.
- Antoine P, Assabaa R, L'Haridon P, Marchand R, Laurent Y, Michel C, et al. Transport properties of the new perovskite-type LaVO_{3-x}N_x oxynitrides. *Mater Sci Eng B* 1989;**5**:43–6.
- Oró-Solé J, Clark L, Bonin W, Attfield JP, Fuertes A. Anion-ordered chains in a d1 perovskite oxynitride: NdVO₂N. *Chem Commun* 2013;**49**:2430–2.

25. Fawcett ID, Ramanujachary KV, Greenblatt M. Synthesis, structure and properties of the oxynitrides SrWO₂N and SrMoO_{2.5}N_{0.5}. *Mater Res Bull* 1997;**32**:1565–70.
26. Liu G, Zhao XH, Eick HA. The Synthesis, Structure. Characterization of (SrMoO_{2.6}N_{0.4})-N-15. *J Alloy Compd* 1992;**187**:145–56.
27. Logvinovich D, Aguiar R, Robert R, Trottmann M, Ebbinghaus SG, Reller A, et al. Synthesis Mo-valence state, thermal stability and thermoelectric properties of SrMoO_{3-x}N_x (x > 1) oxynitride perovskites. *J Solid State Chem* 2007;**180**:2649–54.
28. Logvinovich D, Hejtmanek J, Knizek K, Marysko M, Homazava N, Tomes P, et al. On the magnetism, thermal- and electrical transport of SrMoO₂N. *J Appl Phys* 2009;**105**:023522.
29. Po Antoine RM, Lament Y, Michel C, Raveau B. On the electrical properties of the perovskites LnWO_xN_{3-x}. *Mater Res Bull* 1988;**23**:953–7.
30. Petrovsky V, Manohar A, Dogan F. Dielectric constant of particles determined by impedance spectroscopy. *J Appl Phys* 2006;**100**:014102.
31. Zhang YR, Motohashi T, Masubuchi Y, Kikkawa S. Sintering and dielectric properties of perovskite SrTaO₂N ceramics. *J Eur Ceram Soc* 2012;**32**:1269–74.
32. Li D, Li WJ, Fasel C, Shen J, Riedel R. Sinterability of the oxynitride LaTiO₂N with perovskite-type structure. *J Alloy Compd* 2014;**586**:567–73.
33. Aguiar R, Logvinovich D, Weidenkaff A, Reller A, Ebbinghaus SG. Thermal oxidation of oxynitride perovskites in different atmospheres. *Thermochim Acta* 2008;**471**:55–60.
34. Tessier F, Le Gendre L, Chevire F, Marchand R, Navrotsky A. Thermochemistry of a new class of materials containing dinitrogen pairs in an oxide matrix. *Chem Mater* 2005;**17**:3570–4.
35. Ahchawarattaworn J. *Perovskite oxynitride dielectrics*. Newcastle: Newcastle University; 2011 [Dissertation].
36. Omori M. Sintering, consolidation, reaction and crystal growth by the spark plasma system (SPS). *Mater Sci Eng A* 2000;**287**:183–8.
37. Munir ZA, Anselmi-Tamburini U, Ohyanagi M. The effect of electric field and pressure on the synthesis and consolidation of materials: a review of the spark plasma sintering method. *J Mater Sci* 2006;**41**:763–77.
38. Shen ZJ, Johnsson M, Zhao Z, Nygren M. Spark plasma sintering of alumina. *J Am Ceram Soc* 2002;**85**:1921–7.
39. Li D, Hu JF, Zhang JZ, Ma J, Shen Z. Densification as an exothermic process revealed by rapid high temperature consolidation of BaTiO₃ nanopowder. *Adv Appl Ceram* 2014;**113**:251–6.
40. Olevsky EA, Froyen L. Impact of thermal diffusion on densification during SPS. *J Am Ceram Soc* 2009;**92**:S122–32.
41. Li WJ, Ionescu E, Riedel R, in preparation.
42. Többs DM, Stüßer N, Knorr K, Mayer HM, Lampert G. E9: The new high-resolution neutron powder diffractometer at the Berlin Neutron Scattering Center. *Mater Sci Forum* 2001;**378–381**:288–93.
43. Thompson P, Cox DE, Hastings JB. Rietveld refinement of Debye–Scherrer synchrotron X-Ray data from Al₂O₃. *J Appl Crystallogr* 1987;**20**:79–83.
44. Rodriguezcarvajal J. Recent advances in magnetic-structure determination by neutron powder diffraction. *Physical B* 1993;**192**:55–69.
45. Pascual EC, Gutierrez VB, Subda M, Puche RS. Synthesis, structural and magnetic characterization of the EuNbO₍₂₎N oxynitride. *Solid State Sci* 2008;**10**:1905–9.
46. Le Paven-Thivet C, Le Gendre L, Le Castrec J, Chevire F, Tessier F, Pinel J. Oxynitride perovskite LaTiO_xN_y thin films deposited by reactive sputtering. *Prog Solid State Chem* 2007;**35**:299–308.



Sinterability of the oxynitride LaTiO_2N with perovskite-type structure



Duan Li^a, Wenjie Li^b, Claudia Fasel^b, James Shen^{a,*}, Ralf Riedel^b

^a Department of Materials and Environmental Chemistry, Arrhenius Laboratory, Stockholm University, S-106 91 Stockholm, Sweden

^b Technische Universität Darmstadt, Institut für Materialwissenschaft, Petersenstrasse 32, D-64287 Darmstadt, Germany

ARTICLE INFO

Article history:

Received 27 August 2013

Received in revised form 9 October 2013

Accepted 10 October 2013

Available online 25 October 2013

Keywords:

Spark plasma sintering

Perovskite-type oxynitride

Sinterability

Thermal analysis

Kinetics

X-ray diffraction

ABSTRACT

Based on a thermal stability study, the sinterability of the oxynitride LaTiO_2N was investigated by spark plasma sintering (SPS). The results show that LaTiO_2N is thermodynamically unstable above ca. 400 °C in air and ca. 800 °C in argon. While it appears impossible to completely avoid decomposition during sintering, LaTiO_2N ceramics with relative density of 74–94% and a residual LaTiO_2N content of 57–90 wt% were prepared. By manipulating kinetics, a relative density of 94% was achieved at 1350 °C under an uniaxially applied pressure of 125 MPa. This density is higher than any other counterparts prepared by conventional sintering so far. SPS appears a feasible tool for manipulating the sintering kinetics. It enables the preparation of almost dense LaTiO_2N bulks with adequate purity.

© 2013 Elsevier B.V. All rights reserved.

1. Introduction

There is an increasing demand of novel perovskite-type materials possessing multifunctional properties for electronic/dielectric [1,2], magnetic [3,4], catalytic and energy conversion applications [5,6]. Oxynitrides with perovskite-type structure are particularly of interest since the progressive introduction of nitrogen into the oxidic perovskite structure leads to the band gap reduction [7–13]. Their structural and functional properties can thus be tailored by modifying the anion partial lattice, and unique physical, thermal and chemical properties are generated accordingly. During the last decade, perovskite-type oxynitrides have been studied as promising candidates for a broad range of applications, e.g. non-toxic pigments [12,13], high-K dielectrics [14–18], ferroelectrics [19], catalysts/photocatalysts [20,21] and magnetic materials [22,23].

As one of the common perovskite-type oxynitrides, LaTiO_2N has been recognized as a candidate for dielectric and photocatalytic applications due to its ferroelectric behaviour and low band gap value (~ 2.0 eV) [9,15]. The so far encountered problem has been the difficulty in obtaining well-sintered dense materials [14]. Most of the reported dielectric constants of LaTiO_2N were measured on thin films prepared by chemical or physical vapour deposition techniques (CVD and PVD) [16,20,24]. The accuracy of those measurements is still under debate [17,19]. Since the dielectric properties of ceramics are sensitive to porosity and interface, it is

desirable to obtain a dense material for meaningful measurement and for feasible practical use [18,25]. Despite many attempts made so far by conventional sintering methods, only densities below 80% of the theoretical density (TD) have been achieved under the condition without other additives. Sintering for longer times at elevated temperatures by these processes also results in severe decomposition of the oxynitride.

As a pressure and external electrical field assisted densification process, spark plasma sintering (SPS) provides the possibility to obtain dense oxynitride ceramics with limited decomposition. Due to the effective heating and the application of a uniaxial pressure, very fast heating rates and rapid densification are assured [26–29]. The aim of this work is to examine the feasibility of applying SPS for obtaining dense perovskite-type oxynitride ceramics by studying LaTiO_2N as a test material. In the first part of this work we investigated the thermal stability of LaTiO_2N both in air and in argon atmospheres at temperatures up to 1400 °C. In the second part of the work we studied how to prepare dense LaTiO_2N ceramics by SPS. In both parts the evolution of the phase composition and the microstructure of the sintered materials at different temperatures were characterized and are discussed below.

2. Experimental procedures

LaTiO_2N powder (labelled as LT0N-0) was synthesized by an ammonolysis nitridation route and provided by Newcastle University in UK.

The spark plasma sintering trials were carried out in vacuum in a SPS apparatus (Dr. Sinter 2050, Sumitomo Coal Mining Co. Ltd., Tokyo, Japan). LaTiO_2N powder with a weight of ~ 1 g was loaded into a cylindrical graphite die with an inner

* Corresponding author. Tel.: +46 8 162388.

E-mail address: shen@mmk.su.se (J. Shen).

Table 1
Sintering parameters, relative density, LaTiO₂N phase content and chemical composition of LaTiO₂N powders and SPSeD samples.

Sample	Sintering parameters				Relative Density (% TD)	LaTiO ₂ N Phase content (wt%)	Chemical Composition (N/O, atomic ratio)
	Heating rate (°C/min)	Temperature (°C)	Dwell time (min)	Pressure (MPa)			
LaTiO ₂ N ^a	–	–	–	–	–	100	0.50
LTON-0	–	–	–	–	–	100	0.46
LTON-0 ^b	–	–	–	–	–	0	0.0034
LTON-0 ^c	–	–	–	–	–	–	0.23
LTON-1	250	1350	1	125	94	86	0.31
LTON-2	250	1250	1	75	74	93	0.33
LTON-3	250	1400	2	100	93	57	–
LTON-4	100	1300	5	75	81	66	–
LTON-5	100	1300	5	100	88	67	–
LTON-6	300	1350	2	100	91	90	–

^a Theoretical stoichiometry.

^b After TGA/DTA/MS measurement in air.

^c After TGA/DTA/MS measurement in argon.

diameter of 12 mm. The temperature was automatically raised to 600 °C over a period of 3 min, and from this temperature and above it was monitored and regulated by a radiation pyrometer focused on the surface of the die. Sintering runs were performed by using different parameters, as shown in Table 1. The highest density was achieved in a sample prepared at 1350 °C for dwelling of 1 min when a heating rate of 250 °C/min was applied, labelled as LTON-1. For this run a uniaxial pressure of 100 MPa was applied at room temperature and held constant from the beginning up to 1300 °C, where it was increased to 125 MPa until the end of the sintering cycle. The shrinkage (ΔL) and linear shrinkage rate (defined as $-d(\Delta L/L_0)/dt$, with L_0 being the thickness of the green body at room temperature) during the sintering process were recorded in one second intervals. To reveal the sintering kinetics, the recorded temperature, shrinkage and shrinkage rate during the preparation of the LTON-1 specimen were plotted versus time. The relative density of the sintered sample was determined by the Archimedes' method by assuming the value of 6.3 g/cm³ as the theoretical density of the fully dense LaTiO₂N ceramics.

The thermal stability of LaTiO₂N was studied by means of thermal gravimetric analysis (TGA) and simultaneous differential thermal analysis (DTA) device (STA 449C Jupiter, Netzsch, Germany) coupled with a quadrupole mass spectrometer (QMS 403C Aeolos, Netzsch, Germany). The measurements were done separately under flowing air and argon at ambient pressure, with a heating rate of 10 °C/min up to 1400 °C. A field emission scanning electron microscope (FE-SEM, JSM-7000F, JEOL, Tokyo, Japan) was used for microstructure characterization. To identify the phase assemblage, X-ray diffraction (XRD) patterns of the powder and sintered ceramic samples were recorded by using a XPERTPRO powder diffractometer (PANalytical, Almelo, the Netherlands) and Cu K α radiation ($\lambda = 1.5418$ Å) operating over a 2θ range of 20–80°. Prior to XRD, the surface of the sintered sample was polished to assure that the surface graphite contamination was removed. The phase contents in the multi-phase ceramic samples were determined semi-quantitatively by Rietveld refinement. Fourier-transform infrared spectrometry (FTIR) spectroscopic measurements were carried out from 4000 to 400 cm⁻¹ using

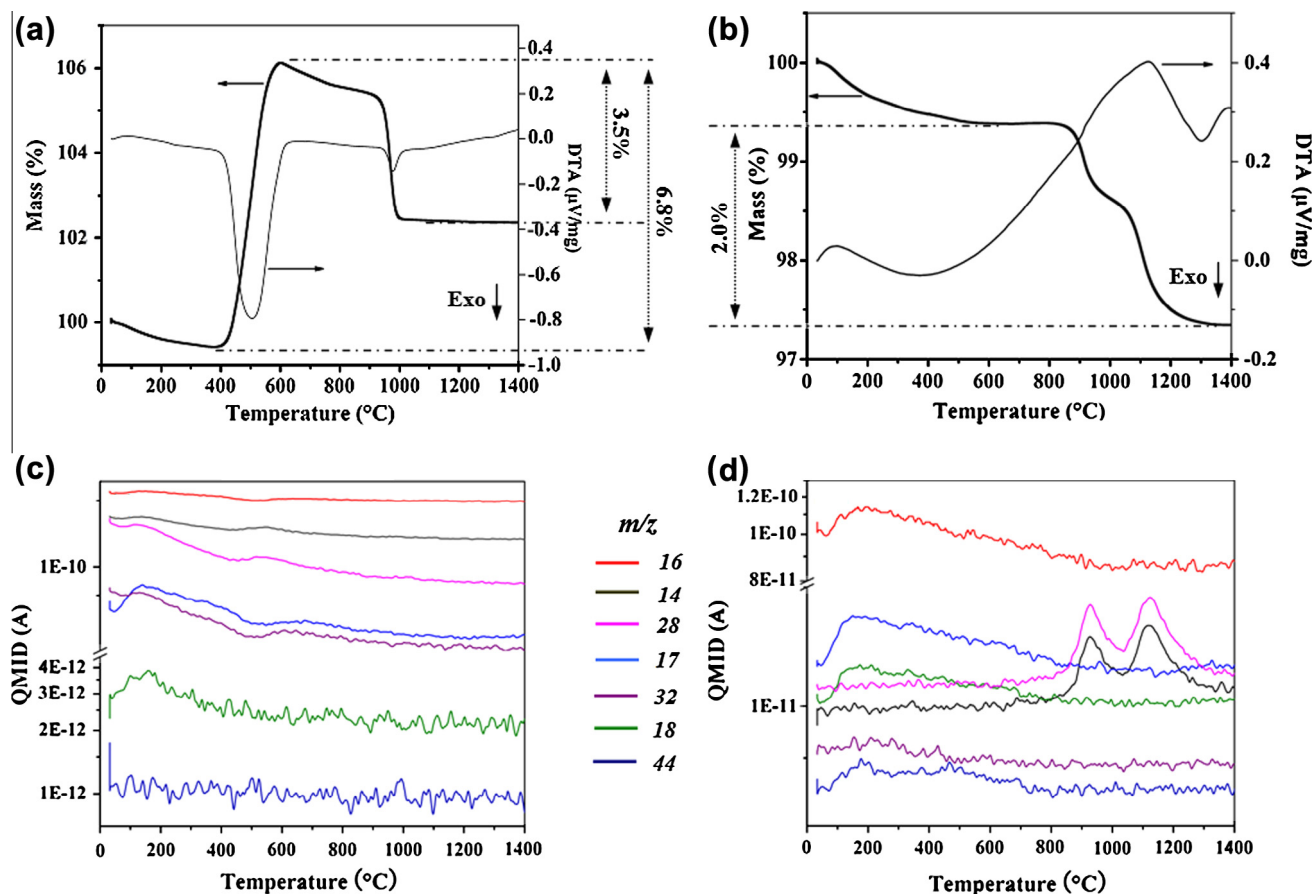


Fig. 1. TGA/DTA curves and corresponding QMID ion current curves for LaTiO₂N under air (a and c) and argon flow (b and d).

a spectrometer (Varian 670-IR, Varian Inc., USA) equipped with a single-reflection Golden Gate ATR accessory with a diamond ATR element. Elemental analyses for nitrogen and oxygen were performed by means of hot gas extraction techniques using a LECO TC-436 analyzer (LECO Corporation, Michigan, USA). Five analyses were performed of each specimen in order to get a better accuracy of the determined chemical composition.

3. Results and discussion

3.1. Thermal stability of LaTiO_2N in air and argon

It is necessary to understand the thermal stability of LaTiO_2N , since during the densification process at high temperature decomposition may take place. In our study, all the SPS runs were performed in vacuum by applying high heating rates (100–300 °C/min) under a uniaxial pressure of 75–125 MPa. Such high heating rates and vacuum can hardly be achieved during the TGA/DTA measurements. However, the thermal behavior of LaTiO_2N in vacuum could be predicted by knowing the thermodynamic results in other atmospheres. Thus, we chose two different atmospheres, air and argon, to generally survey the thermal behaviour of LaTiO_2N for a guidance of the optimized sintering parameters.

The results generated by the TGA/DTA combined with MS analysis are summarized in Fig. 1. The mass change during heating in air flow undergoes three stages. During the first stage (RT to ~400 °C) a slight mass loss of ~0.6 wt% is found, which is ascribed to the removal of adsorbed and chemically bonded water (see Fig. 1(a)) as confirmed by the appearance of the MS peaks $m/e = 17$ and 18 (see the corresponding mass spectra in Fig. 1(c)). The presence of minute amounts of chemically bonded water results from traces of H_2O present in the ammonia gas during the synthesis process of the oxynitride. At the second stage, between ~400 °C and ~600 °C, a major mass gain (~6.8 wt%) is analyzed during an exothermic process revealed by the DTA curve. The observed reaction is due to a hydrolysis reaction of LaTiO_2N [30–33]. The concurrent release of N_2 is confirmed by the presence of the MS peaks with $m/e = 28$ and 14. In the third stage, from ~600 °C to ~1000 °C, the sample reveals a total weight loss of 3.5 wt% corresponding to the continuing removal of residual N_2 as it has been recently suggested for analogous perovskite-type oxynitrides [22,31,32].

The thermal stability of LaTiO_2N under argon flow is quite different as seen in Fig. 1(b and d). A continuous weight loss is found all the way from RT up to 1400 °C, with a total loss of 2.6 wt%. As mentioned above, a small weight loss of ~0.6 wt% occurring below 600 °C can be ascribed to the removal of adsorbed and chemically bonded water [13], which is supported by the observation of the MS peaks at $m/e = 18, 17$, and 16, see Fig. 1(d). A broad MS peak at $m/e = 44$ suggests the formation of N_2O in association with the partial decomposition of LaTiO_2N or the desorption of CO_2 [30]. Between ~820 °C and ~1300 °C an additional stepwise mass loss of ~2.0 wt% is measured, accompanied with a simultaneously release of nitrogen indicated by the presence of the MS peaks at $m/e = 14$ and 28. This result indicates a further decomposition of the oxynitride during this temperature interval. It is interesting to note that although the large part of the nitrogen is released as N_2 , small amounts of NO_x ($\text{NO}, \text{NO}_2, \text{N}_2\text{O}$, etc.) may also be detected. The formation of NO_x is probably due to the presence of nitrogen species that are bonded in the perovskite structure, which react with residual O_2 and form NO_x instead of recombining to N_2 [30]. Although the sensitivity of the mass spectrometer is not completely identical for the various masses, a comparison of the ion currents clearly indicates that the major part of the nitride anions in our study form N_2 while the formation of any nitrogen oxide compounds is only a small side fact. The DTA curve indicates that all the processes involved in argon atmosphere are endothermic, especially those occurring between ~900 °C and ~1300 °C.

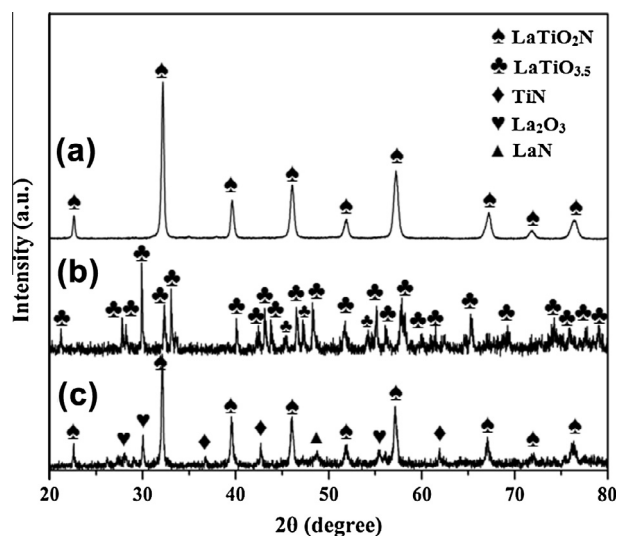


Fig. 2. XRD patterns of LaTiO_2N powder (a) before TGA/DTA/MS measurement and after TGA/DTA/MS measurement under air (b) and argon flow (c).

To further clarify the reactions and residual species during heating, XRD and FTIR measurements were performed on LaTiO_2N powders before and after the TGA/DTA/MS studies. As illustrated in the XRD patterns only characteristic peaks of LaTiO_2N is observed in the starting powder, see Fig. 2(a) [14]. However, after heating in different atmospheres, different phases can be identified besides LaTiO_2N . Heat treatment in air promotes the formation of crystalline $\text{LaTiO}_{3.5}$ which is confirmed both by the recorded XRD pattern (Fig. 2(b)) and the white colour of the product observed by the naked eye (Fig. 3(b)) [13]. In contrast, after the TGA/DTA/MS measurement in flowing argon, the XRD diffractogram (Fig. 2(c)) reveals that decomposition is slow and the major phase is still remaining LaTiO_2N (dark brown) with smaller amounts of La_2O_3 (white) and TiN (yellow–brown), see Fig. 2(c) [30]. The formation of traces of LaN (black) cannot be excluded. Therefore this mixture appears blackish by the naked eye as seen in Fig. 3(c). The elemental analysis results of the N and O contents are listed in Table 1. A severe loss of nitrogen after the TGA/DTA thermal cycle in air occurs as the N/O ratio decreases from 0.46 to 0.0034, while for using an argon flow the corresponding value is 0.23. All our findings based on TGA/DTA/MS, XRD and element analysis are in agreement.

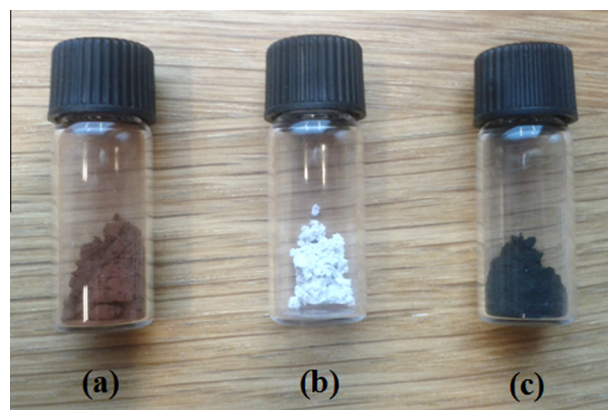


Fig. 3. The reference LaTiO_2N powder before TGA/DTA/MS measurement is seen in (a). The same powder after TGA/DTA/MS measurement under air (b) and argon flow (c). The change of the colour is distinct. (For interpretation of the references to colour in this figure legend, the reader is referred to the web version of this article.)

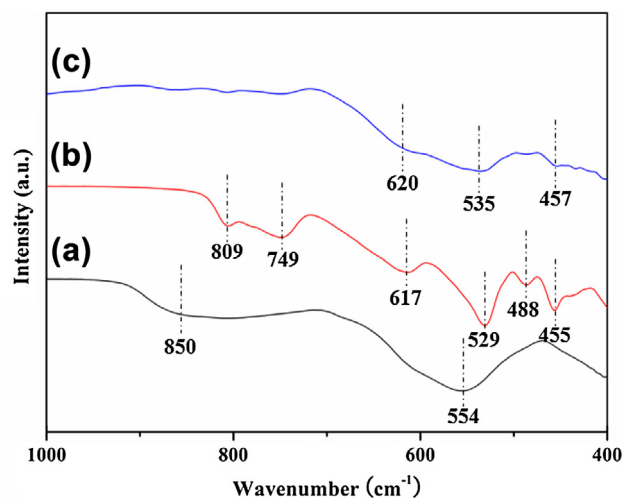


Fig. 4. FTIR spectra of LaTiO₂N powder (a) before TGA/DTA/MS measurement and after TGA/DTA/MS measurement under air (b) and argon flow (c).

The FTIR spectra of the thermally heated specimens also prove the chemical and structural changes taking place in air/argon as illustrated in Fig. 4(a and b) [21,23]. As a reference material the as-received LaTiO₂N powder displays two broad peaks located at 700–900 cm⁻¹ and 500–650 cm⁻¹, see Fig. 4(a). The first peak is related to the vibration of Ti(O,N)₆ octahedra bonds while the second corresponds to the Ti–O–Ti stretching modes [21]. Concerning the sample heated in air, a prominent absorption band at 529 cm⁻¹, a broad band at 617 cm⁻¹, several weak bands between 400 and 500 cm⁻¹ and two bands above 700 cm⁻¹ are present, see Fig. 4(b). This multitude of split bands can be attributed to complex bond vibrations involving the participation of both La and Ti cations in LaTiO_x octahedral sites [21]. When heated in argon, the higher vibrational bands (>700 cm⁻¹) are fairly unaffected and then gradually decline with broad peaks within the range of 460–700 cm⁻¹, see Fig. 4(c). The XRD indicated a fair amount of unreacted LaTiO₂N to be present that may correspond to the strong broad peak in 4(c) that has similarities with the LaTiO₂N reference spectrum 4(a). However, the shape is slightly distorted probably due to the formation of binary La₂O₃ and TiN as detected by XRD.

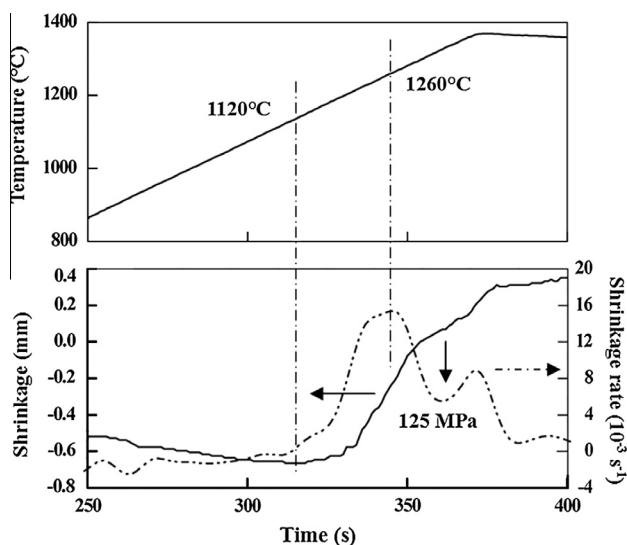
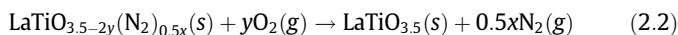
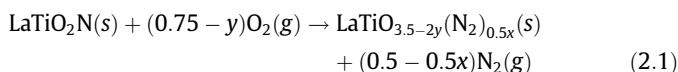
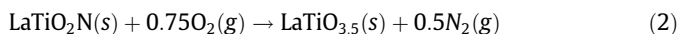
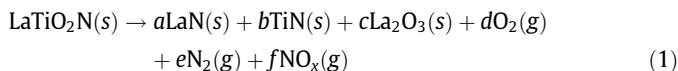


Fig. 5. The sintering data are shown as curves for specimen LTON-1. Recorded temperature, shrinkage rate and shrinkage plotted versus time.

Hence, the oxidation and decomposition of LaTiO₂N oxynitride under different atmospheres seems to occur by following the sequence listed below:



$$0 < x < 1, \quad 0 < y < 0.75$$

where reactions (1) and (2) represent the LaTiO₂N decomposition at high temperature in argon and air atmospheres, respectively. The decomposition of LaTiO₂N in argon atmosphere was not completed in our study and the proposed complex reaction (1) is a hypothesis. Still the three solid reaction products have been seen by XRD besides the residual LaTiO₂N. It may also be pointed out that both TiN and LaN may form solid solutions with some oxygen replacing nitrogen. Further it is intriguing to learn from literature that the oxidation reaction of LaTiO₂N in air does not take place in a single step as indicated by the reaction (2). In our heating conditions, reaction (2) seems to proceed rapidly resulting in a white colored oxide. Previous studies indicate the intermediate formation of organometallic-type phases resulting from the metal–nitrogen interaction (M–N≡N–M or N≡N–M) [13,30–32]. In that case, the reaction apparently follows different stages (reaction (2.1) and (2.2)): Part of the nitrogen leaves the lattice as molecular dinitrogen and is replaced by incoming oxygen which locates at the anionic positions, while the remaining nitrogen forms dinitrogen bridges between metallic atoms leading to the intermediate phases with the formula of LaTiO_{3.5-2y}(N₂)_{0.5x}. At elevated temperatures, LaTiO_{3.5-2y}(N₂)_{0.5x} further gives LaTiO_{3.5} with the release of gaseous N₂. In other studies the thermal behavior of LaTiO₂N, SrNbO₂N and SrTaO₂N were investigated in mixed gases of argon and oxygen with varying oxygen content [30]. It was found that the thermal behavior of the studied oxynitrides changes drastically with the oxygen concentration as the oxidation reaction rate increases with the oxygen content.

3.2. Preparation of dense LaTiO₂N bulk by SPS

It appears that the decomposition and structural change is inevitable by heating LaTiO₂N to above 800 °C in oxygen and argon atmosphere, as discussed in Section 3.1 above. As nitrogen is one of the gaseous products of the decomposition of LaTiO₂N, heating in nitrogen containing atmospheres (e.g. NH₃ or N₂) would suppress such decomposition from a thermodynamic point of view. Previous studies did show that pressure-less sintering at 1100 °C and hot-pressing sintering at 1250 °C/75 MPa under flowing ammonia atmosphere for several hours yielded LaTiO₂N ceramics with high purity [24,34]. However, by using these conventional sintering methods only very low density ceramics (<70% TD) have been achieved. In comparison, spark plasma sintering demonstrated that it is possible to achieve a relative density of 78% at 1250 °C and 125 MPa with only a small amount of dissociation, even in vacuum, according to our previous investigation [34]. The decomposition of LaTiO₂N and the reactions shown in Section 3.1 would be accelerated in vacuum, particularly in the presence of graphite. It is thus a rather challenging task to simultaneously achieve high density and high purity in sintered LaTiO₂N ceramics.

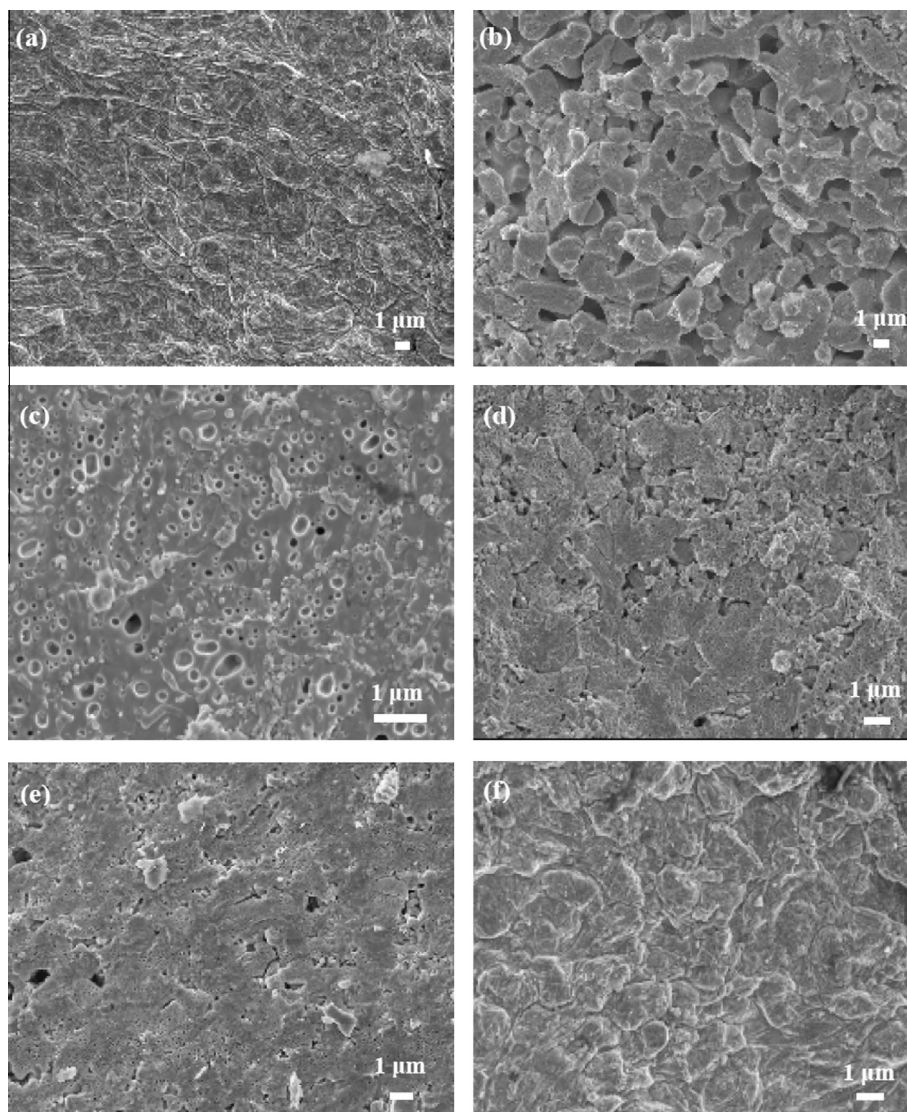


Fig. 6. SEM micrographs of the sintered LaTiO_2N samples LTON-1 to -6 in the order (a–f). See comments of images in the text and sintering conditions in Table 1.

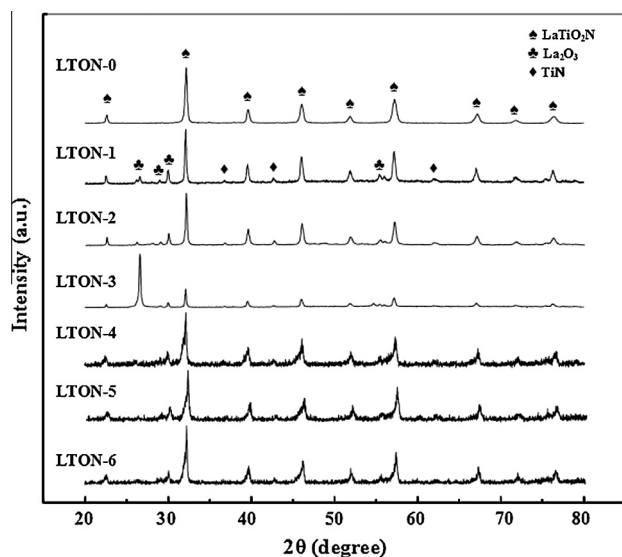


Fig. 7. XRD patterns of as-received LaTiO_2N powder (LTON-0) and the sintered samples named LTON-1 to LTON-6 in Table 1.

Manipulation of kinetics tends to be the only possible way for achieving such a goal.

SPS trials were performed by using different parameters characterized by rapid heating and the application of higher pressure levels. The applied sintering parameters and the relative densities achieved are shown in Table 1. In addition, the sintering curves of the LTON-1 sample, that gives the best result of the LaTiO_2N density (94% TD) and content (86 wt%), are shown in Fig. 5. A positive shrinkage rate is analysed when the sample reaches 1120 °C indicating the start of the densification process. When the temperature reaches 1260 °C the shrinkage achieves a maximum rate. Thus, a minimum temperature of 1260 °C is needed for facilitating densification under a normally applied pressure of 100 MPa, but sufficient densification was not achieved. Higher temperature increases the risk of decomposition and time and maximum temperature must be limited. Therefore the applied pressure was increased from 100 to 125 MPa at 1300 °C, which further enhances densification by compression. The heating rate determines the total sintering time; applying a low heating rate means extended exposure at high temperatures, whereas applying a too high rate will generate high thermal stresses and even yield cracks in the sintered samples as shown in the case of sample LTON-5 when the highest heating rate of 300 °C/min was applied.

The microstructures analysed by SEM of all the sintered ceramic samples are illustrated in Fig. 6(a–f). The SEM images are shown in the order (a–f) following the sintered LTON numbers 1–6, where the sintering conditions are given in Table 1. Note that the two LaTiO₂N ceramics sintered up to 1350 °C appear much denser than the other samples, i.e. LTON-1 in Fig. 6(a) and LTON-6 in Fig. 6(f). A porous structure is found in the specimen sintered at the lowest temperature 1250 °C indicating insufficient densification, see LTON-2 in Fig. 6(b). Raising the temperature to 1300 °C is not sufficient as the materials are not well densified with the existence of visible pores, see LTON-4 and -5 in Fig. 6(d and e). On the other hand the specimen sintered at the highest temperature 1400 °C contains a large amount of gas voids generated by the severe decomposition at this temperature, see LTON-3 in Fig. 6(c).

XRD results suggest that besides the characteristic peaks of crystalline LaTiO₂N, all the sintered compacts contained some impurities which can be ascribed to La₂O₃ and TiN, see Fig. 7 and Table 1 [34–36]. This result supports the occurrence of decomposition, but the relative intensities of the impurity peaks compared to that of the crystalline phase LaTiO₂N are varying. It is obvious that specimen LTON-2 has the highest purity, followed by specimens LTON-6 and LTON-1. This can be further confirmed by the results obtained by elemental analysis as listed in Table 1, i.e. the N/O ratio declines from 0.46 for the reference LaTiO₂N specimen LTON-0 to 0.31 for LTON-1. All other specimens fall in a logical order regarding decomposition. The LTON-2 sample has higher residual nitrogen content (4.61 wt%), whereas higher temperatures or longer dwell time at elevated temperature facilitate decomposition. Consequently, the specimen LTON-3 produced with the highest temperature applied (1400 °C) has the lowest purity and encountered most severe decomposition. Overall, specimen LTON-1 and LTON-6 are desirable in terms of density and purity, but the LTON-6 pellet was fragile and cracked into small pieces after sintering. This behaviour suggests that residual stresses formed using a very high heating rate (≥ 300 °C/min).

The impurities formed during sintering can have some influences on both densification process and dielectric properties of LaTiO₂N. Decomposition of LaTiO₂N is a time-dependent process, as shown above. The TGA/DTA/MS results at 10 °C/min confirm that the structural change mainly occurs at temperatures above ~ 800 °C, see Fig. 1(b). This is much lower than the major densification temperature needed. The generated multiphases can to some extent discourage densification. In SPS, assuming a natural cooling rate of 400 °C/min, the total time consumed above 800 °C is ~ 5 min for specimen LTON-1 and always < 12 min, which kinetically reduces the LaTiO₂N decomposition. According to the parallel mixing model [37], the dielectric constant of a compound can be empirically calculated by the combination of individual dielectric constant multiplying the volume fraction of each phase. In our case, the dielectric constant of sintered LaTiO₂N ceramic mainly depends on LaTiO₂N, La₂O₃, TiN, and the voids. The dielectric constant of LaTiO_xN_y have been measured to be ~ 1000 (room temperature, 10 kHz) based on films form, and it varies a lot with different nitrogen contents [38]. The doping of La₂O₃ into a perovskite phase can lead to high value of dielectric constant (the order of 1000) due to space charge polarization [39,40], as well as low temperature coefficient of permittivity and weak losses at medium frequencies (100 kHz–1 MHz) [41]. In contrast, TiN and voids would act a negative role for enhancing the dielectric constant of LaTiO₂N. Through manipulating kinetics we can obtain bulk ceramics with up to $> 90\%$ TD and with LaTiO₂N as the major phase. In this case, a limited decomposition of LaTiO₂N may be acceptable in practice [39]. The achievement reported in this work enables the preparation of bulk oxynitride based materials suitable for performance evaluation that will be done in the near future.

4. Conclusions

The sinterability of a perovskite-type oxynitride LaTiO₂N is investigated through spark plasma sintering supported by the thermal stability study. Analysis by TGA/DTA/MS, XRD, FTIR and element analysis show that LaTiO₂N is thermodynamically unstable, especially for temperatures > 400 °C in air and > 800 °C in argon. By the SPS technique LaTiO₂N oxynitride ceramics in our study have achieved 74–94% of TD and with 57–90 wt% LaTiO₂N as the major phase. The achieved density of 94% of the TD (and 86 wt% LaTiO₂N) at 1350 °C using 125 MPa sintering pressure is significantly higher than that of any counterparts prepared by conventional sintering.

Acknowledgements

We thank Prof. Derek Thompson and Dr. Jutharat Ahchawatarn at Newcastle University in UK for preparing and providing LaTiO₂N powder. This work was supported by European Commission through the Marie-Curie ITN project “FUNctional Nitrides for Energy Applications, FUNEA” (FP7-PITN-GA-2010-264873).

References

- [1] Ray L. Withers, L. Bourgeois, A. Snashall, Y. Liu, L. Noren, C. Dwyer, J. Etheridge, *Chem. Mater.* 25 (2013) 190–201.
- [2] Z. Ren, G. Jing, Y. Liu, J. Gao, Z. Xiao, Z. Liu, S. Yin, S. Zhou, G. Xu, X. Li, G. Shen, G. Han, *RSC Adv.* 3 (2013) 5453–5458.
- [3] S. Parida, S.K. Rout, N. Gupta, V.R. Gupta, *J. Alloys Comp.* 546 (2013) 216–223.
- [4] M. Cernea, F. Vasiliu, C. Plapcianu, C. Bartha, I. Mercioniu, I. Pasuk, R. Lowndes, R. Trusca, G.V. Aldica, L. Pintilie, *J. Eur. Ceram. Soc.* 33 (2013) 2483–2490.
- [5] N. Nuraje, X. Dang, J. Qi, Mark A. Allen, Y. Lei, Angela M. Belcher, *Adv. Mater.* 24 (2012) 2885–2889.
- [6] S. Fu, H. Niu, Z. Tao, J. Song, C. Mao, S. Zhang, C. Chen, D. Wang, *J. Alloys Comp.* 576 (2013) 5–12.
- [7] P. Maillard, F. Tessier, E. Orhan, F. Chevire, R. Marchand, *Chem. Mater.* 17 (2005) 152–156.
- [8] G. Sierra Gallego, N. Marín Alzate, O. Arnache, *J. Alloys Comp.* 549 (2013) 163–169.
- [9] S.G. Ebbinghaus, R. Aguiar, A. Weidenkaff, S. Gsell, A. Reller, *Solid State Sci.* 10 (2008) 709–716.
- [10] Y. Masubuchi, T. Hata, T. Motohashi, S. Kikkawa, *J. Alloys Comp.* 582 (2014) 823–826.
- [11] D. Logvinovich, L. Bocher, D. Sheptyakov, R. Figi, S.G. Ebbinghaus, R. Aguiar, M.H. Aguirre, A. Reller, A. Weidenkaff, *Solid State Sci.* 11 (2009) 1513–1519.
- [12] F. Chevire, F. Tessier, R. Marchand, *Eur. J. Inorg. Chem.* (2006) 1223–1230.
- [13] S.G. Ebbinghaus, H.P. Abicht, R. Dronskowski, T. Muller, A. Reller, A. Weidenkaff, *Prog. Solid State Chem.* 37 (2009) 173–205.
- [14] Y.I. Kim, P.M. Woodward, K.Z. Baba-Kishi, C.W. Tai, *Chem. Mater.* 16 (2004) 1267–1276.
- [15] Y.I. Kim, P.M. Woodward, *J. Solid State Chem.* 180 (2007) 3224–3233.
- [16] L. Le Gendre, C. Le Paven, J. Pinel, D. Fasquelle, J.C. Carru, F. Chevire, F. Tessier, R. Marchand, *Silic. Ind.* 69 (2004) 165–171.
- [17] Y.I. Kim, W.D. Si, P.M. Woodward, E. Sutter, S. Park, T. Vogt, *Chem. Mater.* 19 (2007) 618–623.
- [18] V. Petrovsky, A. Manohar, F. Dogan, *J. Appl. Phys.* 100 (2006) 014102.
- [19] A. Rousseau, V. Laur, S. Deputier, V. Bouquet, M. Guilloux-Viry, G. Tanne, P. Laurent, F. Huret, A. Perrin, *Thin Solid Films* 516 (2008) 4882–4888.
- [20] C. Le Paven-Thivet, A. Ishikawa, A. Ziani, L. Le Gendre, M. Yoshida, J. Kubota, F. Tessier, K. Doment, *J. Phys. Chem. C* 113 (2009) 6156–6162.
- [21] K.K. Kartha, M.R. Pai, A.M. Banerjee, R.V. Pai, S.S. Meena, S.R. Bharadwaj, *J. Mol. Catal. A: Chem.* 335 (2011) 158–168.
- [22] E.C. Pascual, V.B. Gutierrez, M. Subda, R.S. Puche, *Solid State Sci.* 10 (2008) 1905–1909.
- [23] N. Kumar, A. Sundaresan, C.N.R. Rao, *Mater. Res. Bull.* 46 (2011) 2021–2024.
- [24] C. Le Paven-Thivet, L. Le Gendre, J. Le Castrec, F. Chevire, F. Tessier, J. Pinel, *Prog. Solid State Chem.* 35 (2007) 299–308.
- [25] Y.R. Zhang, T. Motohashi, Y. Masubuchi, S. Kikkawa, *J. Eur. Ceram. Soc.* 32 (2012) 1269–1274.
- [26] M. Omori, *Mater. Sci. Eng. A* 287 (2000) 183–188.
- [27] Z.A. Munir, U. Anselmi-Tamburini, M. Ohyanagi, *J. Mater. Sci.* 41 (2006) 763–777.
- [28] J. Hu, Z. Shen, *Acta Mater.* 60 (2012) 6405–6412.
- [29] M. Zhou, D. Rodrigo, Y. Cheng, *J. Alloys Comp.* 547 (2013) 51–58.
- [30] R. Aguiar, D. Logvinovich, A. Weidenkaff, A. Reller, S.G. Ebbinghaus, *Thermochim. Acta* 471 (2008) 55–60.
- [31] L. Le Gendre, R. Marchand, Y. Laurent, *J. Eur. Ceram. Soc.* 17 (1997) 1813–1818.
- [32] F. Tessier, L. Le Gendre, F. Chevire, R. Marchand, A. Navrotsky, *Chem. Mater.* 17 (2005) 3570–3574.

- [33] T. Katsumata, A. Nakamura, M. Nakanishi, H. Yoshioka, Y. Inaguma, T. Ohba, T. Tsurui, *J. Ceram. Soc. Jpn.* 117 (2009) 1345–1348.
- [34] J. Ahchawarattaworn, *Perovskite Oxynitride Dielectrics* [dissertation], Newcastle University, Newcastle, 2011.
- [35] D.W. Hwang, H.G. Kim, J.S. Lee, J. Kim, W. Li, S.H. Oh, *J. Phys. Chem. B* 109 (2005) 2093–2102.
- [36] J.S. Byun, J.H. Shim, Y.W. Cho, *Scripta Mater.* 50 (2004) 279–283.
- [37] K. Wakino, T. Okada, N. Yoshida, K. Tomono, *J. Am. Ceram. Soc.* 76 (1993) 2588–2594.
- [38] A. Ziani, C. Le Paven-Thivet, L. Le Gendre, D. Fasquelle, J.C. Carru, F. Tessier, J. Pinel, *Thin Solid Films* 517 (2008) 544–549.
- [39] Y.R. Zhang, Y. Masubuchi, T. Motohashi, S. Kikkawa, K. Hirota, *Ceram. Int.* 39 (2013) 3377–3380.
- [40] C.R. Gautam, P. Singh, O.P. Thakur, D. Kumar, O. Parkash, *J. Mater. Sci.* 47 (2012) 6652–6664.
- [41] D. Fasquelle, J.C. Carru, L. Le Gendre, C. Le Paven, J. Pinel, F. Cheviré, F. Tessier, R. Marchand, *J. Eur. Ceram. Soc.* 25 (2005) 2085–2088.

Perovskite-type Solid Solution $\text{SrMo}_{1-x}\text{W}_x(\text{O},\text{N})_3$ Oxynitrides: Synthesis, Structure, and Magnetic Properties

Wenjie Li,^[a] Aleksander Gurlo,^[b] Ralf Riedel,^[a] and Emanuel Ionescu*^[a]

Dedicated to Professor Rüdiger Kniep on the Occasion of His 70th Birthday

Keywords: Perovskite phases; Oxynitrides; Solid solution; Scheelite; Magnetic properties

Abstract. Phase-pure scheelite-type solid solution $\text{SrMo}_{1-x}\text{W}_x\text{O}_4$ oxides ($x = 0.05, 0.15, 0.25, 0.4, 0.5, 0.6, 0.75, 0.85, 0.95$) were synthesized by solvothermal methods and subsequently thermally treated in ammonia atmosphere at temperatures between 700 and 900 °C. As revealed by X-ray diffraction (XRD) and neutron diffraction as well as elemental analysis data, $\text{SrMo}_{1-x}\text{W}_x\text{O}_4$ convert into their corresponding solid solution perovskite-type oxynitrides $\text{SrMo}_{1-x}\text{W}_x(\text{O},\text{N})_3$ only for $x \leq 0.25$ and $x \geq 0.6$; whereas for $0.25 \leq x \leq 0.6$ the formation of

Sr_3WO_6 with double perovskite structure and of other binary oxides and nitrides was observed. The solid solution oxynitrides were investigated concerning their magnetic properties. Thus, the magnetic susceptibility of the $\text{SrMo}_{1-x}\text{W}_x(\text{O},\text{N})_3$ oxynitride samples was measured by Superconducting Quantum Interference Device (SQUID). The influence of different parameters (such as phase composition, ratio between Mo and W or nitrogen content) on the magnetic behavior in the solid solution oxynitrides is briefly discussed.

Introduction

Oxynitride materials which adopt the ABX_3 perovskite-type structure exhibit various promising and intriguing properties.^[1–6] Moreover, the nitrogen substitution for oxygen allows for the stabilization of compositions that are not achievable for perovskite oxides, e.g. MnTaO_2N ,^[7] RZrO_2N ($R = \text{Pr, Nd, and Sm}$)^[8] or LnNbO_2N ($\text{Ln} = \text{Pr, Nd, and Dy}$)^[9] (the analogous perovskite-type oxides MnTaO_3 , RZrO_3 , and LnNbO_3 are not known), and which can be applied to alter the concentration of charge carriers and consequently the properties in the perovskite-type materials. For instance, the electrical and magnetic properties of SrMoO_3 and $\text{SrMoO}_{2.4}\text{N}_{0.6}$ were shown to significantly differ from each other.^[10]

Well known perovskite-type oxynitrides contain d^0 transition metals such as Ti^{4+} , Nb^{4+} , or Ta^{4+} . Also solid solution perovskite-type oxynitrides such as $\text{LaTiO}_2\text{N-ATiO}_3$ ($A = \text{Sr, Ba}$)^[11] (La,Ca) $\text{Ti}(\text{O},\text{N})_3$,^[12] $\text{SrTi}_{1-x}\text{Nb}_x(\text{O},\text{N})_3$ ^[13] and $\text{Ca}_{1-x}\text{Eu}_x\text{Ta}(\text{O},\text{N})_3$ ^[14] have been reported. It was shown that

some of these solid solution oxynitrides can be synthesized only within a limited compositional range.^[12] Molybdenum and tungsten-containing perovskite-type oxynitrides^[10,15–19] have been discussed in recent years due to their unique combination of properties. For instance, $\text{SrMo}(\text{O},\text{N})_3$ was shown to exhibit interesting electrical and magnetic properties. Moreover, SrMoO_4 is an electrical insulator, whereas its perovskite-type counterparts SrMoO_3 and $\text{SrMo}(\text{O},\text{N})_3$ show metallic and semiconducting behavior, respectively. Also it has been shown that $\text{SrMo}(\text{O},\text{N})_3$ possess Pauli paramagnetism behavior with an anomalous hyperbolic crest at temperatures below 70 K.^[16] Unlike $\text{SrMo}(\text{O},\text{N})_3$, $\text{SrW}(\text{O},\text{N})_3$ has been rather poorly investigated.

Within this context, the synthesis of perovskite-type solid solution $\text{SrMo}_{1-x}\text{W}_x(\text{O},\text{N})_3$ oxynitrides from their corresponding scheelite-type $\text{SrMo}_{1-x}\text{W}_x\text{O}_4$ oxide precursors might be of high interest concerning their formability, as well as magnetic properties. In the presented work, the synthesis of solid solution scheelite-type $\text{SrMo}_{1-x}\text{W}_x\text{O}_4$ was performed for the first time via a solvothermal method. The oxides were subsequently thermally treated in ammonia atmosphere at varying conditions in order to investigate the formability of the solid solution perovskite-type $\text{SrMo}_{1-x}\text{W}_x(\text{O},\text{N})_3$ oxynitrides. The detailed synthesis, structural characterization, and magnetic properties of the resulting materials are presented herein.

Experimental Section

Synthesis of Solid Solution Scheelite-type $\text{SrMo}_{1-x}\text{W}_x\text{O}_4$ Oxide Precursors: $\text{Sr}(\text{NO}_3)_2$ (Sigma-Aldrich, >99.0%) was mixed with $\text{Na}_2\text{MoO}_4 \cdot 4\text{H}_2\text{O}$ (Sigma-Aldrich, >99.5%) and $\text{Na}_2\text{WO}_4 \cdot 4\text{H}_2\text{O}$ (Sigma-Aldrich, >99.5%) in ethylenediamine (FLUKA, >99.5%)

* Dr. E. Ionescu

Fax: +49-6151-16 6346

E-Mail: ionescu@materials.tu-darmstadt.de

[a] Fachbereich Material- und Geowissenschaften
Technische Universität Darmstadt
Jovanka-Bontschits-Str. 2
64287 Darmstadt, Germany

[b] Fachgebiet Keramische Werkstoffe
Institut für Werkstoffwissenschaften und -technologien
Fakultät III Prozesswissenschaften
Technische Universität Berlin
Hardenbergstraße 40
10623 Berlin, Germany

Supporting information for this article is available on the WWW under <http://dx.doi.org/10.1002/zaac.201500098> or from the author.

under vigorous stirring. The ratio of Mo/W was adjusted according to $x = 0.05, 0.15, 0.25, 0.4, 0.5, 0.6, 0.75, 0.85,$ and 0.95 (referred to as SMW1, 2, 3, 4, 5, 6, 7, 8, and 9, respectively). Subsequently, the reaction mixture was transferred into an autoclave with Teflon lining and heated at $200\text{ }^{\circ}\text{C}$ for 24 h. The resulting mixture was rinsed 5 times with de-ionized water and ethanol alternately. Centrifugation and drying at $60\text{ }^{\circ}\text{C}$ overnight led to the powdered scheelite-type oxides.

Thermal Ammonolysis: The oxide precursors (0.5 g) were placed in silica crucible, and sealed into a Schlenk tube furnace. The Schlenk tube was evacuated and filled with argon gas before turning on the ammonia gas for the reaction. The temperature range for the thermal ammonolysis experiments ranged from 700 to $900\text{ }^{\circ}\text{C}$ for 6 or 12 h (heating and cooling rate $100\text{ K}\cdot\text{h}^{-1}$).

Sample Characterization: The finely ground powders were examined by powder X-ray diffraction (XRD, STOE STADI P) with $\text{Mo-}K_{\alpha}$ radiation (wavelength 0.7093 \AA). The oxygen and nitrogen contents of as-synthesized samples were determined by the hot gas extraction method using a LECO TC436 analyzer. High resolution transmission electron microscopy (HRTEM, JEOL JEM-2100F) was applied to assess the morphology and the local crystallinity of selected sample. Neutron diffraction (ND) experiments were performed at the high resolution powder diffractometer for thermal neutrons (HRPT)^[20] located at the Swiss Spallation Neutron Source (SINQ) of the Paul Scherrer Institute in Switzerland and the High-resolution two-axis diffractometer (DIF, D2B) at the Institute Laue-Langevin (ILL, Grenoble) in France. The measurements were performed at room temperature using a neutron wavelength of $\lambda = 1.494\text{ \AA}$ at SINQ and $\lambda = 1.6\text{ \AA}$ at ILL. Crystallographic parameters were confirmed by the individual Rietveld refinements of the XRD and ND patterns. The peak shapes were modeled with pseudo-Voigt function for XRD and Thompson-Cox-Hastings pseudo-Voigt function^[21] for ND patterns. Isotropic thermal parameters of O/N were constrained to the same value for the anions. All refinements were performed with the Fullprof software.^[22] Electrical conductivity was measured applying the Powder-Solution-Composites (PSC) method (preparation details can be found in the Supporting Information). The magnetic susceptibilities were recorded by a Quantum Design Magnetic Properties Measurement System (MPMS) Superconducting Quantum Interference Device (SQUID) magnetometer.

Supporting Information (see footnote on the first page of this article): Diffraction patterns (Rietveld plots) including crystal structure data of scheelite-type oxide, as well as corresponding elemental analysis and comparative SQUID measurement for SMW8 prepared in glove box and air.

Results and Discussion

Structure of Scheelite-type $\text{SrMo}_{1-x}\text{W}_x\text{O}_4$ Oxide

As shown in Figure 1, phase-pure scheelite-type oxides $\text{SrMo}_{1-x}\text{W}_x\text{O}_4$ were obtained for all compositions via the solvothermal synthesis method. The x-ray powder Rietveld refinement (Figure S1, Supporting Information) reveals in all cases the formation of solid solution scheelite-type oxide phase with $I41/a$ space group. The slightly gradual shift of the diffraction peaks to lower 2θ values as the value of x increases from 0.05 to 0.95 illustrates the expected change of the lattice constants with increasing tungsten content (increase from 5.39517 \AA to 5.4142 \AA along the a axis; while decreasing from

12.01575 \AA to 11.9518 \AA along the c axis). The crystallographic data are summarized in Table S1 (Supporting Information). These slight changes are consistent with those reported for other molybdenum-/tungsten solid solution oxides.^[23,24] This is probably related to a deformation of the coordination polyhedra around W, Mo, and Sr, evidenced also by the small but significant modifications of the bond lengths and angles, as reported by *Daturi et al.*^[24] The gradual substitution of tungsten for Mo in SrMoO_4 leads to a slight increase of the metal–O bond length and affects the (a)symmetry of the Mo/W–O–Mo/W bridges, despite that fact that the ionic radii of Mo^{6+} and W^{6+} are more or less same.^[25,26] The increase of the bond lengths can be compensated by the deformation of the coordination polyhedra.^[24]

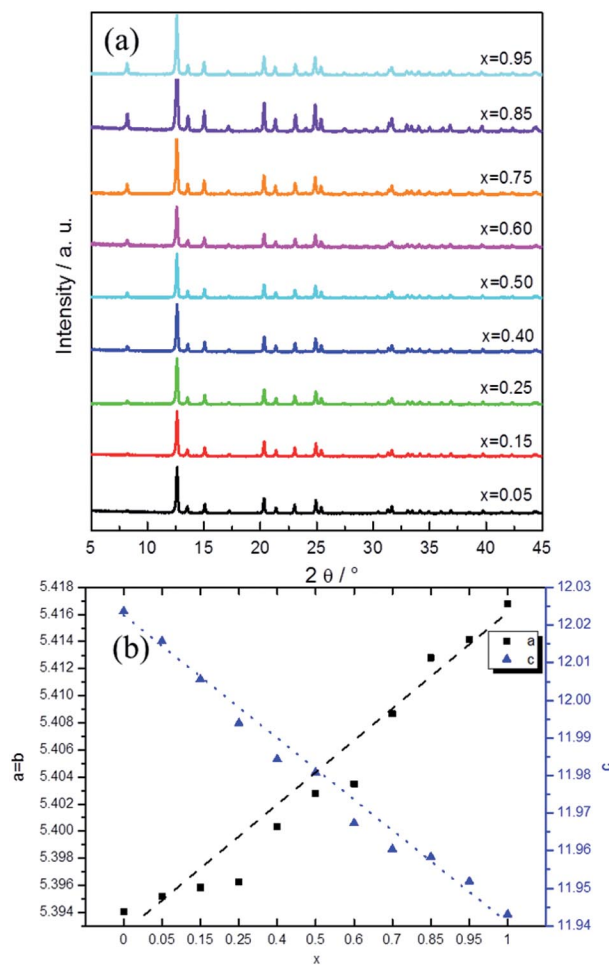


Figure 1. X-ray diffraction patterns of different compositions (a) and lattice constants obtained by Rietveld refinement in Table S1 (b) for the as-synthesized solid solution oxide precursors ($\text{SrMo}_{1-x}\text{W}_x\text{O}_4$) when $x = 0.0, 0.05, 0.15, 0.25, 0.4, 0.5, 0.6, 0.75, 0.85, 0.9,$ and 1.0 .

Thermal Ammonolysis

Due to the different thermal ammonolysis temperatures required for the synthesis of the perovskite-type $\text{SrMo}(\text{O},\text{N})_3$ and $\text{SrW}(\text{O},\text{N})_3$,^[27] the ammonolysis of the solid solution oxide

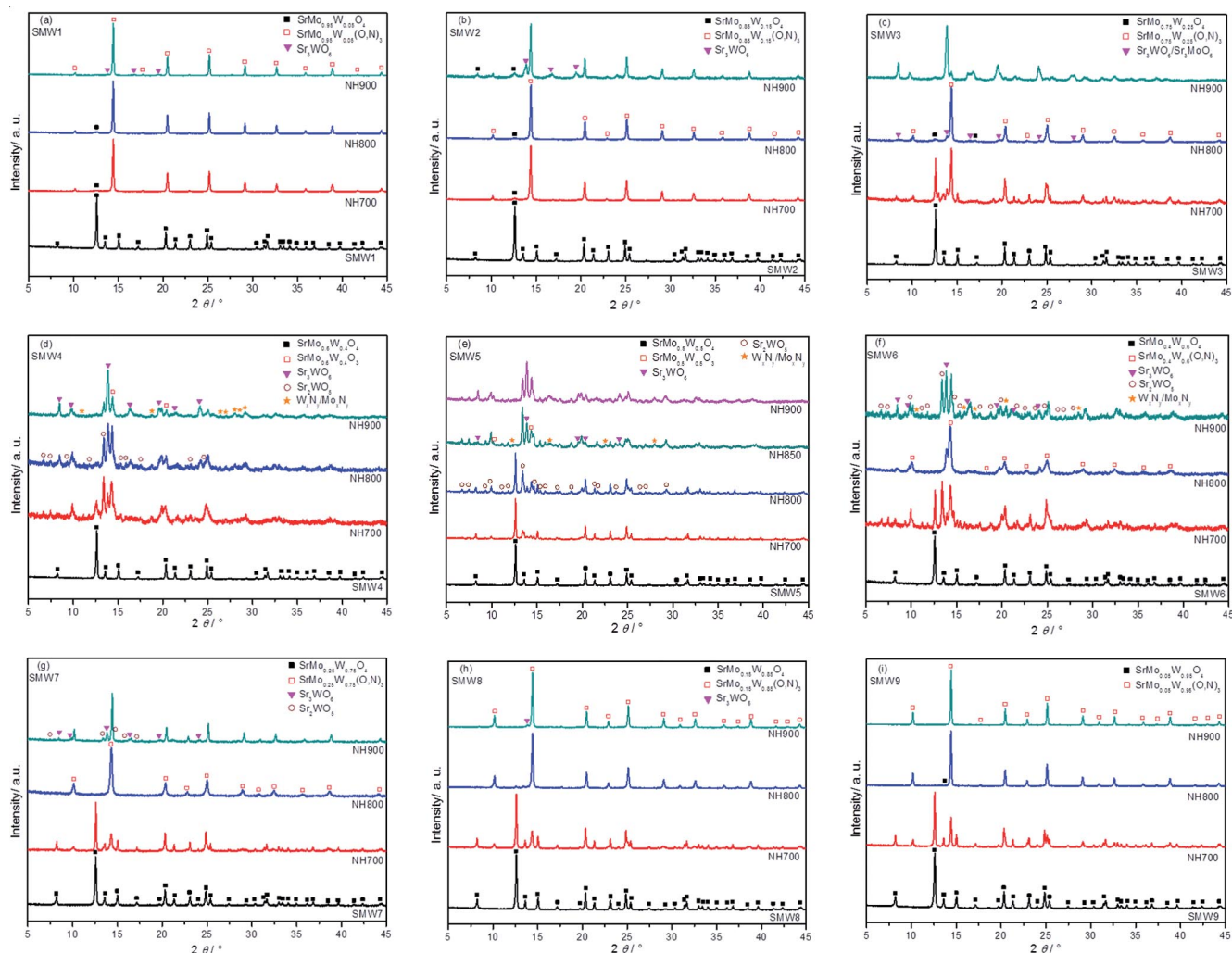


Figure 2. X-ray diffraction patterns of $\text{SrMo}_{1-x}\text{W}_x\text{O}_4$ and $\text{SrMo}_{1-x}\text{W}_x(\text{O},\text{N})_3$ with different compositions, i.e. $x = 0.05, 0.15, 0.25, 0.4, 0.5, 0.6, 0.75, 0.85,$ and 0.9 , before and after annealing under in an ammonia flow between 700 and 900 °C for 6 h.

precursors was performed at temperatures between 700 and 900 °C (Figure 2). For $x = 0.05$ (SMW1) and 0.15 (SMW2), the expected solid solution oxynitride phase was formed as the main phase upon ammonolysis at 700 °C, whereas the ammonolysis at 900 °C leads in both cases to the formation of small amounts of Sr_3WO_6 . Thus, in order to avoid the formation of Sr_3WO_6 , the samples prepared upon ammonolysis at 800 °C were selected for the neutron powder Rietveld refinement analysis (Figure 3 and Table 1). For SMW1, the fraction of the perovskite-type oxynitride phase was 71.2 wt-% and the scheelite-type oxide precursor was still present with a fraction of 28.8 wt-%. In the case of SMW2, only less than half amount (45.8 wt-%) of the perovskite $\text{SrMo}_{0.85}\text{W}_{0.15}\text{O}_{2.15(6)}\text{N}_{0.85(6)}$ was formed and showed a slightly lower nitrogen content as compared to that of the perovskite $\text{SrMo}_{0.95}\text{W}_{0.05}\text{O}_{1.96(4)}\text{N}_{1.04(4)}$ obtained from SMW1.

For $x = 0.25$ (SMW3) a new oxidic phase is formed (Sr_3MoO_6) even upon ammonolysis at temperature as low as 700 °C and shows increasing mass fraction as the ammonolysis temperature increases. Thus, $\text{Sr}_3\text{WO}_6/\text{Sr}_3\text{MoO}_6$ oxides represent the main phase in the sample ammonolyzed at

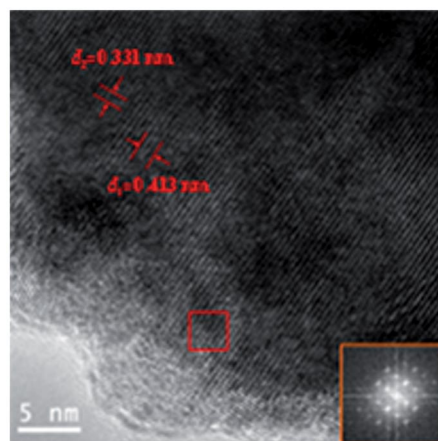


Figure 3. HRTEM micrograph of SMW8 obtained upon annealing of the scheelite precursor at 800 °C in an ammonia flow for 12 h.

900 °C (Figure 2c). Ammonolysis of SMW3 at 800 °C delivered a mixture consisting of ca. 70 wt-% of $\text{SrMo}_{0.75}\text{W}_{0.25}\text{O}_{1.97(7)}\text{N}_{1.03(7)}$, beside 9 wt-% of

Table 1. Crystallographic data, phase compositions, and details of the structure refinement of as-synthesized solid solution oxynitrides in an ammonia flow at 800 or 900 °C for 6 or 12 h.

Composition		Sr(Mo,W)(O,N) ₃ <i>Pm3m</i> , no. 221	Sr(Mo,W)O ₄ <i>I41a</i> , no. 88	SrWO ₆ , <i>Fm3m</i> , no. 225	Sr ₃ MoO ₆ , <i>Fm3m</i> , no. 225
SMW1_NH800_6H	Phase composition	SrMo _{0.95} W _{0.05} O _{1.96(4)} N _{1.04(4)}	SrMo _{0.95} W _{0.05} O ₄ <i>a</i> = 5.39778(359), <i>c</i> = 12.02487(1463)	–	–
	Lattice constants /Å	<i>a</i> = 3.98403(23),			
	Mass fraction	71.17(2.1) wt-%	28.83(2.29) wt-%		
	Refinement	$\chi^2 = 1.072$, $R_{\text{exp}} = 3.76$, $wR_p = 4.03$, $\text{chi2} = 1.15$			
SMW2_NH800_6H	Phase composition	SrMo _{0.85} W _{0.15} O _{2.15(6)} N _{0.85(6)}	SrMo _{0.85} W _{0.15} O ₄ <i>a</i> = 5.40252(139) <i>c</i> = 12.00821(444)	–	–
	Lattice constants /Å	<i>a</i> = 4.00282(72)			
	Mass fraction	45.79(1.42) wt-%	54.21(1.93) wt-%		
	Refinement	$\chi^2 = 1.61$, $R_{\text{exp}} = 1.76$, $wR_p = 2.84$, $\text{chi2} = 2.61$			
SMW3_NH800_6H	Phase composition	SrMo _{0.75} W _{0.25} O _{1.97(7)} N _{1.03(7)}	SrMo _{0.75} W _{0.25} O ₄ <i>a</i> = 5.40908(317), <i>c</i> = 11.93866(1070)	Sr ₃ WO ₆ <i>a</i> = 8.25285(291)	Sr ₃ MoO ₆ <i>a</i> = 8.29774(244)
	Lattice constants /Å	<i>a</i> = 4.00311(21)			
	Mass fraction	69.86(2.66) wt-%	9.04(1.06) wt-%	12.25(1.95) wt-%	8.84(1.14) wt-%
	Refinement	$\chi^2 = 1.12$, $R_{\text{exp}} = 3.48$, $wR_p = 3.91$, $\text{chi2} = 1.27$			
SMW6_NH800_12H	Phase composition	SrMo _{0.4} W _{0.6} O _{1.35(5)} N _{1.65(5)}	–	Sr ₃ WO ₆ <i>a</i> = 8.2756(37)	–
	Lattice constants /Å	<i>a</i> = 4.01072			
	Mass fraction	46.77(1.35) wt-%		53.23(1.69) wt-%	
	Refinement	$\chi^2 = 1.7$, $R_{\text{exp}} = 2.17$, $wR_p = 3.69$, $\text{chi2} = 2.9$			
SMW7_NH800_12H	Phase composition	SrMo _{0.25} W _{0.75} O _{1.77(4)} N _{1.23(4)}	SrMo _{0.25} W _{0.75} O ₄ <i>a</i> = 5.3398(19), <i>c</i> = 12.57928(674)	–	–
	Lattice constants /Å	<i>a</i> = 4.00358(53)			
	Mass fraction	92.87(1.69) wt-%	7.13(0.65) wt-%		
	Refinement	$\chi^2 = 1.58$, $R_{\text{exp}} = 2.5$, $wR_p = 3.95$, $\text{chi2} = 2.51$			
SMW8_NH800_12H	Phase composition	SrMo _{0.15} W _{0.85} O _{1.21(6)} N _{1.79(6)}	SrMo _{0.15} W _{0.85} O ₄ <i>a</i> = 5.45002(222), <i>c</i> = 11.82211(798)	–	–
	Lattice constants /Å	<i>a</i> = 4.00086(36)			
	Mass fraction	82.43(2.05) wt-%	17.57(1.29) wt-%		
	Refinement	$\chi^2 = 1.28$, $R_{\text{exp}} = 2.57$, $wR_p = 3.28$, $\text{chi2} = 1.65$			
SMW9_NH900_12H	Phase composition	SrMo _{0.05} W _{0.95} O _{1.49(3)} N _{1.51(3)}	SrMo _{0.05} W _{0.95} O ₄ <i>a</i> = 5.41561(216), <i>c</i> = 12.0045(85)	–	–
	Lattice constants /Å	<i>a</i> = 3.98997(10)			
	Mass fraction	74.01(1.26) wt-%	25.99(1.27) wt-%		
	Refinement	$\chi^2 = 1.23$, $R_{\text{exp}} = 2.51$, $wR_p = 3.08$, $\text{chi2} = 1.51$			

SrMo_{0.75}W_{0.25}O₄, and 21.2 wt-% of Sr₃WO₆/Sr₃MoO₆. Thus, it seems that for $x \leq 0.25$ solid solution perovskite-type oxynitrides with an O/N ratio of ca. 2:1 can be formed. However, some decomposition of the oxynitride phase to deliver double-perovskite-type Sr₃WO₆/Sr₃MoO₆ occurs. This process seems to be favored as the annealing temperature increases.

For higher values of x (as for 0.4 and 0.5, i.e. SMW4 and SMW5) a different behavior during the ammonolysis of the scheelite precursors was observed. Thus, Sr₂WO₅/Sr₃WO₆ were the main phases in the samples prepared at 800 °C, whereas at higher temperatures also tungsten and molybdenum nitride (W_{*x*}N_{*y*}/Mo_{*x*}N_{*y*}) were formed. Due to the complex composition of the ammonolyzed samples, no suitable neutron diffraction data were obtained and thus it is rather difficult to state whether the perovskite-type oxynitride is formed. Based on the elemental analysis data (Table S2, Supporting Information) as well as the formation of the binary nitrides, perovskite-type Sr(Mo, W)O₃ oxide might be formed instead of the expected oxynitride phase.

SMW6 ($x = 0.6$) was shown to yield upon ammonolysis for 12 h at 800 °C about 46.8 wt-% of perovskite-type oxynitride

SrMo_{0.4}W_{0.6}O_{1.35(5)}N_{1.65(5)}, whereas ca. 53.2 wt-% of Sr₃WO₆ was also formed. The ammonolysis of the oxide precursors at lower temperatures (i.e. 700 °C) was shown to also lead to the formation of Sr₂WO₅/Sr₃WO₆; at 900 °C they were found to be the major phases.

It seems thus that for $0.25 \leq x \leq 0.6$, Sr₃WO₆ is inevitably formed as by-product and thus phase-pure solid solution perovskite-type oxynitride is not achievable in this compositional range.

On the contrary, SMW7 ($x = 0.75$) did not show any decomposition upon preparation at 800 °C and yielded ca. 93 wt-% of oxynitride phase (SrMo_{0.25}W_{0.75}O_{1.77(4)}N_{1.23(4)}). Unlike in SMW2, SMW3 and SMW6, the perovskite-type oxynitride phase is still the major phase in SMW7 even upon ammonolysis at 900 °C.

SMW8 and SMW9 ($x = 0.85$ and 0.95) reveal similar behavior. However, a higher ammonolysis temperature (800 instead of 700 °C) is required to obtain the oxynitride phase as main phase. This is consistent with the results related to the synthesis temperature of SrMo(O,N)₃ (700 °C) and SrW(O,N)₃ (800–900 °C).^[27,28] Ammonolysis of SMW8 at 900 °C leads to the

formation of Sr_3WO_6 ; whereas in the case of SMW9 the phase-pure perovskite-type oxynitride was likely obtained.

Furthermore, the extension of the annealing time in ammonia from 6 to 12 h was shown to enhance the conversion from oxide to oxynitride. For instance, in the case of SMW7 the yield of the perovskite-type oxynitride phase increases from 80.7 to 92.9 wt-% as the annealing time is extended from 6 to 12 h. Also the nitrogen content in the resulting oxynitride is higher as the annealing time increases (i.e., O/N ratio decreases from 1.88 upon 6 h annealing to 1.44 in the perovskite obtained after 12 h ammonolysis time).

Interestingly, the formation of solid solution seems to favor the nitrogen incorporation capability. Thus, in SMW8 the nitrogen content ($\text{SrMo}_{0.15}\text{W}_{0.85}\text{O}_{1.21(6)}\text{N}_{1.79(6)}$, O/N ratio 0.68, see Figure 3f) was significantly higher than that reported for SrMoO_2N and $\text{SrWO}_{1.5}\text{N}_{1.5}$ ^[27] (O/N ratio of 2 and 1, respectively).

As shown in the HRTEM micrograph in Figure 4, the crystalline phase in the SMW8 sample obtained after ammonolysis at 800 °C for 12 h was indexed with the space group $Pm\bar{3}m$, indicating the perovskite-type cubic structure as reported also for $\text{SrMo}(\text{O},\text{N})_3$ and $\text{SrW}(\text{O},\text{N})_3$.

Except for SMW9, all samples showed the formation of Sr_3WO_6 phase upon thermal treatment at 900 °C. Interestingly, Sr_3WO_6 is not accessible from the scheelite-type SrWO_4 oxide,^[10,27] whereas its formation has been reported to be favored for the case of A-site solid solution $\text{Ca}_x\text{Sr}_{1-x}\text{WO}_2\text{N}$ ^[17] (though the authors marked the Sr_3WO_6 as unknown phase). Consequently, the presence of solid solution (either at A or B site) significantly changes the thermal behavior of the scheelite-type oxides. As reported by Mizusaki et al.,^[29] the entropy and enthalpy of formation for solid solutions strongly depends on the composition, which may be further attributed to the difference in the electronic state of the B-site ions.

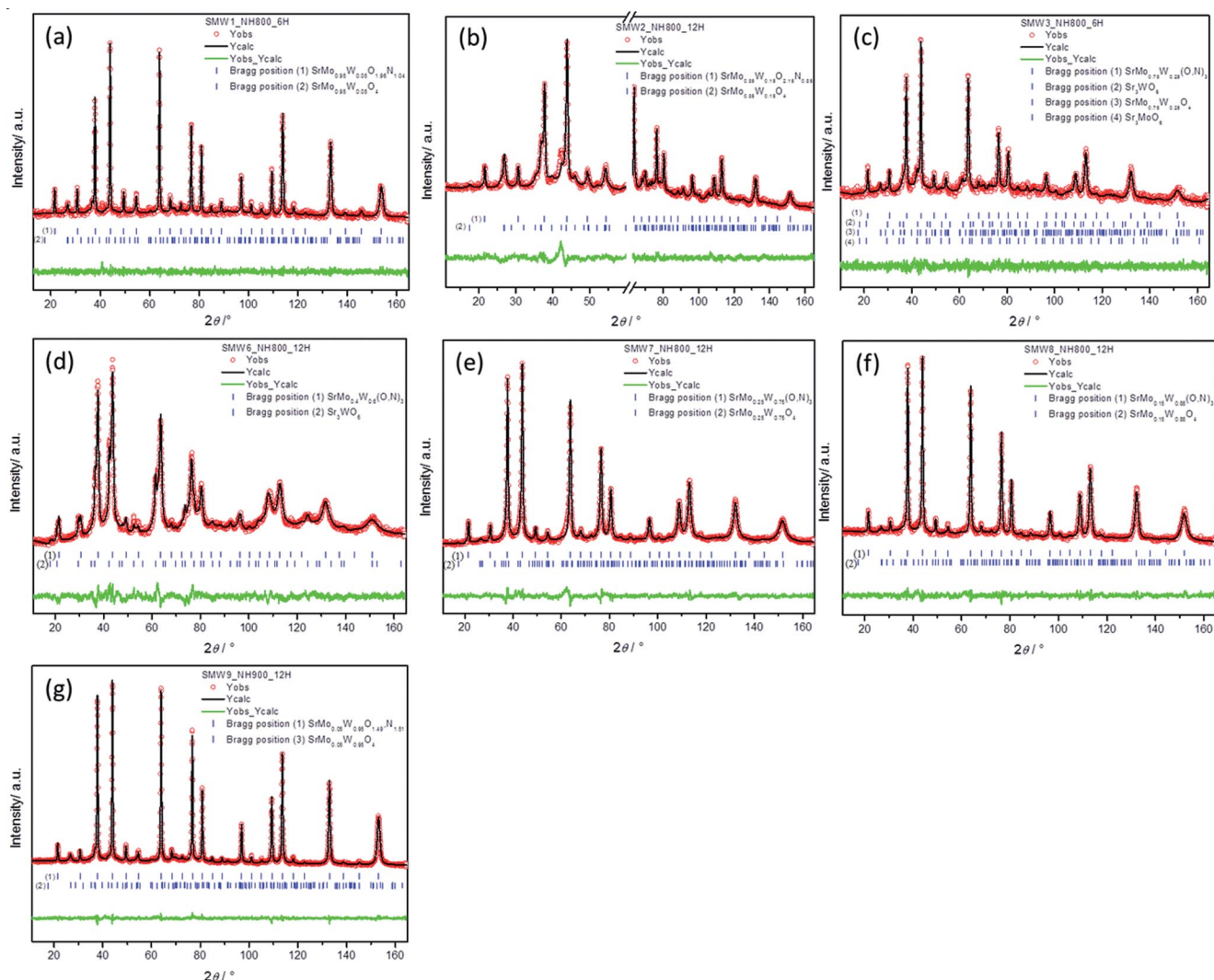


Figure 4. Rietveld refinement of neutron powder diffraction patterns of the as-synthesized solid solution oxynitrides when $x = 0.05$ (a), 0.15 (b), 0.25 (c), 0.6 (d), 0.75 (e), 0.85 (f), 0.95 (g) after annealing in an ammonia flow at 800 or 900 °C for 6 or 12 h. Blue tick marks are Bragg peak positions of different phases. The green lines at the bottom denote the different intensities between the observed and calculated profiles. The break part in (b) is related to an unknown diffraction peak, which was excluded from the refinement.

The electronegativity difference between molybdenum and tungsten (e.g. 2.2 and 1.7, respectively)^[30] can probably lead to structural distortion due to B–O/N bond changing, especially for Mo/W ratios close to 1. Furthermore, double perovskite (for instance as for Sr_3WO_6 , i.e. $A_2BB'O_6$, with $A, B: \text{Sr}$ and $B': \text{W}$) can be derived from the ABO_3 perovskite structure due to the large difference in ionic radius between Sr^{2+} and W^{6+} ($\Delta R = 0.58 \text{ \AA}$),^[31] where corner sharing connectivity is not maintained anymore.

Magnetic Properties of Solid Solution Oxynitrides

The variation of the magnetic susceptibility of selected as-synthesized solid solution oxynitrides in the range from 10 to 300 K is shown in Figure 5. The zero-field-cooled (ZFC) and field-cooled (FC) susceptibility measurements were performed under an applied field of 2 T. All samples exhibit a temperature-independent paramagnetic behavior between 70 K and 300 K. The magnetic susceptibility increases below 70 K, which relates to a Curie behavior superposed to the temperature-independent Pauli paramagnetism. This behavior is consistent with that reported for SrMoO_2N previously.^[10,16,32]

Similarly with SrMoO_2N , an anomalous hyperbolic crest at ca. 45.5 K was observed as well. According to the literature^[10,16,32] this might relate to molecular oxygen trapped within the perovskite oxynitride. Bulk oxygen melts at $T = 54 \text{ K}$ and the paramagnetic γ phase transforms into the antiferromagnetic β phase at $T = 44 \text{ K}$. The generation of molecular oxygen is thought occurring during the nitrogen incorporation. In order to rule out other possible sources for the incorporation of oxygen within our samples, they were handled in inert gas atmosphere glove box. A comparative magnetic measurement of SMW8 handled in air was performed under the same experimental conditions (see Figure S3, Supporting Information). The presence of same anomalous hyperbolic crest indicates that these measured signals result from molecular oxygen in materials and that the effect of external factors (i.e. sample holder or chamber, environment, etc.) can be ruled out. We consider here an analogous mechanism for the generation of molecular oxygen within our perovskite solid solution oxynitrides as recently proposed and discussed for SrMoO_2N and $\text{SrWO}_{1.5}\text{N}_{1.5}$.^[27] Thus, a scheelite-type oxynitride phase might have formed intermediary and leads to the formation of molecular oxygen, which is trapped within the pores and shows the anomalous magnetic behavior mentioned above.

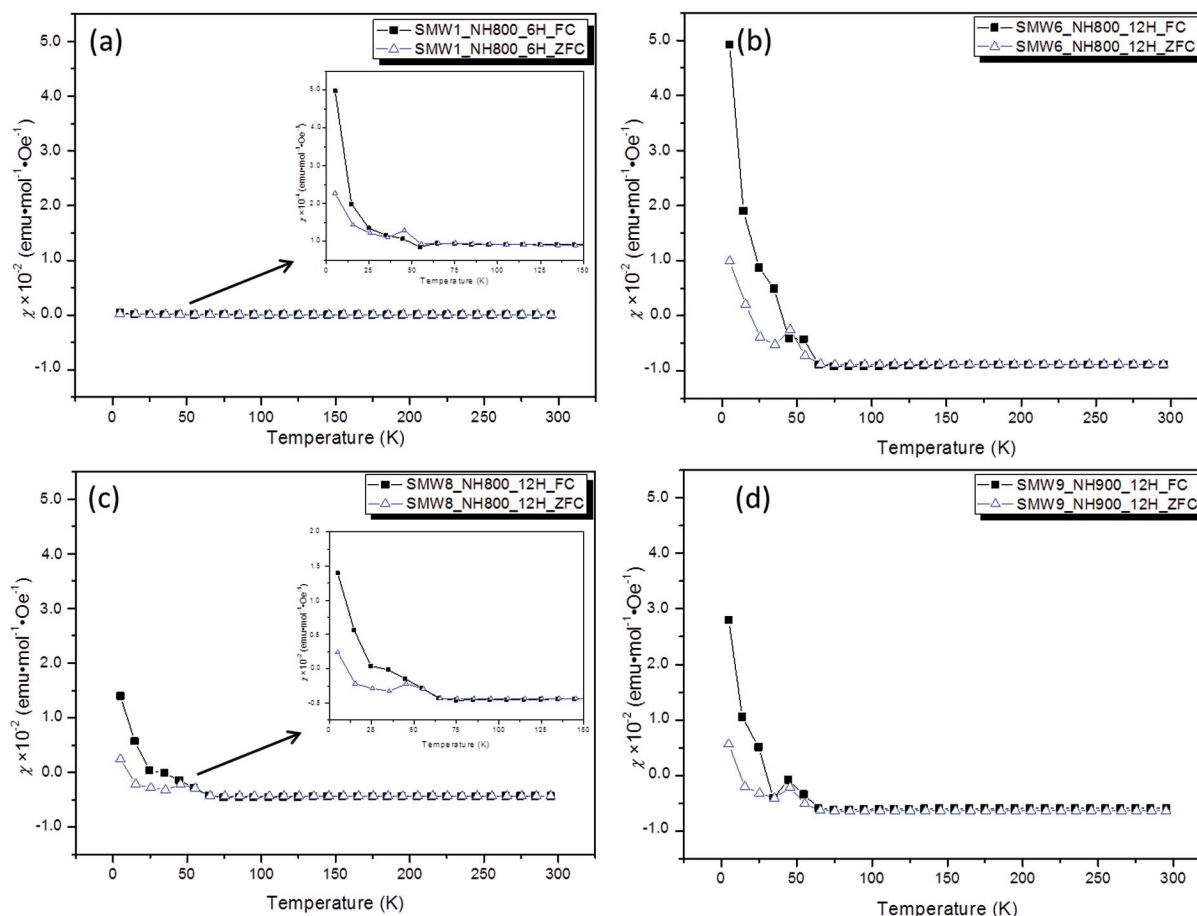


Figure 5. Temperature-dependent SQUID measurements of the magnetic susceptibility of (a) SMW1 ($x = 0.05$) prepared in an ammonia flow at $800 \text{ }^\circ\text{C}$ for 6 h (the inset shows a magnification of the curves), (b) SMW6 ($x = 0.6$) prepared in an ammonia flow at $800 \text{ }^\circ\text{C}$ for 12 h, (c) SMW8 ($x = 0.85$) prepared in an ammonia flow at $800 \text{ }^\circ\text{C}$ for 12 h (the inset shows a magnification of the curves), and (d) SMW9 ($x = 0.95$) prepared in an ammonia flow at $900 \text{ }^\circ\text{C}$ for 12 h.

There was no correlation between the position of the discussed anomalous hyperbolic and the Mo/W ratio in the solid solution oxynitrides. However, the magnetic susceptibility of the tungsten-rich ($x \geq 0.6$) solid solution oxynitrides is about two orders of magnitude larger than that of molybdenum-rich compositions (i.e., SMW1), which is consistent with the results reported by Fawcett^[10] and probably relates to the stronger paramagnetic susceptibility of tungsten^[33] compared to that of molybdenum.

Conclusions

Scheelite-type solid solution $\text{SrMo}_{1-x}\text{W}_x\text{O}_4$ oxide precursors were synthesized by using solvothermal methods within the full compositional range (i.e., x from 0 to 1). The corresponding perovskite-type oxynitrides are formable upon thermal treatment of the scheelite-type solid solution oxides in ammonia atmosphere only in a limited compositional range, i.e. for $x \leq 0.25$ and $x \geq 0.6$; whereas for $0.25 \leq x \leq 0.6$ decomposition processes occur and furnish different oxides and nitrides.

A Pauli paramagnetic behavior was observed for the solid solution oxynitrides above 70 K. The magnetic susceptibility increased with the increasing of tungsten. An anomalous hyperbolic crest at ca. 45.5 K is considered to likely relate to the presence of molecular oxygen within the measured materials, which is similar with the case of SrMoO_2N and $\text{SrWO}_{1.5}\text{N}_{1.5}$.

Acknowledgements

The authors acknowledge the European Union Seventh Framework Program (FP7/2007–2013) under grant agreement no 264873 (FUNEA-Functional Nitrides for Energy Applications) for financial support, Dr Vladimir Pomjakushin (SINQ) and Dr Emmanuelle Suard (ILL) for the technical assistance and Duan Li (Department of Materials and Environmental Chemistry, Stockholm University) for the HRTEM measurement and discussion. This work is partly based on the experiments performed at the SINQ, Paul Scherrer Institute (Villingen, Switzerland) and DIF D2B, Institut Laue-Langevin (ILL, Grenoble, France).

References

- [1] Y. I. Kim, P. M. Woodward, *J. Solid State Chem.* **2007**, *180*, 3224–3233.
- [2] A. Fuertes, *J. Mater. Chem.* **2012**, *22*, 3293–3299.
- [3] S. G. Ebbinghaus, H. P. Abicht, R. Dronskowski, T. Müller, A. Reller, A. Weidenkaff, *Prog. Solid State Chem.* **2009**, *37*, 173–205.
- [4] F. Tessier, P. Maillard, F. Chevire, K. Domen, S. Kikkawa, *J. Ceram. Soc. Jpn.* **2009**, *117*, 1–5.
- [5] W. J. Li, E. Ionescu, R. Riedel, A. Gurlo, *J. Mater. Chem. A* **2013**, *1*, 12239–12245.
- [6] W. Li, A. Gurlo, E. Ionescu, R. Riedel, *Z. Anorg. Allg. Chem.* **2012**, *638*, 1631.
- [7] C. Tassel, Y. Kuno, Y. Goto, T. Yamamoto, C. M. Brown, J. Hester, K. Fujita, M. Higashi, R. Abe, K. Tanaka, Y. Kobayashi, H. Kageyama, *Angew. Chem. Int. Ed.* **2015**, *54*, 516–521.
- [8] M. H. Yang, J. A. Rodgers, L. C. Middler, J. Oro-Sole, A. B. Jorge, A. Fuertes, J. P. Attfield, *Inorg. Chem.* **2009**, *48*, 11498–11500.
- [9] N. Kumar, A. Sundaresan, C. N. R. Rao, *Mater. Res. Bull.* **2011**, *46*, 2021–2024.
- [10] I. D. Fawcett, K. V. Ramanujachary, M. Greenblatt, *Mater. Res. Bull.* **1997**, *32*, 1565–1570.
- [11] F. Chevire, F. Tessier, R. Marchand, *Eur. J. Inorg. Chem.* **2006**, 1223–1230.
- [12] A. E. Maegli, T. Hisatomi, E. H. Otal, S. Yoon, S. Pokrant, M. Gratzel, A. Weidenkaff, *J. Mater. Chem.* **2012**, *22*, 17906–17913.
- [13] A. Maegli, S. Yoon, E. Otal, L. Karvonen, P. Mandaliev, A. Weidenkaff, *J. Solid State Chem.* **2011**, *184*, 929–936.
- [14] T. Motohashi, Y. Hamade, Y. Masubuchi, T. Takeda, K. Murai, A. Yoshiasa, S. Kikkawa, *Mater. Res. Bull.* **2009**, *44*, 1899–1905.
- [15] D. Logvinovich, R. Aguiar, R. Robert, M. Trottmann, S. G. Ebbinghaus, A. Reller, A. Weidenkaff, *J. Solid State Chem.* **2007**, *180*, 2649–2654.
- [16] D. Logvinovich, J. Hejtmanek, K. Knizek, M. Marysko, N. Homazava, P. Tomes, R. Aguiar, S. G. Ebbinghaus, A. Reller, A. Weidenkaff, *J. Appl. Phys.* **2009**, *105*, 023522.
- [17] M. Yashima, U. Fumi, H. Nakano, K. Omoto, J. R. Hester, *J. Phys. Chem. C* **2013**, *117*, 18529–18539.
- [18] M. Yang, J. Oro-Sole, A. Kusmartseva, A. Fuertes, J. P. Attfield, *J. Am. Chem. Soc.* **2010**, *132*, 4822–4829.
- [19] P. Bacher, P. Antoine, R. Marchand, P. Lharidon, Y. Laurent, G. Roul, *J. Solid State Chem.* **1988**, *77*, 67–71.
- [20] P. Fischer, G. Frey, M. Koch, M. Konnecke, V. Pomjakushin, J. Schefer, R. Thut, N. Schlumpf, R. Burge, U. Greuter, S. Bondt, E. Berruyer, *Physica B* **2000**, *276*, 146–147.
- [21] P. Thompson, D. E. Cox, J. B. Hastings, *J. Appl. Crystallogr.* **1987**, *20*, 79–83.
- [22] J. Rodriguezcarvajal, *Physica B* **1993**, *192*, 55–69.
- [23] M. Kacimi, S. Gharbage, F. Bozon-Verduraz, M. Ziyad, *J. Phys. IV* **2005**, *123*, 213–218.
- [24] M. Daturi, G. Busca, M. M. Borel, A. Leclaire, P. Piaggio, *J. Phys. Chem. B* **1997**, *101*, 4358–4369.
- [25] R. D. Shannon, *Acta Crystallogr., Sect. A* **1976**, *32*, 751–767.
- [26] R. D. Shannon, C. T. Prewitt, *Acta Crystallogr., Sect. B* **1969**, *25*, 925–946.
- [27] W. J. Li, D. Li, X. Gao, A. Gurlo, S. Zander, P. Jones, A. Navrotsky, Z. J. Shen, R. Riedel, E. Ionescu, *Dalton Trans.* **2015**, *44*, 8238–8246.
- [28] W. J. Li, D. Li, A. Gurlo, J. Shen, R. Riedel, E. Ionescu, *J. Eur. Ceram. Soc.* **2015**, in press.
- [29] J. Mizusaki, M. Yoshihiro, S. Yamauchi, K. Fueki, *J. Solid State Chem.* **1987**, *67*, 1–8.
- [30] C. Housecroft, A. G. Sharpe, *Inorganic Chemistry*, 4th ed., Pearson Education, Harlow, **2012**.
- [31] G. King, A. M. Abakumov, J. Hadermann, A. M. Alekseeva, M. G. Rozova, T. Perkisas, P. M. Woodward, G. Van Tendeloo, E. V. Antipov, *Inorg. Chem.* **2010**, *49*, 6058–6065.
- [32] G. Liu, X. H. Zhao, H. A. Eick, *J. Alloys Compd.* **1992**, *187*, 145–156.
- [33] Hugh D Young, F. W. Sears, *University Physics*, 8th ed., Addison-Wesley, Reading, **1992**.

Received: February 21, 2015
Published Online: June 29, 2015

SUPPORTING INFORMATION

Title: Perovskite-type Solid Solution $\text{SrMo}_{1-x}\text{W}_x(\text{O,N})_3$ Oxynitrides: Synthesis, Structure, and Magnetic Properties

Author(s): W. Li, A. Gurlo, R. Riedel, E. Ionescu*

Ref. No.: Z201500098

Supporting information

Perovskite-type solid-solution $\text{Sr}(\text{Mo},\text{W})(\text{O},\text{N})_3$ oxynitrides: synthesis, structure and magnetic properties

Wenjie Li, Aleksander Gurlo, Ralf Riedel and Emanuel Ionescu

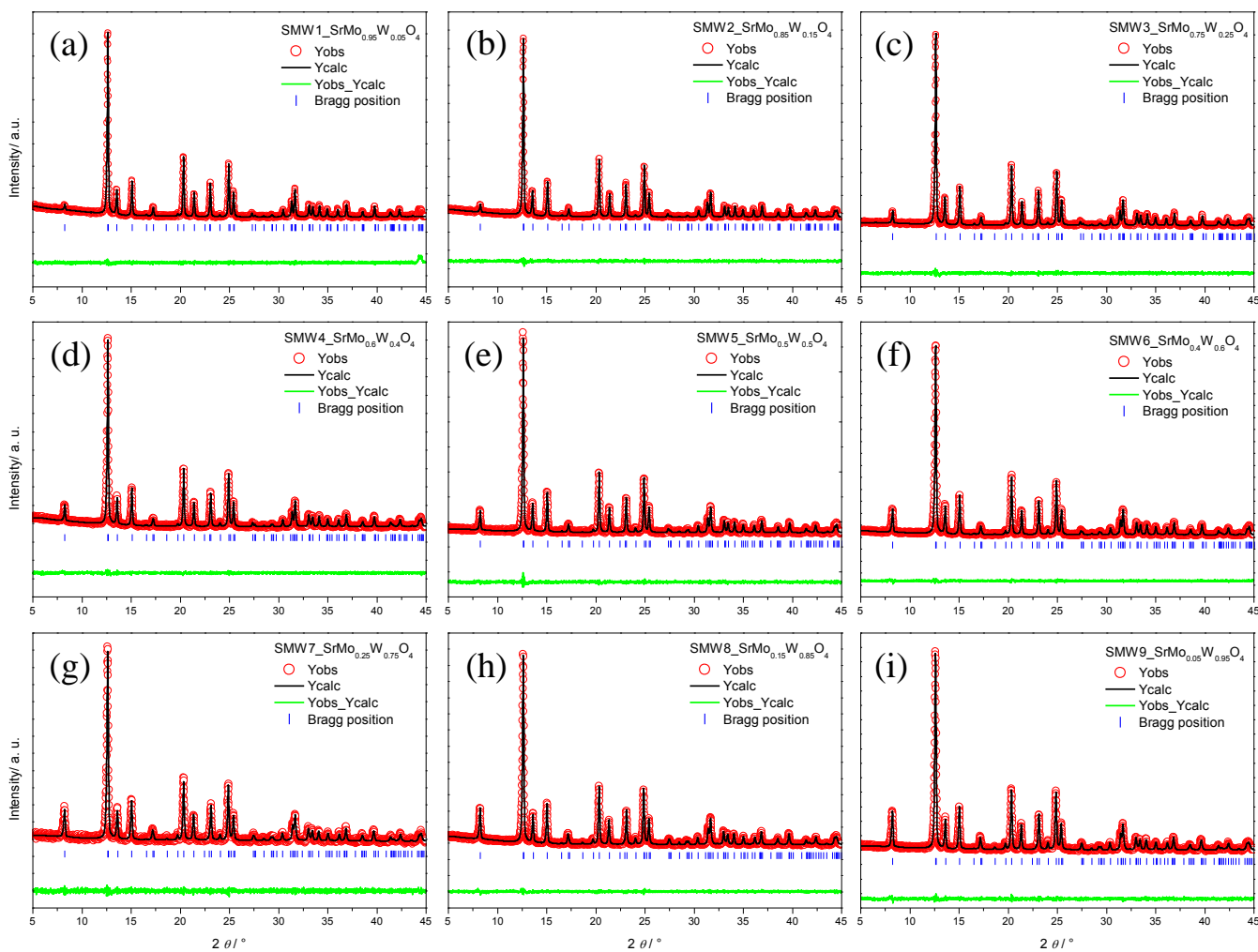


Figure S 1. Rietveld refinement of X-ray diffraction patterns of the as-synthesized solid-solution oxide precursors ($\text{SrMo}_{1-x}\text{W}_x\text{O}_4$) when $x=0.05, 0.15, 0.25, 0.4, 0.5, 0.6, 0.75, 0.85, 0.95$ (a - i). Blue tick marks are Bragg peak positions of $\text{Sr}(\text{Mo},\text{W})\text{O}_4$. The green lines at the bottom denote the different intensities between the observed and calculated profiles.

Table S 1 Crystallographic data for scheelite-type SrMo_{1-x}W_xO₄ oxide precursors

Parameters	x=0.05	x=0.15	x=0.25	x=0.4	x=0.5	x=0.6	x=0.75	x=0.85	x=0.95
Radiation					X-ray Mo K _α				
λ, Å					0.7093				
S.G.					<i>I 41/a</i> , No. 88				
Z					4				
a, b, Å	5.39518(37)	5.39584(33)	5.39625(36)	5.40036(33)	5.40284(25)	5.40348(26)	5.40866(62)	5.41269(32)	5.41417(38)
c, Å	12.01575(88)	12.00562(80)	11.9939(87)	11.98436(78)	11.98082(63)	11.96732(62)	11.96046(149)	11.95821(76)	11.95186(93)
Sr					0.0, 0.25, 0.625				
x, y, z									
Biso, Å ²	0.293(108)	0.107(100)	0.54(96)	0.402(81)	0.647(84)	0.672(56)	0.844(134)	0.533(57)	0.558(79)
Occ.					1.0				
Mo/W					0.0, 0.25, 0.125				
x, y, z									
Biso, Å ²	0.225(95)	0.535(84)	0.46(62)	0.317(51)	0.447(43)	0.485(27)	0.638(65)	0.39(26)	0.577(39)
Occ.					1.0				
O									
x, y, z	0.23889(112), 0.112111(99), 0.04290(41)	0.241(103), 0.11337(94), 0.04282(40)	0.24142(108), 0.1155(105), 0.0431(44)	0.23964(103), 0.1106(103), 0.04284(42)	0.24357(121), 0.11004(126), 0.04124(52)	0.24175(89), 0.1086(99), 0.0425(38)	0.2418(206), 0.10251(235), 0.04262(88)	0.24253(109), 0.10851(113), 0.04258(46)	0.24206(142), 0.10833(155), 0.04184(63)
Biso, Å ²	-0.203(185)	0.535(84)	0.476(231)	0.121(227)	0.818(288)	1.11(220)	1.167(508)	0.520(237)	0.941(339)
Occ.	0.95/0.05	0.85/0.15	0.75/0.25	0.6/0.4	0.5/0.5	0.4/0.6	0.25/0.75	0.15/0.85	0.05/0.95
χ ²	1.003	1.01	0.994	0.984	1.003	1.035	0.978	1.03	0.982
R _p	3.40	3.17	3.42	3.02	3.73	2.65	5.67	2.96	3.80
wR _p	3.39	3.14	3.44	3.07	3.72	2.56	5.80	2.87	3.87
Chi2	1.05	1.07	1.04	1.04	1.09	1.12	0.992	1.10	0.999

Table S 2 The oxygen and nitrogen content by elemental analysis of as-synthesized samples under ammonia flow between 700 – 900 °C for 6 hours

Samples	Oxygen wt%	/	Nitrogen wt%	/	Samples	Oxygen wt%	/	Nitrogen wt%	/
SMW1_NH700_6H	14.500(97)		5.858(84)		SMW6_NH700_6H	17.334(464)		2.861(147)	
SMW1_NH800_6H	14.201(120)		5.944(255)		SMW6_NH800_6H	15.226(315)		4.162(39)	
SMW1_NH900_6H	13.850(388)		6.009(45)		SMW6_NH900_6H	14.967(76)		5.019(38)	
SMW2_NH700_6H	14.120(88)		6.000(39)		SMW7_NH700_6H	16.325(332)		2.098(25)	
SMW2_NH800_6H	13.600(240)		6.109(214)		SMW7_NH800_6H	10.763(116)		5.367(51)	
SMW2_NH900_6H	13.370(389)		5.542(68)		SMW7_NH900_6H	10.049(79)		5.585(26)	
SMW3_NH700_6H	12.640(986)		5.811(59)		SMW8_NH700_6H	15.920(42)		2.234(38)	
SMW3_NH800_6H	12.970(308)		5.761(225)		SMW8_NH800_6H	10.150(284)		5.615(83)	
SMW3_NH900_6H	12.860(2)		4.050(48)		SMW8_NH900_6H	9.471(140)		5.775(53)	
SMW4_NH700_6H	14.960(384)		4.494(73)		SMW9_NH700_6H	15.340(423)		2.182(66)	
SMW4_NH800_6H	13.150(557)		5.086(171)		SMW9_NH800_6H	8.542(47)		6.524(69)	
SMW4_NH900_6H	13.060(268)		4.251(47)		SMW9_NH900_6H	8.313(26)		6.683(1)	
SMW5_NH700_6H	18.110(202)		2.082(53)						
SMW5_NH800_6H	17.110(235)		2.256(6)						
SMW5_NH900_6H	13.280(342)		3.846(32)						

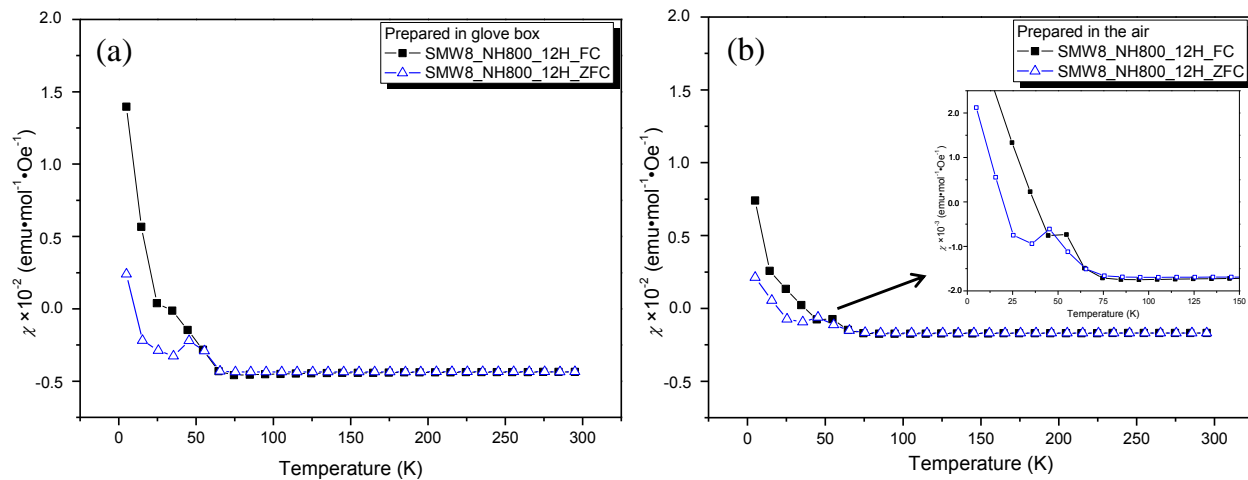


Figure S 2. The temperature-dependent magnetic susceptibility of sample SMW8 oxynitride measured with a SQUID magnetometer prepared (a) in glove box and (b) in the air (the insert shows that in smaller scale ($\chi \sim 10^{-3}$)).

List of publications (2010 - 2015)

- 1) W. Li, D. Li, X. Gao, A. Gurlo, S. Zander, P. Jones, A. Navrotsky, Z. Shen, R. Riedel and E. Ionescu, "A study on the thermal conversion of scheelite-type ABO_4 into perovskite-type $AB(O,N)_3$ " *Dalton Trans*, **2015**, 44, 8238.
 - 2) Li WJ, Li D, Gurlo A, Shen ZJ, Riedel R and Ionescu E, "Synthesis and rapid sintering of dense $SrA(O,N)_3$ ($A=Mo, W$) oxynitride ceramics", *J. Euro. Ceram. Soc.*, 35 (**2015**), 3273-3281
 - 3) Li W, Gurlo A, Riedel R and Ionescu E, "Perovskite-type solid solution $SrMo_{1-x}W_x(O,N)_3$ oxynitrides: synthesis, structure and magnetic properties", *Z. Anorg. Allg. Chem.*, **2015**, 641, (8-9), 1533-1539
 - 4) W. Li, E. Ionescu, R. Riedel and A. Gurlo, "Can we predict the formability of perovskite oxynitrides from tolerance and octahedral factors?" *J. Mater. Chem. A*, (**2013**); 1: 12239-45.
 - 5) Li, W., Gurlo, A.; Ionescu, E.; Riedel, R., "Perovskite structure stability in metal oxynitrides", *Z. Anorg. Allg. Chem.* **2012**, 638, (10), 1631.
 - 6) Nguyen VL, Zera E, Perolo A, Campostrini R, Li WJ, Sorarù GD, "Synthesis and characterization of polymer-derived SiCN aerogel", *J. Euro. Ceram. Soc.*, 35 (**2015**), 3295-3302
 - 7) Li D, Li WJ, Fasel C, Shen J, Riedel R., "Sinterability of the oxynitride $LaTiO_2N$ with perovskite-type structure," *J. Alloy Compd.*, (**2014**); 586: 567-73.
 - 8) A. Navrotsky, W. Li, P. Jones, E. Ionescu, R. Riedel, "Calorimetric studies on perovskite-type solid solution $SrMo_{1-x}W_x(O,N)_3$ oxynitrides", *to be submitted*
 - 9) W. Li, A. Gurlo, R. Riedel and E. Ionescu, "The novel single-source-precursor synthesis and properties investigation of $Gd_2O_2(NCN)$ ", *under preparation*
 - 10) Li, W. J., Zhou, S. M., Liu, N., Lin, H., Teng, H., Li, Y. K., Hou, X. R., Jia, T. T., "Effect of additives on optical characteristic of thulium doped yttria transparent ceramics", *Opt. Mater.* **2010**, 32, (9), 971-974.
 - 11) Li, W. J., Zhou, S. M., Liu, N., Lin, H., Teng, H., Li, Y. K., Hou, X. R., Jia, T. T., "Synthesis and spectral properties of $Yb^{3+}/Ho^{3+}:Y_2O_3$ co-doped yttria mid-infrared transparent ceramics", *Mater. Lett.* **2010**, 64:1344-1346
 - 12) Li, W. J., Zhou, S. M., Lin, H., Teng, H., Liu, N., Li, Y. K., Hou, X. R., Jia, T. T., "Controlling of grains size with different additives in $Tm^{3+}:Y_2O_3$ transparent ceramics", *J. Am. Ceram. Soc.* 93[11] 3819-3822 (**2010**)
-

-
- 13) Li, W. J., Zhou, S. M., Lin, H., Teng, H., Liu, N., Li, Y. K., Hou, X. R., Jia, T. T., “Synthesis and optical properties of Yb³⁺, Ho³⁺ co-doped yttria transparent ceramics”, *Chinese J. of Inorg. Chem.* **2010**,26(4):687-692
 - 14) H. Lin, S. M. Zhou, H. Teng, Y. K. Li, W. J. Li, X. R. Hou and T. T. Jia, “Near infrared quantum cutting in heavy Yb doped Ce_{0.03}Yb_{3x}Y_(2.97-3x)Al₅O₁₂ transparent ceramics for crystalline silicon solar cells”, *J. App. Phys.*, 107 (**2010**) 043107.
 - 15) H. Lin, S. M. Zhou, X. R. Hou, W. J. Li, Y. K. Li, H. Teng and T. T. Jia, “Down-conversion from Blue to Near Infrared in Tm³⁺/Yb³⁺ Co-doped Y₂O₃ Transparent Ceramics” *IEEE Photonics Tech. Lett.*, 22 (**2010**) 866-868.
 - 16) X. R. Hou, S. M. Zhou, H. Lin, H. Teng, Y. K. Li, W. J. Li and T. T. Jia, “Violet and blue up-conversion luminescence in Tm³⁺/Yb³⁺ co-doped Y₂O₃ transparent ceramic” *J. App. Phys.*, 107 (**2010**) 083101
 - 17) X. R. Hou, S. M. Zhou, W. J. Li, Y. K. Li, H. Lin, H. Teng and T. T. Jia, “Investigation of Up-conversion Luminescence in Er³⁺/Yb³⁺ codoped Yttria Transparent Ceramic” *J. Am. Ceram. Soc.*, 93 [9] (**2010**) 2779–2782.
 - 18) X. R. Hou, S. M. Zhou, Y. K. Li and W. J. Li, “Effect of ZrO₂ on the sinterability and spectral properties of (Yb_{0.05}Y_{0.95})₂O₃ transparent ceramic” *Opt. Mater.*, 32 (**2010**) 920-923.
 - 19) X. R. Hou, S. M. Zhou, W. J. Li and Y. K. Li, “Study on the effect and mechanism of zirconia on the sinterability of yttria transparent ceramic” *J. Euro. Ceram. Soc.*, 30, (**2010**) 3125-3129.
 - 20) X. R. Hou, S. M. Zhou, Y. K. Li and W. J. Li, “Luminescent properties of nano-sized Y₂O₃:Eu fabricated by co-precipitation method” *J. Alloy Compd.*, 494 (**2010**) 382-385.
 - 21) Y. K. Li, S. M. Zhou, H. Lin, X. R. Hou and W. J. Li, “Intense 1064nm emission by the efficient energy transfer from Ce³⁺ to Nd³⁺ in Ce/Nd co-doped YAG transparent ceramics”, *Opt. Mater.*, 32 (**2010**) 1223-1226.
 - 22) Y. K. Li, S. M. Zhou, H. Lin, X. R. Hou, W. J. Li, H. Teng and T. T. Jia, “Fabrication of Nd:YAG transparent ceramics with TEOS, MgO and compound additives as sintering aids” *J. Alloy Compd.*, 502 (**2010**) 225-230.
-

Curriculum Vitae

Wenjie Li

Address: Nieder-Ramstädter-str. 11, 64283 Darmstadt, Germany

Email: w.li@materials.tu-darmstadt.de or lwjtt@hotmail.com

Personal status

Gender: Male

Date of Birth: 25/11/1984

Citizenship: China

Scientific background

- **2011 - 2014 PhD in Materials Science, Technische Universität Darmstadt (TUD), Germany**
Thesis: Formability, synthesis and properties of perovskite-type oxynitrides
Advisor: Prof. Ralf Riedel
- **2007 – 2010 Master in Materials Science and Engineering, Shanghai Institute of Fine Optics and Mechanics, Chinese Academy of Science, P. R. China**
Thesis: Fabrication and spectral of yttria transparent ceramics for 2 μm mid-infrared laser application
Advisor: Prof. Shengming Zhou
- **2003 – 2007 Bachelor in Materials Science and Engineering, Central South University, P. R. China**
Thesis: Dispersion and stability of γ -alumina/ceria nanocomposite materials in water system
Advisor: Prof. Xiaolan Song

Research experiences

- **2011 - 2014 Research Assistant, Technische Universität Darmstadt (TUD), Germany**
 - Studied the formability of novel perovskite oxynitrides by a self-developed approach
 - Synthesized the oxide precursors by complementary approaches and novel perovskite oxynitrides
 - Investigated on their multifunctional properties such as magnetic, electronic conductivity, semiconducting, photocatalytic etc. Developed fundamental understanding of their structure and properties.
- **2007 – 2010 Research Assistant, Shanghai Institute of Fine Optics and Mechanics, Chinese Academy of Science**
 - Synthesized the rare earth doped yttrium oxide ceramic powders via co-precipitation and solid state reaction method
 - Fabricated transparent ceramics (especially the Tm^{3+} and Ho^{3+} doped Y_2O_3 ceramic) in mid-infrared range, focusing on their optical and laser performance
 - Developed large-scale (2 inch) $\text{Tm}^{3+}:\text{Y}_2\text{O}_3$ transparent ceramics with high optical quality
- **2006 – 2007 Research Assistant, Central South University**
 - Synthesized the γ -alumina/ceria nanocomposite materials as a candidate of chemical-mechanical polishing material by sol-gel approach
 - Studied the dispersion and stability properties of γ -alumina/ceria nanocomposite materials by zeta-potential and absorbance

Activities

- Teaching the lab courses of “Synthesis and characterization of BaTiO₃” and “Characterization of polymer-derived silicon-containing ceramics” in 2012/2013 at TU Darmstadt
- Carried out the neutron powder diffraction at synchrotron radiation center at “ILL Grenoble”, “PSI Villigen” and “HZB Berlin” intervals from 2011 to 2014
- Participated the 33rd Berlin School on Neutron Scattering at Helmholtz-Zentrum Berlin für Materialien und Energie with both theoretical and practice on different neutron scattering techniques in March, 2013
- Trained with Transferable skills at Marie Skłodowska-Curie Conference: ESOF 2014 in Copenhagen, Denmark
- Participated the practical course under FUNEA project
 - “Spark Plasma Sintering Course” at Stockholm University, Sweden
 - “Mechanical properties characterizations Course” at Institute of Inorganic Chemistry, Slovak Academy of Sciences
 - “Si₃N₄ based materials from industrial perspective-past, current and future Course” at MDA Advanced Ceramics Ltd., Turkey
 - “Case studies involving porous ceramics in household appliances for energy saving” at Electrolux Ltd. and “Processing, characterization and applications of porous ceramics Course” at University of Padova, Italy
 - “Toward tailored properties of SOFC” at SOFC Power Ltd. and “Electrical and optical properties of nitride materials Course” at University of Trento, Italy
 - “Upscaling synthesis methods in industry” at AZ Electronic Materials GmbH, Wiesbaden and “Design and testing of TBCs, Patent writing, IPR and Project Management” at Faurecia Emissions Control Technologies GmbH, Germany
 - “Solid state hydrogen storage in nitride ceramics” at University of Montpellier 2, France
 - “Electronic structure of solid nitrides” at University of Rennes, CNRS, France
 - “Solvothermal synthesis techniques and high-temperature high-pressure synthesis” at TU Darmstadt, Germany

Conference Presentations and Posters

- 1) W. J. Li, A. Gurlo, E. Ionescu and R. Riedel, Formability of perovskite oxynitrides, 6th International Workshop on Spinel Nitrides and Related Materials in Conjunction with the Marie Curie ITN 7th Framework Programme FUNEA, September 9 - 14, 2012 Ruedesheim/Rhine, Germany (**Oral presentation**)
 - 2) W. J. Li, A. Gurlo, E. Ionescu and R. Riedel, Scheelite ABO₄ to perovskite AB(O,N)₃ transition induced by nitrogen substitution, 13th International Conference of the European Ceramic Society, June 23 – 28, 2013 Limoges, France (**Oral presentation**)
 - 3) W. J. Li, E. Ionescu, R. Riedel and A. Gurlo, The structure and properties investigation of solid solution Strontium-Molybdenum-Tungsten perovskite oxynitride, 8th International Symposium on Nitrides in Conjunction with the 7th International Workshop on Spinel Nitrides and Related Materials and the Marie Curie ITN 7th Framework Programme FUNEA, August 31 – September 05, 2014 Wildbad Kreuth, Germany (**Oral presentation**)
 - 4) W. J. Li, A. Gurlo, E. Ionescu and R. Riedel, Perovskite Structure Stability in Metal Oxynitrides, The Euroscience Open Forum and Marie Curie Actions Conference, July 9 – 15, 2012 Dublin, Ireland (**Poster**)
 - 5) W. J. Li, A. Gurlo, E. Ionescu and R. Riedel, Perovskite Structure Stability in Metal Oxynitrides, Zeitschrift für anorganische und allgemeine Chemie, 638(10):1631, Vortragstagung der FG Festkörperchemie und Materialforschung, September 17 - 19, 2012 Darmstadt, Germany (**Poster**)
 - 6) W. J. Li, A. Gurlo, R. Riedel and E. Ionescu, Single-source-precursor synthesis and properties investigation of Gd₂O₂(NCN), GDCh-Wissenschaftsforum Chemie, September 01 – 04, 2013 Darmstadt, Germany (**Poster**)
-

- 7) W. J. Li, E. Ionescu, R. Riedel and A. Gurlo, The structure and properties investigation of solid solution Strontium-Molybdenum-Tungsten perovskite oxynitride, Materials Science and Engineering Congress, September 23 – 25, 2014 Darmstadt, Germany (**Poster**)
-